

DISS. ETH N°. 20804

Droplet Target for Laser- produced Plasma Light Sources

DISSERTATION

submitted to

ETH ZURICH

for the degree of

DOCTOR OF SCIENCES

presented by

Bob Rollinger

MSc ETH ME

born March 26, 1981

citizen of Luxembourg

accepted on the recommendation of
Prof. Dr. Reza S. Abhari, examiner
Prof. Dr. Dimos Poulikakos, co-examiner

2012

Acknowledgments

In 2007, the Laboratory for Energy Conversion (LEC) at the Swiss Federal Institute for Technology in Zurich launched the ALPS research project on laser-produced plasma light sources. The present work is the first PhD thesis that has been completed at LEC in this area of research. Being involved in the development of this new facility has been an invaluable experience.

First and foremost I would like to acknowledge my supervisor Prof. Reza S. Abhari, who has provided an outstanding research environment. Prof. Abhari has been a constant source of knowledge and guidance over the course of my PhD. I am deeply thankful for being given the opportunity to work on this exciting research topic. I particularly appreciated the team work in the lab, the numerous visits to conferences all over the world and the possibility to develop many interdisciplinary skills.

I am very grateful to Prof. Dimos Poulidakos for accepting the role of co-examiner and for his corrections and suggestions concerning this thesis.

I want to particularly thank Dr. Oran Morris, firstly for his overall support as a team member of the ALPS group and secondly for reviewing the thesis.

Special thanks go to all members of the ALPS group. I would like to sincerely thank Dr. Ndaona Chokani for his very valuable supervision during the initial phase of the project. I would like to express my gratitude to Dr. Davide Bleiner, who supported my work in the initial stages. My thanks also go to Ian Henderson for his important support during the experimental phase. I want to particularly thank Andrea Giovannini for the several years of team work and for the many discussions, which helped to clear many hurdles. Additional thanks go to Dr. Nadia Gambino and Luna Bozinova. I would also like to acknowledge Dr. Samir Ellwi and Fariba Abreau from Adlyte. I express my gratitude to Flori Alickaj for his help in terms of electronic equipment. I thank Dr. Michel Mansour for his support during the development of the liquid metal pressure probe. Thanks also go to Ilias Bosdas for making the shock tube measurements possible and to Johannes Hengstler from IMES for his support during the vibrometry measurements. I also acknowledge Armin Zemp for the useful discussions about mechanical response measurements. I would like to thank Michel

Busquet and Prof. Marcel Klapisch from the Hullac development team, as well as Prof. Graeme Bird for providing the source code of his DSMC simulation tool.

I would like to extend my thanks to all members of the LEC for creating this highly productive, but also friendly atmosphere. I always enjoyed working at LEC. Special thanks go to Marlene Hegner for her great support and patience in all administrative matters. Ein grosses Dankeschön geht auch an die LEC Werkstatt. Ich habe stets die Qualität der Arbeit, die Flexibilität und das angenehme Arbeitsklima geschätzt. Ein spezieller Dank geht an Thomas Künzle für die grossartige Arbeit im Zusammenhang mit dem Tropfengenerator. Desweiteren möchte ich mich aber auch bei Rolf Rüttimann und Claudio Troller für ihren Einsatz bedanken.

Finally I would like to thank my family and friends in Switzerland and Luxembourg. Thanks go to my parents for all the support they have given me throughout my studies. Fabienne deserves a very special thank you for the constant support, patience, understanding and encouragement throughout the years of my PhD.

Abstract

The present work is related to the field of droplet-based laser-produced plasmas (LPP) in soft X-ray and, more specifically, extreme ultraviolet (EUV) sources. EUV sources generate light at 13.5 nm and are employed in EUV lithography, which is the leading candidate to become the semiconductor manufacturing technology for post-193nm immersion lithography. One of the key factors, which limits the operating time of EUV sources, is the generation of tin droplets within the required specifications, such as large droplet spacing, micrometer droplet size and high stability. This work is conducted in the context of the development of a fully functional tin droplet-based high power LPP light source at the Laboratory for Energy Conversion, ETH Zurich.

The first objective of this work is to develop, manufacture and assess the performance of a tin droplet dispenser, which is required to generate a monodisperse stream of droplets with frequencies above 10 kHz in the harsh vacuum and plasma environment of an EUV source. Preliminary droplet requirements demand droplet sizes in the range of tens of micrometers, maximized droplet spacings and high temporal and spatial stability with respect to the laser focus. Droplet generation is based on the Rayleigh breakup of the tin jet. The modular design relies on replaceable cartridges, which consist of the high pressure rated (>50 bar) source material reservoir and the micrometer-sized nozzle. The forced excitation of the tin jet is ensured via an oscillating piston inside the tin reservoir. Acoustic pressure fluctuations form at the tip of the piston and propagate to the nozzle. Active cooling of the piezoelectric actuator ensures long operating times and permits large temperatures (>300°C) in the rest of the system.

The experimental methods, which are required for the performance assessment of the newly developed dispenser, rely on the imaging of the droplet train with a fast CCD and LED flash, as well as droplet tracking with a laser-photodiode light barrier. It is observed that for a fixed nozzle size, small droplet diameters are obtained at high frequencies and low backpressures, while large droplet spacings are generated for the inverse conditions. The lateral displacement is split up into high and low frequency contributions. Although low frequency lateral displacements are in the range of ten droplet diameters (3σ), they can be compensated for by position control of the dispenser. High frequency fluctuations of the lateral position yield three standard deviations of one droplet diameter. Lateral displacements are correlated with the level of flow impurities in the nozzle, which can be mitigated by efficient contamination control. The drop-to-drop timing jitter equals

5% of the mean droplet interval at typical operating conditions. A strong sensitivity of the droplet jitter with respect to the excitation frequency is observed.

A high temperature (255 °C) fast response (< 100 kHz) pressure sensor for use in liquid tin is developed and employed to measure the frequency dependent pressure at the nozzle inlet. Real-time monitoring of the nozzle inlet pressure is possible. A reference measurement, at representative conditions for source operation, reveals a complex pressure response, with a maximum pressure amplitude of 440 mbar. The dispenser is investigated by laser Doppler vibrometry. A validated finite element analysis shows that the structural resonances at the piston tip result from the coupling of axial eigenmodes of the piston and the axial eigenmodes of the piezoelectric actuator. Good agreement is found between the structural and the pressure response. This implies that the fluid-structure interactions and the fluid do not significantly add or shift resonance peaks.

The correlation between the measured nozzle inlet pressure and the droplet timing jitter is determined by a frequency sweep of the excitation frequency with simultaneous measurements of droplet timing. The corresponding pressure signal is used as an input for a droplet formation model, which predicts the corresponding timing jitter. Experimental and numerical results follow the same trend. A noise level (RMS) of 0.3% of the peak pressure amplitude is determined. With the help of computational fluid dynamics, the largest possible droplet spacing is estimated to be seven droplet diameters, which is comparable to the experimental results. With decreasing perturbation wave number, the growth rate of the main excitation decreases, while noise contributions with wave numbers with higher growth rates dominate and lead to a non-deterministic structure of the droplet train. The requirements for operation in a laser plasma source are best fulfilled when the dispenser excitation system is tuned to generate high acoustic pressures at the desired operating frequency and when the noise level on the jet is limited. The jet velocity is then adjusted by varying the reservoir pressure to find the optimum droplet stream wave number, according to the trade-off between lowest wave number and acceptable timing jitter.

Multi-scale computational tools are employed to predict the emission and debris characteristics of the previously generated tin droplets. For this purpose, an existing hydrodynamic code is extended with a radiation transport model, which is based on the flux-limited multigroup diffusion approximation. The emissivity and opacity terms in the electron energy and radiation energy density equations are derived from an atomic physics code. The validated radiation hydrodynamic (RHD) code is applied to a baseline case, which is representative of the experiments conducted at ETH Zurich. The expanding plume develops a significant anisotropy in terms of electron temperature and density. The radiation transport from the high temperature plasma core to the vacuum environment is strongly influenced by the non-uniformities in the plasma plume. From the laser axis (0°) to the direction perpendicular to the laser axis (90°), the full-band and EUV fluxes decrease by 34% and 61%, respectively. A source size of 100 µm is determined. A particle code, which is based on the Particle-In-Cell and Direct Simulation Monte Carlo approach for rarefied flows, is fully coupled to the RHD code. This hybrid particle-hydrodynamic code simulates the

plasma expansion up to the collector. The velocity and particle density distributions at the EUV collector are not uniform. The particle and kinetic energy distributions, together with the sputtering yields of molybdenum and silicon, are used to predict the collector life-time. On the outer border of the collector, a reflectivity loss of 10% is obtained after only two hours of source operation. The overall life-time is expected to be 3 hours in the absence of a debris mitigation system at an operating frequency of 6 kHz. The tin deposition, for the baseline case, is on the order 10^{-3} nm per pulse. As a conclusion, a highly efficient debris mitigation subsystem is required in order to meet the source requirements.

The selection of the droplet size results from a trade-off between the amount of acceptable debris and the required EUV energy per pulse. The tin droplet is fully vaporized for a droplet diameter of 10 μm . However, the EUV energy per pulse, generated using a 10 μm droplet, is almost 30 times smaller than for the 50 μm droplet. Therefore, very high (> 200 kHz) repetition rates would be required to meet the EUV source criteria. The interaction of the plasma with the subsequent droplet is very critical and estimated to lead to droplet fragmentation for the typical droplet spacings obtained from Rayleigh breakup. The largest experimental droplet spacings of 7.5 droplet diameters are estimated to be at the limit of fragmentation. The influence of the laser-droplet misalignment on EUV emission is quantified. At typical conditions, 80% overlap between the droplet and the laser yields a drop in EUV emission of 6 to 8%. The measured lateral stability is used to derive the corresponding dose stability. The EUV source requirements are fulfilled for a lateral instability (3σ) below 23 % of the droplet diameter (at a laser irradiance of 100 GW/cm^2). Larger laser irradiances increase this threshold. The same findings are valid for laser-droplet misalignments due to the timing jitter. Under typical operating conditions, the high frequency (> 0.5 Hz) part of the lateral droplet instability has three standard deviations of one droplet diameter. For a laser spot size of 80 μm and droplet diameter of 50 μm , the corresponding dose stabilities equal 0.8% and 0.3% for laser irradiances of 100 GW/cm^2 and 400 GW/cm^2 , respectively.

Zusammenfassung

Die vorliegende Arbeit befasst sich mit tropfenbasierten laserproduzierten Plasmas, welche im Wellenlängenbereich der weichen Röntgenstrahlen emittieren. Der Schwerpunkt der Arbeit liegt auf Lichtquellen im extremen Ultravioletten (EUV). Solche EUV-Quellen produzieren Licht mit einer Wellenlänge von 13.5 nm und werden in der EUV Halbleiterlithographie benützt. Diese Technologie zur Herstellung von Computerchips wird voraussichtlich in der nächsten Lithographie-Generation zum Einsatz kommen, welche der heutigen 193nm-basierten Immersionslithographie folgen wird. Einer der Hauptfaktoren, welcher die Laufzeit von EUV-Quellen einschränkt, ist die Herstellung von Zinntropfen mit den erforderlichen Eigenschaften wie ausreichendem Tropfenabstand, Grösse im Mikrometerbereich und hoher zeitlicher und räumlicher Stabilität. Diese Arbeit wurde im Rahmen der Entwicklung einer voll funktionsfähigen laserproduzierten Plasma EUV-Quelle am Laboratory for Energy Conversion der ETH Zurich durchgeführt.

Ein erstes Arbeitsziel besteht in der Entwicklung, Herstellung und Leistungsbewertung eines Tropfengenerators, welcher den geforderten monodispersen Tropfenstrahl mit Frequenzen über 10 kHz in der Hochvakuumumgebung der EUV-Quelle liefert. Die vorläufigen Anforderungen beschränken sich auf einen Tropfendurchmesser im Mikrometerbereich, einen maximalen Tropfenabstand, sowie hohe zeitliche und räumliche Stabilität gegenüber dem Laserfokus. Der zugrundeliegende Tropfenbildungsprozess ist der Rayleigh'sche Zerfall eines Flüssigkeitsstrahles. Die modulare Auslegung des Tropfengenerators basiert auf austauschbaren Kartuschen, welche aus einem Hochdruckbehälter (> 50 bar) und der Düse mit einer Öffnung im Mikrometerbereich bestehen. Die externe Anregung des Flüssigkeitsstrahles erfolgt über einen schwingenden Kolben, welcher im Behälter installiert ist. An der Spitze des Kolbens bilden sich akustische Druckschwellen aus, welche sich zur Düse hin ausbreiten. Eine aktive Kühlung des piezoelektrischen Aktuators erlaubt lange Laufzeiten und hohe Temperaturen (> 300 °C) des Gesamtsystems.

Die experimentellen Methoden, welche für die Leistungsbewertung des Tropfengenerators erforderlich sind, basieren auf der Visualisierung des Tropfenstrahls mit Hilfe eines schnellen Bildsensors (CCD) und eines LED Blitzes. Zusätzlich wird für die zeitliche Auflösung des Tropfenstrahls eine laserbasierte Lichtschranke benützt. Es kann gezeigt werden, dass, für eine gegebene Düsengrösse, kleine Tropfendurchmesser bei hohen Frequenzen und bei tiefem Behälterdruck erzeugt werden. Die lateralen Verschiebungen des Tropfenstrahls wird in einen tief- und hochfrequenten Teil aufgespaltet. Im tieffrequenten Anteil treten Verschiebungen bis zu 10

Tropfendurchmesser (3σ) auf, wobei diese Verschiebungen über ein Positionierungssystem kompensiert werden können. Die dreifache Standardabweichung der hochfrequenten lateralen Verschiebungen liegt im Bereich von einem Tropfendurchmesser. Des Weiteren kann gezeigt werden, dass die auftretenden lateralen Verschiebungen mit dem Grad der Verunreinigungen in der Düse korrelieren. Dieser negative Einfluss kann über ein effizientes Filtersystem reduziert werden. Die gemessenen zeitlichen Schwankungen des Tropfenabstandes entsprechen 5% des mittleren Abstandes unter typischen Betriebsbedingungen. Es wird eine starke Abhängigkeit der Schwankungen des Tropfenabstandes bezüglich Anregungsfrequenz festgestellt.

Um die frequenzabhängige Druckantwort am Düseneintritt zu bestimmen wurde eine schnell ansprechende (< 100 kHz) Hochtemperatur-Drucksonde (255 °C) entwickelt, welche die Druckwellen im flüssigen Zinn erfassen kann. Eine Überwachung in Echtzeit der Druckantwort am Düseneintritt wird somit ermöglicht. Eine Referenzmessung, welche bei typischen Betriebsbedingungen durchgeführt wurde, zeigt eine komplexe Druckantwort mit einer maximalen Amplitude von 440 mbar. Zusätzlich wurde der Tropfengenerator noch schwingungstechnisch mit einem Laser Doppler Vibrometer (LDV) analysiert. Eine experimentell validierte strukturmechanische Finiten-Elemente Simulation zeigt, dass die resonanten Auslenkungen an der Kolbenspitze durch die Kopplung von axialen Eigenmoden des Kolbens und des piezoelektrischen Aktuators bestimmt werden. Allgemein wird eine gute Übereinstimmung zwischen der Druckantwort und der Strukturantwort festgestellt. Dies heisst auch, dass die zusätzliche Interaktion zwischen der Struktur und dem Fluid die Druckantwort nicht signifikant verändert.

Der Zusammenhang zwischen der Druckantwort am Düseneintritt und den Schwankungen des Tropfenabstandes wird mit Hilfe eines Frequenzhubes des piezoelektrischen Aktuators mit gleichzeitigem Messen des zeitlich aufgelösten Tropfenabstandes bestimmt. Das entsprechende Drucksignal wird als Eingabe für ein Modell zur Tropfenbildung benützt, das helfen soll die entsprechende Schwankung des Tropfenabstandes vorauszusagen. Experimentelle und numerische Resultate stimmen weitgehend überein. Ein Rauschniveau (RMS) von 0.3% der maximalen Druckamplitude kann zusätzlich bestimmt werden. Mit Hilfe von numerischen Strömungssimulationen wird der maximal erreichbare Tropfenabstand von 7 Tropfendurchmessern bestimmt. Dieses Resultat deckt sich mit den Erkenntnissen aus den Experimenten. Eine Verminderung der Anregungswellenzahl führt zu einer Verminderung der Wachstumsrate der Hauptstörung, so dass Rauschanteile mit günstigeren Wellenzahlen dominieren und es somit zu einem nichtdeterministischen Zerfall des Strahles kommt. Die Anforderungen für den Betrieb des Tropfengenerators innerhalb einer laserproduzierten Plasmaquelle sind am besten erfüllt wenn das Anregungssystem auf hohe akustische Drücke bei der Betriebsfrequenz ausgelegt ist und wenn das Rauschniveau im Strahl minimiert wird. Die Strahlgeschwindigkeit wird anschliessend über den Behälterdruck so angepasst, dass die optimale Anregungswellenzahl erreicht wird, entsprechend dem Kompromiss zwischen tiefer Wellenzahl, sprich hohem Tropfenabstand und der annehmbaren Schwankung des Tropfenabstandes.

Im zweiten Teil der Arbeit werden numerische Werkzeuge entwickelt und eingesetzt um die Strahlungs- und Debris-Eigenschaften des tropfenbasierten Plasmas zu untersuchen. Zu diesem Zweck wird ein bestehender hydrodynamischer Simulationscode mit einem Strahlungstransportmodell erweitert, welches auf der Multigruppen-Diffusionsnäherung mit Flussbeschränkung basiert. Die Opazitäten und Emissivitäten, welche für die Lösung der Energiegleichungen der Elektronen und der Strahlungsenergiedichte erforderlich sind, werden mit Hilfe eines detaillierten numerischen Atommodells bestimmt. Das validierte strahlungshydrodynamische Programm (radiation hydrodynamic code, RHD) wird auf einen Referenzfall angewendet, welcher repräsentativ für die Betriebsbedingungen der EUV-Quelle der ETH Zürich ist. Das expandierende Plasma entwickelt eine ausgeprägte Anisotropie der räumlichen Verteilungen der Elektronendichte und Elektronentemperatur. Der Strahlungstransport vom Hochtemperaturkern des Plasmas zur Vakuumumgebung wird stark durch diese Anisotropie des Plasmas beeinflusst. Der Fluss der Ausserband- und der EUV-Strahlung nehmen von der Laserachse (0°) bis zur Richtung senkrecht zum Laserachse (90°) um 34%, beziehungsweise 61% ab. Die Quellengrösse wurde auf $100\ \mu\text{m}$ bestimmt. Ein Partikelcode, welcher auf den Particle-In-Cell und Direct Simulation Monte Carlo Methoden basiert, erweitert die Fähigkeiten des RHD Codes. Dieser hybride Simulationscode ermöglicht dann die Berechnung der Plasmaexpansion vom Tropfen bis zum EUV Kollektor der Lichtquelle. Die Partikel- und Geschwindigkeitsverteilungen am EUV Kollektor sind nicht homogen. Die Partikelverteilungen, sowie die Verteilungen der kinetischen Energie der Ionen können, zusammen mit den Abtragungsraten für Molybdän und Silizium benützt werden um die erwartete Lebensdauer des Kollektors abzuschätzen. Am äusseren Rand des Kollektors wird ein Verlust der Reflektivität von 10% nach zwei Stunden Betriebszeit vorausgesagt. Dies gesamte Lebensdauer liegt im Bereich von drei Stunden bei einer Betriebsfrequenz von 6 kHz und ohne Debrisschutz. Die Zinnablagerungen im Referenzfall liegen in der Grössenordnung von $10^{-3}\ \text{nm}$ pro Puls. Daraus wird der Schluss gezogen, dass ein hocheffizienter Debrisschutz benötigt wird um die Betriebsanforderungen der Quelle zu erfüllen.

Die Wahl des Tropfendurchmessers ergibt sich aus dem Kompromiss zwischen der annehmbaren Menge an Debris und der emittierten EUV Strahlung pro Puls. Der Zinntropfen wird bei einem Durchmesser von $10\ \mu\text{m}$ vollständig verdampft. Andererseits, ist die EUV Energie, welche pro Puls mit einem $10\ \mu\text{m}$ Tropfen erzeugt wird, rund 30 mal kleiner als bei einem $50\ \mu\text{m}$ Tropfen. Somit wären sehr hohe Betriebsfrequenzen notwendig um die erforderliche Leistung der EUV-Quelle zu erreichen. Die Interaktion zwischen dem expandierenden Plasma und dem nachfolgenden Tropfen wird als kritisches Problem eingestuft, da diese Interaktion zu einer Aufspaltung des nachfolgenden Tropfens führen kann. Die Tropfenabstände, welche typischerweise über den Rayleigh'schen Zerfall erzeugt werden liegen in diesem kritischen Bereich. Der grösste gemessene Abstand von 7.5 Tropfendurchmessern liegt an der Grenze der Fragmentierung des nachfolgenden Tropfens. Des Weiteren wird der Einfluss einer Falschrichtung des Lasersfokusses und des Tropfen auf die EUV Stabilität untersucht. Unter typischen Betriebsbedingungen führt eine Überlappung vom Laserfokus und Tropfen von 80% zu einem Abfall von 6%, beziehungsweise 8% der EUV Energie

pro Puls bei einer Laserleistungsdichte von 100 GW/cm^2 und 400 GW/cm^2 . In einem nächsten Schritt, werden die gemessenen lateralen Auslenkungen benützt um die Stabilität der EUV Dosis abzuschätzen. Die allgemeinen Anforderungen der EUV-Quellen sind erfüllt wenn die laterale Stabilität des Tropfenstrahles kleiner als 23% (3σ) des Tropfendurchmessers (bei einer Leistungsdichte des Lasers von 100 GW/cm^2) ist. Höhere Leistungsdichten erhöhen diese Grenze. Die gleichen Erkenntnisse sind gültig im Fall der Instabilitäten, welche durch Schwankungen des Tropfenabstandes hervorgerufen werden. Bei typischen Betriebsbedingungen beträgt der hochfrequente Anteil der lateralen Instabilität ein Tropfendurchmesser (3σ). Daraus ergibt sich bei einer Grösse des Laserbrennfleckes von $80 \mu\text{m}$ und einem Tropfendurchmesser von $50 \mu\text{m}$ eine Stabilität der EUV Dosis von 0.8%, beziehungsweise 0.3% für Leistungsdichten des Lasers von 100 GW/cm^2 und 400 GW/cm^2 .

Contents

Chapter 1 Introduction	1
1.1. <i>Laser-produced plasma soft X-ray sources</i>	1
1.1.1. Sources for X-ray microscopy.....	2
1.1.2. Sources for radiobiology	2
1.1.3. Sources for laser-driven fusion	2
1.2. <i>EUV lithography</i>	3
1.2.1. Optical lithography in semiconductor manufacturing.....	3
1.2.2. EUV lithography	7
1.2.3. EUV sources.....	9
1.2.4. LPP sources	12
1.2.5. EUV lithography source requirements	16
1.2.6. Droplet requirements in an EUV source.....	18
1.3. <i>Motivation</i>	19
1.4. <i>Literature survey</i>	20
1.4.1. Droplet generation	20
1.4.2. LPP modeling.....	21
1.5. <i>Research objectives</i>	22
1.6. <i>Thesis outline</i>	24
Chapter 2 Droplet dispenser design	25
2.1. <i>Introduction</i>	25
2.1.1. General remarks	25
2.1.2. Droplet dispenser requirements	26
2.1.3. Droplet generation	27
2.2. <i>Dispenser design</i>	28
2.2.1. Design overview	28
2.2.2. Thermal design.....	31
2.2.3. Mechanical design	36
2.2.4. Acoustic excitation.....	36
2.2.5. Nozzle design and contamination control.....	38
2.3. <i>Summary</i>	40

Chapter 3 Droplet dispenser performance	43
3.1. <i>Introduction</i>	43
3.2. <i>Experimental setup.....</i>	44
3.2.1. Diagnostics.....	44
3.3. <i>Results.....</i>	48
3.3.1. Droplet train imaging.....	49
3.3.2. Dispenser operating map	51
3.3.3. Droplet stability	53
3.4. <i>Summary and conclusion.....</i>	58
Chapter 4 Excitation dynamics.....	61
4.1. <i>Introduction</i>	61
4.2. <i>High temperature fast response pressure probe.....</i>	62
4.2.1. Introduction.....	62
4.2.2. Pressure probe design and performance	63
4.2.3. Validation and liquid tin measurements.....	72
4.3. <i>Fluid dynamic and structural response measurements.....</i>	77
4.3.1. Approach.....	77
4.3.2. Results.....	79
4.4. <i>Modeling of structural dynamics.....</i>	83
4.4.1. Simulation setup.....	83
4.4.2. Results.....	85
4.5. <i>Discussion.....</i>	90
4.6. <i>Summary and conclusion.....</i>	96
Chapter 5 Droplet formation	99
5.1. <i>Introduction</i>	99
5.2. <i>Numerical approach.....</i>	101
5.2.1. Droplet formation model.....	101
5.2.2. CFD simulation	106
5.3. <i>Experimental approach.....</i>	108
5.3.1. Non-dimensional numbers	108
5.4. <i>Results.....</i>	110
5.4.1. Basic observations.....	110
5.4.2. Influence of the excitation pressure on droplet timing.....	113
5.4.3. Prediction of operating boundaries	117
5.5. <i>Summary and conclusion.....</i>	120
Chapter 6 Numerical modeling of droplet-based laser-produced plasmas	123
6.1. <i>Physical processes in laser-produced plasma.....</i>	123
6.1.1. Laser coupling into matter and plasma formation	124

6.1.2. Radiation emission	126
6.1.3. Debris formation, propagation and damage potential	127
6.1.4. Multi-scale considerations.....	129
6.2. <i>Numerical modeling</i>	129
6.2.1. Radiation hydrodynamic code	130
6.2.2. Atomic physics code	142
6.2.3. Particle code	143
6.3. <i>Numerical results</i>	150
6.3.1. EUV opacity and emissivity.....	150
6.3.2. Baseline tin droplet results	160
6.3.3. Studies.....	186
6.4. <i>Summary and conclusion</i>	200
Chapter 7 Conclusions, summary and future work	203
7.1. <i>Conclusions</i>	203
7.2. <i>Summary and concluding remarks</i>	206
7.3. <i>Future work</i>	211
7.3.1. Droplet generation	212
7.3.2. Droplet-based LPP modeling in an EUV source	212
Appendix	215
REFERENCES	215
NOMENCLATURE.....	224
LIST OF PUBLICATIONS.....	227
CURRICULUM VITAE.....	228

Chapter 1

Introduction

1.1. Laser-produced plasma soft X-ray sources

Spectrally tailored emission can be produced by irradiating a specific target material with a high power laser. A laser-produced plasma (LPP) is formed above the surface of the target. In a first stage of the irradiation process, the electromagnetic laser light wave penetrates only a short distance (typically a fraction of the wavelength) into the target material. Multi-photon absorption leads to heating and vaporization of the target material. At sufficient laser irradiances, the target vapor is further heated by the incident laser pulse. The departing vapor induces a recoil pressure on the target. A compressive shock front travels through the target. The vapor temperature continues to increase as long as the incident laser energy compensates for radiation, expansion and thermal conduction losses. At sufficiently high vapor temperatures, a plasma is created. Plasma is considered to be the fourth state of matter and is reckoned to constitute around 99% of the universe. A plasma can be considered as a partially or fully ionized gas, which is composed of ions, electrons and neutral atoms. The free electrons in the plasma increase the rate of laser energy absorption by inverse bremsstrahlung. At the critical electron density, the plasma frequency, which corresponds to the electron oscillation frequency, approaches the laser frequency and the absorption is maximized. At higher electron densities, laser energy is no longer absorbed, but fully reflected.

Plasma temperatures of several hundred thousands of Kelvins are typically reached in soft X-ray sources. Indeed, the high plasma densities will ensure efficient energy transfer from the laser to the

plasma. The plasma therefore intensively emits in the soft X-ray wavelength window of the electromagnetic spectrum. The spectral emission strongly depends on the excited ions and their respective atomic structure. In the laboratory, the extreme conditions of laser-produced plasmas can only be maintained for a very short time. Typical time durations of the soft X-ray emission are in the range of nanoseconds. This time scale corresponds to the duration of the laser pulse. The physical processes, which are involved in the creation and evolution of LPPs, are described more in detail in Sec. 6.1. A large amount of literature is available on the physics of LPPs and X-ray emission.¹⁻⁴

The high spectral brightness of LPP based X-ray sources is due to line emission. This limits the possibilities of wavelength tuning of such sources, as the line emission depends on the atomic structure of the target material. The wavelength can be changed by switching from one or a set of emission lines of one element to other emission lines of the same element, or to a completely different element. LPP light sources are not continuously tunable like synchrotron sources. Nevertheless, many applications require a fixed wavelength emission. Typical applications include X-ray microscopy, radiobiology, laser-driven fusion and X-ray lithography.

1.1.1. Sources for X-ray microscopy

X-ray microscopy is used to overcome the inherent resolution limits of optical microscopy, as the typical X-ray wavelengths are two orders of magnitude smaller than visible light. A major application of X-ray microscopy is the inspection of biological tissues. The optimum inspection wavelength is located in the “water window”, which lies between the absorption edges of oxygen and water. The corresponding wavelengths are located in the spectral range from 2.3 to 4.4 nm. High contrast images of biological tissues, which consist of carbon structures in aqueous solutions are obtained. Examples of X-ray sources for biological tissue inspection are given in Turcu *et al.*¹ The first operative compact X-ray microscope for the water window region has been developed by Hertz *et al.*^{5,6} The microscope includes a 100 Hz liquid-jet-target LPP X-ray source, a normal-incidence multilayer condenser optic, diffractive zone plate optics and a CCD detector. Hard X-rays for microscopy with zone plate optics have been generated in the work of Tompkins *et al.*⁷

1.1.2. Sources for radiobiology

Laser plasma sources with line emission around 1 nm are attractive for experiments in radiobiology.¹ The motivation for studying radiobiological effects is given in the review of Goodhead.⁸

1.1.3. Sources for laser-driven fusion

One of the first droplet-based LPP sources has been developed for the study of laser-driven fusion by Schwenn *et al.*⁹ The hot dense plasma, which is produced by laser heating of a droplet target in a vacuum environment, is studied in the field of controlled nuclear fusion. In the early work on laser

fusion, micrometer sized pellets of hydrogen isotopes have been irradiated. Repetition rates went up to 1 kHz. The pellet's spatial deviation from the irradiation point had to be small compared with the diameter of the pellet. Limitations in guiding precision, reproducibility issues and limited pellet roundness led to the development of the first droplet-based LPP sources. Typically liquid deuterium from a helium cooled container has been dispensed. A significant amount of pioneering work in droplet-based LPPs dates back to the initial studies of laser-driven fusion.¹⁰⁻¹²

The present work is related to the use of LPP sources in X-ray lithography. With the advent of EUV lithography, the research effort in the field of X-ray sources significantly increased.

1.2. EUV lithography

1.2.1. Optical lithography in semiconductor manufacturing

1.2.1.1. Economic perspective

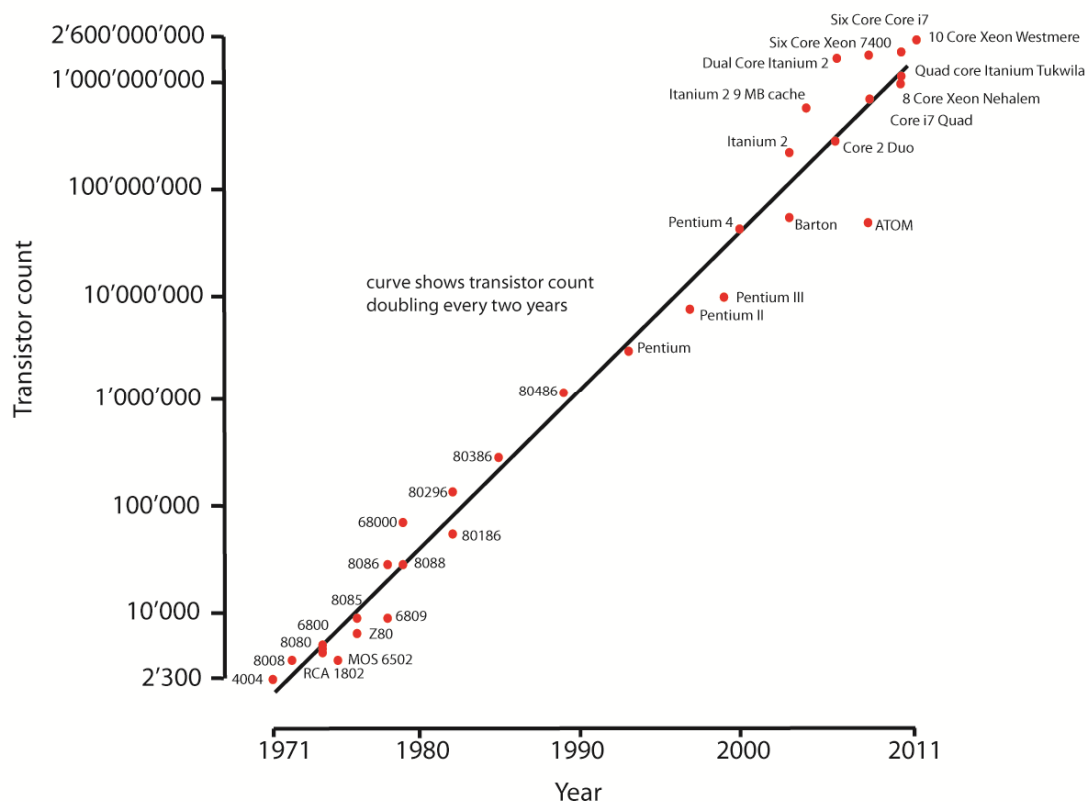


Fig. 1. Illustration of Moore's law from 1971 to 2011 for Intel's microprocessors

Gordon Moore, co-founder of the semi-conductor manufacturer Intel, was challenged in 1965 with predicting what would happen to the number of transistors on an integrated circuit over the

following 10 years. During his analysis, he noticed that from the first days of the planar transistor about 10 years ago, the amount of transistors on a chip had doubled approximately every year. His predictions held for nine of the ten following years. In 1975, he revisited his law by declaring that the number of transistors on a chip would double every two years. This law is today well-known as Moore's law. The semi-conductor industry has maintained the rate predicted by Gordon Moore for the last 37 years. The evolution of the number of transistors is illustrated for Intel's microprocessors in Fig. 1.

The semiconductor industry formed around 1960, when the manufacturing of semiconductors became a viable business. In 2011, the semiconductor market grew to a \$249 billion dollar market and is projected to break the \$300 billion dollar threshold in 2012-2013.¹³ The end application drivers have evolved over time. Initially, chips were almost exclusively employed in aerospace and military applications. With the rise of the personal computer after 1980, the semiconductor market started to grow significantly. Today the market is substantially driven by mobile internet devices.¹⁴

1.2.1.2. Present lithography

Optical lithography is the manufacturing technique used to fabricate integrated circuits (ICs) and microelectromechanical systems (MEMS). Presently, three different approaches are employed in optical lithography, namely projection, contact and proximity lithography. In optical projection lithography, a mask pattern is imaged onto the wafer by a reduction lens, as shown in Fig. 2. The condenser optics usually have a variable numerical aperture (NA), which is useful in defining the angular distribution of the incident light on the mask. The numerical aperture NA is given by $NA = n \sin \theta$, where n is the refractive index of the background medium and θ is the maximum angle of incidence of the focused light. The condenser forms an image of the source on the so-called pupil plane, before undergoing a typical demagnification of 4:1 on the wafer surface. The surface of the wafer is coated with a photoresist, which is a light-sensitive polymeric substance. The light changes the chemical structure of the resist so that it becomes more soluble in a developing solution. The resist is then washed away by the solution and leaves an exact copy of the reticle pattern on the wafer. Some types of resist work in the opposite manner, as they harden when exposed to light.

In projection lithography, the minimum achievable line width L_w on the wafer is given by²

$$L_w = k_l \times \frac{\lambda}{NA} \quad (1.1)$$

where k_l is a process constant and λ is the wavelength of the incident light. The equation is similar to Rayleigh's law, where k_l equals 0.61. In projection lithography, the process constant depends on the optical system, the photoresist and the overall process. Downscaling of semiconductor devices is achieved by varying the numerical aperture of the optical system and the wavelength of the employed light source.

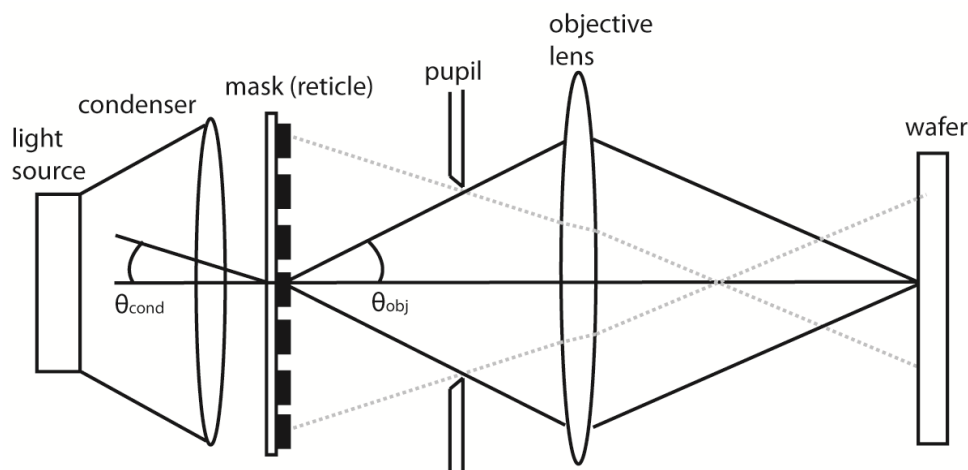


Fig. 2. Schematic of projection lithography. A mask pattern on a transmissive reticle is imaged to the wafer plane by an objective lens. The light source illuminates the mask through the condenser optics.²

Presently, semiconductor devices are manufactured using the double patterning approach in combination with immersion lithography. Double or multiple patterning increases the density of features. In immersion lithography, the usual air gap between the wafer and the final lens is filled with highly purified water. By doing so, the refractive index n increases to a value more than one and the optical resolution increases accordingly. The light source, which is employed in today's lithography tools is a deep ultraviolet (DUV) laser. Argon fluoride lasers with a wavelength of 193 nm are commonly used. These technologies enable feature sizes of 22 nm in multiple processors units (MPUs). The transition to a new process wavelength is becoming necessary, as multi-patterning is not cost-effective. The next generation lithography will be based on extreme ultraviolet (EUV) light. The transition to EUV lithography (EUVL) is inevitable due to cost reduction issues.

1.2.1.3. Semiconductor roadmaps

The manufacturing of semiconductor devices involves the use of specialized tools, which are built by a variety of companies. In order to ensure good coordination between the different suppliers, a consortium of semiconductor industry experts defines a technological roadmap, which anticipates the evolution of the market and controls the technological needs for semiconductor manufacturing. The group of experts generates the International Technology Roadmap for Semiconductors (ITRS).¹⁵

When defining the roadmap for semiconductors, the requirements related to lithography are taken into account. One of the key requirements for lithography is critical dimension (CD) control. The size of printed features needs to be maintained in each exposure field, on each wafer and from wafer-to-wafer. CD control determines the overall circuit performance. The second requirement is overlay, which is related to the accurate placement of the image with respect to the underlying layers. Thirdly, defect control is required for the desired pattern to print correctly. The cost of tools,

1.2 EUV lithography

materials and masks should be minimized, without compromising the previous three requirements. The proposed potential manufacturing technologies for MPUs and DRAM (dynamic random access memory), as well as NAND (flash memory, non-volatile memory) devices are presented in Fig. 3 and Fig. 4 respectively.¹⁵

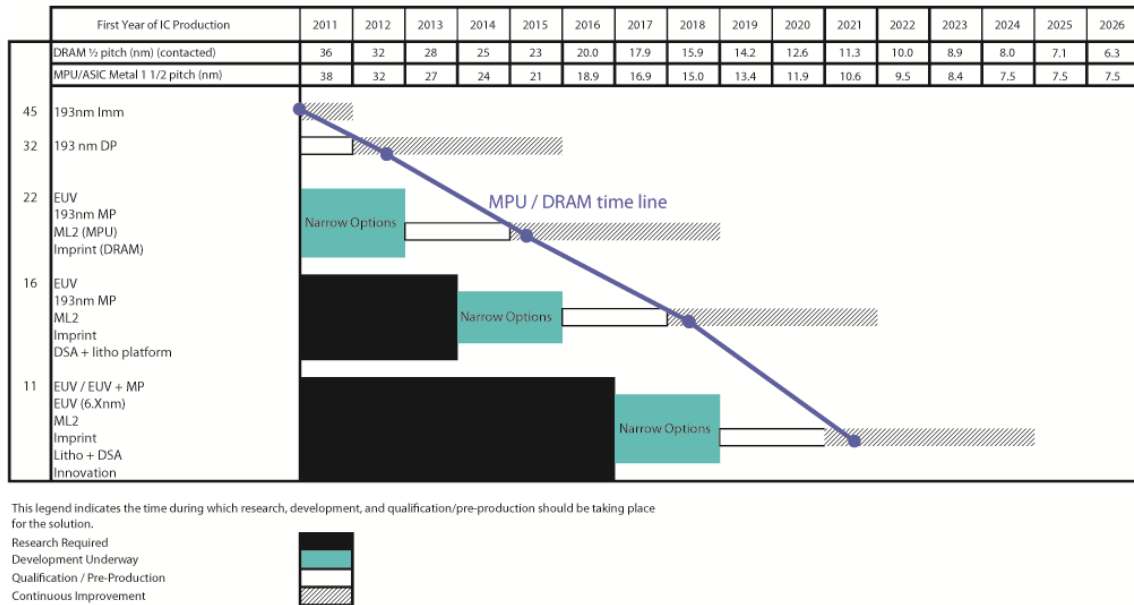


Fig. 3. ITRS roadmap for MPU and DRAM devices. EUVL is a candidate technology for node sizes below 32 nm.¹⁵

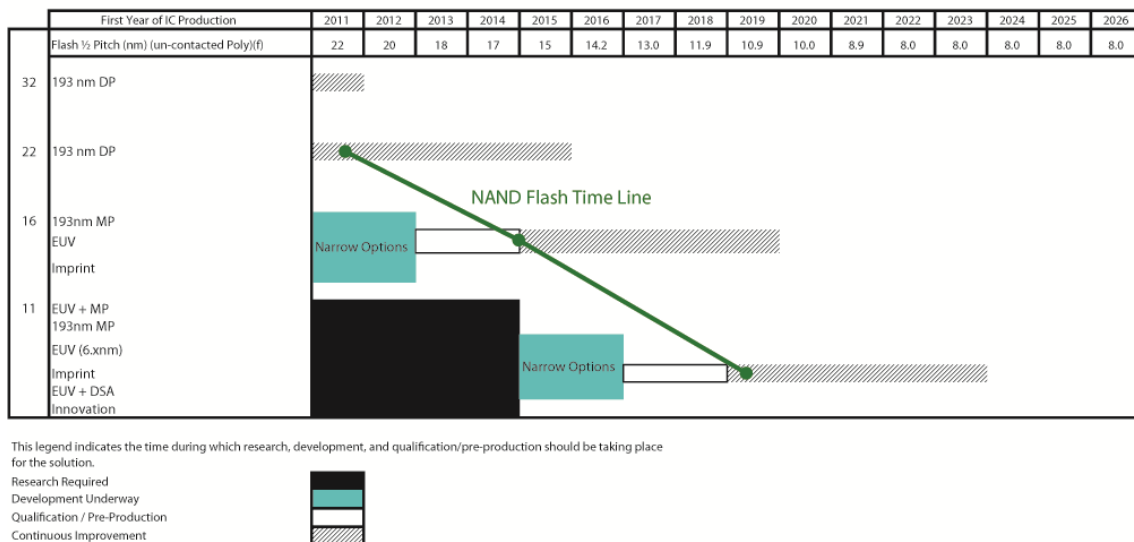


Fig. 4. ITRS roadmap for NAND devices. EUVL is a candidate technology for node sizes below 22 nm.¹⁵

Different manufacturing technologies, such as imprint, direct self-assembly (DSA) and maskless lithography (ML2), which includes direct writing with e-beams, are considered besides EUVL. For

small node sizes, the so-called BEUV (“Beyond EUV”) technology, with wavelengths around 6 nm, is considered. The main candidate technologies for future node sizes beyond 32 nm are multi-patterning and EUVL. For the 22 nm node, the qualification phase is scheduled for 2013. The pre-production phases for 16 nm and 11 nm node sizes are planned for 2016 and 2019, respectively. For NAND devices, the potential EUVL qualification and pre-production phases are scheduled for 2013 with an introduction into pilot lines in 2015 for a target feature size of 16 nm. A similar qualification phase for the 11 nm node size will start in 2017. EUVL has benefits in terms of cost per wafer¹⁶ and gives room for downscaling opportunities.¹⁷ Furthermore, the technology does not induce a radical change in the manufacturing process, which facilitates its acceptance in industry. The challenges related to the pilot line introduction of EUVL are described in the next sections.

1.2.2. EUV lithography

EUVL will be based on EUV light with a central wavelength of 13.5 nm in a 2% bandwidth centered on 13.5 nm. This wavelength choice is due to the molybdenum / silicon (Mo/Si) multilayer (ML) mirrors,¹⁸ which have very high reflectivity (up to 70%) at 13.5 nm.¹⁹ A typical EUV ML reflectivity curve,²⁰ together with a tin emission spectrum from this work (Sec. 6.3.1.2.1) is presented in Fig. 5. Measured reflectivity curve of an EUV ML sample.²⁰ The tin emission spectrum, which is shown for comparison (not scaled), is taken from Sec. 6.3.1.2.1. As EUV radiation is strongly absorbed by all materials, the optics are reflective (as opposed to the refractive optics of the present lithography). A single molybdenum interface will reflect a small fraction of an incident EUV beam. For this reason, ML mirrors, which consist of substrates coated with a large (>50) number of bilayers of Mo and Si are employed. If the layer thicknesses are properly chosen for a given wavelength and angle of incidence, the mirrors obey Bragg’s law. In this case, the reflectivity of the optics drastically increases, as the reflected beams from the individual layers add up, when in phase. The layer thicknesses in the EUV mirrors are 4.2 nm and 2.8 nm for Si and Mo, respectively.

EUVL scanners differ significantly from today’s DUV based scanners, not only because of the use of reflective optics, but the entire system must be enclosed in a vacuum environment. The typical layout of an EUVL scanner is shown in Fig. 6. The EUV source, which is extensively described in the next section, generates light at a central wavelength of 13.5 nm in a bandwidth of 2% centered at 13.5 nm. EUV light is emitted from a plasma and reflected by the source collector to the intermediate focus (IF). The IF constitutes the interface between the EUV source and the rest of the EUVL scanner. The source is part of the source collector module (SoCoMo) of the EUVL scanner. After IF, light enters the (illuminator) condenser optics section. A key element of the illuminator section is the fly’s eye mirror, which defines the illumination type (annular, dipole,...) of the mask.²² EUV masks, which are located at the so-called reticle stage, consist of a reflective ML and an absorber layer in order to define the mask pattern. Mask manufacturing is based on e-beam removal of the absorber.²³ After mask illumination, light enters the projection optics module, which determines the NA of the system. Although the drop in transmitted EUV energy per mirror is on

the order of 60%, configurations with up to 8 mirrors are considered for NA larger than 0.5.²¹ In the first tools, 6 mirrors are planned for the illumination module with a NA of 0.32. A major challenge in the manufacturing of the ML optics is the low surface roughness, which is on the order of 80 pm.²¹ Light is projected onto the wafer, which is covered by a specific EUV resist. A first pre-production tool, which has been delivered to chipmakers in 2011, is the NXE:3100 tool from ASML.²⁴ This first fully integrated EUVL scanner is shown in Fig. 7.

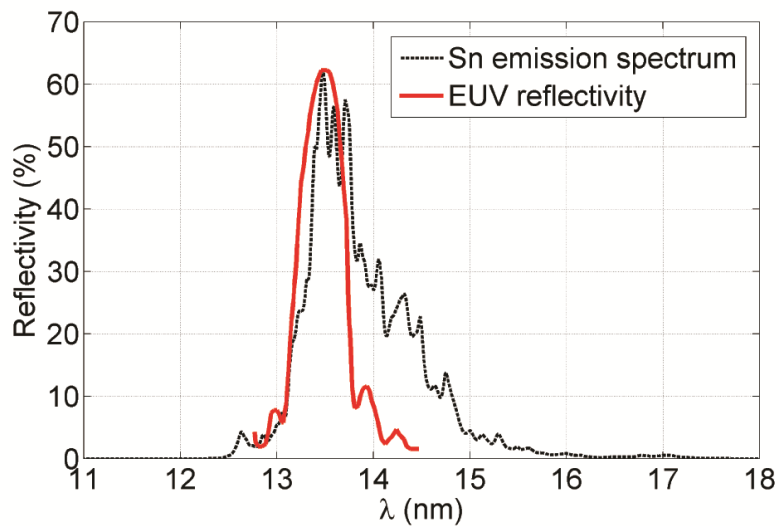


Fig. 5. Measured reflectivity curve of an EUV ML sample.²⁰ The tin emission spectrum, which is shown for comparison (not scaled), is taken from Sec. 6.3.1.2.1.

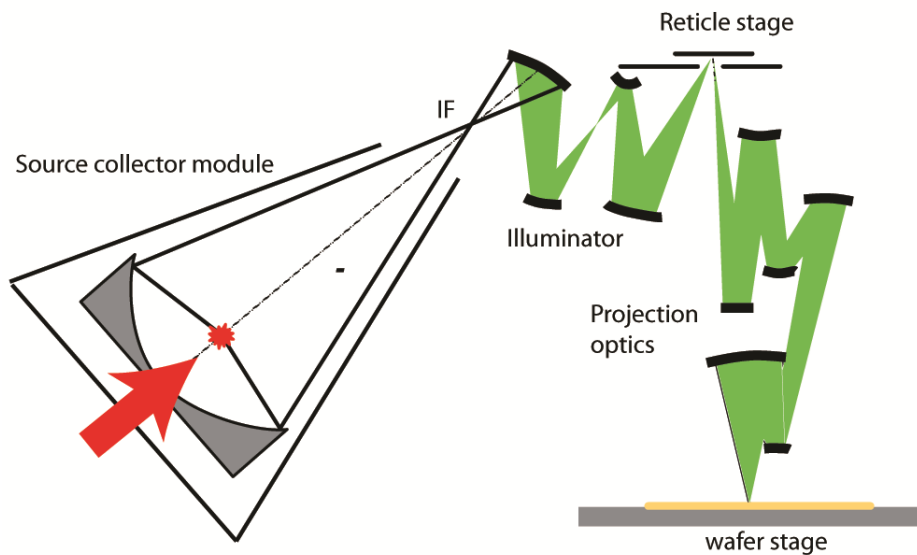


Fig. 6. EUVL scanner layout with source module and illuminator/ projection optics design according to Zeiss for $NA=0.32$.²¹

A critical issue in semiconductor manufacturing is mask inspection. Inspection of EUV masks at the actinic wavelength is required in order to detect small defects, which would otherwise print onto the wafer and result in an unacceptable yield.^{25, 26} Such tools also require EUV light sources with different performance characteristics than the high power sources in the EUVL scanner. Details are provided in the next sections. Mask inspection and metrology tools include Actinic Blank inspection (ABI), Actinic Pattern Inspection (API) and the Aerial Image Measurement System²⁷ (AIMS). The AIMS tool is being designed to emulate the aerial image formed by an EUVL scanner.

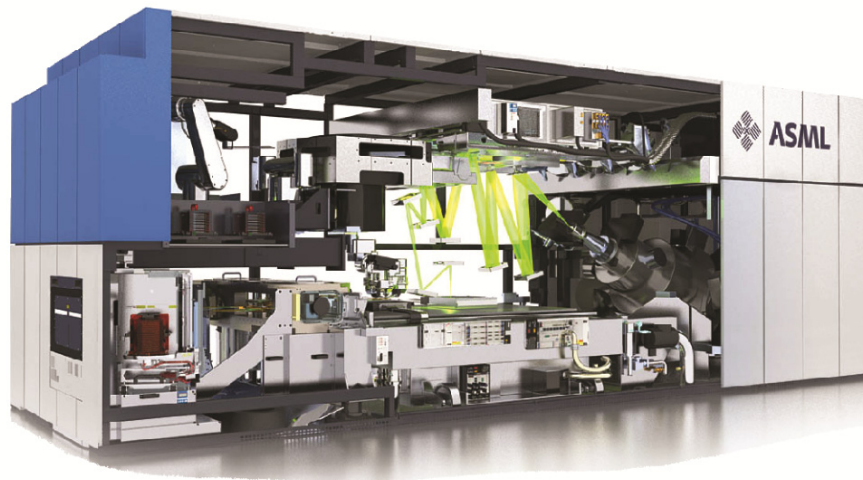


Fig. 7. Overview of ASML's NXE:3100 EUVL scanner.²⁴ The SoCoMo is located on the right side. EUV light is marked in green. The reticle stage is located on top of the system and the wafer stage at the bottom. The whole system is enclosed in vacuum. Cost of the scanner is estimated at >\$50 million.²³

1.2.3. EUV sources

EUV emission is obtained from specific elements, which have a high spectral emission at 13.5 nm. A criterion for choosing an element is the conversion efficiency (CE), which corresponds to the ratio of emitted EUV energy into 2π sr with respect to the input energy. Elements, which are capable of producing radiation at the required EUV wavelengths, include lithium, xenon and tin. Lithium is not regarded as a suitable source material due to its high level of reactivity. Additionally, low CEs have been measured.²⁸ The ability of these elements to produce in-band radiation is due to the fact that they have atomic structure transitions, which emit brightly in this bandwidth. In the case of xenon atoms, the main emission is located near 11 nm and the in-band emission from a xenon atom originates from transitions in a single ion stage, namely Xe^{10+} .²⁹ The maximum CE attained for Xe is approximately 1%.³⁰

Tin transitions in ions ranging from Sn^{8+} to Sn^{12+} form a line group near 13.5 nm.³¹ Emissions from these transitions are the strongest features in the tin EUV spectrum. The contribution of these five tin ion stages results in a theoretical CE of 6 to 8%.³² Experimental measurements of approximately 5% have already been reported for the CE of tin plasmas on solid targets.³³ The

plasma temperature, which corresponds to the generation of the required tin ions can be derived from the collisional radiative model of Colombant *et al.*³⁴ More details follow in Sec. 6.2.1.2. Tin ions from Sn^{8+} to Sn^{10+} are the strongest EUV emitting ion stages.³⁵ As a consequence, a plasma temperature around 30 eV ($\approx 300'000$ K) is required, as shown in Fig. 8. For plasma temperatures around 40 eV, all EUV emitting ions of tin contribute to the in-band emission, which is centered at 13.5 nm and contained in a 2% bandwidth window centered at 13.5 nm. As mentioned, this is not the case for a xenon plasma, where only one ion stage, namely Xe^{10+} contributes to EUV emission. This explains the discrepancy in CE between tin and xenon. The low CE of xenon turned out to be a severe limitation for use in EUVL scanners. Xenon-based sources are still used in discharge-produced plasmas (DPPs) in laboratory-type sources.³⁶

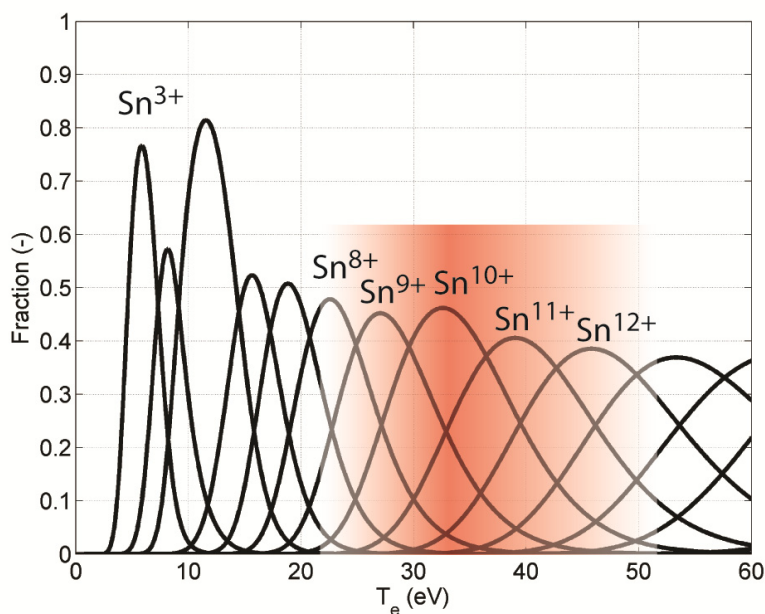


Fig. 8. Fractional distribution of tin ions as a function of electron temperature. EUV emitting ions are generated at temperatures from 25-45 eV. EUV emission is strongest for nearly ten times charged ions.³⁵

1.2.3.1. DPP versus LPP sources

Two main methods for generating the EUV emitting plasma are being used in EUV sources. The alternative to a LPP is the DPP, where the excitation is achieved through an electrical discharge. The LPP and DPP source layouts are presented in Fig. 9. Both source types comprise an EUV emitting plasma and a collector, which is either based on normal incidence (LPP) or grazing incidence (DPP). Both sources feature a plasma debris mitigation system to protect the collection optics.

Current high power DPP sources use tin as a source material. The main issue with the first EUV DPP sources has been power dissipation at the stationary electrodes, which limited power scalability

for high volume manufacturing (HVM). A more promising source concept is based on a so-called laser-assisted discharge plasma (LDP).³⁷ Rotating, tin-covered electrodes are employed. Tin pumps constantly feed the rotating electrodes with liquid tin. A laser is used to ablate material from one of the liquid electrodes. The vapor expansion, which is normal to the electrode surface, leads to a good axial symmetry of the pinching dynamics. A detailed comparison of LPP and LPD technologies is given in Schriever *et al.*³⁸ The debris mitigation system is based on a rotating foil trap, which catches most of the debris, while radiation can pass through.³⁹ The actively cooled collector is based on grazing incidence and coated with ruthenium.⁴⁰

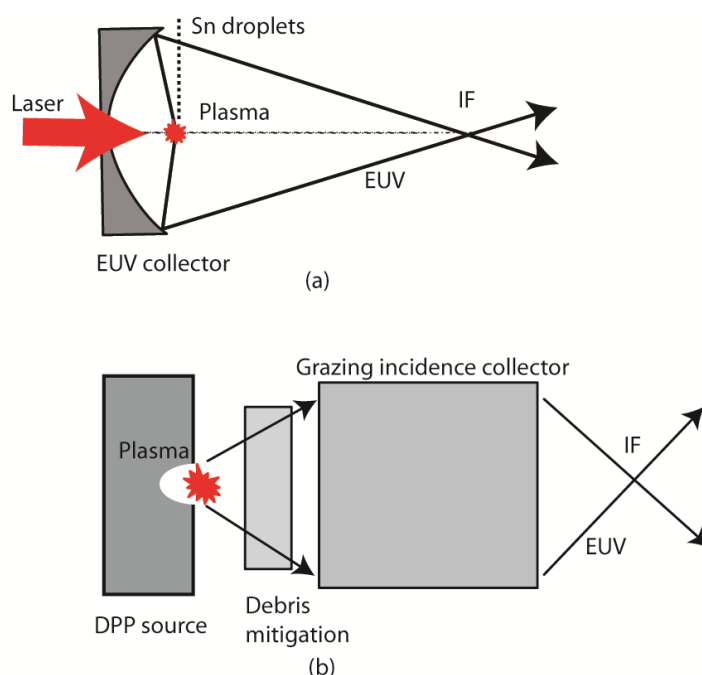


Fig. 9. (a) LPP source layout with droplet target and normal incidence collector. (b) DPP source layout with discharge-based source, debris mitigation system and grazing incidence collector.

In practice, LPP sources have a much smaller source size than DPP sources. In addition, as the laser beam is delivered onto the target surface from a distance in vacuum, the focusing optics are kept away from the plasma, as shown in Fig. 9. For this reason, no special thermal management of the focusing optics is required. For the DPP case, electrodes in close proximity to the plasma are required, where significant heating takes place in the partial vacuum environment, potentially limiting the input system power. This gives the LPP approach an edge in achieving higher power and brightness, compared to a DPP. High power is required in HVM applications, while high brightness is needed in metrology tools. The LPP EUV source has the potential to fulfill future application requirements due to its adaptability and scalability. The area where, in general, a DPP tends to perform better than an LPP is in achieving the stability requirements. This is primarily due to the inherent difficulty in delivering the focused laser beam at exactly the same position onto a regenerative fuel in vacuum. For the DPP however, the target tends to be stationary, making it easier to achieve the required stability.

1.2.4. LPP sources

1.2.4.1. Working principle

The EUV LPP source relies on the generation of a LPP by target heating, vaporization and ionization, as described in Sec. 1.1. The simplified system layout of a LPP source is shown in Fig. 9. A high power laser (kilowatt range) irradiates a tin target. Source material is usually delivered in the form of tin droplets. Droplets are mandatory for long-term operation, as they form a regenerative target. The soft X-ray emission in the EUV window is reflected by a normal incidence ML collector to the IF. The collector is of an elliptic shape with the LPP being located at the first focus and the IF at the second focus. The generation of the EUV emitting ions is inherently coupled to the generation of plasma debris, which is harmful to the multilayer optics. Debris should not pass into the other stages of the EUVL scanner. Power scaling is mainly achieved by increasing the repetition rate. An increase of EUV energy by increasing the irradiation time⁴¹ and irradiated surface⁴² per pulse affects the amount of debris and the obtained CE. Increasing the CE increases EUV output without requiring more laser power. The four main subsystems are the droplet dispenser, the normal incidence collector, the debris mitigation system and the laser.

1.2.4.2. Targets

Solid tin slab targets were used in the past, rotating at a sufficient speed to present a fresh target surface for each laser pulse. The thermal load from the incident laser light and radiation from the LPP melts the target surface. The interaction of the molten tin with the drive laser leads to tin splashing in the source chamber, generating additional uncontrollable debris.⁴³ Fundamental research is typically conducted with low repetition rate lasers, which irradiate planar tin targets.

In order to meet the current LPP source requirements (detailed in Sec. 1.2.5) for EUVL or actinic mask inspection, a method of accurately delivering target material at a high repetition rate (many kHz) is required. A variety of targets have been investigated, including porous low density SnO₂ targets,⁴⁴⁻⁴⁶ mass limited Sn targets,^{47, 48} Sn doped foam targets,⁴⁹ laser evaporated cavity confined tin vapour targets,⁵⁰ liquid-metal tin jets,⁵¹ tin-rich thin layer targets⁵² and water/tin chloride⁵³ droplet targets. However, today the common target of choice, with the highest EUV conversion efficiency for continuous long-term operation, is the micrometer-sized tin droplet.^{54, 55}

1.2.4.3. Debris

Basically three types of debris are distinguished for droplet targets, namely high energy ions, low energy particles and small droplet fragments. Fast ions cause erosion of the surface of the ML collector. The sputtering of the ML collector results in an unacceptable drop in reflectivity. Low energy particulate debris deposits onto the surface of the optics and also causes a reflectivity drop. Deposition thicknesses on the order of 1 nm are sufficient to induce a replacement of the collector.⁵⁶ Debris from droplet fragmentation also leads to tin deposition on the EUV collector.

The control of droplet fragmentation is done by selecting an optimum laser-target irradiation scheme. Debris mitigation strategies for tin ions and low energy particles are described in Sec. 1.2.4.5.3.

1.2.4.4. Implementation

A typical LPP source is a complex machine designed to operate at the highest level of performance and system integration. At the Laboratory for Energy Conversion, ETH Zurich, a fully functional high power LPP light source has been developed over the last 5 years. This system is representative for other droplet-based LPP sources. The EUV source is used as an engineering test stand (ETS). Different collector optics are used to either run the source in high power HVM mode⁵⁷ or as a metrology source with high brightness⁵⁸.

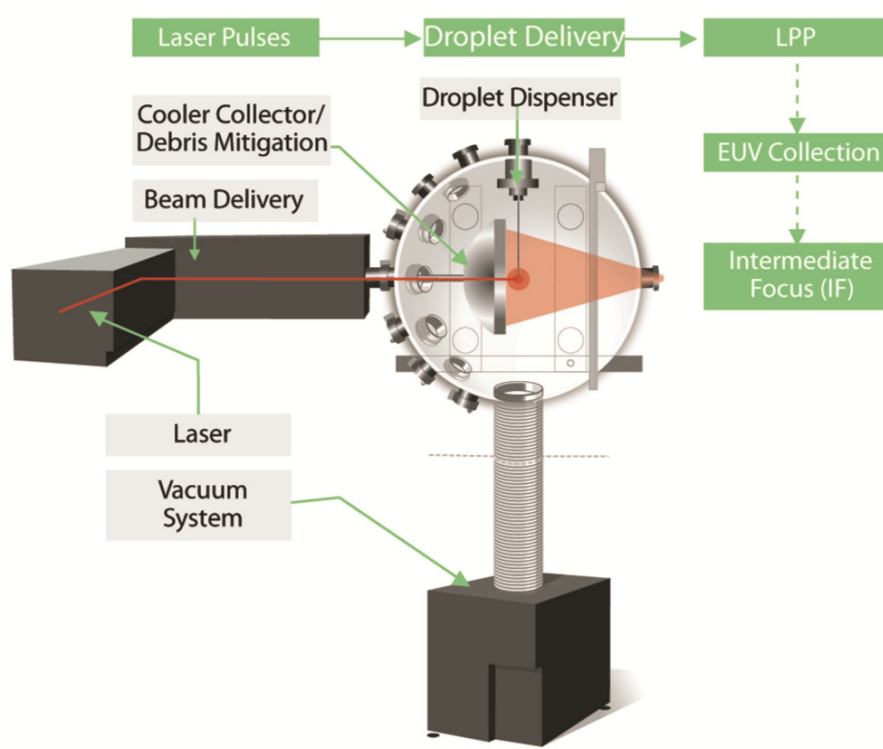


Fig. 10. Schematic of the Laser Plasma Source at the ALPS Facility, LEC, ETHZ.

A schematic of the LPP Source at the Applied Laser Plasma Science (ALPS) facility is shown in Fig. 10. The LPP light source consists of a number of sub-systems: the droplet dispenser, other fuel handling equipment such as the fuel recovery system, a high energy laser with laser focusing optics, multilayer coated collector optics, a debris mitigation system, cooling and thermal management systems for the collector optics, triggering and alignment systems, an IF vacuum interconnect, spectral purity filtration, a vacuum pumping sub-system, a laser beam dump, sensors and in-situ diagnostics, auxiliary systems and a control system and system level software. System integration is

of paramount importance in the design of all subsystems in order to build an operating LPP source. The key subsystems are described in the next section.

The IF vacuum interconnect must ensure the transfer of light to the illumination optics without any transmission of debris. Spectral filtering at the IF is essential. Both xenon DPPs and tin based LPPs are emissive in the 100 to 1000 nm region, where Mo/Si multilayer mirrors are highly reflective.⁵⁹ Radiation at these wavelengths, known as out-of-band radiation (OOB) can cause flare, heat the mask/wafer and create CD variations. Additionally, scattered light from the drive laser, which is used to generate the plasma is a critical issue. This scattered light heats up components of the LPP source and is transmitted to the IF. Currently, thin foils of zirconium, with a thickness on the order of 100 nm, are the material of choice for filtering OOB radiation at the IF.

1.2.4.5. LPP source components

1.2.4.5.1. Droplet generator

The droplet generator is a key component of EUV LPP sources. Droplets enable long-term operation, as they form a regenerative target. They can be synchronized with the pulsed lasers used for EUVL, hence only the required target material is delivered to the irradiation site. This reduces the amount of tin, which is introduced into the source. Therefore consumable cost is also optimized. The yearly tin consumption for a droplet size of 30 μm and a repetition rate of 50 kHz is 22 liter at 100% duty cycle. The design and operation of the droplet dispenser is one of the topics of this thesis. The specific requirements, as well as a review of existing designs for other applications, are presented in Sec. 1.4.1.

1.2.4.5.2. Normal incidence collector

The optical collector is considered to be one of the most critical components of an EUV source. For a LPP EUV source, a normal-incidence collector is an attractive design solution. Indeed, due to the small etendue of the source, large collection angles are possible, as opposed to DPP sources. The manufacturing of ML collectors is a highly advanced process.⁶⁰ In order to achieve low flare and scattering of the reflected light, high precision is required in the manufacturing of the substrate and the deposition of the MLs. Magnetron sputtering is used for deposition on the elliptical collector surface. Diameters up to 660 mm with a collection angle of 5.2 sr have been manufactured.⁶⁰ The complexity in manufacturing makes the cost of the collector one of the most expensive parts in the EUV source. Collectors are considered to be consumables. The life-time requirement is on the order of 1 year.⁶¹ The drive laser is usually focused through a central aperture onto the target. The back side accommodates the thermal management of the collector, which is needed to ensure the optical quality of the mirror during operation.^{57, 62} The space between the LPP and the collector surface accommodates debris mitigation techniques. The collector mirrors are also damaged by deposition of background impurities such as hydrogen, carbon, nitrogen and oxygen.⁶³

1.2.4.5.3. Debris mitigation

Capping layers are employed to reduce the sputtering of the MLs.⁶² Sacrificial MLs are commonly employed to enhance collector life-time.²³ Debris mitigation systems can be categorized as active and inertial. Active mitigation techniques for ion debris include electrostatic repeller fields⁶⁴ and magnetic fields⁵⁵. The large magnetic fields of more than 1 T are generated by superconducting magnets. In these approaches, ions are deflected away from the collector. The inertial approaches include gas curtains^{54,65} and background gases^{66,67}. The gas is used to absorb the kinetic energy of the ions, which would otherwise damage the EUV collector. Here, the gas flow must be optimized for EUV absorption and stopping power. Combinations of these methods are also explored.⁶⁸

The particle debris can be reduced by limiting the mass of the target droplet. Cleaning techniques have been developed, which etch away the deposited tin layer during system operation.^{54, 69} Typically hydrogen is employed for collector cleaning, as hydrogen reacts with tin to form the highly toxic stannane (SnH_4). Inertial debris mitigation systems also reduce the low energy deposition, while repeller fields are inefficient with respect to low energy debris.

1.2.4.5.4. Drive laser

An estimate of the laser power, which is required to generate a tin laser plasma with the ion stages required to emit EUV radiation, can be obtained from the collisional-radiative model described by Bates *et al.*^{70, 71}. This model relates both, the laser irradiance (power density) and the laser wavelength to the plasma temperature, for the case of high electron densities. For a Nd:YAG laser, operating at the fundamental frequency, the beam must be focused to a power density in the range of 8×10^{10} to 5×10^{11} W/cm².

Currently, there are two types of drive lasers used for LPP EUV sources; the CO₂ laser at wavelength of 10.6 μm and the Nd:YAG laser at 1.064 μm . Both technologies have already been used for decades in different industrial applications with a proven record for excellent uptime in continuous operations. The CO₂ laser is the most commonly used laser to drive the EUV source for the lithography application^{54,72} CO₂ lasers are able to deliver more than 10 kW of laser power by using short pulse oscillators and conventional continuous wave (CW) CO₂ modules.⁷² Typical focal spot diameters (full width half maximum (FWHM)) for the high power lasers used in EUV lithography are in the range of 100 to 500 μm for CO₂ lasers^{73,74} and less than 80 μm for Nd:YAG lasers⁷⁵.

The lasers pulse has to be synchronized with the target droplet. In case of very high droplet stability, the laser can be directly synchronized with the frequency of the droplet generator.⁷⁶ In the case of small timing variations in the droplet train, the laser needs to be triggered for each droplet. Generally, the resulting laser frequency variation causes fluctuations in the laser energy. Indeed, when the laser period is shorter than the storage lifetime of the gain medium, the energy per pulse is frequency dependent. A representative example of the dependence of the laser energy per pulse on

frequency is shown in Fig. 11 for a Nd:YAG laser⁷⁷ and a CO₂ laser⁷⁸. The laser energy, which is deposited into the plasma defines the plasma temperature, hence the EUV emission.

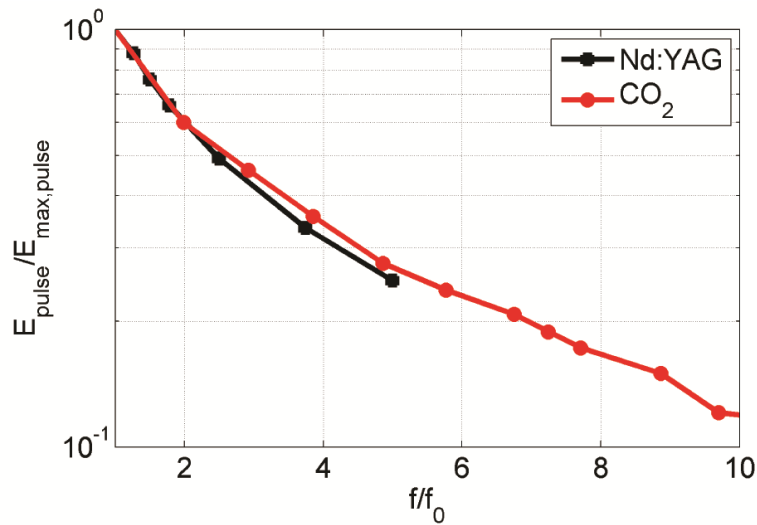


Fig. 11. Frequency dependence of laser pulse energy for for a Nd:YAG laser and a CO₂ laser.

An advantage of using a Nd:YAG laser over a CO₂ laser is that the spectral filtering of light at 1064 nm is substantially easier to accomplish without a large percentage decrease in EUV transmission. The wall-plug efficiency of the Nd:YAG laser is higher than that of the CO₂ laser with 10% and 0.5-2%, respectively.²³ In order to meet the source requirements (presented in the next section), the CO₂ power consumption could reach several megawatts.

A Nd:YAG (diode pumped solid state) laser is currently used in driving the LEC source. The laser has an average power of up to 1600 W operating at frequencies of up to 20 kHz, a compact footprint and a pulse-to-pulse stability greater than ±1% peak-to-peak. This is due to the fact that it has a shorter wavelength and can be manufactured to achieve a small M2 and hence have a very tight spot size, maximizing the brightness of the EUV source.

1.2.5. EUV lithography source requirements

The requirements for lithography and mask inspection sources are well defined. The main focus for lithography sources is the power at IF, which is projected to be larger than 115 W (for a resist sensitivity of 5 mJ/cm²). This is a very important parameter as it maximizes the throughput and hence, the ability to print more wafers. The power output is also determined by other system parameters, such as the optic's reflectivity, the resist sensitivity and the overhead of the system. The production-level requirements for EUV sources have been jointly agreed upon by major scanner suppliers. The latest agreement is shown in Table 1-I.⁷⁹

The repetition frequency requirement is derived from a dose (light per exposure) uniformity specification. LPP sources need to operate at high repetition rates to yield the required power. The

dose uniformity depends on the integrated energy stability of the source, but also on the control and measurement accuracy in the scanner. With an EUV source power of 115 W at a repetition rate of 10 kHz, the correct dose is obtained with 50 pulses and the source dose stability has to be $\pm 0.2\%$ in 3σ . For the large repetition rates of HVM sources^{54, 80} (>50 kHz), the number of pulses is much larger and the energy stability requirement is easier to fulfill. Feedback loops are used in sources to control the dose stability. For example, the adjustment of the laser energy for the 50th pulse controls the EUV energy generated by the last plasma in order to ensure that the required dose stability is achieved.⁵⁹ The required power at the wafer is 0.321 W (versus 115 W at IF), according to the commonly used wafer throughput model. The typical exposure time for a 5 mJ/cm² resist is 7.8 ms, which gives a required EUV energy of per exposure of 2.5 mJ at the wafer level. The equivalent energy at IF equals 896 mJ per dose.

Table 1-I. Joint EUV source requirements by major scanner manufacturers.⁷⁹

Source Characteristic	Requirement
Wavelength	13.5 (nm)
EUV power at IF	115W @ 5mJ/cm ² - 200W @ 10 mJ/cm ²
Repetition frequency	>10 kHz There is no upper limit.
Integrated energy stability	0.2%, 3σ
Source cleanliness (debris)	Reflectivity degradation $\leq 10\%$ (in relative) after 30,000 light-on hours
Etendue of source output	Max 3.3 mm ² sr
Max. solid angle input to illuminator	0.03 - 0.2 (sr)
Spectral purity:	
130-400 [nm] (DUV/UV)	<1% at wafer values at IF- design dependent
≥ 400 [nm] (IR/Vis) including 10.6 μm	<10 – 100% at wafer values at IF- design dependent

The source cleanliness requirement is 30'000 hours. This corresponds to a 10-year lifetime of the illuminator. The EUV collector is expected to be replaced more frequently, depending on its cost-of-ownership. Etendue is the “light collection” power of the optical system. Light from the source, which is emitted in a larger etendue than specified, is simply not coupled into the illuminator. The specified etendue corresponds to a reticle area of 50 mm², a coherence of 0.5 and a NA of 0.25.²³ The spectral purity is specified as DUV/UV and IR light cause flare and other issues with CD control.²³

The power requirements at the IF for mask inspection tools are less stringent than those for scanner applications. However, the etendue for mask inspection applications is smaller than for scanner applications. Given the sensitivity of the imaging sensors and the required throughput, source brightness is critical for HVM mask inspection applications.⁵⁹ As the source brightness is inversely proportional to the source area, the smaller the source size, the higher the brightness, resulting in higher throughput. In addition to the higher brightness, there is also a stringent stability requirement for the source, driven primarily by the need to be able to detect a required CD.

1.2.6. Droplet requirements in an EUV source

No official agreement upon requirements for the droplet target exists. Although the requirements are dependent on source design, a generic preliminary list can be formulated. The list is derived from the EUVL requirements and the basic knowledge about the source, which has been presented in this section. The requirements assume that the droplets are delivered as a stream of droplets to the irradiation site. The nomenclature for droplet instabilities, which is used in this work, is presented in Fig. 12.

- (1) A specific requirement for EUVL droplet dispensers is that the operating frequency is a multiple of the drive laser frequency. For EUVL, droplet dispenser frequencies greater than 10 kHz are required,⁷⁹ while for metrology tools the frequency depends on the tool design.
- (2) The droplet size is determined by the amount of tin atoms required for EUV generation. The amount of debris can be controlled by the droplet size.
- (3) The droplet spacing is required to exceed the focal spot radius of the drive laser. Indeed, the irradiation of subsequent droplets should be avoided. Typical focal spot diameters (FWHM) for the high power lasers used in EUV lithography are in the range of 100-500 μm for CO_2 lasers and 80 μm for Nd:YAG lasers (as described in Sec. 1.2.4.5.4).
- (4) Another major requirement is the minimization of the drop-to-drop timing jitter, which is the standard deviation of the droplet timing at the irradiation site. The drop-to-drop jitter could lead to laser pulse/ droplet de-synchronizations. This could result in energy fluctuations, which impact the dose stability of an EUV source.
- (5) Spatial instabilities need to be minimized. The droplet is required to be aligned to the focus of the laser beam. Lateral displacements are possible along the laser axis and in the direction perpendicular to the laser axis and the droplet stream. Misalignments can be expected to have a negative influence on the dose stability of the source.

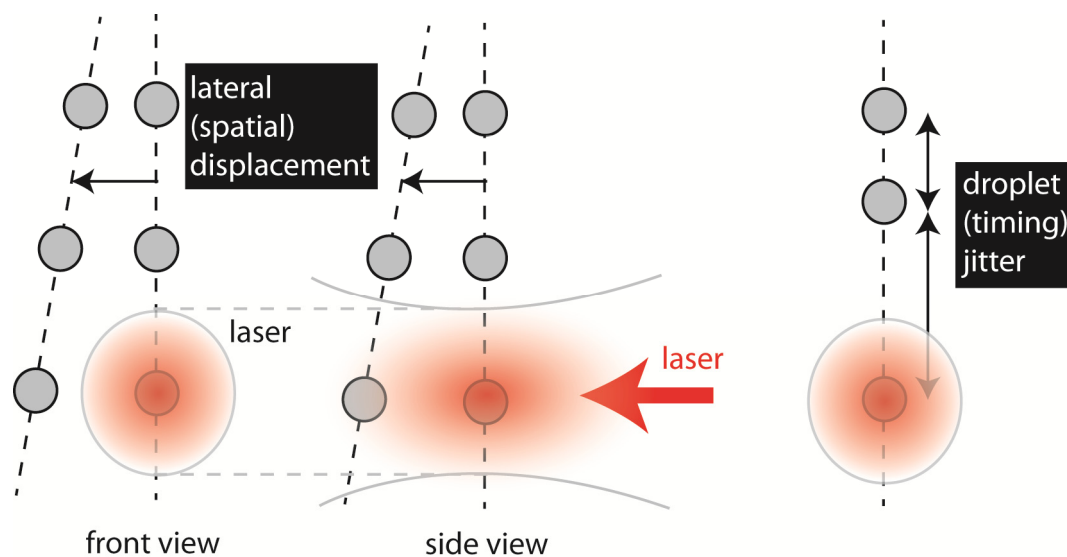


Fig. 12. Illustration of the lateral (spatial) instability and the droplet timing (temporal) jitter.

1.3. Motivation

Laser-produced plasma sources are attractive soft X-ray light sources with spectrally tailored emission. Along with important applications in X-ray microscopy, radiobiology and laser-driven fusion, interest in LPPs drastically increased more than a decade ago, when the semi-conductor industry started seeking options for next generation lithography. Today, the semiconductor market is a \$249 billion dollar market and is estimated to represent close to 10% of the world's GDP.¹³ The semiconductor industry is widely considered to be a main driver for economic growth. For this reason, the datum research work on future manufacturing technologies, which enable the path to further downsizing of ICs, is of high impact. A candidate technology for the manufacturing of the next generation semi-conductor devices is EUV lithography. The wavelength of 193 nm, associated with the currently used immersion lithography, will be replaced by the EUV wavelength of 13.5 nm. The emission at the EUV wavelengths is obtained from a tin-based LPP, formed by the interaction of a tin target and a high power (kW) laser. Despite several years of research, EUV sources are ranked high risk and considered a potential show stopper to EUV lithography. Indeed, SEMATECH, a consortium of several international semiconductor manufacturers, annually issues a ranking of focus areas for EUVL. With the exception of the years 2009 and 2010, the first challenge to be focused on has always been long-term reliable EUV source operation.⁸¹ In 2011, the EUV symposium steering committee unanimously ranked the source as the number one concern. EUV sources are also required for driving actinic inspection tools, which are part of EUVL. Mask defect inspection infrastructure, which includes EUV sources for actinic inspection is also ranked very critical by SEMATECH.⁸¹

Stable droplet generation over an extended period of time, with accurate positioning in three dimensions and precise timing control of the droplets is a major scientific and engineering challenge

in soft X-ray and more specifically EUV sources. Indeed, the laser with a pulse duration of a few nanoseconds is focused to about the same size as the droplets in order to yield the required plasma temperatures at a decent CE. Any fluctuations of the droplet position within the laser focal region cause EUV energy fluctuations. On the other hand, the requirement on dose stability is very stringent with a tolerable fluctuation at the wafer level of less than 0.2% (3σ). In addition, the droplet stability must be ensured for micrometer-sized droplets, which help to control the level of debris in the source. The amount of debris directly determines the EUV collector life-time, hence the cost-of-ownership of the EUV source. In order to meet the EUV source requirements, research on the control of the fluid dynamic instabilities related to droplet generation is needed. This research then enables the development of a robust droplet dispenser for EUVL.

Modeling of the emission and debris characteristics of a given laser-target configuration supports the development of long-term reliable EUV sources. Results for droplet-based LPP sources are very limited. Research laboratories experience the same issues with droplet generation as the source industry. As a consequence, EUV research is almost exclusively conducted on stationary planar tin targets with low repetition rate (<1 kHz) lasers. The results are assumed to be representative for the droplet target, although significant differences between the emission and debris characteristics of a liquid droplet and solid slab target are expected. Numerical tools are useful in studying the impact of the main droplet characteristics, such as spatial and temporal instabilities on source performance.

1.4. Literature survey

1.4.1. Droplet generation

For the generation of a stream of monodisperse droplets, two major approaches exist, namely droplet-on-demand (DoD) or continuous Rayleigh breakup.⁸²

DoD dispensers typically produce single droplets or a series of a few droplets, which are expelled from a nozzle. The design of a DoD dispenser is often based on a capillary tube, which is enclosed by a cylindrical piezoelectric element with concentric electrodes.⁸³ By changing the polarity of the piezoelectric voltage, the inner volume of the capillary tube is modified. The droplet expulsion velocity is determined by the characteristics of the electrical pulse. The ratio of the kinetic energy of the droplet to its surface energy is quantified by the non-dimensional Weber number. The detailed mechanisms of the generation of compression and rarefaction waves in the capillary tube and their impact on the droplet expulsion velocity has been studied by Bogy *et al.*⁸⁴ When using series of pulses, droplet frequencies of a few kilohertz may be reached.⁸²

Rayleigh breakup is only one of the multiple breakup regimes of a jet.⁸⁵ In atmospheric conditions, jet breakup is either classified as Rayleigh breakup, wind-induced breakup or spray. The quantification is based on the gas Weber number, which corresponds to the ratio of the kinetic

energy of the ambient gas to the droplet surface energy. The gas pressures in vacuum systems are however very low (<1 Pa) and the wind-induced conditions are not even reached for jet velocities of several 100 m/s. Experimental evidence of a high speed jet in vacuum is given in Otendal *et al.*⁸⁶ The controlled break-up of the tin jet is however limited by the turbulence in the jet flow. Indeed turbulence causes local disturbances on the jet surface, which result in small, unwanted droplets. McCarthy *et al.* classify the breakup due to turbulence as primary atomization.⁸⁷ Stable continuous generation of a coherent and monodisperse stream of droplets is accomplished by the capillary (Rayleigh) breakup of a liquid jet.

The initial work dates back to Lord Rayleigh, who first quantified the growth of a temporal disturbance on a capillary stream in 1896. Lord Rayleigh showed that an inviscid jet is unstable with respect to an axisymmetric harmonic perturbation in jet radius, if the wavelength of the perturbation is larger than the circumference of the jet.⁸⁸ Weber extended Rayleigh's theory for viscous flows and ambient pressures.⁸⁹

After the pioneering work of Rayleigh and Weber, capillary jet breakup has been extensively studied by linear⁹⁰⁻⁹³ and non-linear analysis,⁹⁴⁻⁹⁷ as well as direct numerical simulations^{98,99} for viscous and inviscid jets. Detailed studies on nozzle design,⁸⁷ satellite formation,⁹⁶ surrounding fluids,¹⁰⁰ variations in surface tension¹⁰¹ and disturbance amplitude modulations¹⁰² have been completed. A review of both experimental and numerical studies is presented by Ashgriz and Mashayek.¹⁰³

The generation of a sequence of liquid metal micrometer droplets of predetermined size and frequency, which are ejected on a predetermined trajectory, is a common challenge for different modern technologies. The most common technical application is inkjet printing.¹⁰⁴ The range of applications also includes biomedical engineering^{105,106}. Solder-based droplet generation is used in micro-manufacturing¹⁰⁷⁻¹⁰⁹ and circuit board printing^{110,111}. In these processes, molten droplets are directly applied to a substrate using a technique similar to inkjet printing. Another relevant technology is metal spray and droplet deposition in micro-casting and advanced coating processes. A review of this technology is presented by Poulikakos and Waldvogel.¹¹²

In soft X-ray sources, the early droplet dispensers (operated in vacuum) were used to dispense ethanol with nozzles based on the inkjet technology.⁶ Later, tin-doped water droplets were used to generate EUV.⁴⁸ Tin jets were also successfully irradiated for EUV generation.¹¹³ The droplet generation and delivery became more challenging when the EUV source suppliers decided to switch to the highly emissive tin droplets. First results for tin droplets, which were generated in an EUV source, were presented in 2005.¹¹⁴ The number of publications on droplet generation in EUV sources is very limited.

1.4.2. LPP modeling

Modelling of the initial stages of the LPP is typically accomplished by so-called radiation magneto-hydrodynamic codes (RMHD). A multitude of such codes exist, due to the large number of

potential fields of application. The most sophisticated codes are found in the field of inertial fusion.^{115, 116} A prominent example is the LASNEX code from the Lawrence Livermore National Laboratory, which is used to design targets for inertial confinement fusion.¹¹⁷ Such codes are usually classified. A one-dimensional code, which has been used for EUV source modelling is the Med103 code.^{32, 47, 118} Proprietary codes used for multi-dimensional EUV modelling include the Z* code¹¹⁹ and the HEIGHTS¹²⁰ code, which have been mainly used (at the beginning of this work) for DPP modelling.⁵⁹ The Z* code has been used in a very limited study to model the hydrodynamics of an irradiated spherical tin target.¹²¹ Accurate LPP emission modelling requires the use of an atomic physics code. The most prominent atomic physics codes are HULLAC¹²² and the COWAN¹²³ suite of codes. Atomic physics codes and RMHD codes are usually decoupled. While atomic physics codes are used for detailed emission spectrum predictions, RMHD codes rely on simplified atomic models to predict emission and radiation transport. Some results on the atomic modelling of tin were available at the beginning of this work.^{35, 124}

1.5. Research objectives

Issues related to the generation of a stream of micrometer-sized tin droplets significantly limit the performance of EUV sources. The Laboratory for Energy Conversion, ETH Zurich started a research project in the beginning of 2007 with the goal to develop a technology platform for conducting research in the field of X-ray sources, with an initial focus on EUV LPP sources. The overall project goal consists of developing a fully functional tin droplet-based high power LPP light source. The research objectives of the present work are related to the generation of the plasma source material and the study of the corresponding droplet-based LPP in EUV sources.

A first, major work objective is to identify the main issues related to droplet generation in an EUV source. Then, a method of generating droplets has to be found, which has the potential to fulfill the EUV source requirements. A second major work objective is to design, build and assess the performance of an apparatus that delivers liquid metal (including tin) droplets to the plasma irradiation site. This droplet dispenser should enable further research on tin droplet-based LPPs. The developed droplet dispenser must be operated in the environment of a high power EUV source. As a consequence, the main requirements for the droplet generator are: compatibility with the vacuum and plasma environment of EUV sources, system integration in the EUV source on a hardware and software level and the generation of micrometer-sized tin droplets at repetition rates of tens of kilohertz.

Experimental methods need to be developed to quantify the droplet quality in terms of spatial and temporal stability, as well as droplet spacing and size. A performance assessment of the newly developed droplet dispenser should lead to the identification of the main issues related to droplet generation in an EUV source. A methodology needs to be provided and integrated to separate and identify the main causes for unstable droplet generation. This methodology shall be based on

experimental measurement techniques, which are applied in synergy with numerical simulations. The studies are required to encompass investigations related to thermal management, as well as structural and fluid dynamics. Eventually, the research aims to conclude on the significance of the relevant design and operating parameters upon dispenser performance. Guidelines for an optimized droplet dispenser design shall be derived.

In a second part, a numerical simulation methodology needs to be developed to investigate the LPP formation and expansion for the case of the previously generated tin droplets, with a focus on emission and debris. A key point is the study of the impact of the spatial and temporal droplet instabilities on source performance. The numerical model is supposed to include all stages of the LPP, from the droplet irradiation to the debris interaction with the collector. An emission assessment for both the in-band and out-of-band contributions needs to be provided for collector design. Debris modeling must include the impact on collector life-time. After experimental validation, the developed model is required to be applied to a baseline case, at conditions representative for the EUV source at ETH Zurich. As a result, a full characterization in terms of emission and debris for a droplet-based LPP source should be obtained. In a set of studies, the measured droplet stream characteristics need to be used as boundary conditions in the numerical simulations. As a result, the preliminary droplet requirements on size, spacing and stability for optimum source operation shall be refined in order to yield guidelines for future optimizations.

1.6. Thesis outline

Chapter 1 gives a comprehensive overview of laser-produced plasma sources with a focus on EUV sources. Preliminary requirements for droplets in EUV sources are presented. The motivation for this work is outlined. A review of existing work and the research objectives are presented.

Chapter 2 presents the design of the developed droplet generator. The dispenser requirements are listed. Details of the applied droplet formation mechanism are given. The key design features are summarized. The general mechanical and thermal design with a focus on the excitation mechanism is outlined. The nozzle design is discussed.

Chapter 3 outlines the experimental methods used to assess the dispenser performance. Images of the obtained droplet stream are presented. The chapter also contains the operating maps and the achieved droplet size, as well as temporal and spatial stability measurements.

Chapter 4 first details the design, calibration and measurement uncertainty of the novel high temperature fast response pressure sensor with first results from its application in liquid tin. Then, the characterization of the excitation system, which is based on pressure and structural response measurements, as well as structural finite-element simulations, is presented. The origins of the complex pressure response are detailed and tuning possibilities suggested.

Chapter 5 gives the correlation between the measured pressure response and the droplet timing jitter. The influence of the excitation amplitude and the perturbation background noise on timing jitter is detailed. The limits of the achievable droplet spacing are explored by computational fluid dynamic simulations of the droplet breakup. A general design approach is derived.

Chapter 6 describes the computational tools, which are used to model the tin droplet LPP. First the relevant physical processes are outlined, before the radiation hydrodynamic code, the atomic physics code and the particle code are detailed. The chapter then presents computational results of the tin droplet-based LPP. First a baseline case, which uses the conditions of experiments conducted at ETH Zurich, is detailed in terms of hydrodynamic expansion, emission and debris. Then, a set of studies outlines the influence of different dispenser related issues, such as instabilities on the LPP.

Chapter 7 summarizes and concludes on the outcome of this work.

Chapter 2

Droplet dispenser design

The reliable formation and delivery of target material to the laser irradiation site is of paramount importance for stable and long-term operation of the LPP light source. The design of the droplet dispenser, which is used in the remainder of this work, is described in this chapter. The droplet dispenser essentially consists of a plasma source material reservoir, a dispensing nozzle and an excitation system. Droplet formation is based on the Rayleigh breakup of a jet. An acoustic excitation system imposes the droplet frequency onto the droplet stream.

2.1. Introduction

2.1.1. General remarks

The development of the droplet generator is a challenging task due to the multitude of scientific disciplines involved in the design of a functional droplet generator. Some of the key issues, which have been encountered during the development and the measurement phase, are described in the next chapters. In the context of this work, four major versions of the droplet dispenser have been developed. The dispenser design, which is detailed in this chapter, corresponds to the fourth version of the droplet generator. In order to make the droplet dispenser work in a LPP source, major revisions were required during the development. Many revisions were related to the excitation and the heating systems. A significant number (>10) of nozzle designs has been explored. Updated

requirements on the maximum operating temperature and backpressure also led to major system updates. The fourth version of the droplet dispenser is patent pending.

While droplet dispensers have been successfully developed for ambient conditions and liquids with lower melting temperatures, as described in Sec. 1.4.1, the requirements for operation in a LPP EUV source are very stringent. The developed droplet dispenser is operated in the ALPS source and in a dedicated facility for droplet studies. This facility has been built in the context of this work. Both systems rely on the fourth version of the droplet generator. The dedicated test chamber is equipped with additional diagnostics and allows autonomous droplet testing. It also adds the capability to optimize the droplet dispenser with measurement data from two systems.

2.1.2. Droplet dispenser requirements

Firstly, the droplet dispenser must deliver the target material without compromising the EUV source requirements. Secondly, the droplet dispenser must ensure the specific requirements for the droplet target, which are detailed in Sec. 1.2.6. The droplet requirements are related to the droplet timing and spatial stability, the droplet frequency and size, as well as to the droplet spacing. In addition to the droplet requirements, the droplet dispenser has to fulfill specific requirements as a component of the LPP source. The droplet dispenser requirements are listed below:

- The dispenser must be compatible with the high-vacuum environment. Outgassing or leaks must not compromise the vacuum level or lead to contamination of the LPP source, especially the multilayer optics.
- The dispenser must be compatible with the plasma environment. Electrical connections must be secured in order not to induce vacuum discharges. All parts exposed to the plasma should be resistant to tin deposition or ion sputtering.
- The dispenser must be able to handle the heat load, which results from laser light reflection and out-of-band radiation of the source.
- The dispensed target material must be pure enough so as not to compromise the desired X-ray emission. No contamination should be added to the initial fuel.
- The vibration level of the dispenser and its support should be low enough to prevent stability issues on the droplet stream.
- The main LPP target material in this work is tin. As a consequence, the operating temperature of the dispenser should exceed the melting temperature of tin.
- Alignment of the droplet dispenser within the EUV source with respect to the laser focus must be ensured.
- Thermal drifts should be minimized in order to limit the correction of the droplet position during operation.
- The dispenser operation should be highly automated.

- The manufacturing cost of the dispenser should be minimized. The device should have low cost-of-ownership, with a minimized amount of consumable items.
- Serviceability in an LPP source should already be considered for the first design.
- The operating time of the developed dispenser should be in the range of 1-2 hours. The design should be scalable for larger running times.

2.1.3. Droplet generation

A monodisperse stream of droplets can be either generated by DoD or continuous Rayleigh breakup. Due to the frequency limitation of the DoD approach (Sec. 1.4.1) and the source requirement for repetition rates larger than 10 kHz (Sec. 1.2.5), droplet generation is based on the Rayleigh breakup of a jet. Other breakup modes of the jet do not yield a monodisperse and coherent stream of droplets.⁸⁵

Potential issues in vacuum environments include the phase changes due to the ambient pressure drop, as well as cavitation.⁸⁶ Droplet evaporation in the vacuum environment is irrelevant for tin, as the vapour pressure of tin equals 10^{-20} mbar at 260 °C.¹²⁵ The oxidation of the tin jet,¹²⁶ as described by Haj-Hariri and Poulikakos, is suppressed in the vacuum environment.

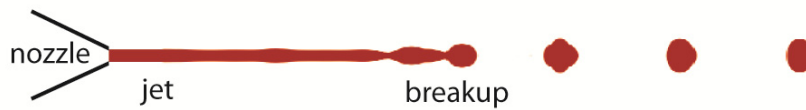


Fig. 13. Rayleigh breakup of a jet (numerical simulation, Sec. 5.4.3). The surface disturbances grow along the jet contour up to the breakup into droplets.

Stable continuous generation of a monodisperse stream of droplets is accomplished by the capillary (Rayleigh) breakup of a liquid jet, as shown in Fig. 13. Lord Rayleigh showed that an inviscid jet is unstable with respect to an axisymmetric harmonic perturbation in jet radius a , if the wavelength of the perturbation λ is larger than the circumference of the jet.⁸⁸ Mathematically, this translates into

$$\frac{2\pi a}{\lambda} < 1 \quad (2.1)$$

The surface energy of the resulting droplets is smaller than the surface energy of the initial cylindrical jet. Lord Rayleigh also showed that the jet is most susceptible to disturbances, which are 1.44 times larger than the circumference of the jet. This corresponds to a perturbation wavelength λ of 4.5 times the droplet diameter D_{drop} . Under these conditions, the droplet diameter D_{drop} is equal to 1.89 times the nozzle diameter D_n . The wavelength of the perturbation is set by the perturbation frequency and the jet velocity. Weber extended Rayleigh's theory to viscous flows.⁸⁹ The non-dimensional number, which relates the viscous forces to the surface tension forces is the Ohnesorg number, which is defined as¹²⁷

$$Oh = \frac{\mu}{\sqrt{\rho\sigma D_{drop}}} \quad (2.2)$$

where μ , σ and ρ are the dynamic viscosity, the surface tension and the density of the liquid, respectively. In the case of tin, Oh is equal to 4.7×10^{-3} . As a result, surface tension forces dominate viscous forces in the case of liquid tin. In conclusion, droplet generation has to be based on the Rayleigh breakup mechanism in order to meet the EUV source requirements. Therefore, the developed dispenser relies on the generation of a tin jet with an imposed perturbation at the desired operating frequency.

2.2. Dispenser design

In a first section, the system layout of the droplet dispenser assembly is presented with a focus on the integration of the excitation system and the dispensing nozzle into the dispenser. Then, the thermal and mechanical design of the fourth version of the droplet dispenser is outlined. The specific design solutions for the most critical components, namely the excitation system and the dispenser nozzle are detailed.

2.2.1. Design overview

The dispenser delivers the plasma source material as a stream of droplets to the plasma generation site, as shown in Fig. 14. The apparatus is completely mounted inside the vacuum chamber by means of a motion stage. The dispenser is typically installed above the EUV collector, although a displacement of the dispenser assembly along the vertical axis is possible. Lowering the dispenser position results in a shadow on the EUV collector. The source layout is described in Sec. 1.2.4.4. In a second source design, which yields high brightness ($\text{W}/\text{mm}^2\text{sr}$), the dispenser is operated at a lower height due to the reduced size of the collection optics.⁵⁸

The core of the droplet dispensing device consists of a replaceable cartridge, which includes the material reservoir and the dispenser nozzle, as shown in Fig. 14. The design is optimized for quick and safe handling of the dispenser cartridges. All replaceable parts, such as nozzles are located on the cartridges. The preparation of the cartridges, which includes refilling of source material, is completed outside of the source. The pre-heated cartridges are simply inserted into the dispenser casing in order to minimize the source downtime. The source material reservoir is refillable and equipped with a removable cover, as depicted in Fig. 15. The removable cover gives full access to the cartridge interior, which is optimal for the refurbishment of the cartridge. The cartridge is of cylindrical shape for manufacturing and uniform heating reasons.

A backpressure connector tube is located on the removable cover of the cartridge. A pressure tube connects the cartridge to a gas feedthrough in a vacuum flange. A compressed gas source is used to establish a pressure in the source material reservoir. This backpressure exceeds the vacuum level by

several orders of magnitude. By inserting an electrically automated pressure regulator between the gas source and the droplet dispensing device, the backpressure can be adjusted. The backpressure gas induces a jet discharge at the exit of the outlet nozzle.

The cartridge is heated using a resistive heater. The resistive heater is wound around an outer, static cylinder containing the replaceable cartridge. The heater winding extends over the full length of the cylinder in order to ensure uniform heat transfer to the source material, which is located in the material reservoir. The heating system is (optionally) extended to include the nozzle. The resistive heater is contained in a groove and may be fixed by laser welding to the cylinder, which contains the cartridge. The reason for this strict tolerance on the fit between the resistive heater and the cartridge lies in the high vacuum environment in which the dispensing device is operated. Indeed, the absence of natural convection in a high-vacuum environment leads large temperature hot spots in the case of an insufficient fit. This easily results in a failure of the heating system. The heating power of the resistive heater is adjusted by a microcontroller. Temperature control is achieved by temperature sensors, which are installed in multiple locations on the dispensing device. The acquired temperature signals are used to drive a heating control system and/or an emergency shutdown system. More details about the thermal management of the dispenser are presented in Sec. 2.2.2.

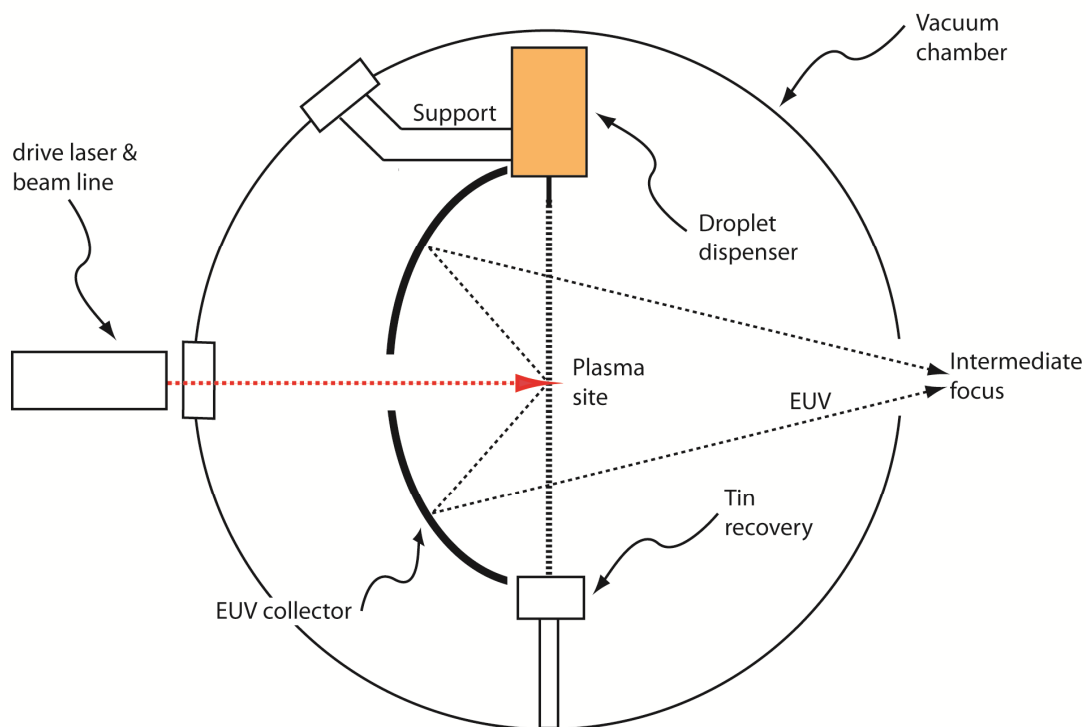


Fig. 14. Sectional view of the light source with the droplet dispenser attached to the vacuum chamber.

The cross-section of the cartridge comprising the reservoir and the outlet nozzle is outlined in Fig. 15. Replaceable nozzles are attached at the lower end of the material reservoir. Different nozzle

2.2 Dispenser design

designs have been studied. Contamination control is also integrated on the nozzle level. The nozzle design and contamination control are described in Sec. 2.2.5.

A piezoelectrically actuated piston, which extends through the reservoir and the molten material contained therein, is attached to the removable cover of the material reservoir. By applying a voltage to the PZT actuator, the piston tip is axially displaced in the molten source material in a vibrating motion and generates pressure waves in the tin. These pressure variations propagate towards the exit of the outlet nozzle. The resulting perturbations at the outlet nozzle modulate the droplet stream at the desired frequency. The frequencies of these imposed disturbances range from 1 kHz to a few 100 kHz. The thermal management of the piezoelectric actuator is crucial for long-term operation of the droplet dispensing device. The heat path is designed such that heat flows along the axis of the oscillating piston from the hot source material at the lower end of the piston to the cooling system of the piezoelectric actuator on top of the cartridge. The thermal and mechanical designs of the excitation system are detailed in Sec. 2.2.4.

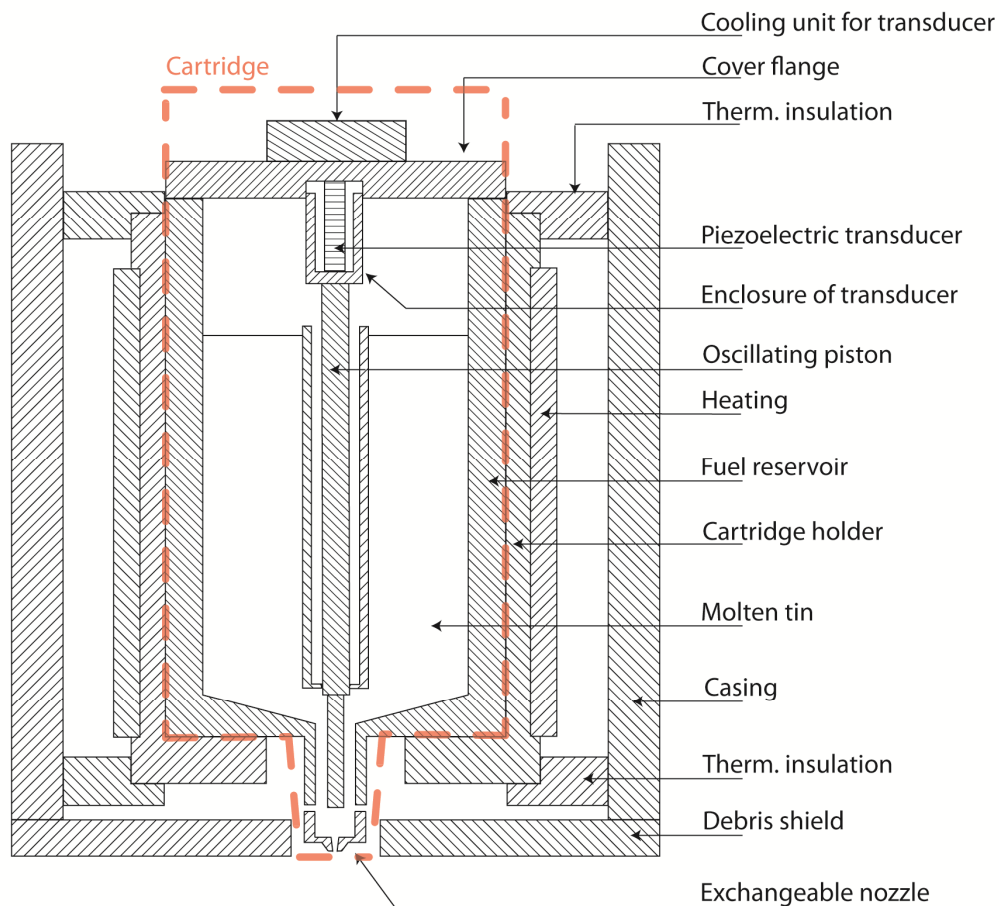


Fig. 15. Sectional view of the droplet dispenser (V4). The main components are the casing and the cartridge (red contour), which includes the dispenser nozzle, the plasma material reservoir and the oscillating piston.

As shown in Fig. 15, the droplet dispensing device is integrated in a casing for protection against plasma debris as well as for alignment purposes. The cartridge section of the dispenser, which corresponds to the hot core of the system, may be contained between two thermally insulating flanges, as depicted in Fig. 15. The material of the flanges is chosen to have low thermal conductivity in order to minimize heat transfer from the cartridge to the casing. The lower part of the dispenser casing, which is directly exposed to the LPP, is designed to be easily exchangeable and actively cooled.

The dispenser is highly automated, which is particularly important for operation in the main source. The dispenser control system is integrated with the main control system of the ALPS source. Operation in the dedicated facility is ensured by an autonomous microcontroller. A graphical user interface on a separate PC is used to set the operating parameters and monitor the dispenser during operation. The key settings include the backpressure level, the signal characteristics for the piezoelectric actuator and the set point temperatures. All operation data is logged for subsequent analysis. Several measurement acquisition subsystems, which are for example related to droplet imaging, droplet tracking and nozzle pressure monitoring, are integrated into the control system.



Fig. 16. Dispenser in operation in the main ALPS source

2.2.2. Thermal design

Thermal design goes hand in hand with mechanical and fluid dynamic design. Although the design steps are presented in a serial way, the real design procedure consists of many design iterations in order to meet the initial requirements.

The thermal requirements are either given by the general dispenser requirements, as described in Sec. 2.1.2, or by requirements that result from specific components of the dispenser assembly, such as the temperature limit on the piezoelectric stack. One general requirement is to ensure the melting of the source material inside the reservoir and the nozzle. In the present case, the primary application is tin, although other liquid metals materials such as indium¹²⁸ or metal alloys such as

SnIn and SnPb have been successfully tested. Water has also been commonly used during the dispenser development. In principle, the light source material could be any liquid droplets of metals, e.g., Sn, Li, In, Ga, Na, K, Mg, Ca, Hg, Cd, Se, Gd, Tb, and alloys of these metals, e.g. SnPb, SnIn, SnZnIn, SnAg. Liquid non-metals, e.g. Br, liquefied gases, e.g. Xe, N₂ and Ar, or a suspension of a target material in a solution, e.g., in water or alcohol are also potentially compatible with the droplet dispenser.

The operating temperature of the developed dispenser is variable, but limited by a maximum temperature, which is given by material temperature limits. Temperatures in excess of the melting temperature of the used material are required. In the case of tin, the melting temperature equals 232 °C. Droplet formation is influenced by the surface tension and viscosity of the target material, as described in Sec. 2.1.3. The temperature dependent viscosity and surface tension for tin, which are shown in Fig. 17, are taken from Thresh *et al.*¹²⁹ and Melford *et al.*¹³⁰, respectively. It can be seen that the surface tension decreases by only 3% from the melting point to a temperature of 500 °C. The decrease in viscosity is more pronounced with a decrease of 35% up to 450 °C. Still, the non-dimensional numbers of droplet formation, such as the Reynolds and Ohnesorg number, are not greatly affected and no significant changes on droplet formation are expected for temperatures up to 450°C. In conclusion, the droplet dispenser is not required to be operated significantly above the melting point of tin.

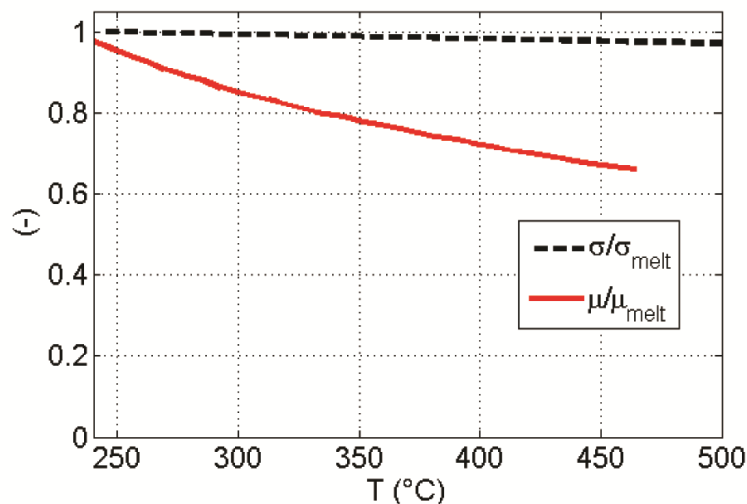


Fig. 17. Temperature dependence of the surface tension and the viscosity, normalized by the respective melting point values.

In the thermal design procedure of the fourth version of the droplet generator, a computational prediction of the temperature distribution in the dispenser assembly (without support) has been used. A computational model of the third version dispenser has been developed and validated against experimental temperatures. The computational model is based on a thermal finite-element (FE) analysis. The analysis is completed with the ANSYS (Release 13.0) FE modeler. Details about

the model can be found in Bachmann.¹³¹ The simulation setup includes the material assignments to the geometry. The three dimensional model is directly derived from the CAD model, which has been used in manufacturing. Boundary conditions for the heat sources, the heat losses through the support and radiation losses strongly determine the predicted temperature distribution. Results are presented in Fig. 18.

The normalized temperature distribution inside the droplet dispenser gives the local drop in temperature, relative to the maximum temperature, which is found on the heating system. The relative drop in nozzle temperature is less than 5%, when compared to the heater temperature. The temperature gradients along the insulating flanges, which separate the dispenser core from the casing, are clearly visible. As a consequence, the temperature on the casing is dropped to one third of the heater temperature. This low casing temperature gives low temperatures on the motion stage. Firstly, the components of the motion stage, such as the vacuum motors and the micrometer position system preferably work at low temperatures. Secondly, the thermal drift, which could be the result of thermal expansion of the support structure, is limited. The main design iterations involved optimizations of the nozzle, casing and piezoelectric stack temperature.

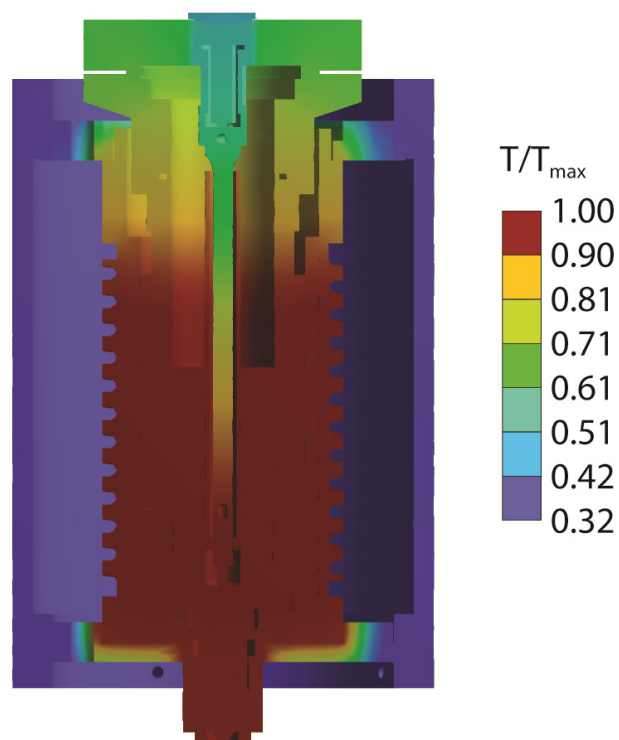


Fig. 18. Sectional view of the temperature distribution inside the droplet dispenser, as predicted by FE analysis. As required, the tin reservoir and nozzle yield the highest temperatures, while the casing and the piezoelectric unit have low temperatures.

The second low temperature region is induced by the cooling unit of the piezoelectric actuator, which controls the operating temperature of the piezoelectric stack. For the simulated cooling heat

flux, the stack's temperature equals 50% of the heater temperature. The positive influence of the heat shield, which encloses the immersed part of the piston, is also confirmed by the strong temperature gradient along the piston axis.

The predicted temperatures from the design phase are compared to temperatures that have been measured on the final prototype. Temperature measurements rely on the use of PT 100 temperature sensors. The droplet generators are equipped with a multitude of temperature sensors, which are used for online monitoring, as well as for temperature control of different components. Results are presented in Table 2-I for different measurements locations on the dispenser.

Minor differences between measured and predicted values can be observed. The largest difference of 6% is found for the casing surface. Firstly, these differences are due to inaccuracies in the FE model, which are mainly due to the inaccurate contact modeling between parts. Secondly, the measurement locations might not match exactly between experiment and simulation. The sensor accuracy is estimated to be in the range of 1%. Additionally, the contact between the sensor and the measured surface constitutes a potential reason for a mismatch between experimental and numerical results.

Table 2-I. Measured and computed temperatures, normalized by the respective maximum operating temperature at discrete locations on the dispenser surface.

Location	Experiment T/T_{\max}	FE simulation T/T_{\max}
Cartridge top	0.88	0.88
Piezo enclosure	0.52	0.52
Casing	0.38	0.35
Heater	1.01	0.99
Nozzle	0.91	0.95

In the previous model, tin is modeled as a solid body with the properties of the liquid. The melting process, which is not included in the model, is studied by experimental means. In order to measure the melt temperature, an initially hollow, thin-walled piston is equipped with a temperature sensor and immersed into tin. The tin temperature is monitored in the center of the fuel reservoir during the heat-up phase of the dispenser. The corresponding measurements are shown in Fig. 19, together with the temporal evolution of the heater temperature. The time scale is normalized by the time duration, which is required for the liquid tin to reach its final temperature. As expected, a time lag between the heater and the tin temperature is observed. This time lag scales with the thermal inertia of the dispenser. The plateau in the tin melting curve is due to the phase change from solid to liquid tin. The tin temperature converges to 97% of the heater temperature. In conclusion, heat is efficiently transferred from the heater to the liquid tin.

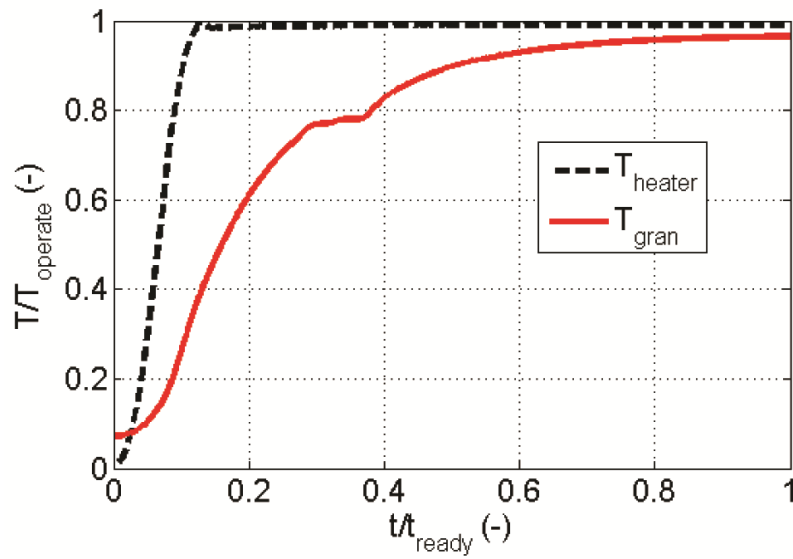


Fig. 19. Time dependence of heater temperature and tin temperature during start-up of dispenser.

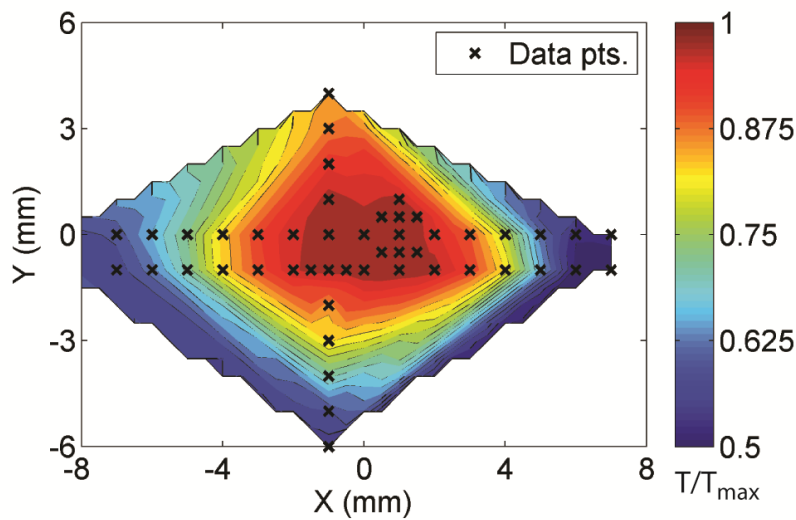


Fig. 20. IR measurement of the nozzle area. The nozzle is located at (0,0) and has a diameter of 3 mm.

The nozzle temperature determines the thermal condition of the tin jet, which eventually breaks up. Indeed, a large convective heat transfer from the nozzle to the tin takes place as a result of increased tin flow velocities in the nozzle. In order to accurately measure the temperature at the nozzle outlet, an infrared probe with a wavelength range from 8 -14 μm and a focal spot size of 0.6 mm is employed. The probe is mounted on a motion stage below the dispenser. The temperature distribution from Fig. 20 is derived from the traversing probe, which scans the surface. The nozzle orifice is located at the point (0,0). The nozzle outlet surface has a diameter of 3 mm. As required, the largest temperatures are found on the nozzle outlet surface.

Different aspects of the thermal design of the droplet dispenser have been described. In conclusion, the key thermal requirements, which are related to the source material, casing and piezoelectric stack temperatures are fulfilled.

2.2.3. Mechanical design

The requirements relevant to the mechanical design of the dispenser are a low vibration level and the alignment of the dispenser with respect to the laser focus. An additional more specific requirement is the high pressure compatibility of the cartridge. The design solutions for manufacturability and serviceability, which are closely related to the mechanical design, should be evident from the design overview, which is given in Sec. 2.2.1.

The droplet dispenser is coupled to the chamber via its support, as shown in Fig. 14. The support is designed with a maximized stiffness, with a first eigenfrequency above 1 kHz. Accelerometer measurements on the vacuum chamber, dispenser support and cartridge showed no significant displacements. The most reliable method to detect dominant structural frequencies is a spectral analysis of the droplet train. The spectral analysis revealed no dominant frequencies, except the excitation frequency of the piezoelectric stack. The frequency spectrum of the droplet train is presented in Sec. 5.4.1. Low frequency vibrations can be compensated for by an active position control.

A motorized support has been developed in parallel with the dispenser. During the development of the motion stage, the emphasis has been on micrometer precision for the dispenser position control. For this purpose, motorized micrometer screws and linear guides are used to ensure the relative motion of the dispenser with respect to the chamber. The two motorized displacement directions are located in the plane, which is perpendicular to the droplet trajectory. A manual adjustment of the vertical position is integrated. The motion stage is driven by the main control system of the ALPS facility. This motion stage is needed in order to compensate for any inaccuracy in the physical alignment of the droplet generator with respect to the laser focus. Potential sources for misalignment are thermal drifts and manufacturing tolerances on cartridges and nozzles.

The static pressure load in the fuel reservoir, the reservoir cover and the nozzle is considered during the mechanical design of these components. The fourth generation dispenser is used for pressures up to 40 bars in the present work. A combination of semi-empirical design rules and FEM analysis are used to design the cartridge components for this high pressure.

2.2.4. Acoustic excitation

The developed dispenser relies on the Rayleigh breakup of a jet for the generation of a stream of droplets. Monodisperse droplets are obtained if an external perturbation at a predetermined frequency is imposed on the jet. This artificial perturbation can be induced by directly vibrating the nozzle¹³² or by imposing a velocity or pressure variation onto the flow¹³³. Practical implementations

mostly rely on piezoelectric transducers. In the present case, magnetostrictive materials are not a viable alternative. Common types of excitation mechanisms include the Berglund-Liu nozzle type,¹³⁴ capillaries enclosed in piezoelectric tubes^{135, 136}, actuated pistons^{137, 138} and membranes^{139, 140}.

The commonly used integration of piezoelectric actuators into the nozzle is disadvantageous for dispensing high temperature materials such as molten tin. Indeed, piezoelectric crystals have a limitation in operating temperature, which typically lies around 50% of the Curie temperature. Common high-temperature piezoelectric materials are limited to 150 °C.¹⁴¹ In the presented design, the piezoelectric actuator can be actively cooled, without directly reducing the nozzle temperature, as shown in Fig. 18. The nozzle is decoupled from the piezoelectric actuator. The cooling unit, which is placed outside of the cartridge, is based on convective cooling. A mass flow controller is employed to regulate the cooling mass flow, hence the temperature of the piezoelectric stack. By changing the coolant, the cooling performance can be further adjusted. The heat path from the piezoelectric stack to the cooling unit is confined in the cover flange by material inserts of low thermal conductivity.

If the piezoelectric actuator is integrated in the nozzle, frequent nozzle exchanges drive up running costs significantly. The harsh environments of laser-plasma sources with vapor deposition and sputtering on exposed components, such as nozzles, favor the installation of the piezoelectric crystal inside the tin reservoir.

In the present work, the oscillating piston solution is chosen for thermal and cost reasons. The overall design is inspired by ultrasonic wire-bonders, which also seek large displacement at the tip of the ultrasonic horn.¹⁴² The core of the system is the piezoelectric actuator. The piezoelectric actuator, a so-called high-temperature multilayer stack, consists of layers of piezoelectric material separated by insulating layers. Such piezoelectric stacks are advantageous for the current application as they yield large displacements at low voltages (<100 V). Low voltages are desirable in high vacuum environments due to breakdown shorting. An equivalent monolithic piezoelectric crystal would require more than 1 kV of supply voltage.

The oscillating piston is attached to the supporting cover flange through the enclosing shell of the piezoelectric actuator. This enclosure is used to pre-stress the piezoelectric actuator. Indeed, piezoelectric material withstands expansion stresses very poorly. The dynamic use of such a stack requires it to be pre-stressed for the clamping force to be larger than expansion forces induced by the alternating voltage. Different enclosures can be used to define (among other parameters) the stiffness of the system. In the present work, two enclosures have been employed, termed system A (standard) and system B, which has a lower stiffness than system A. The dynamics of the complex coupling of the piezoelectric actuator to the piston are detailed in Sec. 4 by numerical and experimental means.

The working principle of the oscillating piston relies on the generation of pressure waves at the piston tip, in the vicinity of the nozzle. The acoustic impedance Z relates the pressure amplitude p' at the tip to the displacement velocity u of tip¹⁴³

$$Z = \frac{p'}{u} = \rho \cdot c \quad (2.3)$$

where ρ and c are the density and speed of sound of the considered acoustic medium. The generated pressure waves are transmitted to the nozzle inlet. A dedicated high temperature pressure probe is used to experimentally quantify the pressure fluctuations as a function of excitation frequency. Details are found in Sec. 4. Viscous damping of the pressure waves in the liquid tin is irrelevant at the considered frequencies. Indeed the damped pressure amplitude p at a frequency f of a wave with an initial pressure amplitude p_0 can be written as a function of distance x

$$p = p_0 \exp \left(\operatorname{Im} \left(\frac{\mu}{\rho} \frac{1}{\sqrt{1 + 8\pi/3 \mu/c^2 f \cdot j}} \right) \cdot x \right) \quad (2.4)$$

For tin, the attenuation cannot be numerically resolved for the typical length scales found in the dispenser. At a frequency of 50 kHz, the attenuation equals 0.1% over a distance of 750 m. The influence of the pressure perturbation on droplet formation is studied in Sec. 5.

2.2.5. Nozzle design and contamination control

The droplet dispenser nozzle sets the boundary conditions for the tin jet. The nozzle is one of the most critical components of the droplet dispenser. Indeed the large drop in length-scales, from tens of millimeters in the reservoir to a few micrometers in the nozzle is the cause for many challenging issues, which are described below.

The jet emanates from the nozzle by applying a constant pressure at the nozzle inlet. The jet velocity, which results from the conversion of potential energy into kinetic energy is a function of the pressure drop between the fuel reservoir and the nozzle outlet. The required backpressure determines the design of the fuel reservoir. The pressure drop is composed of different contributions:

$$\Delta p = \frac{1}{2} \rho (v_l^2 - v_0^2) + \Delta p_{visc} + \Delta p_{geo} \quad (2.5)$$

where v_l and v_0 are the velocities in the reservoir and exit of the nozzle, respectively. The velocity in the reservoir equals zero, as a result of the large difference in the flow cross-sections in the reservoir and the nozzle. The term Δp_{visc} corresponds to the viscous pressure loss. The term Δp_{geo} includes

the pressure loss, which results from a specific nozzle geometry. Streamlined nozzles have lower pressure loss than sharp edged nozzles. Important sources for pressure loss are the nozzle inlet and outlet. Another pressure drop to be considered results from the porosity of contamination filters, which are employed to prevent clogging of the nozzle. The influence of wall roughness is typically negligible. Large roughness could act as a turbulence promoter and negatively influence droplet formation. The influence of the roughness on droplet formation is elaborated in Sec. 5.

The viscous pressure drop depends on the flow regime in the nozzle, which is determined by the Reynolds number $Re = \rho v D_n / \mu$, where v is the mean flow velocity and D_n is the nozzle diameter. The dependence of the Reynolds number for typical flow velocities and droplet diameters is shown in a. The transition from laminar to turbulent flow occurs around $Re=2300$ (black contour in a). As mentioned, the Reynolds number also induces breakup of the jet at sufficiently high values. Heat transfer between the inner nozzle surface and the flow also scales with Reynolds number.

The flow regime, which is obtained for the nozzles diameters and jet velocities of this work, is laminar. If the nozzle aspect ratio is sufficiently large ($> 0.057Re$) to have a fully developed flow, the pressure drop can be derived from the Hagen-Poiseuille pipe flow equation as

$$\Delta p_{visc} = 8 \frac{\mu L v}{(D_n/2)^2} \quad (2.6)$$

where L is the length of the nozzle. For turbulent jets, the viscous pressure drop is larger. The backpressure required to overcome the viscous losses is plotted in b for a nozzle length of 0.4 mm and a nozzle diameter of 20 μm . The backpressure requirement, which is only due to the viscous losses, is already considerable. As the velocity increases, the viscous losses become less dominant and most of the potential energy is transformed into kinetic energy.

As the jet forms, the velocity relaxes to yield a uniform velocity profile, which is due to absence of wall shear stresses. Part of the potential energy is also transformed into free surface energy. The corresponding pressure drop contribution equals $\Delta p_{surf} = \sigma/a$. As a consequence, the generation of lower diameter jets requires high pressure, not only due to viscous losses, but also due to the surface tension losses. A guide to nozzle design for droplet generation is given in McCarthy *et al.*⁸⁷

The nozzle design is not only determined by fluid dynamic aspects. The nozzle material and the manufacturing technique play major roles. The nozzle material should have a thermal conductivity, which enables sufficiently high orifice wall temperatures. The nozzle wettability by the target material should be limited. A low contact angle between the nozzle and the source material limits the capillary and adhesive forces, which otherwise cause lateral wetting around the nozzle orifice.¹⁴⁴ This wetting can induce disturbances on the jet.

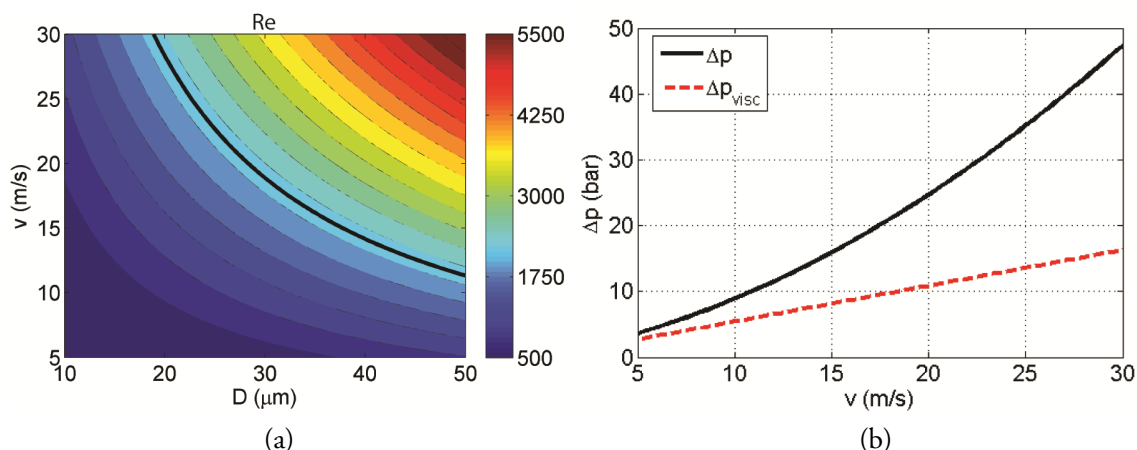


Fig. 21. (a) Reynolds number of the nozzle flow as a function of the nozzle diameter and the mean flow velocity. The black contour marks the transition between laminar and turbulent flow. (b) Backpressure requirement and viscous loss contribution for a $20\ \mu\text{m}$ nozzle of $0.4\ \text{mm}$ length.

A multitude of different nozzle types and materials has been investigated in the context of this work. The typical nozzle types include the commonly used glass capillaries¹⁴⁵, micro-fabricated^{146, 147} nozzles and micro-machined holes in different bodies, such as orifice plates.^{82, 134, 148} Nozzle manufacturing has been extensively investigated for inkjet printing.¹⁰⁴ During the dispenser development, the nozzle size has been continuously reduced.

Contamination control correlates directly with the nozzle size. Indeed, contamination issues became more significant with decreasing orifice sizes. Particles with similar dimensions to the nozzle diameter can clog the nozzles. As a consequence, a particle filter is placed upstream of the nozzle exit. Different particle sources have been identified during the development of the dispenser. Particles are either introduced from outside, typically during the handling and assembly of all parts with surfaces exposed to liquid tin. According to ISO 14644-1 cleanroom standards, room air contains around $300'000$ particles per m^3 , which are larger than $5\ \mu\text{m}$. A class 1 cleanroom contains 25 such particles per m^3 . One of these particles is sufficient to clog the nozzle or cause significant disturbances, such as angular deflections on the jet. On the other hand, the formation of chemical compounds, due to interaction of tin with the exposed surfaces in the dispenser, must be controlled in order to ensure a constant mass flow through the nozzle.

2.3. Summary

The droplet generator has been developed according to the requirements for operation of a droplet based LPP source. Monodisperse droplet generation in the kHz range is based on the Rayleigh breakup of jet. A modular design, based on cartridges, which are composed of the fuel reservoir and the dispensing nozzle, is proposed. Cartridges are inserted into a static, protective and low temperature casing, which is positioned with the help of a motion stage. The dispenser assembly is completely integrated in the EUV source chamber. The dispenser operation is controlled by the

source control system, which also handles the measurement data acquisition. The excitation mechanism relies on the generation of pressure waves at the tip of an oscillating piston, which is immersed in the liquid tin. Pressure waves propagate to the dispenser nozzle. The excitation frequency of the piston, which is generated by a piezoelectric actuator, is imposed on the tin jet and leads to a droplet breakup at the desired frequency. Thermal management of the piezoelectric actuator is crucial for reliable operation. In the present design, high operating temperatures are possible due to the direct cooling of the piezoelectric actuator. A multitude of nozzle designs and contamination control devices have been studied in the context of this work. The development of the droplet dispenser is a highly challenging task due to the multitude of issues encountered during tin droplet generation. An overview of the disciplines, which are involved in the design and operation of a reliable droplet dispenser is given in the following list:

- Thermal management
- Fluid dynamics
 - Micronozzle flows
 - Droplet formation
 - Acoustic waves
- Piezoelectrics (high temperature)
- Control systems & automation
- Sensors & electronics
- Plasma surface interaction / protection
- Surface chemistry
- Tin chemistry
- Contamination control
- Vacuum science
- Manufacturing
- Quality control

Chapter 3

Droplet dispenser performance

The developed droplet dispenser, which has been described in the previous chapter, is experimentally studied in terms of the main droplet train characteristics. First, the droplet size is measured using imaging techniques. The measured droplet diameter is then correlated to the key operating parameters of the droplet generator. The visualization of the droplet train is also useful in determining the droplet velocity, which is a measure for the droplet spacing. Results for the droplet train instabilities are presented. The instabilities are separated into timing instabilities (fluctuations of the droplet timing interval) and lateral instabilities, which correspond to displacements of the droplet in the direction perpendicular to the main trajectory.

3.1. Introduction

The dispenser performance is characterized with respect to the EUVL droplet requirements. One of these requirements is that the operating frequency is a multiple of the drive laser frequency, for frequencies greater than 10 kHz. As a consequence, the operating frequency range is investigated for the developed dispenser. The dispenser operating maps, which give the droplet diameter and velocity as a function of frequency and backpressure, indicate the typical frequency range. A major part of the droplet analysis in later chapters is conducted to determine the relationship between excitation frequency and droplet timing stability.

A second droplet parameter, which plays a significant role in LPP light sources is the droplet size. The computational studies of EUV LPPs, which are described in Sec. 6, reveal that the EUV emission and plasma debris strongly depend on the droplet size. In the dispenser performance assessment, the droplet diameter is determined by direct visualization. Different imaging techniques have been developed in the past for visualizing droplet streams.⁸² Most techniques are based on the stroboscopic illumination of the droplets. In the present work, a high speed camera and a back-illuminating flash are used for single (versus averaged) droplet imaging. The images are calibrated in terms of length scale in order to derive the droplet diameter. The visualization technique is also used to determine the average droplet spacing, as a portion of the droplet stream is recorded. The droplet spacing is crucial for the interaction of the LPP with the subsequent droplet. This topic is investigated by numerical means in Sec. 6.3.3.4.

Another major requirement is the minimization of the drop-to-drop timing jitter, which is the standard deviation of the droplet timing at a fixed observation point. Firstly, the timing jitter induces unwanted variations in droplet diameter. Secondly, the drop-to-drop jitter leads to laser pulse/ droplet de-synchronizations. Both mechanisms lead to fluctuations in the EUV energy per pulse. The consequences of droplet size variations and drive laser-droplet misalignment for the EUV LPP are discussed in Sec. 6.3.3. The droplet timing jitter is measured by a laser-photodiode system, which tracks the droplets in time. The concept is similar to a light barrier. Alternatively, the droplet jitter is also quantified (at a lower sampling frequency) with imaging techniques.

A second instability mode is related to the lateral displacement of the droplet in directions perpendicular to the drive laser beam. The consequences are again a misalignment of the droplet with respect to the laser focus resulting in fluctuations in the source's output energy. The time dependence of the lateral displacement is also quantified with the help of camera images. The limitation on the number of image frames per second yields a low sampling rate for the measurement of lateral stability, when compared to the droplet frequency.

3.2. Experimental setup

The performance assessment is completed using the droplet dispenser, which is described in detail in Sec. 2.2. During operation, online monitoring of the droplet train is accomplished by two different techniques.

3.2.1. Diagnostics

3.2.1.1. Droplet train visualization

In a first approach, a portion of the droplet stream is directly imaged. The droplet stream is back-illuminated by a high intensity LED flash (3 W) in order to produce shadowgraphs of a section of the droplet train. The setup for droplet visualization is shown in Fig. 22. Droplets are imaged onto

a high speed CCD (SONY ICX625) with a resolution of 2452×2054 pixels. Frame rates can go up to 15 frames per second. Pictures are recorded in 14-bit grayscale with pixel values from 0 to 255. The CCD's sensitivity is high enough to yield exposure times at ambient light conditions of $30 \mu\text{s}$. The camera is combined with a custom made macroscopic lens. The imaging lens allows a large working distance of 150 mm and a resolution of $1.7 \mu\text{m}$ per pixel. The working distance is mainly required in order to keep the camera at a safe distance from the LPP. Furthermore, the camera needs to be operated at ambient conditions and is therefore integrated in a tube with a front window, which protrudes into the vacuum chamber, as shown in Fig. 22.

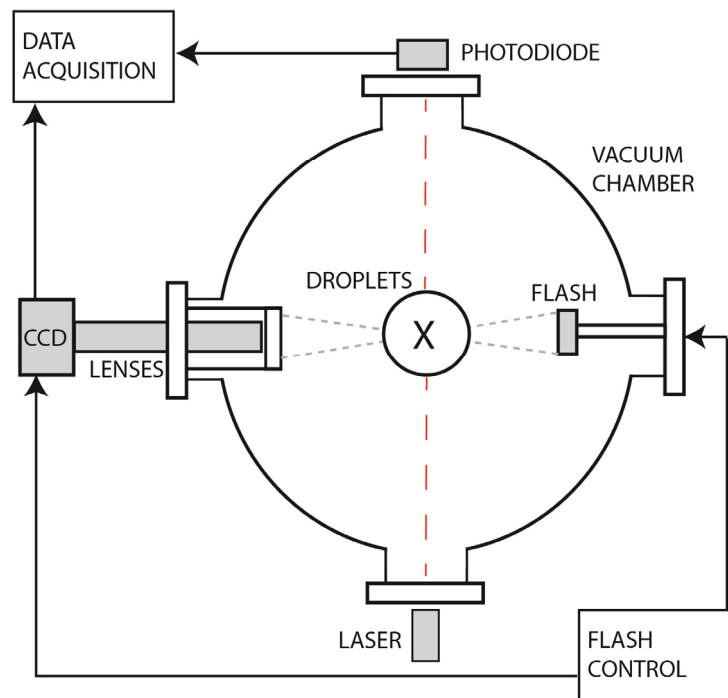


Fig. 22. Experimental setup with two droplet train diagnostics. The CCD camera, together with a macroscopic lens and a back-illuminating flash are used to image a section of the droplet stream. A photodiode, together with a HeNe laser is used to track the droplets in time. The propagation direction of the droplets is perpendicular to the plane of the schematic.

Correct triggering of both the camera and the LED flash yields exposure times lower than $1 \mu\text{s}$. The trigger signal is generated by the drive electronics of the LED flash. The LED emission, which corresponds to a $100 \mu\text{s}$ ultra-bright flash pulse, is shown in Fig. 23. The signal is also used to trigger the camera shutter. The camera adds a predefined delay to the trigger signal of the LED, before the shutter is opened. As shown in Fig. 23, the camera is triggered at the end of the LED pulse, which provides more reproducible results than triggering at the beginning of the pulse. At large exposure times, blurring of the droplet contour occurs. However, the exposure must provide enough light to produce a useful image with an acceptable signal to noise ratio. As mentioned

above, the camera exposure time is $30\ \mu\text{s}$, but the light intensity of the flash is high enough to produce an image in less than $1\ \mu\text{s}$.

As a result of the small exposure time, single droplet exposure is possible, as opposed to the averaged droplet imaging of the commonly used stroboscopic techniques. Beside the fact that no averaging of droplet contours takes place, the major benefit of single droplet exposure is an increased sharpness for measuring the droplet diameter.

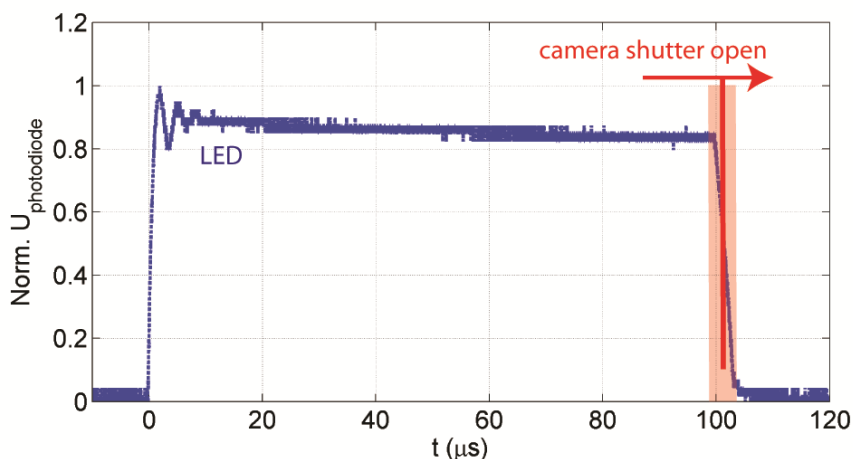


Fig. 23. $100\ \mu\text{s}$ LED flash emission recorded by a photodiode. The camera shutter opens at a fixed delay of more than $100\ \mu\text{s}$ after the flash trigger signal.

The recorded images can be processed online or at the end of each run. In a first step, a static background image is subtracted from the image to be processed in order to compensate for inhomogeneities in the illumination. Each picture is then converted to a black and white image, according to a threshold grayscale value found at the droplet contour. Different filters, such as a Wien filter are applied to eliminate the influence of sensor noise in the droplet contour detection. In the present work, the droplet contour threshold value needs to be determined manually (once) if the illumination conditions are changed. The droplet contour is numerically derived from the processed images. The diameter of the droplet is taken as the dimension of the droplet in the direction perpendicular to the droplet trajectory. The reason for this approach is the blurring of the droplets along their trajectory, which is due to a finite exposure time and potentially high velocities. The derivation of the circularity of the droplet contour is also implemented in the image processing. The coordinates of the center of mass are computed from the droplet contour. The information about size and position of each droplet is then saved for further processing. The second post-processing step includes the derivation of additional quantities, such as the droplet spacing and the lateral jitter. The timing jitter is derived as the standard deviation of the droplet spacing, divided by the mean droplet spacing.

The high speed camera, together with the macroscopic lens, has to be calibrated in order to assign dimensions to the pixels. First the magnification of the macroscopic lens, as specified by the

supplier, is used to determine the magnification of the lens. This magnification is then used together with the physical pixel size of the CCD to estimate the resolution. In a second step, objects of a predetermined size are used to calibrate the camera. Although a zoom lens has been used for most of the measurements, the typical resolution equals $1.7 \mu\text{m}$ per pixel length. It is worth noting that the optical resolution is usually higher than this digital resolution. A major source for this discrepancy is the manual focusing onto the droplet train. The uncertainty on the droplet diameter is mainly resulting from the blurred droplet contour. For the considered droplet size and lens settings, the diameter uncertainty is in the range of $\pm 3\%$, while the measurement uncertainty on the droplet spacing equals $\pm 0.5\%$.

3.2.1.2. Droplet timing acquisition

The second diagnostic tool used to characterize the droplet train consists of a HeNe (633 nm) milliwatt laser beam, which is focused onto the droplet stream. The laser spot size typically exceeds the droplet size, to allow for lateral motion of the droplet stream. The transmitted and scattered light is captured by a photodiode, which is located on the laser axis. The photodiode response details the droplet timing at the studied location. The droplet jitter is derived as the standard deviation of the drop-to-drop time intervals. The experimental setup is shown in Fig. 22. Details about the data processing are presented in Sec. 5.4.1.

In the experiments, the droplet timing jitter is derived either from camera images or from the laser-photodiode measurements. It will be shown in detail in Sec. 5.2.1 that the droplet jitter results from the droplet velocity dispersion, which develops during droplet breakup. The derivation of the timing jitter from the photodiode signal is straightforward, as it captures the droplet timing in an equivalent way to the drive laser. The camera images are however discrete snapshots in time, which include several droplet spacings.

The difference between the two measurement approaches is quantified with the help of a Monte-Carlo simulation. Droplets are sampled with random velocities, which are taken from a defined dispersed velocity distribution. The droplets are initialized at the breakup point and move according to their individual velocity. The situation is depicted in Fig. 24a. In a first approach, their timing jitter is derived at a fixed observation height, in analogy to the laser-photodiode measurement. Then a virtual photograph is taken, when a droplet passes in front of the observation point. The additionally captured droplets are located upstream of this droplet, as shown in Fig. 24a. In a second approach, the timing jitter is derived from the standard deviation of the respective droplet spacings, which are captured in the virtual photograph.

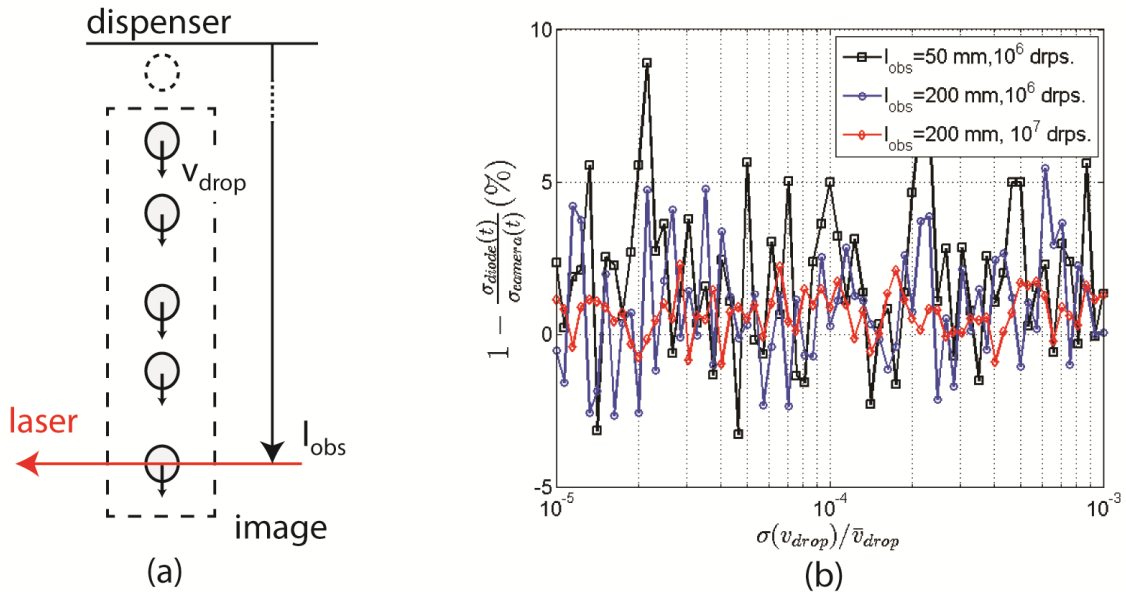


Fig. 24. (a) Droplet train with imaged section and laser beam at observation height l_{obs} . (b) Simulated difference between laser-photodiode and camera measurements of the droplet jitter for a droplet frequency of 20 kHz, a droplet velocity of 10 m/s and an image acquisition rate of 5 Hz.

The Monte-Carlo simulations are run for a mean droplet velocity of 10 m/s. The droplet velocity dispersion is assumed to be in the range of 10^{-5} to 10^{-3} . Similar values are experimentally determined in Sec. 5.4.2. The image acquisition rate is 5 Hz, while droplets are generated at 20 kHz. The observation height l_{obs} and the number of generated droplets are varied in the simulation. The largest difference between the jitter determined by the laser-photodiode and the jitter determined by the camera is found for the lowest observation height (50 mm) and the lowest number of observed droplets (10^6). In this case, the measured jitters can differ by up to 9%, as shown in Fig. 24b. The number of observed droplets correlates with the measurement time. A droplet number of 10^6 corresponds to a measurement time of 50 s. For a larger observation height (200 mm) and a larger number of droplets (10^7 droplets, equivalent to 500 s measurement time), the largest differences between the two measurement methods are in the range of 2%. In conclusion, care must be taken if the jitter is determined with camera measurements. The main parameter to increase the accuracy in the determination of the droplet jitter is the measurement time. The observation height, which corresponds to the location of the irradiation site, is typically fixed.

3.3. Results

Experimental results are required to assess the performance of the developed droplet dispenser. All measurements are completed with the same nozzle type and size. The main operating parameters are the excitation frequency and backpressure. Firstly, droplet train images for some specific operating points of the dispenser are presented. The droplet size and spacing are derived. Then, all the measurements are summarized in the dispenser operating maps, which indicate the average droplet

diameter and average velocity (or droplet spacing) as a function of frequency and backpressure. Finally, the timing jitter and the lateral stability are detailed.

3.3.1. Droplet train imaging

The droplet imaging setup, which is described in Sec. 3.2.1.1 is employed to visualize the droplet stream. A raw image of the droplet, as recorded by the high speed CCD and flash, is shown in the top part of Fig. 25. The image is rotated by 90° and the droplets move from left to right. The recorded image is characterized by an inhomogeneous illumination with a central spot and some image sensor noise. The droplets are generated at a frequency of 20 kHz and at backpressure of 20 bar.

The image processing, which is described in detail in the previous section, is illustrated in Fig. 25. In a first step, a background image is subtracted from the camera image and noise filtering is applied. The resulting image is converted to a binary (black and white) image, which is then scanned pixel-wise to detect single droplets and derive the droplet contour.

In the context of the performance assessment of the developed droplet dispenser, the droplet train is imaged at different operating conditions. Each operating point is defined by the system backpressure and excitation frequency. It must be noted that the presented images are derived directly from camera images by adjusting the brightness and the contrast. The droplet dimensions and spacings are not at exactly the same scale for different images, but the quantitative trend is conserved.

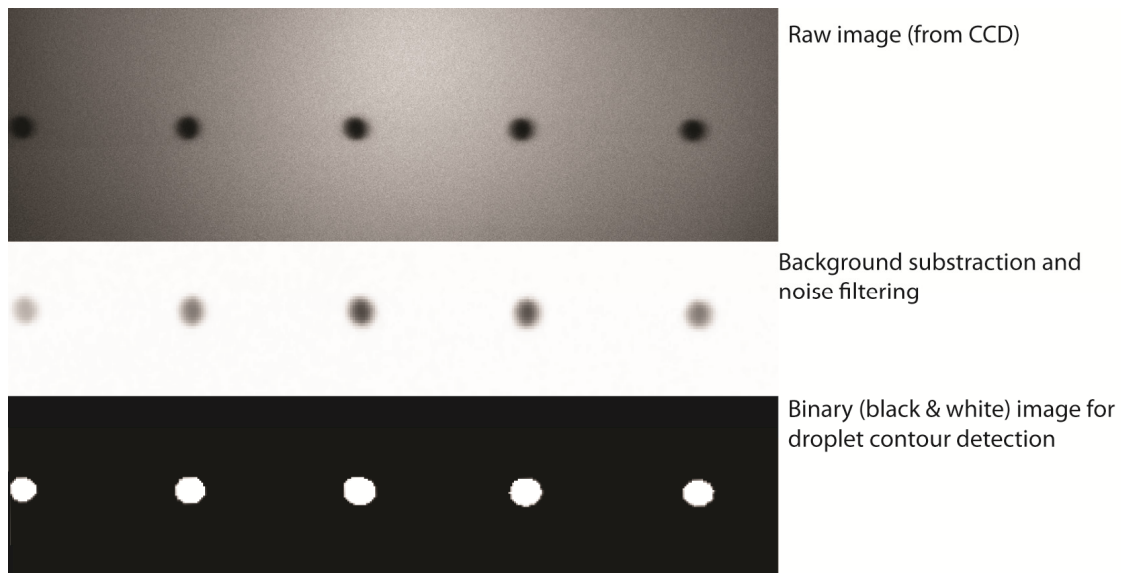


Fig. 25. Image processing from raw camera image to black & white image for droplet contour derivation.

Firstly, the droplet train is visualized at a constant backpressure of 10 bar, for frequencies of 18 kHz and 50 kHz respectively. This first set of measurements is completed with a contamination filter with a lower pressure drop than the standard filter. The frequency change influences both the droplet spacing and the droplet diameter, as shown in Fig. 26. The droplet diameter equals 59 μm at 18 kHz, while the droplet diameter decreases to 50 μm at 50 kHz. The droplet spacing decreases by a factor 2.5 for the measurements at 50 kHz when compared to 18 kHz data. The droplet velocity is derived as the product of the droplet spacing, which is derived by image processing, and the excitation frequency. Interestingly, a velocity increase of a few percent is observed. The droplet velocity at 50 kHz equals 12.8 m/s. The average droplet spacing at 18 kHz equals 7 droplet diameters. The change in droplet diameter can be expected. Indeed, at the same backpressure, the jet mass flow should remain constant. At high frequencies, the droplet diameter must decrease according to mass conservation.

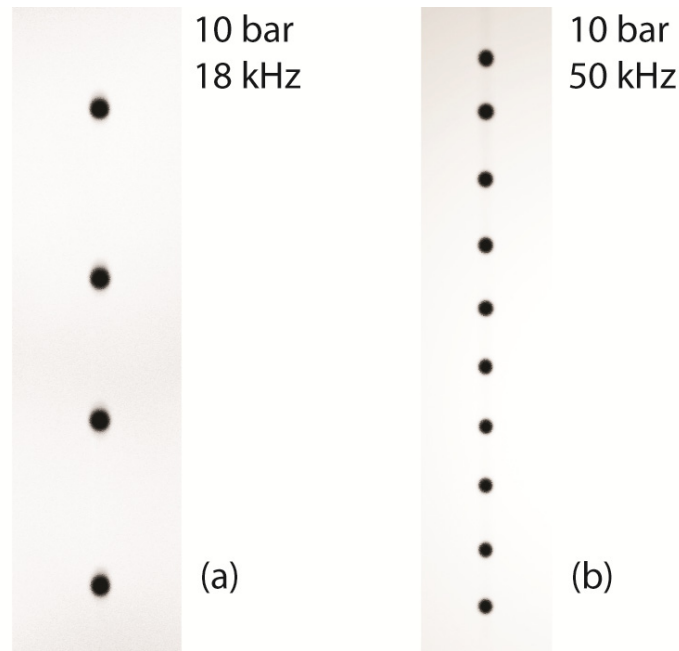


Fig. 26. Droplet train images for a constant backpressure of 50 bar. (a) The excitation frequency equals (a) 18 kHz and (b) 50 kHz.

The next set of measurements has been recorded for the standard configuration of the droplet dispenser. A filter with a larger pressure loss than the filter of the measurement from Fig. 26 is employed. In Fig. 27a and Fig. 27b, the droplet train is shown at a constant frequency of 20 kHz, for backpressures of 20 bar and 40 bar, respectively. At a constant frequency, the backpressure variation from 20 bar to 40 bar influences the droplet spacing, which is equivalent to the droplet velocity. The change in droplet velocity is 6%. The droplet velocity at 40 bar and 20 kHz equals 9.5 m/s. The backpressure variation increases the jet mass flow. Therefore, at a constant frequency, the droplet diameter and the velocity must increase. The droplet diameter at 20 bar equals 60 μm ,

while the increased diameter at 40 bar equals $65\ \mu\text{m}$. Droplet spacings are in the range of 7 droplet diameters.

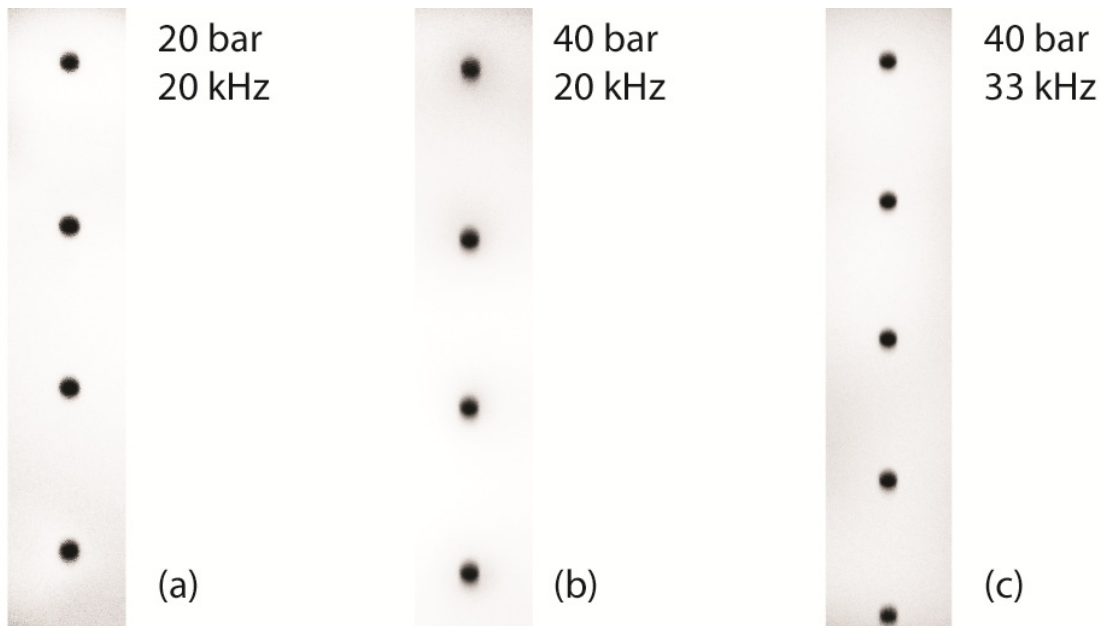


Fig. 27. Droplet train images for different operating conditions (backpressure p and frequency f) (a) $p=20\ \text{bar}$, $f=20\ \text{kHz}$. (b) $p=40\ \text{bar}$, $f=20\ \text{kHz}$. (c) $p=40\ \text{bar}$, $f=33\ \text{kHz}$.

The droplet train is shown in Fig. 27b and Fig. 27c at a constant backpressure of 40 bar, for frequencies of 20 kHz and 33 kHz, respectively. The frequency change influences the droplet spacing / velocity and the droplet diameter. The droplet diameter reaches $57\ \mu\text{m}$ at 33 kHz. The droplet spacing at 33 kHz is reduced to 5.5 droplet diameters. The trends in Fig. 27b and Fig. 27c are similar to the trends observed for the lower pressure loss filter in Fig. 26.

Similar droplet train images to the ones presented in this section are used to derive the mean spacing, the droplet velocity and the diameter at different operating points.

3.3.2. Dispenser operating map

In order to summarize the evolution of the droplet diameter and the velocity as a function of excitation frequency and backpressure, operating maps of the dispenser are derived. These operating maps are based on discrete measurements at different frequencies and backpressures. The discrete measurements are then used to interpolate a continuous operating map. The quantities of interest are the droplet diameter, the droplet velocity and the drop-to-drop distance.

The operating maps are derived for the standard version of the developed droplet dispenser. Three of the discrete measurements, from which the operating maps are interpolated, are presented in Fig. 27. The droplet diameter mainly depends on the excitation frequency, as shown in Fig. 28a. At constant backpressure, an increase in excitation frequency leads to a decrease in droplet size. This

observation is straightforward from mass conservation, as the jet velocity is set by the backpressure. At low frequencies and large backpressures, droplet diameters of up to $65\ \mu\text{m}$ have been observed. The smallest droplet diameter of $38\ \mu\text{m}$ is found at frequency of $100\ \text{kHz}$ at a backpressure of $40\ \text{bar}$.

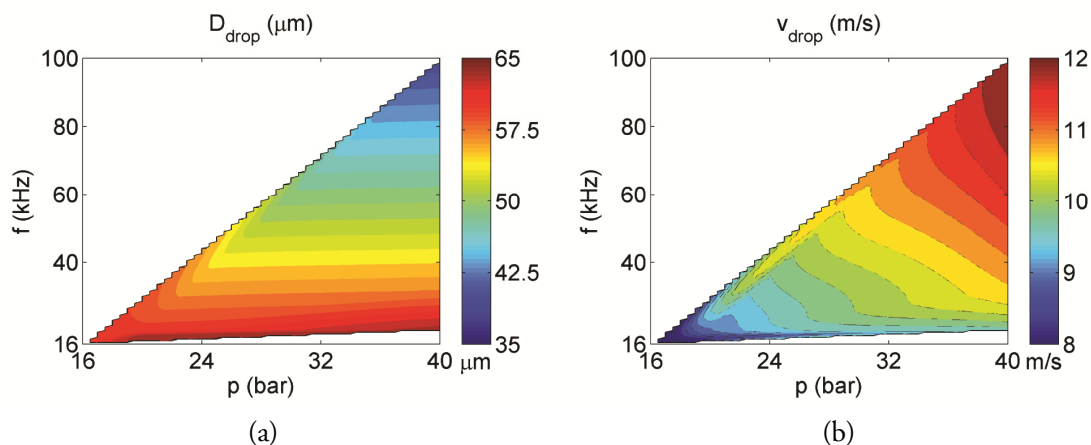


Fig. 28. (a) Droplet diameter and (b) droplet velocity as a function of frequency and backpressure. The operating map is interpolated from discrete measurements.

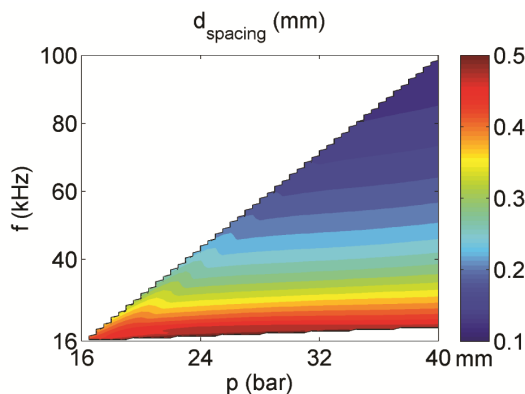


Fig. 29. Interpolated map of droplet spacing as a function of backpressure and frequency.

The droplet velocity, which is directly derived from the measured droplet spacing and the excitation frequency, varies in the range from 8 to 12 m/s, as shown in Fig. 28b. The velocity depends on both operating parameters, namely the frequency and the backpressure. Increases in frequency and / or backpressure increase the droplet velocity. The largest droplet velocity of 12 m/s is obtained at a backpressure of 40 bar and an excitation frequency of 100 kHz. At a constant excitation frequency, the increase in velocity with backpressure is intuitive. Indeed, an increased backpressure leads to increased jet velocities and therefore larger droplet velocities. The dependence of the droplet velocity on the excitation frequency is not trivial. It will be shown later in Sec. 5.2.1, that the droplet velocity is smaller than the jet velocity, due to a momentum exchange between the jet and

the forming droplet. For smaller droplets, this momentum exchange is expected to be smaller, hence the resulting droplet velocity is closer to the jet velocity.

Droplet spacings range from 0.1 to 0.5 mm. The smallest droplet spacing is found at the highest operating frequency. The largest droplet spacing, which is desirable in EUV LPP sources, is found at the highest velocity. It is obtained at a backpressure of 40 bar and the lowest possible frequency, which in the present measurements is equal to 20 kHz. The corresponding droplet train image is shown in Fig. 27a. The largest measured droplet spacing equals 7.5 droplet diameters. The uncertainty on the droplet spacing is $\pm 0.5\%$.

In conclusion, a trade-off is required to meet the low droplet size and large droplet spacing requirements of EUV sources. Indeed, at a constant nozzle size, large droplet spacings imply large droplet diameters.

3.3.3. Droplet stability

A key requirement for EUV sources is EUV energy stability. The EUV output stability directly depends on the droplet stability. Although droplets are a regenerative target, the initial conditions for the laser-droplet irradiation might vary. The two typical instability modes of the droplet train are the lateral stability and the droplet timing jitter, as shown in Fig. 12. A third variation could be introduced by temporal variations of the droplet diameter. It will be shown in Sec. 6.3.3.3 that the droplet size plays an important role in EUV emission and debris generation.

The results in this section are derived for an operating backpressure of 20 bar. The standard version of the droplet dispenser is used. The droplet frequency equals 20 kHz if no other frequency is specified. The observation point is located at 55 mm from the dispenser nozzle.

3.3.3.1. Droplet diameter stability

Image processing of continuously recorded droplet stream images yields the temporal dependence of the droplet diameter. Multiple droplets are recorded per image. The droplet diameter, which is assigned to the time instance of the recorded image, is derived from one droplet in each image. The droplet diameter at a time instance t is not an averaged quantity. The threshold in image processing for the detection of the droplet contour is taken in the same region where the diameter is determined. The time dependence of the droplet diameter is recorded over a time period of 600 s, as shown in Fig. 30.

The temporal variation of the droplet diameter over a time range of 600 s is not negligible for the recorded data. The mean droplet diameter is 60 μm and three standard deviations are 15% of droplet diameter. This size variation corresponds to a droplet mass variation of 52%. A slow variation of the mean value of the droplet diameter is observed. The fluctuations in droplet diameter result from variations in the jet mass flow, as the droplet frequency is constant at 20 kHz.

Thermal transients and fluid impurities are proposed to be potential causes. The influence of the droplet size on the EUV LPP is detailed in Sec. 6.3.3.3.

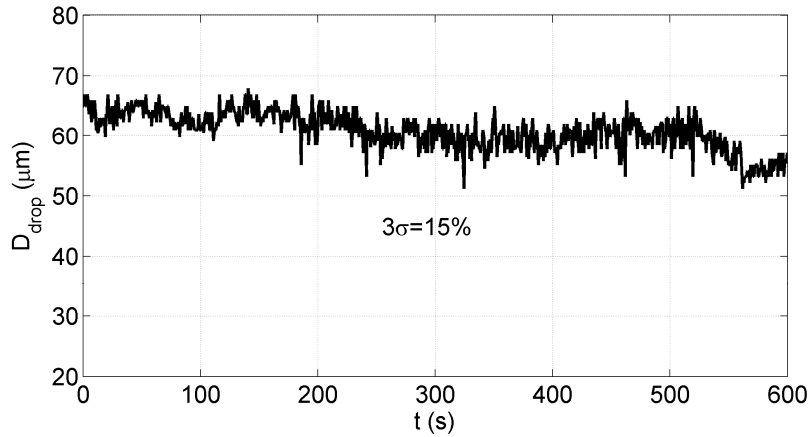


Fig. 30. Time dependence of the droplet diameter at a droplet frequency of 20 kHz and a backpressure of 20 bar. Lateral stability

The lateral droplet stability, which is one of the major challenges encountered in LPP sources, is also quantified by imaging techniques. The experimental setup, which is described in Sec. 3.2, permits the visualization of the droplet stream in one plane only. As the dispenser nozzle is axisymmetric, the measurements are supposed to be statistically representative for the droplet displacements in three dimensions. The isotropy of the droplet instability has been observed for different runs.

The lateral droplet displacement is derived from the displacement of the mean line across the droplet centers of one image. Droplet displacements for single droplets are not observed. The deviation of individual droplets from this mean line lies within the measurement uncertainty. A standard deviation of 0.6% of the droplet diameter has been determined for the droplet deviation from the mean line. The lateral displacement, which is assigned to a time instance t is equal to the coordinate of the droplet mean line at mid-height of the image. The lateral droplet displacement is split up into the low and high frequency contributions of the signal. The low frequency signal is obtained from a running average over a signal windows of 2 s. The corresponding frequency is equal to 0.5 Hz. The high frequency signal of the droplet displacement contains all frequencies above 0.5 Hz. This separation into high and low frequency contributions is particularly useful when designing a dispenser position control system, which, limited by the inertia of the dispenser, operates at low frequencies, when compared to the droplet frequency.

The lateral droplet displacement is recorded over a time duration of 600 s, as shown in Fig. 31 and Fig. 32. The droplet train displacements are normalized by the mean droplet diameter from Fig. 30. The low frequency part of the lateral droplet displacement signal varies in a range of 10 droplet

diameters, as shown in Fig. 31. A spectral analysis reveals no dominant frequencies, hence the variation of the droplet displacement can be assumed to be non-deterministic for the recorded data.

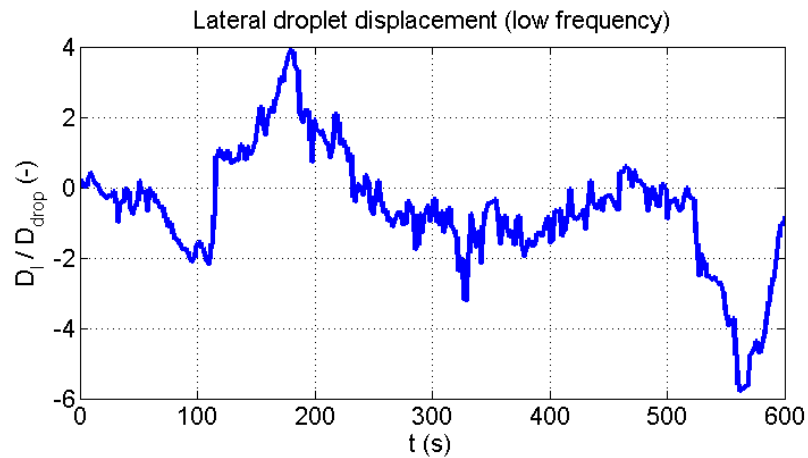


Fig. 31. Temporal evolution of the low frequency content of the lateral droplet displacement, measured at 20 kHz and 20 bar.

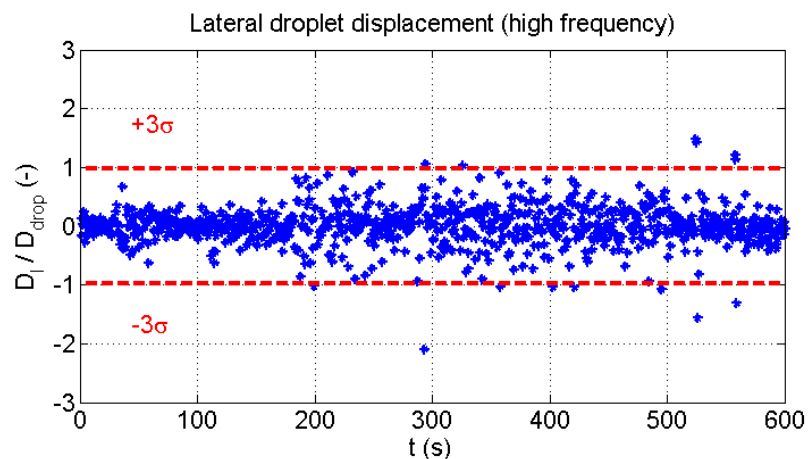


Fig. 32. Temporal evolution of the high frequency content of the lateral droplet displacement, measured at 20 kHz and 20 bar. Three standard deviations of the high frequency droplet displacements are equal to one droplet diameter.

The high frequency part of the droplet displacement signal is presented in Fig. 32. Three standard deviations (3σ) are equal to one droplet diameter. This high frequency droplet displacement mainly determines the source stability. Indeed the low frequency variations of the lateral droplet position can be compensated by active position control. Increasing the controller response time yields lower standard deviations for the high frequency part of the droplet displacement signal. The experimentally measured displacement variation is used to predict the corresponding fluctuations in EUV energy in Sec. 6.3.3.5. Potential causes for the lateral displacements, as well as solutions are described in Sec. 2.2.5.

3.3.3.2. Timing jitter

The drop-to-drop jitter determines the source stability by influencing the laser-droplet synchronization. Two measurement techniques can be used to determine the timing jitter, namely laser-photodiode measurements and imaging techniques.

The droplet jitter is extracted from the recorded images by determining the droplet spacing d_{drop} . The droplet jitter is then derived as the standard deviation of the droplet spacings, which are normalized by the mean droplet spacing. Details and a validation of this approach are presented in Sec. 3.2.1.2. The threefold standard deviation of the droplet spacing is equal to 6.6 % of the mean spacing at a frequency of 20 kHz and a backpressure of 20 bar. For the recorded data, this deviation of 6.6% of the mean droplet spacing is equivalent to a deviation of 50% (3σ) of the droplet diameter.

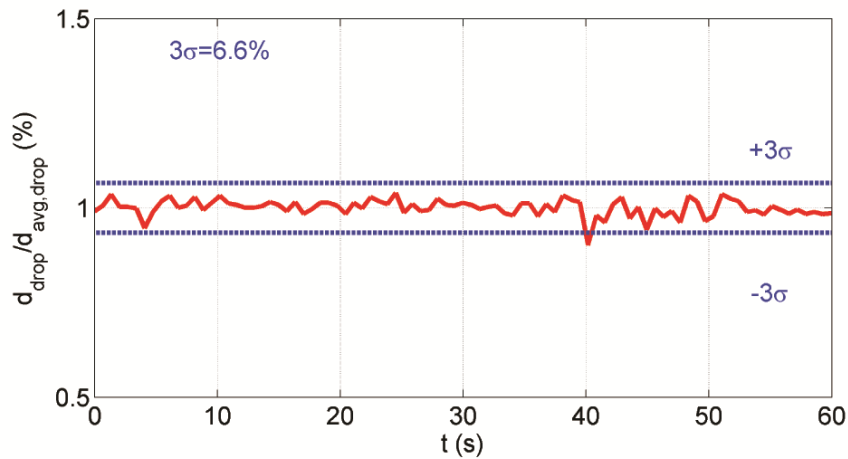


Fig. 33. Time dependence of the droplet spacings, normalized by the mean droplet spacing. Three standard deviations of the droplet jitter are equal to 6.6% of the mean droplet spacing.

In a second approach, the droplet jitter is measured by the laser-photodiode system. In the present experimental setup, the droplet signal is recorded at 1 MHz in windows of 1s at a duty cycle of 50%. The 50 % duty cycle is required for data storage. As a consequence, each window contains 10^4 droplets at 20 kHz. The droplet timing jitter is derived for each window. The value corresponding to three standard deviations of the droplet timing interval is assigned to the time instance t of the measurement window.

A sample photodiode signal, which is recorded over a time duration of 1000 μ s, is presented in Fig. 34. The photodiode signal equals unity for the undisturbed laser beam. The blocking of the laser beam by droplets induces a dip in the photodiode signal. The droplet timing jitter is derived from the differences between subsequent local minima (red dots in Fig. 34) of the photodiode signal. The droplet frequency equals 15.7 kHz.

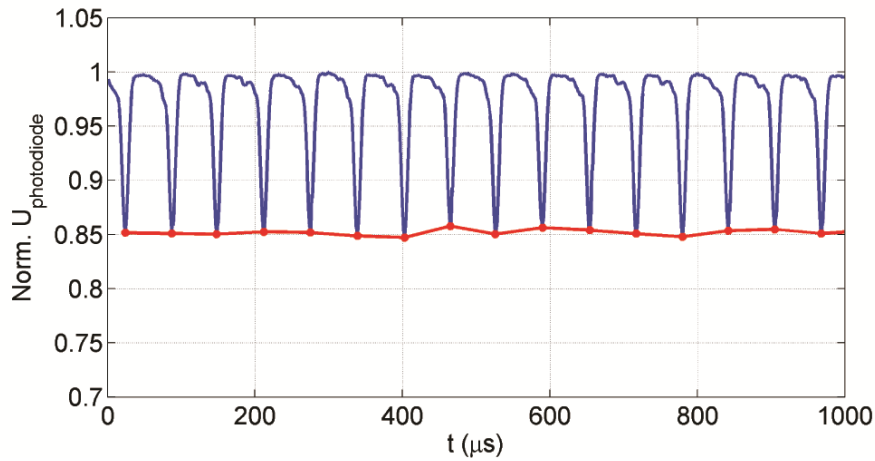


Fig. 34. Sample photodiode signal. The undisturbed laser beam yields a (normalized) photodiode signal, which is equal to unity. The crossing of the droplets with the laser beam induces a decrease in photodiode voltage. The droplet timing is derived as the time difference between local minima (red dots).

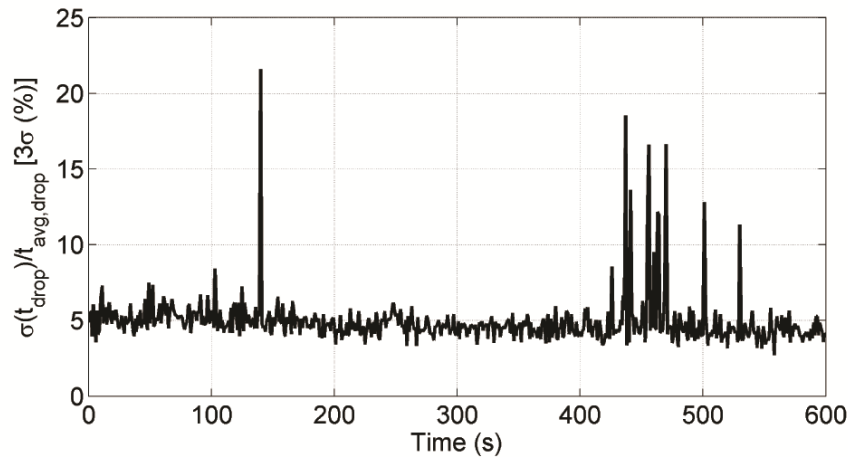


Fig. 35. Temporal evolution of three standard deviations of the droplet timing at a droplet frequency of 15.7 kHz. The droplet jitter is computed in windows of 1 s.

The temporal evolution of three standard deviations of the droplet timing is shown in Fig. 35 for a recording time of 600 s and a droplet frequency of 15.7 kHz. The timing jitter is equal to one third of the plotted signal. The three standard deviations of the droplet timing are normalized by the mean droplet timing interval. The average value of the droplet jitter (3σ) is equal to 5%, with an average variation of $\pm 1\%$. A few outliers with threefold droplet jitters (3σ) of up to 20% are detected.

In a next step, the temporal evolution of the droplet jitter is compared for droplet frequencies of 15.7 and 20.0 kHz, respectively. Interestingly, the average value of the droplet jitter of the 20 kHz droplet train is 6% higher than the droplet jitter of the 15.7 kHz droplet train. The mean threefold droplet jitter (3σ) for the 20 kHz droplet train is equal to 5.1% for the laser-photodiode measurement. The image-based method yields a value of 6.6% for three standard deviations of the droplet spacing. First, it has been shown in Sec. 3.2.1.2 that differences between the two measurement methods can be expected for the considered observation height and measurement duration. The difference in this case is however larger than expected from Fig. 24. The second cause for the discrepancy is the reproducibility of the experiments. Indeed the timing jitter is also affected by impurities in the nozzle.

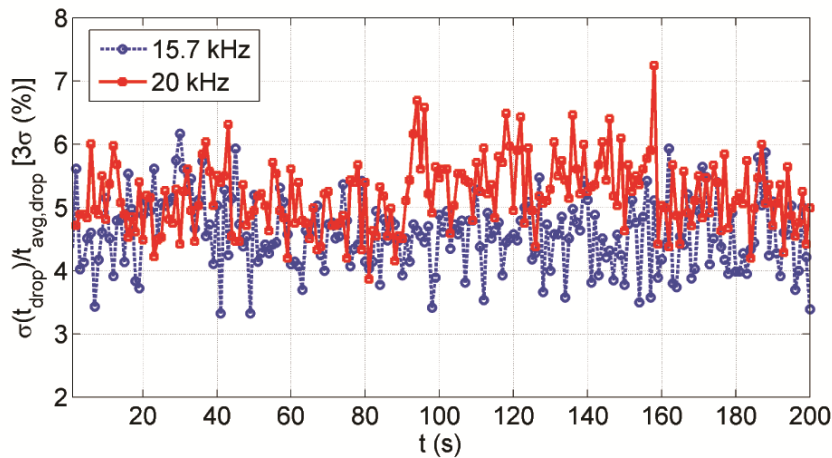


Fig. 36. Comparison of the droplet jitter for droplet frequencies of 15.7 kHz and 20 kHz. Data is plotted for a time interval of 200 s.

During the performance assessment of the dispenser, a large sensitivity of the droplet jitter to the excitation frequency has been observed. Small changes in excitation frequency yield large differences in droplet jitter, which range from low jitter of a few percent to large jitter, such that the droplet train has a non-deterministic structure. The corresponding droplets are unusable in LPP sources. This important dependence is investigated in the next chapters.

3.4. Summary and conclusion

The performance assessment of the developed droplet dispenser is based on results, which are either obtained by imaging the droplet train or by tracking the droplets with a laser-photodiode light barrier. Droplet visualization relies on the use of a high speed CCD, combined with a macroscopic lens and a high speed flash. Correct triggering of both units yields exposure times lower than 1 μ s, which leads to sharp droplet contours for the recorded droplet velocities. Image processing is based on the conversion of the raw CCD image into a black and white image in order to detect the

droplet contour. The droplet contour is used to derive the coordinates of the droplet center, as well as the droplet size.

The droplet train is visualized for different operating points, which are characterized by the excitation frequency and backpressure. It is found that, at constant frequency, an increase in backpressure increases the droplet diameter and the droplet velocity. At constant backpressure, the droplet diameter decreases with increasing frequency and the velocity increases with increasing frequency. The largest droplet diameter is found at the lowest droplet spacing. As a consequence, a trade-off between droplet size and spacing is required in the design of LPP sources.

Time series of droplet images are processed to yield the temporal evolution of the droplet diameter. A variation of 15% of the droplet diameter is observed over a time window of 600 s. Potential reasons include thermal transients and fluid impurities. The lateral displacement of the droplet train is also studied with the help of recorded droplet stream images. The time signal of the droplet train position is split into a high and low frequency contribution at a frequency of 0.5 Hz. Although, the low frequency fluctuations are in the range of ten droplet diameters, they can be compensated by active position control of the dispenser. The high frequency variations of the lateral position yield three standard deviations of one droplet diameter.

The laser-photodiode setup is used to determine the droplet jitter. The blocking of the laser beam by a droplet yields a decrease of the photodiode voltage. The local minima are assigned to the droplet centers. The droplet jitter is equal to the standard deviation of the droplet timing intervals. Both, the imaging and the laser-photodiode approach can be used for measuring the droplet jitter. For the case where the jitter is derived with the help of the imaging approach, care must be taken that a sufficient number of droplets is considered, at a sufficient distance from the nozzle. At a droplet frequency of 20 kHz and a backpressure of 20 bar, the imaging and the laser-photodiode approaches yield droplet jitters (3σ) of 6.6% and 5.1%, respectively. The corresponding three standard deviations of the droplet timing for 15.7 kHz are 6% smaller. Overall a strong dependence of the droplet jitter on the excitation frequency is observed. The influence of the excitation frequency on this important stability mode is studied in detail in the next chapters.

Chapter 4

Excitation dynamics

The excitation system is based on a piezoelectrically actuated piston, which generates pressure disturbances at the piston tip. The focus of this chapter is the study of the non-ideal pressure boundary conditions, which lead to droplet breakup. First, an in-house developed miniature fast-response pressure probe is used to measure the pressure response at the nozzle inlet for different excitation frequencies. In order to understand the complex pressure response, which contains pressure amplitudes distributed over several orders of magnitude, laser Doppler vibrometer (LDV) measurements are completed. The structural response is reproduced by a full finite element analysis of the assembly, including the piezoelectric stack. The numerical analysis is used to explain the origins of the resonance peaks. The quasi-linear relationship between the structural displacements around the piston tip and the pressure amplitudes is verified for two different excitation systems. At the end of the chapter, tuning guidelines for the pressure response, as a function of desired droplet frequency, are proposed.

4.1. Introduction

The developed droplet dispenser is based on the capillary breakup of the tin jet. The external excitation is imposed as an axisymmetric harmonic perturbation on the jet radius (Sec. 2.1.3). The origin of the perturbation, in the absence of a forced excitation, is noise, as described in Sec. 5.1. In the present application, an external pressure excitation is imposed to bypass the natural breakup frequencies. The role of a pressure disturbance on droplet formation is derived in detail in Sec. 5.1

from a linearized one-dimensional droplet formation model. Eq.(2.3) shows that the magnitude of the jet disturbance is directly proportional to the pressure amplitude introduced by the external excitation. As a consequence, the jet breakup efficiency, which is related to the minimization of the drop-to-drop jitter and the maximization of the droplet spacing, is given by the efficiency of the excitation mechanism to generate sufficient pressure amplitudes at the desired frequency.

In the work that follows, the non-ideal boundary conditions of droplet formation will be studied as a function of the external excitation. The performance of the excitation mechanism is characterized by measuring the pressure disturbance at the nozzle inlet using a high temperature piezoresistive pressure sensor. In order to understand the origins of the pressure response, the structural response is experimentally determined by the use of a laser Doppler vibrometer. In addition, the structural response helps to separate the fluid dynamic and structural influences on the pressure response.

The design of a novel high temperature fast response pressure probe for use in liquid tin is detailed in the next section. The probe is useful in determining the non-ideal boundary conditions, which lead to droplet breakup. Furthermore, the probe enables real-time monitoring of the pressure at the inlet of the dispenser nozzle.

4.2. High temperature fast response pressure probe

4.2.1. Introduction

The excitation mechanism of the droplet generator, which is developed in this work is based on a piezoelectrically actuated oscillating piston, as described in Sec. 2.2.4. The piston generates acoustic pressure waves at the nozzle inlet, as shown in Fig. 37. While droplet formation itself has been extensively studied over the last decades, the non-ideal boundary conditions of droplet formation due to disturbance dynamics have not been investigated for liquid metal dispensers. Time-resolved pressure measurements at the position of the nozzle are highly desirable. To date, a piezoelectric pressure transducer has only been used in the vicinity of a dispenser nozzle at room temperature, for monitoring the pressure disturbance induced by an amplitude-modulated excitation source.¹⁴⁹

In this work, the technology of a fast response (greater than 10 kHz) and high temperature (up to 255 °C) pressure probe, which is based on a miniature piezoresistive silicon pressure sensor, is demonstrated. Probe design is derived from the fast response aerodynamic probe (FRAP) technology from ETH Zurich, which has been extensively utilized in the past decades for aerodynamic measurements in turbomachinery flow fields.^{150, 151} The high temperature version of the FRAP probe has been developed by Lenherr *et al.*¹⁵² Other state-of-the-art high temperature pressure probes are based on silicon-on-insulator (SOI)¹⁵³ sensors, which are, however, not commercially available for the required size. Another probe type relies on water cooled piezoresistive

sensors,¹⁵⁴ which have the severe disadvantage of cooling the liquid in contact with the sensor. Furthermore, water circuits should be avoided in high vacuum systems.

A major requirement is long-term reliability of the probe in the harsh environment of a liquid metal droplet dispenser. The probe is either used for studying disturbance dynamics in the dispenser development phase or for monitoring the performance of the excitation system during long-term operation. Although the probe is developed for use inside an EUV tin droplet dispenser, its ability to measure high frequency pressure fluctuations can be applied to liquid metals with compatible melting points.

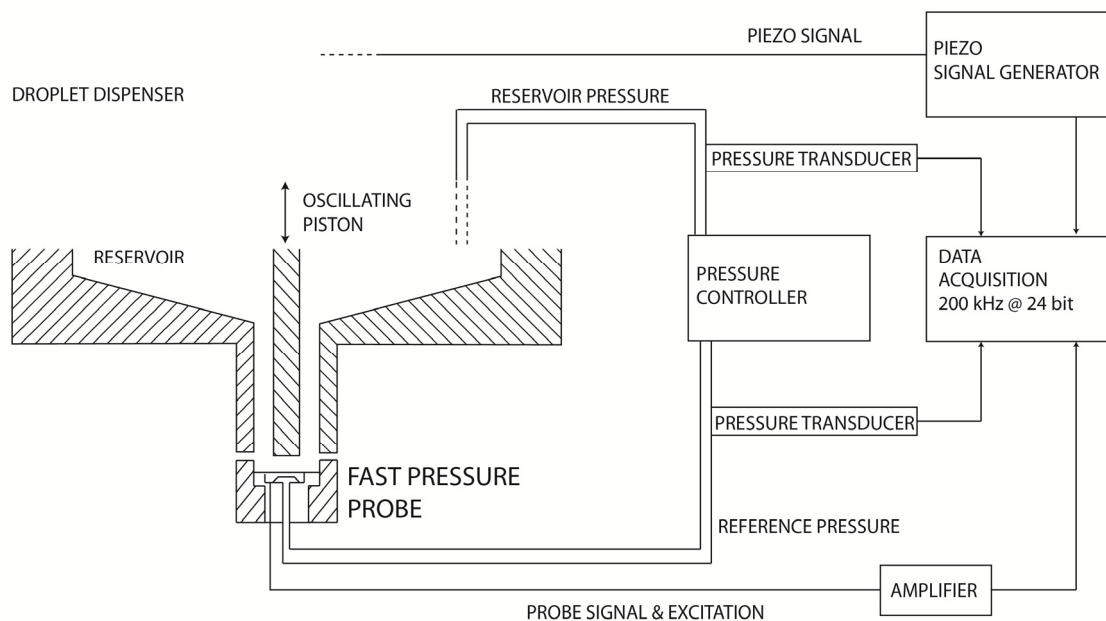


Fig. 37. Experimental setup of the tin pressure probe in an EUV droplet dispenser. The fast pressure probe either replaces the nozzle or is mounted on the side of the nozzle orifice (not shown). The sensor captures acoustic pressure fluctuations generated by an oscillating piston inside a heated reservoir. A pressure controller sets the reservoir pressure and the reference pressure of the differential pressure probe. The data acquisition system records electrical signals from the pressure probe, two pressure transducers and the piezoelectric signal generator.

4.2.2. Pressure probe design and performance

4.2.2.1. Requirements

The key probe requirements are related to the maximum operating temperature, measurement bandwidth and size. Sensor and probe material limits, as well as signal to noise ratio issues typically determine the probe's maximum operating temperature. Pressure fluctuations in liquid metals at temperatures up to 255 °C have been measured by the developed probe. Typical media to be

4.2 High temperature fast response pressure probe

studied include tin with a melting point (MP) of 232 °C. Other compatible media are metals such as Li, In, Ga, Na, K, Hg, Cd and Se and common solder materials such as SnPb, SnIn, SnZnIn and SnAg with melting points below the probe operating temperature. The measurement bandwidth is set by the typical frequency range (10 to 50 kHz) of EUV droplet dispensers. The probe's measurement bandwidth is quantified in Sec. 4.2.2.4 by studying its dynamic frequency response in a shock tube facility. Typical dispenser nozzles have orifice sizes below 100 μm , with an overall nozzle size in the millimeter range. As the probe must be integrated into the nozzle, it is required to be sized in the millimeter range.

Additional requirements are related to the pressure range. First, the sensor must withstand the large average pressures (greater than 10 bar) used in EUV dispensers to force liquid through filters and the micrometer scale nozzle. Secondly, the sensor must capture the full range of generated acoustic pressures. For a typical displacement $d = 0.1 \mu\text{m}$ of the piezoelectric actuator at a frequency $f = 50 \text{ kHz}$, the equation of acoustic impedance Z is

$$Z = \frac{p'}{d \cdot f} = \rho \cdot c \quad (4.1)$$

where ρ and c are the liquid density and speed of sound of tin, respectively. Rearranging Eq.(4.1) gives an expected unsteady pressure amplitude p' of 780 mbar. Pressure amplitudes of 350 mbar have been observed in the work of Orme *et al.* for a diffusion pump oil.¹⁴⁹



Fig. 38. High temperature fast response probe presented with a pen for scale comparison. The presented probe replaces the nozzle at the dispenser outlet.

4.2.2.2. Probe design and manufacturing

Piezoresistive sensors, which are well established for fast response measurements, have the advantage of measuring average pressure. This is in comparison with piezoelectric sensors, which only capture the fluctuating pressure component. Piezoresistive silicon sensors are based on strain gage technology. The core of the probe described in this study consists of a piezoresistive sensor of monocrystalline silicon structure. The sensor is not rated for high temperatures by the manufacturer. The sensor performance assessment for temperatures up to 260 °C has been completed at ETH Zurich.¹⁵⁵ The sensor is 2.2 mm in length, 1.3 mm wide and has a thickness of 0.4 mm. It works in differential mode, as the average pressure inside the dispenser reservoir can exceed the sensor burst pressure. Therefore, the non-exposed side of the silicon membrane can be pressurized at a reference pressure.

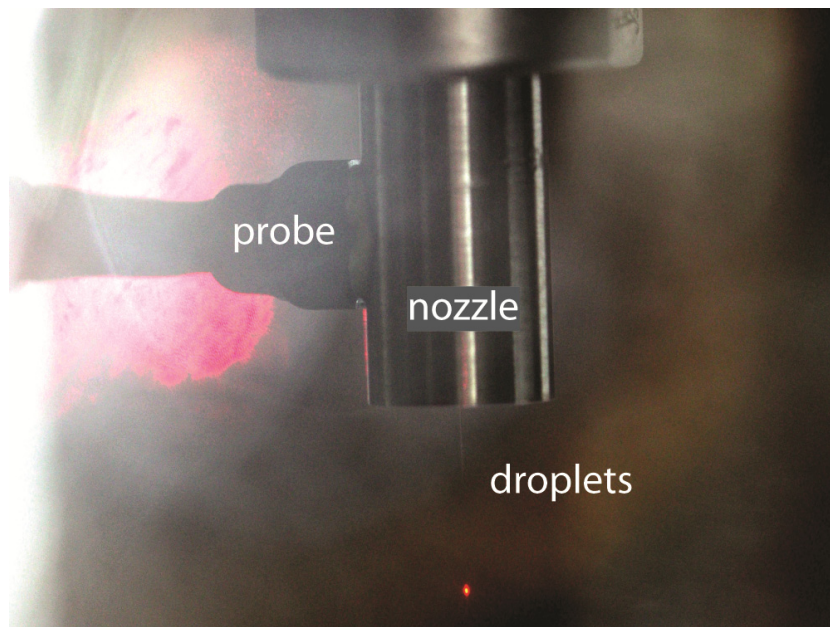


Fig. 39. High temperature fast response probe integrated into the dispenser nozzle. The probe is integrated in the side wall of the nozzle. The red dot corresponds to the spot of a diode laser pointing at the droplet train. The picture is taken through a vacuum window.

The piezoresistive pressure sensor is integrated into a non-conductive housing, which accommodates the connection pads and wires from the signal amplifier and power supply, as well as the reference pressure tube for the non-exposed side of the sensor membrane. Electronic connections between the AlSi sensor pads and both the signal amplifier and power supply connection pads are completed using a high temperature rated bonding technique. Such compounds lower the mechanical strength of the connections and influence the local resistance. Stresses on the pressure membrane, which are induced by the mismatch of thermal expansion coefficients between sensor and housing, could falsify the pressure measurements. Therefore, the

4.2 High temperature fast response pressure probe

sensor is installed into the housing using a high temperature (260 °C for long-term stability) room-temperature-vulcanizing (RTV) silicon elastomer. At the end of the packaging process, the sensor is also coated with a 200 μm layer of the same silicon elastomer, for electrical insulation and mechanical protection from the liquid metal. No degradation of the protective layer was observed after days of exposure to water and liquid tin. Two different version of the packaged pressure probe are manufactured. In the first version, the pressure sensor replaces the nozzle, as shown in Fig. 38 . In a second version, the sensor is mounted on the side of the nozzle orifice, as shown in Fig. 39. Unless otherwise stated, the pressure measurements are conducted with the first version of the pressure probe.

The pressure sensor's working principle is based on a Wheatstone bridge, which is fed by a constant current source. The sensor excitation voltage U_e is proportional to the temperature. The sensor signal voltage U_p is proportional to the pressure difference across the silicon membrane. The pressure signal is connected to a boxed amplifier, which is positioned close to the sensor to minimize white noise collection.

4.2.2.3. Static probe calibration

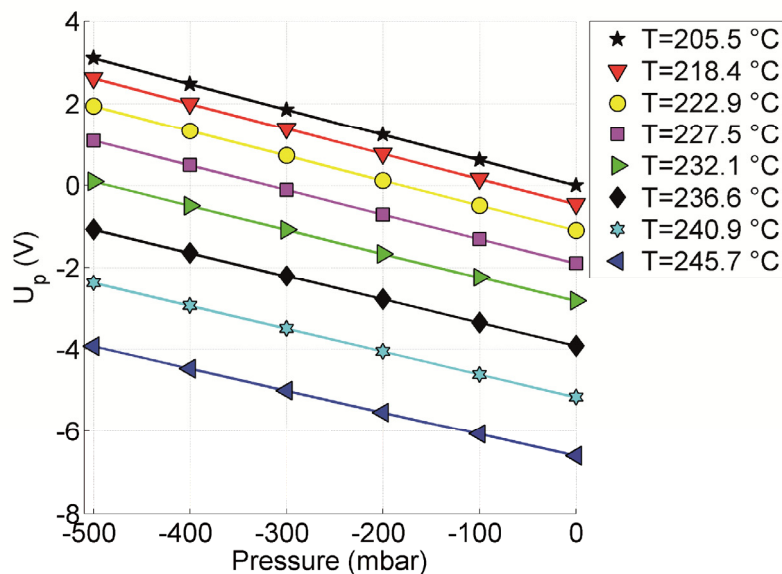


Fig. 40. Calibration of the pressure sensor in a dedicated oven, showing the linearity of the pressure signal at different temperatures up to 245.7 °C for a pressure range from 0 to 500 mbar.

Calibration is mandatory for each manufactured pressure probe due to variations in the packaging process. An example of such a variation is the tolerance of the thickness of the protective layer. First, the probe is calibrated in a dedicated oven in order to determine the linearity of the pressure signal by varying the reference pressure at fixed temperatures. Results for a pressure range from 0 to 500 mbar and a temperature range from 205.5 to 245.7 °C are shown in Fig. 40. In Lenherr *et al.*,¹⁵⁵ the

same pressure sensor has been calibrated in air for temperatures up to 260 °C (533 K). With increasing temperatures, the non-linearity of the sensor is expected to increase due to transistor leakage currents. However, the assumption of a linear pressure response is valid for all considered temperature values. The linear correlation coefficient at 245.7 °C equals 0.9999. As a consequence, the mean pressure sensitivity can be derived for each temperature value, as shown in Fig. 41. The pressure sensitivity decreases by 14% for a temperature increase from 205.5 to 245.7 °C. A 3rd order polynomial fit matches the relationship between pressure sensitivity and temperature.

Leakage currents across the PN junctions in the sensor, which increase with operating temperature, are responsible for a decrease in signal-to-noise ratio with temperature. The root mean square (RMS) of the pressure signal is shown in Fig. 42, for a temperature range from ambient to 245 °C. An acceptable increase of the noise level of 38% is observed when heating from ambient temperatures to 245 °C.

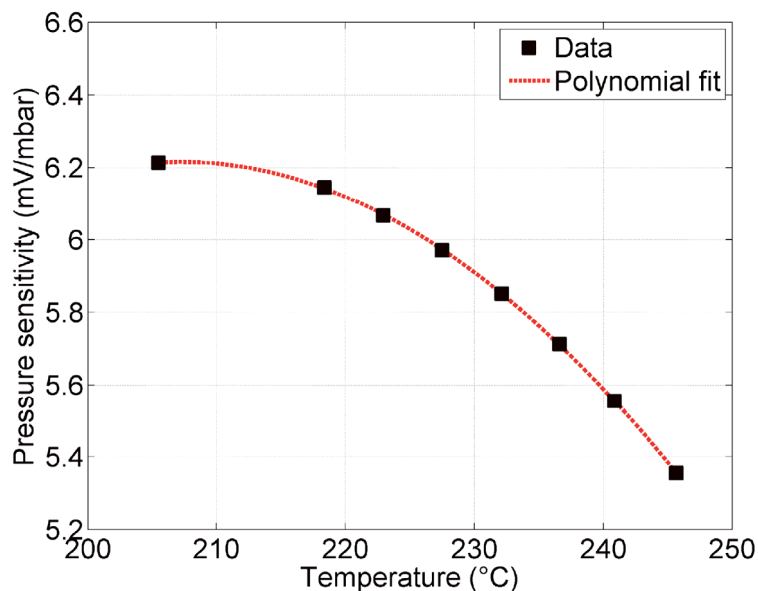


Fig. 41. Mean pressure sensitivity at temperatures from 205.5 to 247.5 °C. The pressure sensitivity decreases by 14% for a temperature increase from 205.5 to 245.7 °C. Data can be fitted by a 3rd order polynomial.

Each sensor is calibrated in-situ at the operating temperature of the dispenser before recording a measurement. This calibration step reveals malfunctions of the sensor, accounts for ageing and gives the pressure sensitivity at the exact operating temperature level. Indeed, as shown in Fig. 41, the pressure sensitivity is strongly temperature dependent in the considered temperature range. Either the reservoir or the reference pressure is varied. The pressure change is recorded by two absolute pressure transducers, which are installed on the reservoir and the reference pressure supply lines, respectively. Typical in-situ calibration results are shown in Fig. 43 for an operating temperature of 255 °C. The close-up in Fig. 43 reveals a typical pressure noise level (RMS) in the range of 3.5

4.2 High temperature fast response pressure probe

mbar (14.3 mV) for an operating temperature of 255 °C. As a consequence, the measurement resolution equals 7.0 mbar.

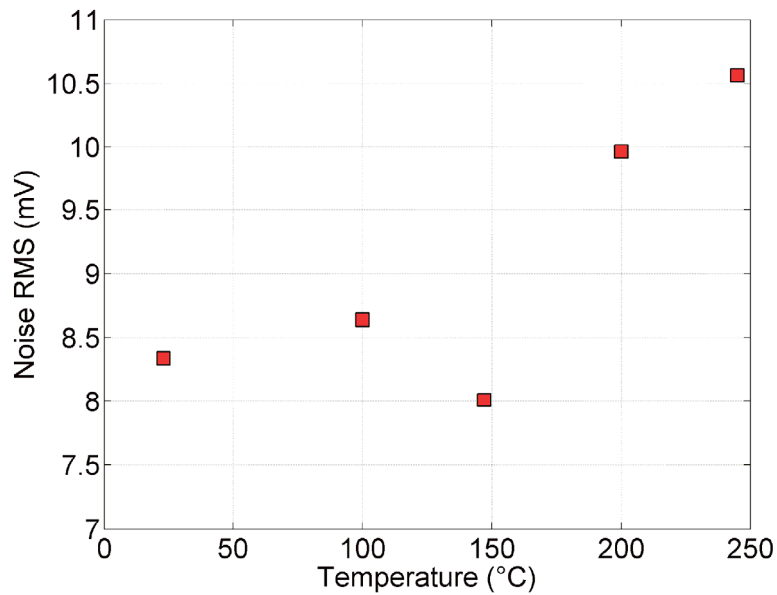


Fig. 42. Noise level RMS of the pressure signal as a function of temperature. An increase of the noise level of 38% is observed when heating from ambient temperatures to 245 °C.

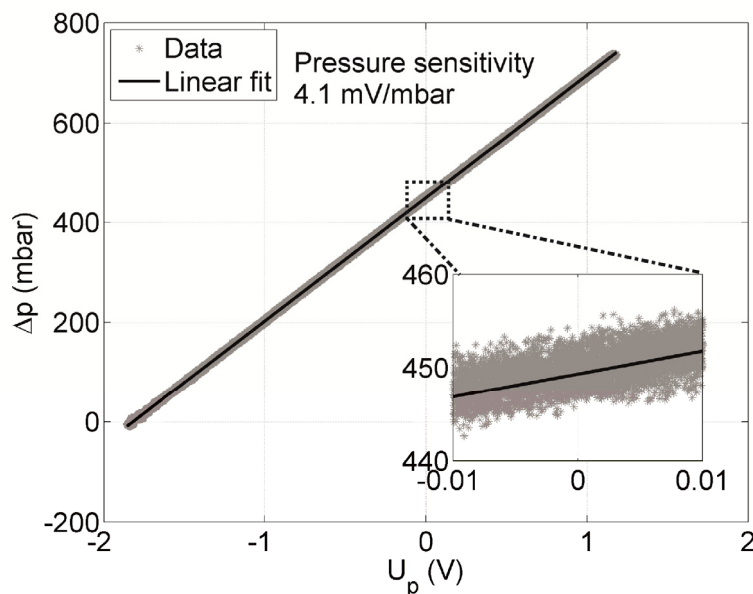


Fig. 43. In-situ calibration of the pressure sensor, showing the linearity of the pressure signal at a tin temperature of 255 °C. A pressure probe noise level in the range of 3.5 mbar is obtained for the considered operating temperature of 255 °C.

The reliability of the probe at high temperatures, when exposed to liquid tin, is demonstrated by plotting the variation of pressure sensitivity over a time duration of 70 minutes, as shown in Fig. 44. The tin temperature is kept constant at 255 °C (± 2 °C). The standard deviation of the pressure

sensitivity over 70 minutes is in the range of 0.5%. As a consequence, no significant changes of the sensor properties are observed.

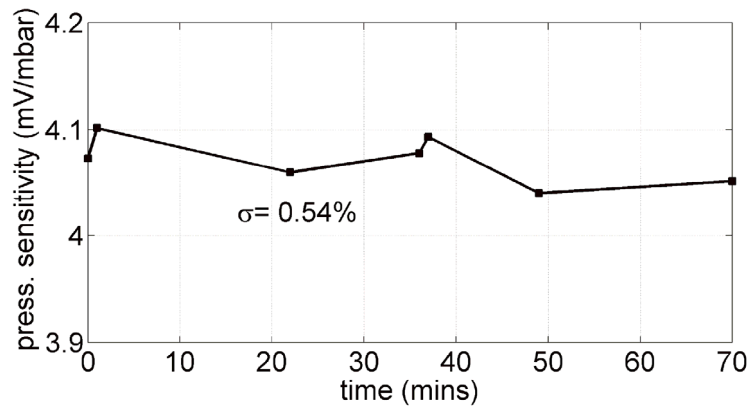


Fig. 44. Pressure sensitivity variation during a typical tin run at 255 °C, over a time period of 70 minutes. The standard deviation from the mean pressure sensitivity is 0.5%.

4.2.2.4. Dynamic probe calibration

The dynamic characteristics of the fast response pressure probe are determined by using a gasdynamic low-pressure shock tube. The low pressure side of the shock tube, where the pressure probe is installed, is evacuated until the rupture of a thin diaphragm occurs. The probe, when installed inside the shock tube is shown in Fig. 45. A shockwave travels from the ambient high pressure side to the low pressure side. The frequency content of the shockwave exceeds 1 MHz, which is sufficient to calibrate probes in the frequency range of interest (smaller than 100 kHz). The generated pressure step, which is measured at the same plane by a flush mounted in-house developed reference sensor, is the input function and the response of the pressure probe is the transient response. The goal of the dynamic calibration is to determine the transfer function of the pressure probe. By modeling the probe as a linear and time invariant system, the transfer function is used to correct the pressure signal for any kind of input signal. The transfer function is computed as the quotient of both the cross power spectral density of the probe and reference signal, and the power spectral density of the reference signal.

The amplitude of the transfer function is plotted in Fig. 46 for a frequency range from 10 to 500 kHz. Results are averaged over 5 measurements in order to account for the imperfect burst of the shock tube diaphragm. Amplitudes do not exceed 1 dB for frequencies up to 100 kHz. The first natural frequency of the sensor membrane, with amplitudes in excess of 20 dB, is found at 250 kHz. The damping ratio, derived from the quality factor of this resonance peak, equals 0.07. This peak is identified by varying the thickness of the silicon layer, which covers the sensor membrane. The natural frequency of the uncovered pressure sensor equals 710 kHz.¹⁵⁵ The +3 dB limit, which is typically specified for pressure sensors, is reached at 140 kHz.

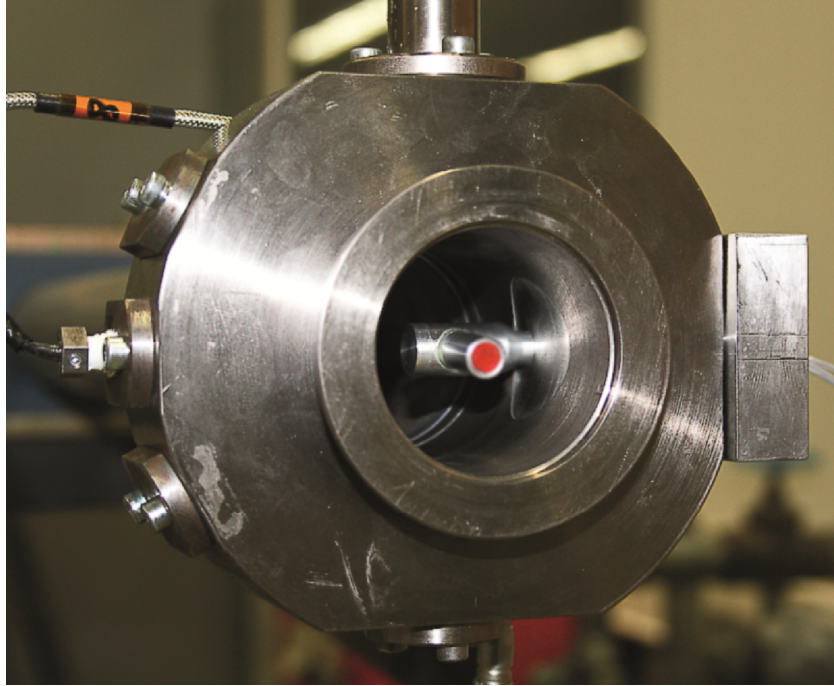


Fig. 45. Pressure probe installed in low pressure side of shock tube for dynamic calibration. The coated sensor membrane faces the diaphragm.

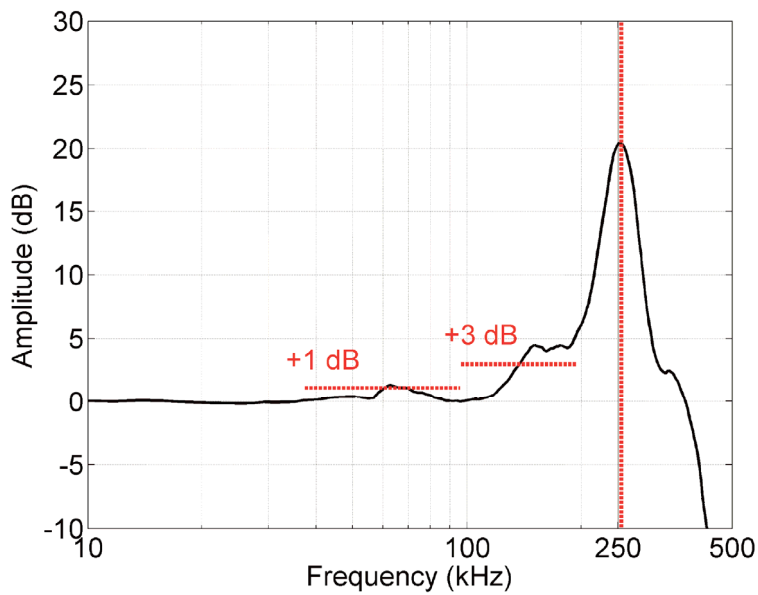


Fig. 46. Transfer function of the pressure probe, as determined by shock tube measurements. The first natural frequency of the pressure probe appears at 250 kHz.

It should be noted that the frequency response of the pressure probe is determined with air. The vibrating diaphragm induces a reaction from the surrounding fluid in the form of added mass and damping. In the case of a liquid, the natural frequency therefore decreases, when compared to air, as the virtual mass and damping increase. The initial model of Lamb¹⁵⁶ has been extended by Kozlovsky¹⁵⁷ to include viscous damping,

$$f_{liq} = \frac{f_{vac}}{\sqrt{1+\beta}}, \quad \beta = 0.67 \cdot \frac{\rho_{liq} a}{\rho_{membr} h} (1 + 1.57 \cdot \xi), \quad \xi = \sqrt{\frac{\nu}{2\pi f_{liq} \cdot a^2}} \quad (4.2)$$

where f_{vac} and f_{liq} are the resonance frequencies in vacuum and with a liquid, respectively. The liquid and membrane densities are denoted by ρ_{liq} and ρ_{vac} , respectively. The kinematic viscosity of the liquid is ν . The membrane thickness equals h and the membrane side dimension is denoted by a . For the liquid properties of tin¹⁵⁸ at 255 °C ($\rho_{liq}=6.96 \text{ g/cm}^3$, $\nu=2.9 \cdot 10^{-7} \text{ m}^2/\text{s}$) and the sensor membrane coated with silicon elastomer ($a=0.5 \text{ mm}$, $h=0.3 \text{ mm}$, $\rho_{membr}=1.8 \text{ g/cm}^3$), the resonance frequency is shifted from 250 kHz to 100 kHz, by assuming that the resonance frequency in air is the same as in vacuum.

4.2.2.5. Uncertainty analysis

The measurement chain of the fast-response probe includes the pressure sensor, the data acquisition and the calibration. The uncertainty due to 24-bit data acquisition is in the order of 10^{-6} % of the full scale and can therefore be neglected. The error band specified by the manufacturer of the pressure transducers comprises linearity, hysteresis and repeatability. The uncertainty of the pressure sensor measurement is related to its linearity, repeatability and hysteresis of the sensor. The largest source of uncertainty is the uncertainty of the reference pressure transducers, which are used during the in-situ calibration. Values specified by the manufacturer are considered in the uncertainty analysis. All uncertainties are summarized in Table 4-I. Relative uncertainties are indicated for a 1 bar full-scale span. The overall uncertainty Δp_s is derived from the following model equation:

$$\Delta p_s = \Delta p_{s,lin} + \Delta p_{s,hys} + \Delta p_{s,rep} + \Delta p_{cal} \quad (4.3)$$

The resulting uncertainty of the pressure probe equals $\pm 6.3 \text{ mbar}$ (1.3%).

Table 4-I. Uncertainties of the fast response high temperature probe.

	Source of uncertainty	Uncertainty (abs. / rel.)
$\Delta p_{s,lin}$	Sensor linearity	$\pm 0.75 \text{ mbar}$ / 0.15%
$\Delta p_{s,hys}$	Sensor hysteresis	$\pm 0.25 \text{ mbar}$ / 0.05%
$\Delta p_{s,rep}$	Sensor repeatability	$\pm 0.25 \text{ mbar}$ / 0.05%
Δp_{cal}	Calibration press. transducers	$\pm 5.0 \text{ mbar}$ / 1%

4.2.2.6. Dispenser integration

For the measurements presented below, the pressure probe is installed into the nozzle casing at the lower end of the tin reservoir, thereby closing the nozzle orifice, as shown in Fig. 37. The effect of tin flowing through the nozzle is neglected. Indeed, the nozzle inlet diameter (~ 10 mm) is typically several orders of magnitude larger than the nozzle orifice (~ 10 μm); hence the tin flow velocity in the nozzle inlet is negligible. The pressure probe signal amplifier is located (inside the vacuum chamber) close to the probe for noise minimization issues. The amplified signal is fed into a data acquisition system with a channel sampling rate of 200 kHz and a resolution of 24-bit.

Time-averaged pressure measurements on the reservoir and reference pressure side of the probe are monitored by absolute pressure transducers. Both pressure lines can be controlled separately. Pressure gradients with larger reference pressure than reservoir pressure must be avoided. Indeed, the silicon elastomer glue between the sensor and housing should only be loaded with compressive stresses. The excitation voltage of the piezoelectric actuator, which is generated by a dedicated signal generator, is recorded as a reference input signal.

4.2.3. Validation and liquid tin measurements

The novel piezoresistive pressure probe is used to measure the pressure response at the inlet of the dispenser nozzle. Transient measurements with respect to the excitation frequency of the piezoelectric stack are performed, i.e. the frequency of the piezoelectric stack is varied at a constant sweep rate for a constant excitation voltage amplitude. By doing so, the piston is effectively excited by a forcing function of constantly changing frequency. In order to ensure a near steady-state response, the sweep rate must be chosen to be sufficiently low for the structure and the fluid to build up a maximum response. A rule of thumb for the maximum linear sweep rate is indicated by Ewins.¹⁵⁹

$$S_{\max} = 3.6 \cdot f_{\text{res}}^2 \zeta^2 \quad (\text{Hz} / \text{s}) \quad (4.4)$$

Realistic values for the minimum resonant frequency (~ 10 kHz) of interest and the damping ratio ($\zeta=0.007$) can be derived from the pressure results presented below. For this application, sweep rates in the order of 16 kHz/s are acceptable, according to Eq.(4.4). For practical reasons, a lower sweep rate of 400 Hz/s has been used for the subsequent results.

The spectral pressure response is derived by fast Fourier transformation of 10 ms pressure signal windows, thereby giving a spectral resolution of 4 Hz. Typical pressure resonance peaks have widths in the range of a few 100 Hz. On the other hand, the window length must be long enough to contain the relevant low frequency content. In the current measurement approach, the window length of 10 ms yields 100 Hz for the lower spectral frequency limit. Window overlapping could be employed to further decrease the lower frequency limit. The upper limit in the frequency spectrum equals 100 kHz, which corresponds to half the sampling rate of 200 kHz.

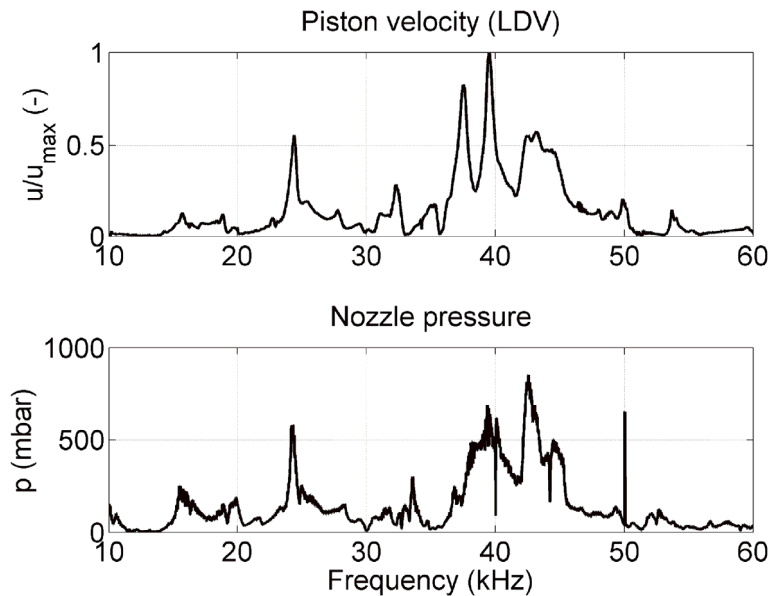


Fig. 47. Comparison of the normalized piston velocity, as determined by LDV, with nozzle inlet pressure measurements. Agreement between LDV and pressure measurements is observed with linear scaling between resonance peaks, except for the peaks around 40 kHz.

4.2.3.1. Comparison with an alternative measurement technique

To validate the pressure measurements an alternative measurement technique has also been investigated. According to Eq.(2.3), piston velocity and pressure are linearly dependent. Therefore, laser Doppler vibrometry (LDV) is used to quantify the velocity of the oscillating piston inside the droplet dispenser. In order to optically access the piston tip, the nozzle hole is enlarged to 2 mm and the reservoir contains no liquid. As the piston is recessed behind the nozzle, as shown in Fig. 37, only the axial displacement of the piston is measured. The LDV measurements are carried out on an optical bench at room temperature. Therefore the liquid used for the equivalent pressure measurements is water. More details about this measurement approach can be found in Sec. 4.3.2.2.

The piston velocity and acoustic pressure as a function of excitation frequency in the range from 10 to 60 kHz are shown in Fig. 47. Uncalibrated LDV measurements are normalized with respect to the maximum velocity of the considered frequency range. Overall, an agreement between LDV and pressure measurements is obtained. Resonance peaks scale linearly between LDV and pressure results, except for the peaks around 40 kHz. Measurement differences are due to the absence of a liquid and the detection of axial oscillations only in the LDV measurements, as well as non-linear acoustic contributions.

4.2.3.2. Liquid tin measurements

In this section, the probe's robustness and ability to measure high frequency pressure fluctuations in high temperature environments is demonstrated. First, the pressure response for a tin reference case is presented in Fig. 48. The results are obtained with the lower stiffness excitation system (system B). The dispenser is operated with pure tin at a temperature of 255 °C and an average reservoir pressure of 9 bar. The initial pressure difference across the sensor membrane is set to 500 mbar. The excitation voltage of the piezoelectric stack is 7.5 V. All conditions are representative for operation with droplet generation. The excitation frequency is varied at a constant sweep rate of 400 Hz/s in the range from 0 to 50 kHz.

The full pressure response spectra in the range from 0 to 100 kHz are plotted as a function of excitation frequency in Fig. 48. The indicated pressure magnitude corresponds to the measured pressure amplitude at a given frequency. The main contributions to the pressure response are located along the line, which corresponds to the actual excitation frequency. The structure of the main response is relatively complex with pressure amplitudes distributed over 3 orders of magnitude. Basically, three major peaks are observed at 17, 25 and 34 kHz, respectively. A maximum pressure amplitude of 440 mbar is observed at 25 kHz. The average mechanical quality factor of the three peaks with similar damping is $Q = 70$, which corresponds to a damping ratio of $\zeta = 0.007$. As a consequence, the pressure response corresponds to a weakly damped system. Overall, pressure amplitudes increase with increasing excitation frequency for the studied range. Weak traces, which are more than two orders of magnitude smaller than the main response, are located along lines corresponding to higher order harmonics of the base excitation frequency. Furthermore, white noise levels increase in frequency spectra with a major resonance peak. Nevertheless, noise levels in the frequency spectra are typically 3 to 4 orders of magnitude smaller than the measurement signals.

The pressure response spectrum, presented in Fig. 48, does not only give peak pressure amplitudes at a given frequency. A close-up view, for the piezo frequency range from 2 to 4 kHz and the spectral frequency range from 20 to 40 kHz, reveals system eigenfrequencies, as shown in Fig. 49. Indeed, system eigenfrequencies are excited independently of the excitation frequency. Additionally the intersection between these eigenfrequencies and the line of base excitation frequency, as well as the lines of higher order harmonics, leads to a resonance peak. In conclusion, the probe signal to noise ratio at temperatures above 250 °C is high enough to reveal system eigenfrequencies, even if the piezoelectric stack is not driven at the corresponding frequency. Furthermore, the match between these eigenfrequencies and the observed resonance peaks proves that the measured results are physically meaningful.

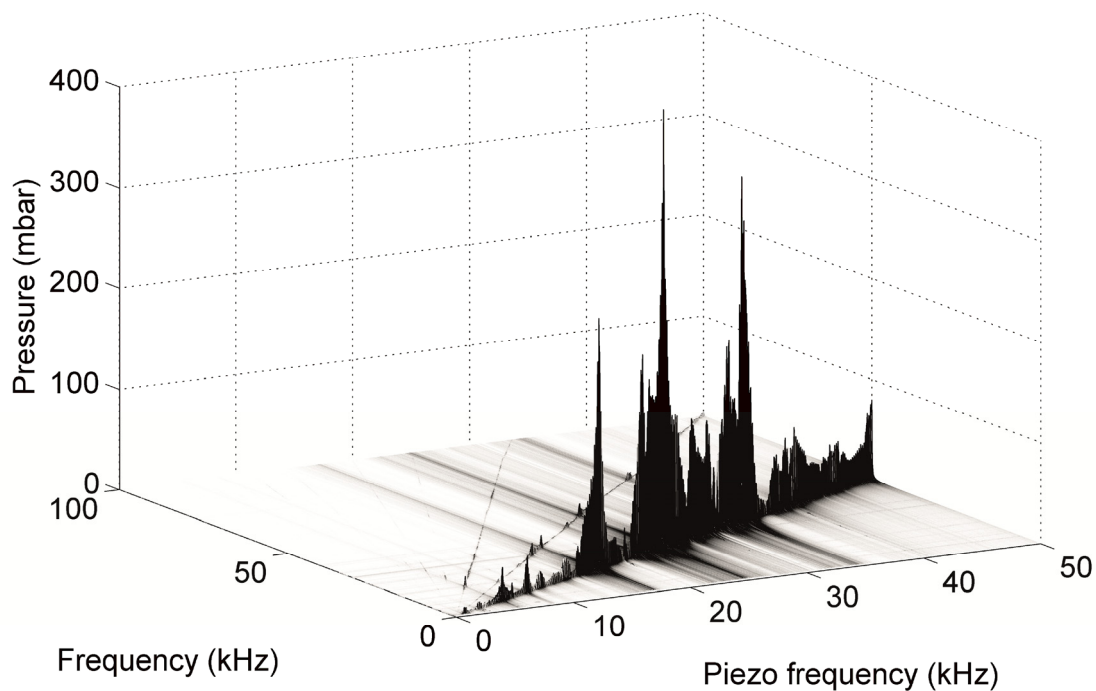


Fig. 48. Sample pressure response as a function of piezoelectric excitation frequency (System B, tin). A maximum pressure amplitude of 440 mbar is found at 25 kHz. As an overall trend, pressure amplitudes increase with excitation frequency in the considered range. Noise levels increase for frequency spectra with resonance peaks.

Time variance of the excitation system can be investigated with the help of the pressure sensor. For this purpose, pressure responses are monitored over time. In this experiment, a different oscillating piston is used than in the reference measurement of the previous section. The reservoir pressure is set to 4 bar with an initial bias pressure difference across the sensor of 500 mbar. The operating temperature is 255 °C and the amplitude of the excitation voltage is 5V. The measured initial pressure response is compared to responses recorded after 20 and 40 minutes, respectively, as shown in Fig. 50. First, it must be noted that the pressure responses differ from the reference pressure response in Fig. 48. A different response is indeed expected, as the piston has been modified in terms of piezoelectric stack integration. The pressure response is the result of a complex coupling between mechanical structures such as the piezoelectric stack, the piston and their supporting structure and the fluid. The pressure probe is useful for systematically determining the origins of pressure peaks.

Average differences between the initial response and the response after 20 minutes, as well as the initial response and the response after 40 minutes are 4.9% and 3.6%, respectively. Indeed, the pressure responses follow the same trend at all times and are generally in good agreement. Mismatches are observed for the narrow peak at 17 kHz and the region around 25 kHz. The variation in pressure sensitivity, which is presented in Sec. 4.2.2.3, is typically lower than the differences between pressure responses reported in this section. As a consequence, thermal transients

4.2 High temperature fast response pressure probe

in the excitation system, including the liquid tin and the mechanical structures such as the piston and the piezoelectric stack, must be responsible for the differences in pressure responses.

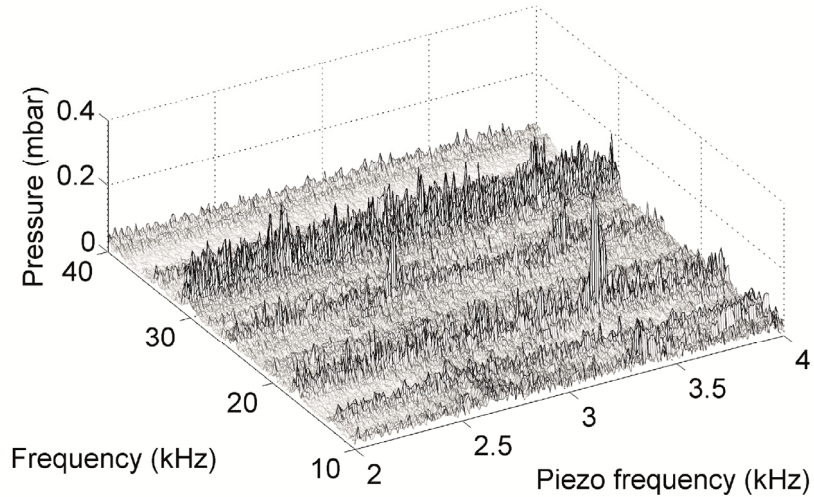


Fig. 49. A close-up view of the pressure response spectrum as a function of piezoelectric excitation frequency. The probe's signal to noise ratio is large enough to reveal system eigenfrequencies, even without excitations at the corresponding frequencies.

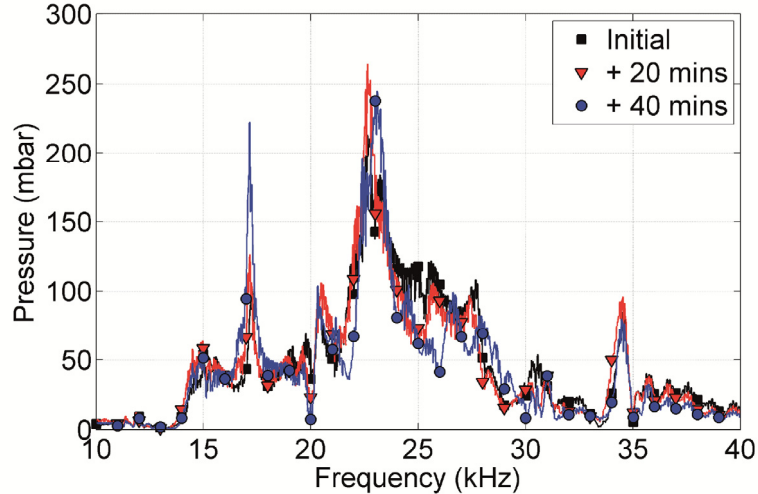


Fig. 50. Pressure responses recorded at 0, 20 and 40 minutes, respectively. Average differences between the initial response and the responses after 20 and 40 minutes are 4.9% and 3.6%, respectively. Thermal transients in the excitation system limit the repeatability of measurements in the considered time period.

Using the experimental setup of the previous reference pressure response measurement, a voltage change in the excitation signal, which is the main input to the excitation system is studied. The reference pressure response, together with the response obtained with a reduced excitation voltage of

4.7 V, is shown in Fig. 51. All other operating parameters are the same as in the reference case. Pressure signals are recorded in the frequency range from 10 to 40 kHz. Results confirm a linear scaling of the two pressure responses following the ratio of the excitation voltages, except for the low frequency range from 10 to 15 kHz. This is due to the resolution limit of the probe at the low pressures (lower than 10 mbar) corresponding to this frequency range. The sensor resolution is decreased due to noise, which is induced by the excitation signal of the piezoelectric stack. For the frequency range from 15 to 40 kHz the ratio of excitation voltages equals 0.627 and the mean ratio between the two responses is 0.631, which results in a deviation of 0.7%. In conclusion, the excitation system can be assumed to be linear with respect to the excitation voltage in the considered range. Scaling is however not infinite due to power limitations of the piezoelectric stack.

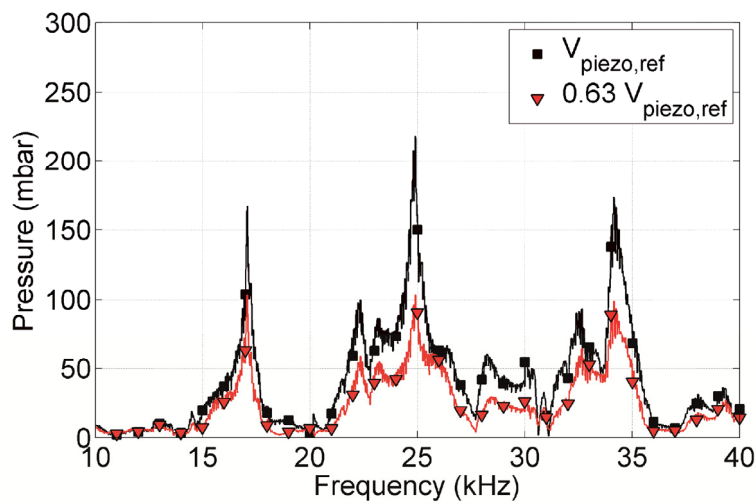


Fig. 51. Reference and reduced excitation voltage pressure responses. Linear scaling between the two responses validates the assumption that the pressure generated by the excitation system scales linearly with the excitation voltage.

4.3. Fluid dynamic and structural response measurements

4.3.1. Approach

In the measurements presented in this chapter, the previously described pressure probe replaces the nozzle at the lower end of the tin reservoir. In the present study, the pressure measurements are completed with water as a liquid, because the corresponding LDV measurements could only be completed at room temperature. The change in acoustic medium is expected to affect the absolute pressure amplitudes and the damping of the oscillating piston. The used excitation system corresponds to system A.

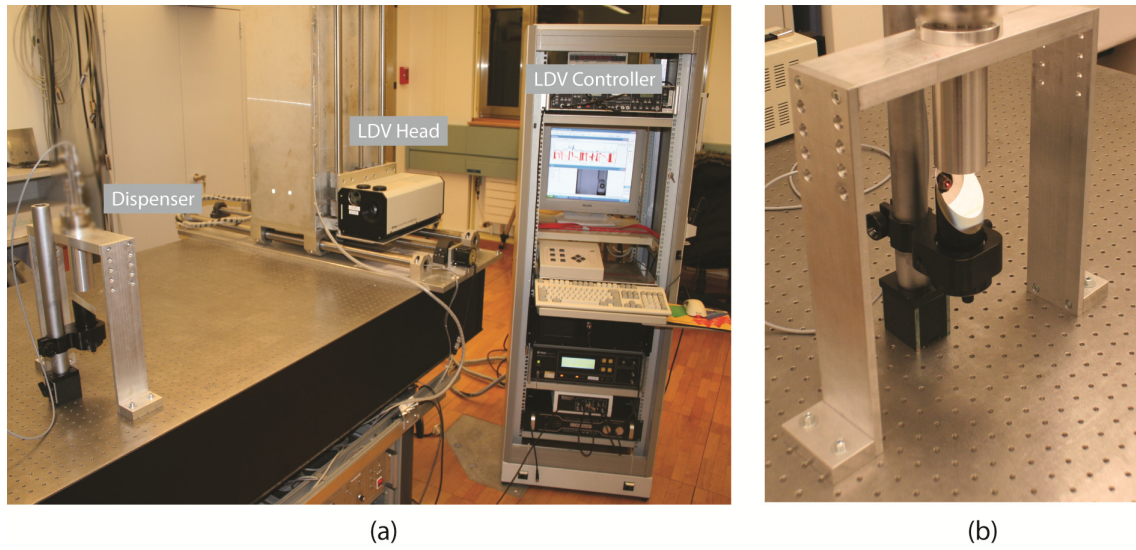


Fig. 52. (a) Experimental setup including LDV measurement system and dispenser with simplified support. (b) LDV laser beam deflected by 45° mirror and deflected onto piston tip.

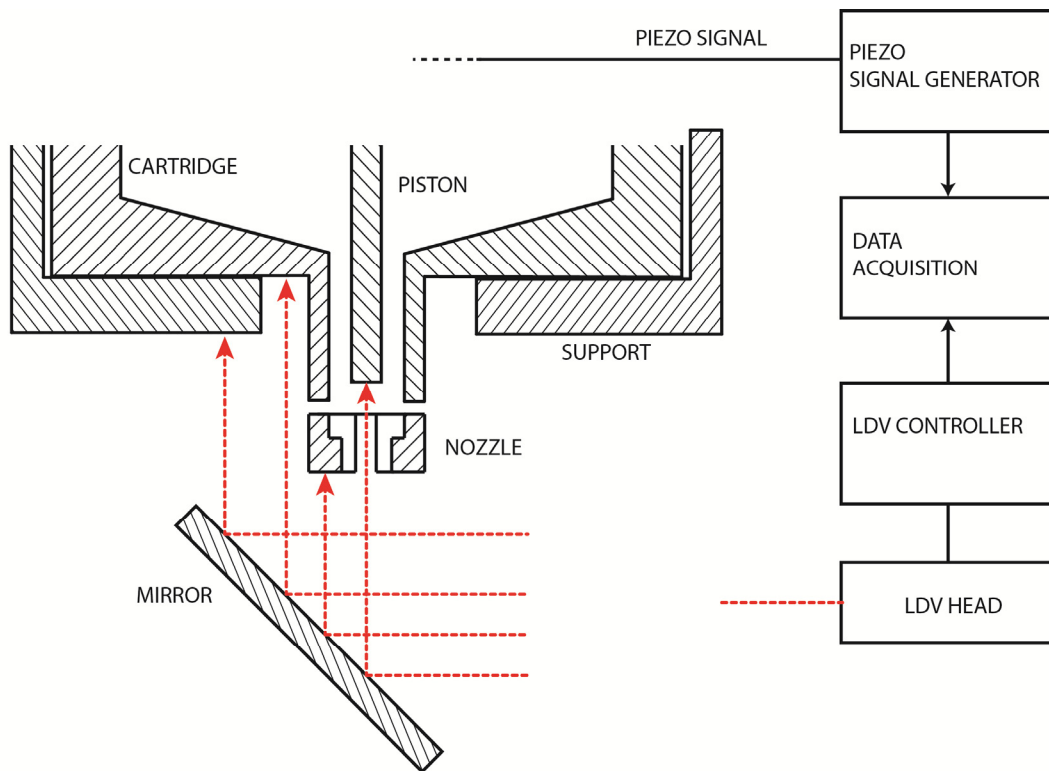


Fig. 53. Schematic of experimental setup of laser Doppler vibrometer. The measurement beam is redirected by a 45° mirror onto the target surfaces of the dispenser for a frequency dependent displacement analysis.

In a second experiment, a laser Doppler vibrometer is used to quantify structural vibrations in the droplet dispenser, in response to the vibration of the piezoelectric actuator. For a decoupling of structural and fluid dynamic effects on the pressure response, the dispenser is studied without

liquid. The measurement device consists of a POLYTEC OFV 050 optical scanning head and a POLYTEC OFV 3001S vibrometer controller. The measurement laser beam is self-focusing onto the target surface. The dispenser cartridge is installed together with the LDV on an optical bench. A simplified support, without the casing and heating systems of the support designed for operation in the vacuum chamber, is used. The LDV setup is shown in Fig. 52. The equivalence of the two supports is verified by pressure measurements on both supports. The mean pressure amplitudes differ by 2%. A schematic of the complete experimental setup, including the measurement locations, is presented in Fig. 53. The surfaces of interest are the piston tip, the filter, the nozzle, the cartridge and the support. In order to gain optical access to the piston tip or filter, the nozzle hole is enlarged to 2 mm. A 45° mirror is used to deflect the vibrometer beam onto the studied surfaces. The excitation signal of the piezoelectric actuator is used as a reference signal for the vibration measurements.

4.3.2. Results

4.3.2.1. Pressure response

The piezoresistive pressure probe is used to study the pressure response at the nozzle inlet with respect to the excitation frequency of the piezoelectric stack. For this purpose, the excitation voltage of the piezoelectric stack is varied at a constant sweep rate, which must be chosen to be low enough to ensure a near steady-state response in each frequency window. The pressure response is recorded for the standard excitation system (system A) with water as the acoustic medium. Indeed these pressure measurements will be compared to LDV measurements at room temperature. Measurements with system B are presented in Sec. 4.5.

Typical time domain pressure and piezoelectric excitation signals are presented in Fig. 54. Both signals are shown over a time period of 10 s. During this period, the initial frequency of 10 kHz is swept up to 14 kHz, in 400 Hz/s increments. Although the excitation signal of the piezoelectric stack is kept constant at 5 V, the pressure signals are found to oscillate with different amplitudes. The largest recorded pressure amplitude is 300 mbar. The strong variation of pressure at constant excitation amplitude further underlines the interest in studying the dynamic behavior of the excitation system.

As a next step, the results for the full frequency range are processed to yield the pressure amplitudes in the frequency domain. At discrete excitation frequencies, spaced by 4 Hz, the spectral response of the pressure signal is computed for a signal window length of 10 ms. The obtained frequency spectra are plotted as a function of the excitation frequency of the piezoelectric stack, as shown in Fig. 55. The main pressure peaks occur along a line, which corresponds to the actual piezoelectric frequency. Weak pressure traces, which are smaller by at least two orders of magnitude than the main response, are observed for multiples of the base excitation frequency. The structure of the main pressure response is relatively complex, with pressure amplitudes distributed over 3 orders of

magnitude. A first discrete peak of 200 mbar is found at 5 kHz. Continuous peaks above 150 mbar start to appear around 15 kHz. For frequencies exceeding 40 kHz, peaks above 400 mbar are obtained. The largest peak is observed at 66.1 kHz with a maximum amplitude of 2.1 bar. This difference in peak amplitude, when compared to the tin measurements, is related to the use of a different excitation systems (differences in stiffness and pre-stress), as well as to lower damping of the pressure amplitudes in the case of water.

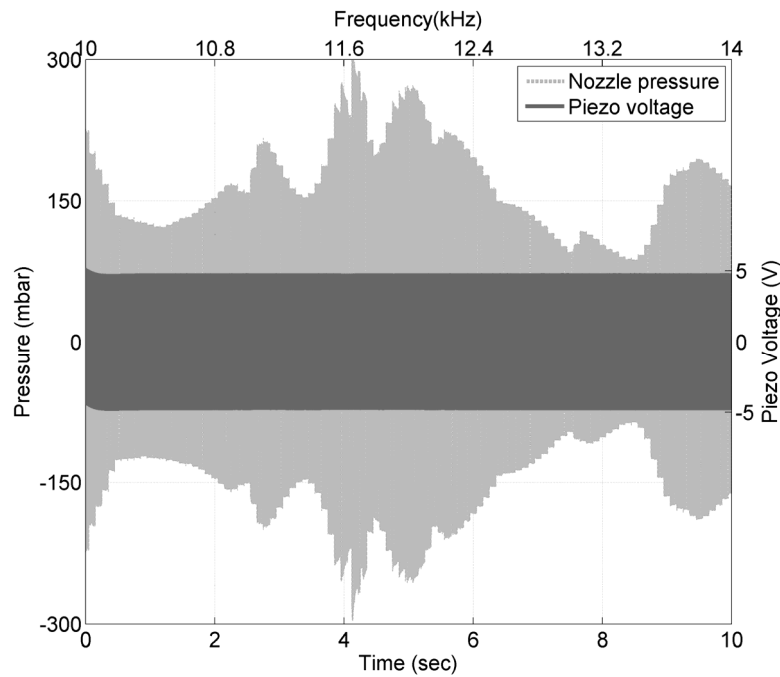


Fig. 54. Sample pressure and piezoelectric excitation signals, recorded over 10 s for a frequency range from 10 to 14 kHz. The excitation signal is a sine wave with an amplitude of 5 V. The pressure signal responds with frequency dependent oscillation amplitudes, which reach 300 mbar.

The same measurement approach is applied to different configurations of the droplet dispenser. The frequency range for this comparison equals 5-50 kHz, which is the most relevant frequency range for EUV droplet dispensers. The results are summarized in Table 4-II. The reference results (A) are the same measurements as above in Fig. 55. First, the system is studied without an acoustic medium (B). For this purpose, the reservoir cartridge contains no liquid and is evacuated to 10^{-2} mbar in order to limit the acoustic transmission through air to the pressure sensor. Secondly, the piston is shortened to a length where the piston tip is not in contact with the liquid, while the fill level is the same as in the reference case (C). In a third case, the shortened piston is used in the evacuated cartridge (D).

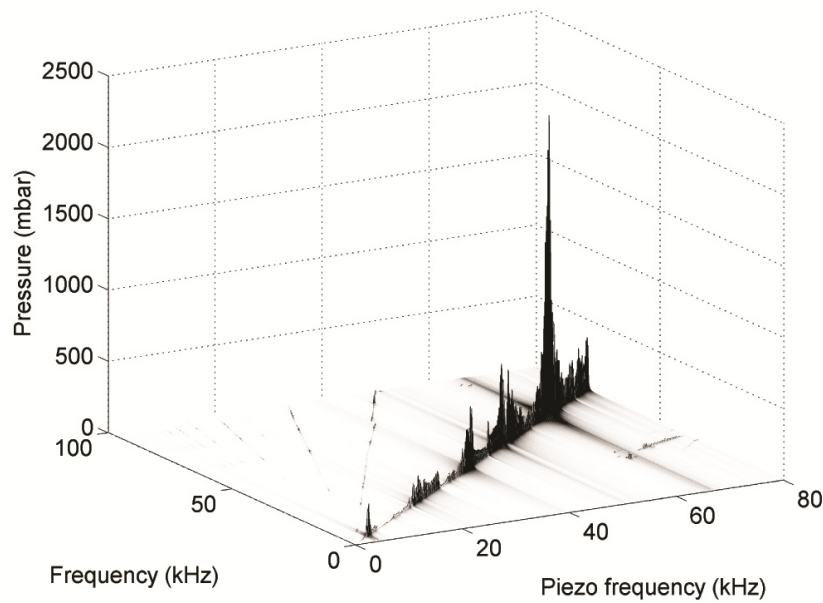


Fig. 55. Pressure response spectra as a function of piezoelectric excitation frequency (System A, water). The excitation frequency resolution is 4 Hz, which is sufficient to resolve the relevant dynamics. Several peaks above 400 mbar are obtained for frequencies above 40 kHz, with a main peak of 2.1 bar at 66.1 kHz.

Table 4-II. Mean and maximum pressure amplitudes for different droplet dispenser configurations for the frequency range from 5-50 kHz.

Configuration	Mean pressure (mbar)	Max pressure (mbar)
(A) Reference	165.7	985.8
(B) No medium	1.1	12.4
(C) No piston contact with medium	10.0	103.3
(D) No medium, no piston	3.7	40.9

The reference pressure amplitudes exceed that of the measurements without a medium by almost two orders of magnitude. In the case of the shortened piston, the pressure response is one order of magnitude smaller than in the reference case. In the case of the shortened piston and no medium inside the cartridge, the pressure amplitudes are also more than one order of magnitude smaller, when compared to the reference case. In conclusion, significant pressure amplitudes are only obtained in the presence of an acoustic medium (of sufficient density) and a piston, which is immersed in the acoustic medium.

4.3.2.2. Structural response

The structural response of the droplet dispenser, with respect to the piezoelectric excitation frequency, is measured using LDV. The LDV determines the velocity of the illuminated surface element in the direction of the incident beam. Only velocities in the direction of the piston axis are quantified as the piston tip is recessed and is therefore optically accessible in the axial direction only, as shown in Fig. 53. The frequency sweeping of the piezoelectric stack is managed by the LDV controller with a frequency resolution of 15 Hz.

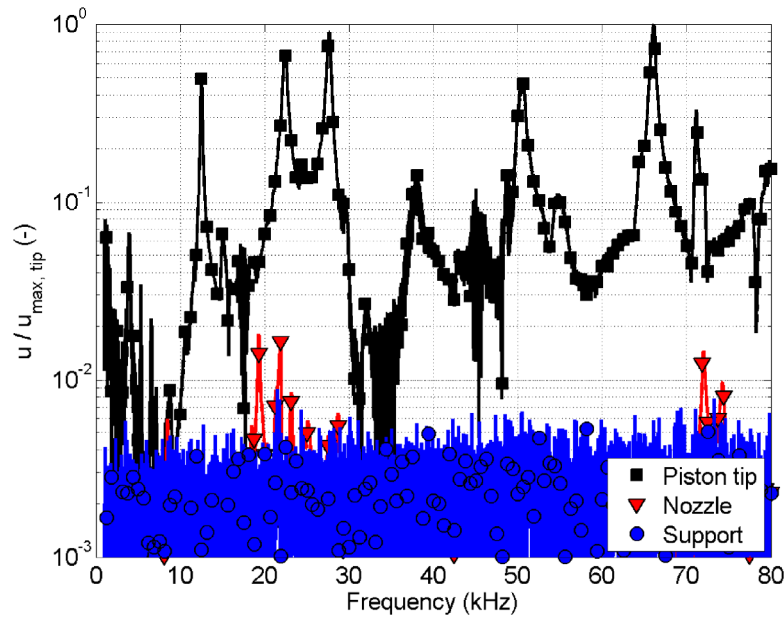


Fig. 56. Structural response determined by LDV measurements. Piston tip velocities exceed nozzle and support velocities by at least a factor of 30.

The normalized piston tip velocity for a linearly changing frequency from 1 to 80 kHz is presented in Fig. 56. The main peaks of tip displacement, which exceed velocities of 10% of the maximum velocity, are located at 12.5, 22.4, 27.7, 38.0, 47.1, 50.5, 66.1 and 72.2 kHz. The tip velocity signal is on average 4 times noisier in the frequency range from 30 to 50 kHz, than the rest of the signal. Overall, the tip velocities are found to be the lowest in the frequency range from 1 to 10 kHz. The average nozzle vibration amplitude is 30 times smaller than the average tip velocity. Peaks of nozzle velocity are observed at 19.3, 21.9 and 72.0 kHz. The support is found to have the lowest vibration level, namely 55 times lower than the piston tip, with one distinct peak at 21.5 kHz. In addition to the presented measurement locations, the displacement has also been measured on the cartridge, as illustrated in Fig. 53. The results are not included in Fig. 56, as no noticeable difference between the cartridge and the support displacement is observed. The comparison between LDV and pressure measurement follows in Sec. 4.5.1.2. In the next section, the origins of the complex structural frequency response are investigated with the help of a FE analysis.

4.4. Modeling of structural dynamics

4.4.1. Simulation setup

The measured structural response of the excitation system is investigated by finite element (FE) analysis. The excitation mechanism is numerically modeled and analyzed using the commercial ANSYS (Release 13.0) FE code. This tool has been used to study piezoelectrically excited bodies, such as wire bonders.¹⁶⁰ The computational model includes the assembly of the piezoelectric multilayer stack, the piston and the cover flange of the reservoir. The modeled bodies are derived from the CAD model of the droplet dispenser. The simulations are run in three-dimensions due to the presence of non-axisymmetric bodies.

The cartridge and support structures are not included. Indeed the structural responses, which are measured on the cartridge and the support, do not contain the characteristic features of the structural response at the nozzle. Additionally, the displacement amplitudes are significantly lower on the support and cartridge.

A detailed electro-mechanical model of the piezoelectric stack is required for accurate simulation results. The full 3D model is using ANSYS SOLID226 elements¹⁶¹ for modeling the piezoelectric stack. The 3D piezoelectric equations, which are commonly used in numerical tools, are

$$\begin{Bmatrix} T \\ D \end{Bmatrix} = \begin{pmatrix} C^E & -e^t \\ e & \epsilon^S \end{pmatrix} \begin{Bmatrix} S \\ E \end{Bmatrix} \quad (4.5)$$

where T and S are the mechanical stress and linear strain vectors, and D and E are the electrical displacement and field vectors. $[C^E]$, $[e]$ and $[\epsilon^S]$ denote the elastic matrix at constant electric field, the stress piezoelectric matrix and the dielectric permittivity matrix at constant strain, respectively. The superscript t denotes a transpose operation. The manufacturer's data for the piezoelectric ceramic PICMA PIC252^{141, 162} are summarized in Table 4-III, using IEEE standard notations.¹⁶³ The material data required for solving Eq.(4.5) must be derived and completed according to the procedure described in Chevallier *et al.*,¹⁶⁴ before being translated to ANSYS notation. Unfortunately, ANSYS does not use the IEEE standard notations. The main equations, which are required to transform the manufacturer's data to useful data for the numerical simulations are

$$[c^E] = [s^E]^{-1}, \quad [e] = [d][c^E], \quad [\epsilon^S] = [\epsilon^T] - [d][e]^t \quad (4.6)$$

where $[s^E]$ is the compliance matrix at constant electric field, $[\epsilon^T]$ is the permittivity matrix at constant stress and $[d]$ is the piezoelectric strain matrix. The stack consists of multilayers of piezoelectric material. These layers are not directly modeled, but instead effective properties are used to model the multilayer as a monolithic crystal in the FE code.^{141, 165} The layers are stacked in

the direction normal to the polarization. The influence of the insulating layers is assumed to be negligible in terms of mechanical and electrical properties. Therefore the effective elastic constant remains unaffected. The effective piezoelectric constant is determined by summing the displacement of each layer

$$d_{33eff} = n \cdot d_{33piezo} \quad (4.7)$$

where n is the number of layers. Similarly, the effective dielectric permittivity of the stack is found by noticing that the piezoelectric layers are electrically in parallel and the total capacitance is the sum of the capacitance of each element. The permittivity is calculated from the total capacitance and the geometry of the stack

$$\epsilon_{33eff}^T = n^2 \epsilon_{33}^T \quad (4.8)$$

The effective electromechanical coupling in the main polarization direction is

$$k_{33eff} = \frac{d_{33eff}}{\sqrt{s_{33}^E \epsilon_{33eff}^T}} \quad (4.9)$$

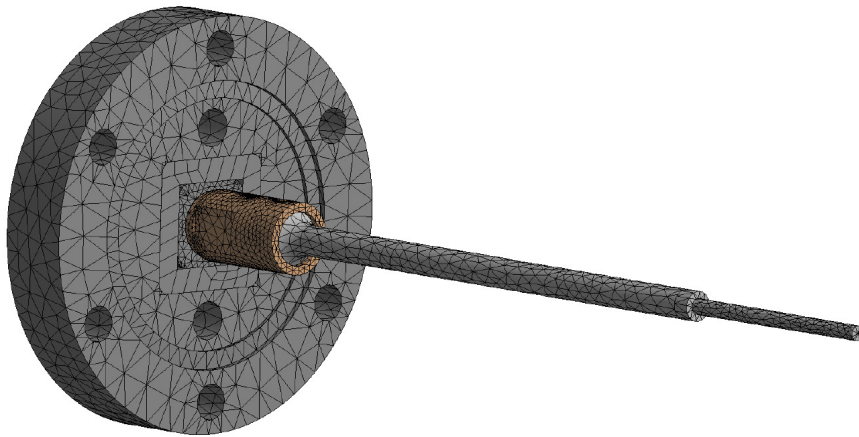


Fig. 57. Meshed geometry of the piston, piezoelectric stack enclosure and cover flange for use in FE simulations.

After assigning material properties to the remaining parts, the full assembly, which is based on a detailed CAD model, is meshed with 13975 nodes and 6664 elements, as shown in Fig. 57. The only boundary condition, which is applied to the assembly, is a fixed support condition on the outer section of the cover flange.

A full harmonic response simulation is used to determine the frequency response of the piston tip with respect to the excitation frequency of the piezoelectric stack. ANSYS uses a parallelized sparse direct matrix solver. Due to the pre-stressing of the piezoelectric element, an initial static structural simulation is coupled in ANSYS to the harmonic response simulation. Additionally, a modal

analysis is run for the same simulation setup. The goal of the modal analysis is to determine the modal forms, which correspond to the resonance peaks in the frequency response.

Table 4-III. Material properties used in ANSYS® FE simulation

Material	Denomination (SI Units)	Notation	Value
PICMA	Mass density (kg m ³)	ρ	7800
		Relative permittivity (-)	$\epsilon_{r,33}^T$
	Piezoelectric voltage coefficient (C N ⁻¹)	$\epsilon_{r,33\text{eff}}^T$	$1.7 \cdot 10^8$
		$\epsilon_{r,11}^T$	1650
		d_{31}	-180
		d_{33}	400
		$d_{33\text{eff}}$	$1.2 \cdot 10^{-7}$
	Elastic compliance coefficient (m ² N ⁻¹)	d_{15}	550
		s_{11}^E	16.1
		s_{33}^E	20.7
	Material coupling coefficient (-)	k_{31}	0.35
		k_{33}	0.69
		$k_{33\text{eff}}$	0.67
		k_{15}	0.66
		k_p	0.62

4.4.2. Results

4.4.2.1. Validation of piezoelectric model

Before simulating the full assembly of the excitation system, the static and dynamic behavior of the piezoelectric multilayer stack is validated against manufacturer specifications. The validation is mainly necessary due to the approximation of the layered structure as a monolithic stack. Furthermore a strong sensitivity of the overall results to the piezoelectric model has been observed. First, the static displacement is verified for an applied voltage difference of 120 V across the electrodes. The voltage and displacement of the stack are presented in Fig. 58. The experimentally measured displacement is specified to be 18 μm (+/- 10%) by the manufacturer.¹⁴¹ The computational model gives a displacement of 19.5 μm , which yields a deviation from the numerical value of 8.2%.

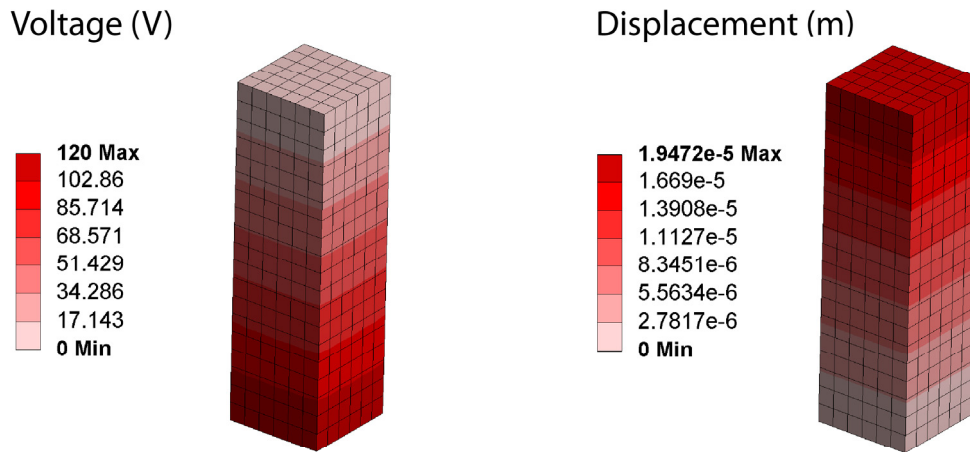


Fig. 58. Static validation results from the piezoelectric multilayer stack numerical FE model. For a voltage difference of 120 V across bottom and top electrodes, the displacement is 19.5 μm (compared to the experimental value of 18.0 μm).

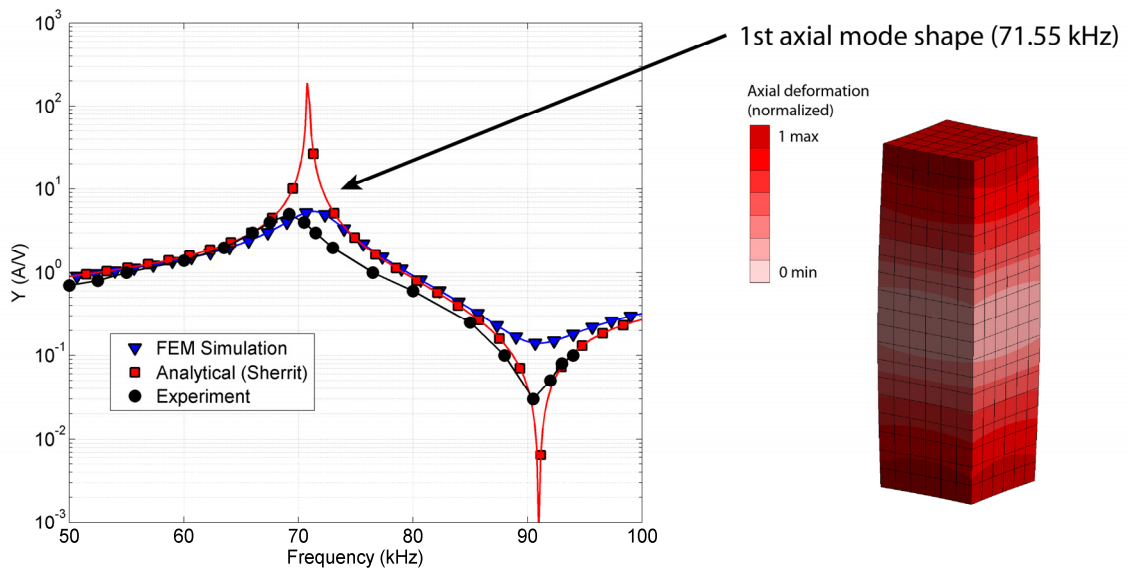


Fig. 59. Dynamic validation of the piezoelectric stack by comparison with numerically, experimentally and analytically determined admittance values. Both resonance and anti-resonance peaks show good agreement. The 1st axial mode shape, which corresponds to the resonance peak in the plotted admittance curve, has an eigenfrequency of 71.55 kHz in the FE analysis (versus 69.5 kHz in the experiment).

The impedance or its inverse, namely the admittance of the piezoelectric stack, is frequency dependent.¹⁶⁶ Therefore the dynamic validation of the piezoelectric FE model is completed by comparing the numerically predicted admittance to the experimentally measured admittance,¹⁶⁷ as

shown in Fig. 59. Although the full range of interest from 1-100 kHz is simulated by the FE code, the plot range is limited to the region of the resonance and anti-resonance peaks around 80 kHz. The piezoelectric model includes damping for the stiffness matrix, which is set in order to match the admittance amplitude of the experimental results. The admittance is computed as the ratio of electrode current over voltage potential across electrodes. Numerically, the current is derived from the accumulated nodal charge Q_i on the electrodes as $I = 2\pi f \sum Q_i$, where f is the frequency of the harmonic excitation. The analytic expression for the (undamped) admittance of a multilayer stack from Sherrit *et al.*¹⁶⁵ is also plotted in Fig. 59.

The admittance for the numerical and experimental results has axial resonance peaks at 71.6 kHz and 69.5 kHz, respectively, while the anti-resonance peaks are at 90.6 kHz and 91.0 kHz, respectively. The manufacturer's data specify a resonance frequency of 70 kHz (+/- 20%).¹⁴¹ The 1st axial mode shape of the piezoelectric stack is shown in Fig. 59, as predicted by FE analysis. The deviations for the resonance and anti-resonance peaks between the experimental and the computational results, equal 3.0% and 0.4%, respectively. The good agreement between FE and experimental results validates the use of the piezoelectric model in the full assembly simulation.

4.4.2.2. Structural response of the excitation system

The harmonic response simulation of the full assembly, which should reproduce the tip dynamics recorded by LDV, is coupled to a static structural analysis in order to include pre-stressing of the piezoelectric stack. The bolt pretension model is used in ANSYS.¹⁶¹ Following the piezoelectric ceramic manufacturer's recommendations,¹⁴¹ the pre-stress is set to 15 MPa average compressive stress on the stack. The corresponding equivalent stress distribution inside the stack, together with the enclosure (brown) and the support (grey), is presented in Fig. 60. A stress peak occurs in the contact region with the ball joint between the piston and the stack. The increased stress is due to a reduced contact area.

The pre-stressed piezoelectric stack is then included in the harmonic response calculation of the full assembly. No structural damping is included in the harmonic response, as its main purpose is the resonance peak identification with the LDV measurements. The normalized piston tip velocity in the axial direction is presented in Fig. 61 for a linearly changing frequency from 1 to 80 kHz. The normalization factor u_{max} corresponds to the largest velocity found in the considered frequency range. The frequencies of the main peaks of the tip displacement, which are located in the range from 10 to 70 kHz for tip velocities above 5% of u_{max} , are summarized in Table 4-IV.

Equivalent stress (Pa)

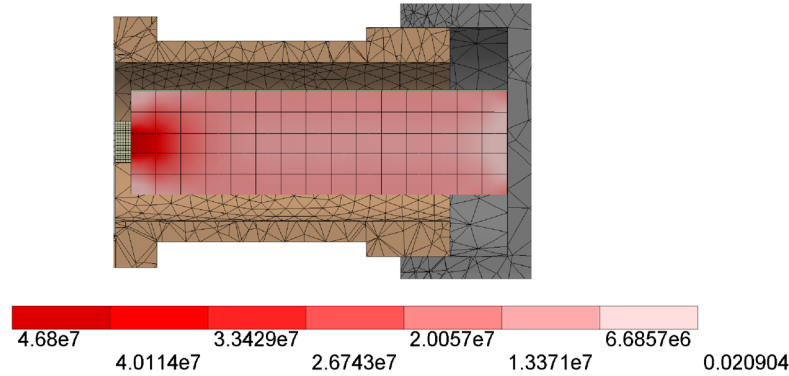


Fig. 60. Equivalent stress distribution inside the piezoelectric stack for an applied target pre-stress of 15 MPa. The pre-stress on the stack is applied by tightening the enclosure (brown) into the threaded support (grey). A stress peak occurs in the contact region with the ball joint due to a reduced contact area.

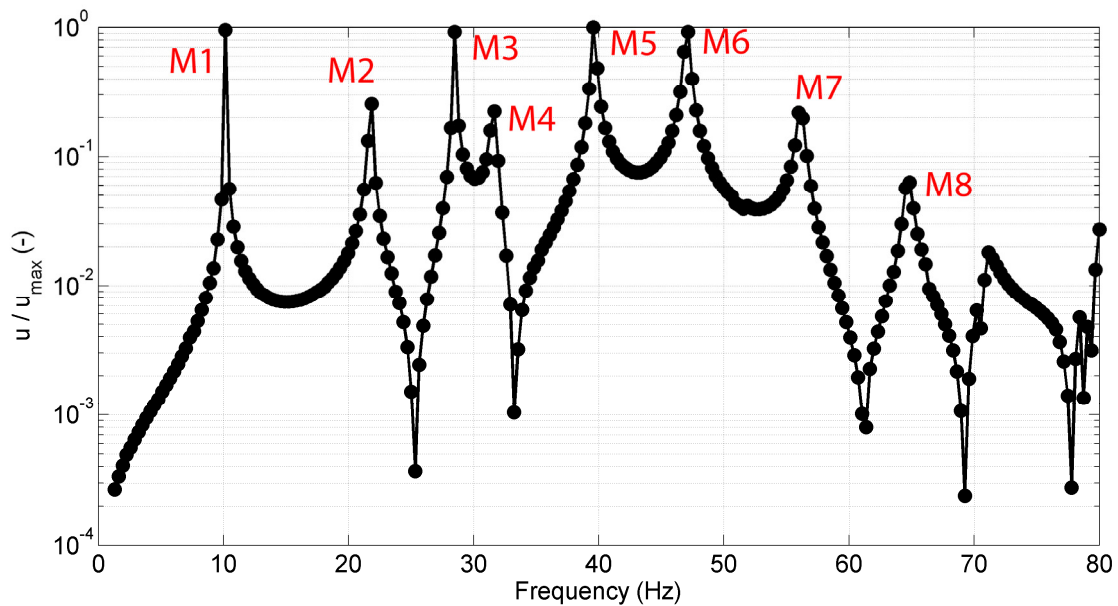


Fig. 61. Tip velocity frequency response in the axial direction for a frequency range from 1 to 100 kHz. The main peaks of tip displacement, with tip velocities above 5% of u_{\max} , are located in the range from 10 to 70 kHz.

In a next step, the modal analysis is used to extract the underlying mode shapes of the complex harmonic response from Fig. 61. For a given resonance peak, the corresponding mode shape is identified. The results of the modal analysis are summarized in Table 4-IV. Mode shapes up to the 5th order are relevant in the frequency range from 1 to 80 kHz. A sophisticated coupling of the full assembly is observed. The location of modal nodes, which are either located within the piston, the piezoelectric stack, the enclosure or the cover flange is also indicated in Table 4-IV. The mode shapes are represented in Fig. 62.

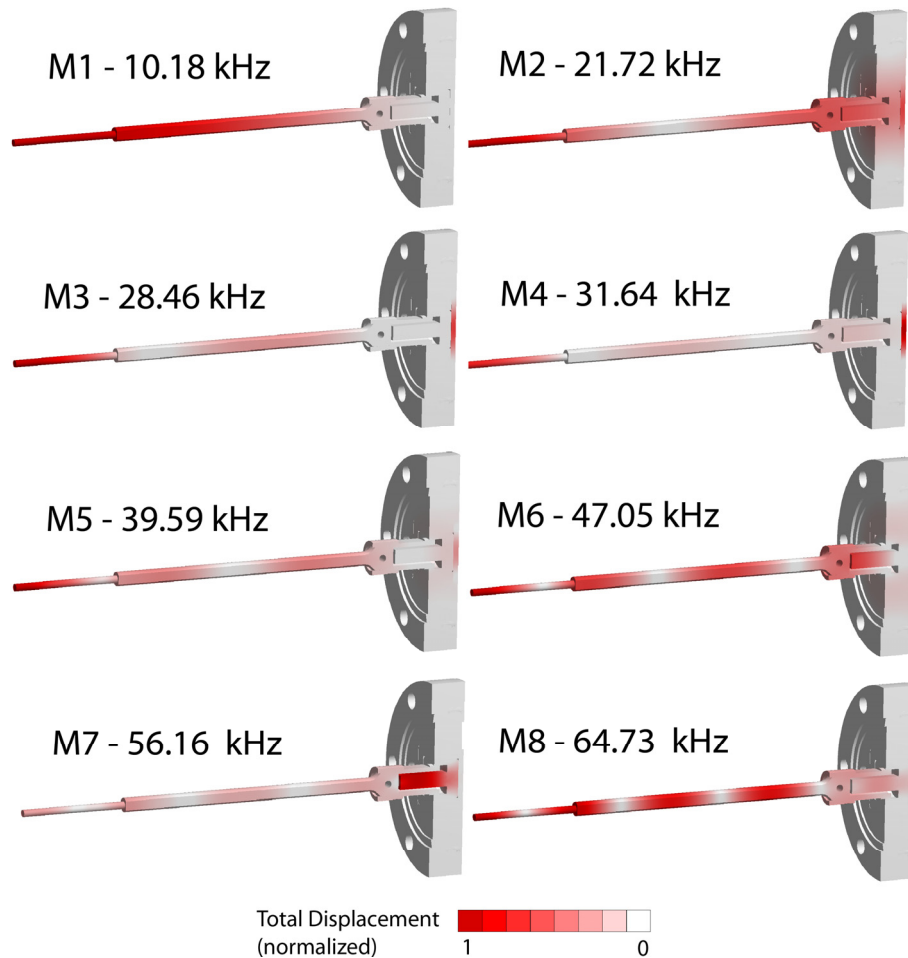


Fig. 62. Main modal shapes responsible for the peaks in the harmonic response of the piston tip velocity in the frequency range from 1 to 80 kHz.

The majority of mode shapes are related to the axial deformation of the assembly, including the piston coupled to the enclosure and support flange. The modal order n can be identified by the number of nodes ($n-1$), which are represented in white in Fig. 62. Depending on the mode shape, the nodes are either located on the piston only (M2, M4, M8) or on the full assembly (M1, M3, M5, M6). If the nodes are located on the piston only, the resulting eigenfrequency is larger. Non-integer ratios between different axial eigenfrequencies are observed. The mode shape M7 contains an axial mode of the piezoelectric stack, beside a weak trace of the 5th axial order M6. The resonance frequency of the piezoelectric stack does not appear directly in the tip velocity response. Due to the coupling to the full assembly, the frequency of the stack's axial mode is reduced by 27%. According to the undamped FE simulation, the mode shapes M1, M3, M5 and M6 with nodes distributed over the full assembly, are predicted to yield the largest tip velocities / pressure amplitudes, as shown in Fig. 61.

Table 4-IV. Main modes and mode shape description of the excitation system.

Mode	Frequency (kHz)	Modal shape
M1	10.18	1 st axial mode (1 node in flange)
M2	21.72	2 nd axial mode (1 node on piston)
M3	28.46	3 rd axial mode (1 node on piston, 1 node on piezo & enclosure)
M4	31.64	3 rd axial mode (2 nodes on piston)
M5	39.59	4 th axial mode (2 nodes on piston, 1 node on piezo & enclosure)
M6	47.05	5 th axial mode (3 nodes on piston, 1 node in flange)
M7	56.16	Axial piezo stack mode
M8	64.73	5 th axial mode (4 nodes on piston)

4.5. Discussion

4.5.1.1. Comparison of measured and computed structural responses

The FE analysis of the excitation mechanism is in good agreement with the piston tip dynamics measured by LDV. The comparison of the numerical and experimental approach in terms of tip velocity is presented in Fig. 63. Both velocity responses have been normalized by their respective maximum velocities. Indeed the velocity amplitude is not relevant in this context, as the study focuses on the origin of the resonance frequencies. The first experimental resonance peak located at 12.5 kHz is reproduced by the FE analysis at 10.2 kHz. Similarly, the two resonances at 22.4 kHz and 27.7 kHz are found in the FE analysis at 21.7 kHz and 28.5 kHz respectively. In the range from 30 to 60 kHz, the match is less accurate. The main experimental peaks, which are less pronounced than in the simulation, are found at 38.0 kHz, 50.5 kHz and 54.8 kHz respectively, while the simulated peaks lie at 39.6 kHz, 47.1 kHz and 56.2 kHz respectively. The experimental peak at 66.1 kHz is predicted in the FE study at 64.7 kHz. For the considered peaks, the average deviation between numerical and experimental values is 6.3%. This relatively low value for the average deviation justifies the use of the FE analysis to explain the origin of the frequency peaks.

The mismatch in terms of resonance frequencies between experimental and numerical results has different sources. One major reason for the mismatch results from the fact that the mechanical model is a multi-body simulation with complex couplings. These couplings are typically difficult to model accurately. The FEM model assumes zero displacement between the contact surfaces of two bodies. Another major source for resonance frequency shifts is the pre-stressing of the piezoelectric stack. In reality, the non-ideal connections result in more complex couplings. For example, bolted

connections influence the coupling between two bodies as a function of the applied tightening torque.

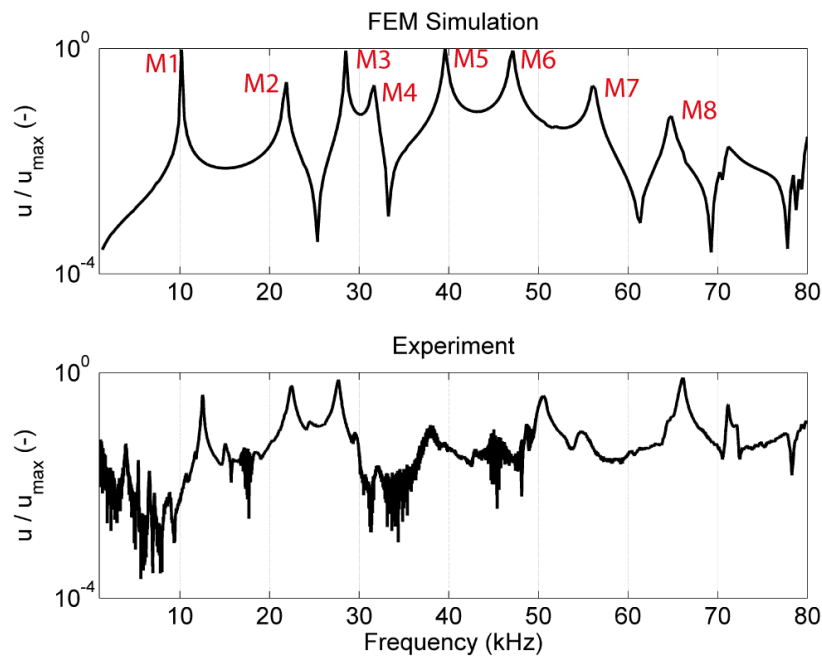


Fig. 63. Comparison of FEM predicted and experimentally determined tip velocities. Both numerical and experimental responses follow the same trend with an average deviation between numerical and experimental values for the resonance frequencies of 6.3%.

Experimentally, a shift of resonance frequency is observed with increasing pre-stress, as shown in Fig. 64. The admittance of the stack installed in the assembly is measured during a frequency sweep. The stack is used in sensor mode and the admittance reflects any system resonances. In the example of Fig. 64, the resonance frequency at 28 kHz is shifted by 3.5 kHz by increasing the pre-stress on the piezoelectric stack. Two reasons are responsible for this shift: first, the piezoelectric coefficients change with the pre-stress induced DC bias electric field.¹⁶⁸ It has been observed that the elastic compliance, the piezoelectric coefficient and the dielectric permittivity linearly decrease with the DC bias field. This change is not modeled in the current FE analysis, as the dependence of the piezoelectric coefficients on the DC bias field has not been quantified. Secondly, the acoustic coupling between the piezoelectric stack and the rest of the excitation system is influenced by pre-stressing.¹⁶⁹ The resulting pre-stress dependent coupling is also not modeled in the current FE analysis.

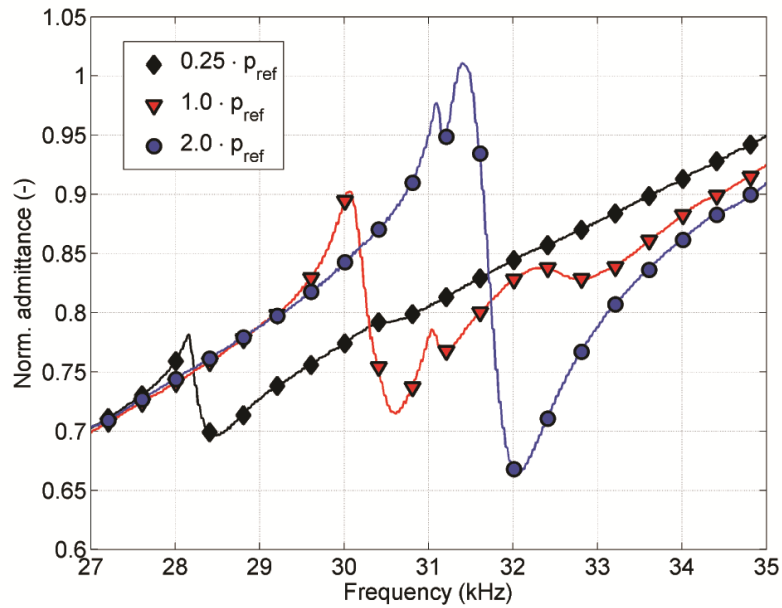


Fig. 64. Shift of the resonance peak around 30 kHz for pre-stress levels of 25%, 100% and 200% (of the reference pre-stress). In this experiment, the resonance frequency is shifted in total by 12% under the influence of the pre-stress.

4.5.1.2. Correlation between structural and pressure response

The experimentally determined structural frequency response is compared to the pressure response at the nozzle inlet. The tip velocity is shown together with the nozzle pressure in Fig. 65 for the frequency range from 1 to 80 kHz. The velocities and pressures are normalized with respect to their peak value. Although the relative amplitudes are not necessarily conserved, an agreement is found for the main resonance peaks between the tip velocity and the pressure distributions. As a consequence, a correlation exists between the resonance peaks of the tip velocity and the nozzle pressure response. In order to confirm this finding, the pressure and displacement measurements are repeated for a second system, which is characterized by a lower stiffness support of the piezoelectric stack (system B). Again, the frequencies of the main resonance peaks remain unchanged, as shown in Fig. 66.

A consequence of the correlation between structural displacements and pressures at the nozzle inlet is that the fluid-structure interaction and the pressure wave propagation in the liquid do not significantly add or shift resonances. These mechanisms are however partially responsible for the discrepancies observed between the pressure and the tip velocity measurements. Fluid resonances in the liquid tin do not introduce any noticeable new resonance peaks.

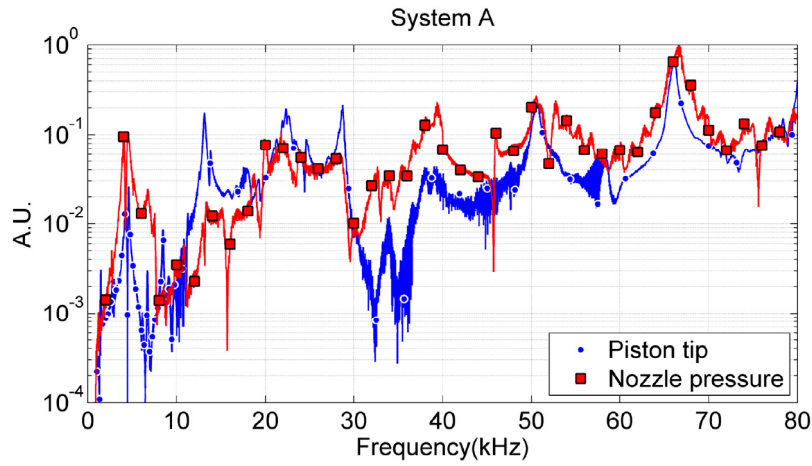


Fig. 65. Normalized tip velocity and pressure responses for the studied system (system A). A strong correlation between the structural displacement and the pressure at nozzle inlet is observed.

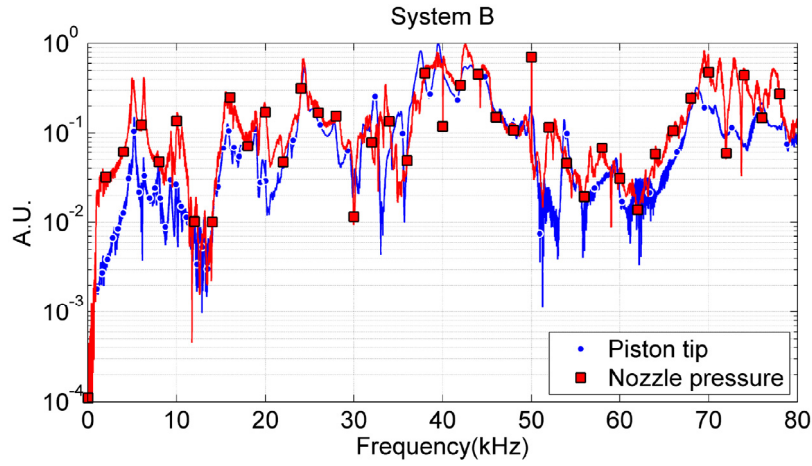


Fig. 66. Normalized tip velocity and pressure responses for a system with a lower stiffness support (system B). Similarly to system A, a strong correlation exists between the structural displacement and the nozzle pressure.

The influence of the fluid damping on the displacement of the piston can be estimated by modeling the piston as a stiff body. The piston is simplified as a cylinder of radius R and of immersed length L . Its center of mass then oscillates harmonically with a displacement amplitude d , a frequency ω and a phase φ

$$x(t) = d \sin(\omega t - \varphi) \quad (4.10)$$

The piston is submitted to viscous damping along its outer surface and to a pressure force at the tip, which is given by the acoustic impedance. For the viscous damping, the shear stress is derived from the velocity gradient along the radial direction at the wall

$$\tau(t) = -\mu \left. \frac{\partial u}{\partial r} \right|_{r=R} \quad (4.11)$$

The shear stresses can be evaluated using the solution to Stokes' second problem, which gives the velocity distribution along an oscillating slab. The oscillating slab solution is valid for the present setup, as the boundary layer induced by the oscillation is smaller than (or in the same range) as the radius R of the piston. Indeed the condition of validity is

$$R\sqrt{\omega / (\rho\mu)} > 1 \quad (4.12)$$

Stoke's solution gives the velocity distribution in the radial direction (normal to cylinder surface) :

$$u(r,t) = -d\omega \exp\left(\sqrt{\frac{\rho\omega}{2\mu}}(r-R)\right) \cos\left(\omega t - \varphi - \sqrt{\frac{\rho\omega}{2\mu}}(r-R)\right) \quad (4.13)$$

The viscous force resulting from the shear stress is derived by multiplying the shear stresses with the immersed cylinder lateral surface:

$$F_t(t) = 2\pi RL \cdot \tau(t) = -2\pi RL \cdot \mu \left. \frac{\partial u}{\partial r} \right|_{r=R} = -d\omega^{3/2} \sqrt{\frac{\rho\mu}{2}} (\cos(\omega t - \varphi) - \sin(\omega t - \varphi)) \quad (4.14)$$

The normal pressure fluctuation at the piston tip is given by the acoustic impedance Z and the tip velocity relationship

$$p'(t) = Z \cdot \dot{x}(t) = \rho c \cdot \dot{x}(t) \quad (4.15)$$

The force induced by the tip pressure fluctuation equals

$$F_p(t) = \pi R^2 p'(t) = \pi R^2 \rho c \cdot \dot{x}(t) \quad (4.16)$$

The amplitudes of the two forces are compared for piston dimensions, which are representative of the developed droplet dispenser. The displacement is integrated from the measured tip velocity. It must be noted that this displacement does not contain the fluid damping, as it is derived from LDV measurements. A first comparison of the damping forces is however possible if it is assumed that the influence of the damping is limited. The resulting forces are plotted as a function of frequency in Fig. 67 in the case of tin. The plot also includes the initially undamped net force, which is derived from the measured (LDV) acceleration and the mass of the piston. It can be seen that both damping forces should have a minor influence on the motion of the piston. This conclusion must be considered with care, as the result strongly relies on the assumption of a stiff body. A more reliable conclusion is that the pressure force at the tip exceeds the viscous damping on the outer cylinder surface on average by almost 2 orders of magnitude. In the case of water, the damping forces are lower than for tin, as the density, the viscosity and the speed of sound of water are lower.

Another evaluation of the overall damping is conducted by comparing the mechanical quality factor for the velocity and pressure peak at 66.1 kHz. The corresponding curves are shown in Fig. 65. The damping increases 1.5 times from the structural response to the pressure response for the peak at 66.1 kHz.

Due to the high signal to noise ratio of the pressure sensor, the structural eigenfrequencies can be resolved in the pressure measurements. Indeed, as shown in Fig. 68, even at system excitation frequencies below 20 kHz, the dominant structural modes at 50.5 and 66.1 kHz are visible in the frequency spectra. The intersection of these eigenfrequency lines with the line of the base excitation frequency leads to the resonances, which are observed in the pressure response. On the other hand, if the piezoelectric stack is operated at a fixed frequency, the pressure response is expected to always contain contributions from these main structural eigenfrequencies. Additional contributions result from the intersection of the structural eigenfrequencies and higher harmonics of the excitation signal, as shown in Fig. 68. These contributions are part of the multi-frequent perturbations, which transmit into the droplet stream, as described in Sec. 5.

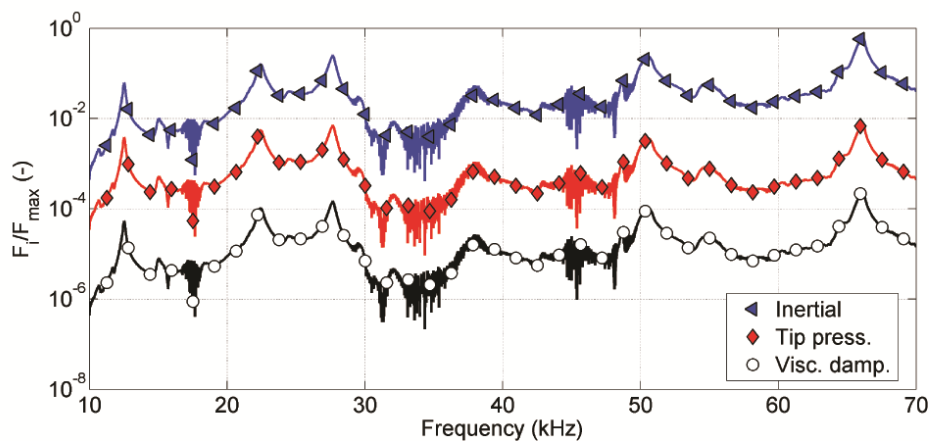


Fig. 67. Estimation of scaling of viscous damping and tip force with respect to the undamped net force.

During the design phase of the dispenser, the displacement requirement for the piezoelectric stack was determined by the target pressure amplitude. It was assumed that the ratio of pressure amplitude to piston tip velocity is constant and equal to the acoustic impedance. The linearity should not be affected by properties of the acoustic medium. The results presented in Fig. 65 and Fig. 66 are useful when trying to validate this design assumption. For both systems, the frequency responses of the tip velocity and nozzle pressure clearly follow the same trend. Non-linear contributions like frequency dependent damping, can be neglected during the design process.

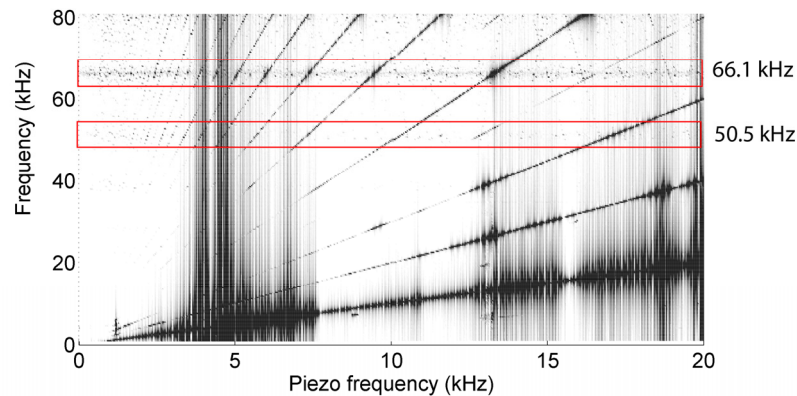


Fig. 68. Pressure response spectra with traces of structural eigenmodes for excitation frequencies up to 20 kHz. The visible traces are induced by the main structural eigenfrequencies at 50.5 kHz and 66.1 kHz. Secondary resonance peaks appear at the intersection of the lines of structural eigenmodes and higher order harmonics of the excitation signal.

In conclusion, the excitation mechanism can be mechanically tuned to yield a desired resonance peak in the pressure response. Tuning possibilities include the adaptation of the physical dimensions (especially length) of the piston to shift the main system modes. On the other side, the resonance behavior of the piezoelectric stack, which is a function of its material properties, dimensions and clamping inside the assembly, also determines the eigenfrequencies of the excitation system. The resulting coupled higher order structural response should be investigated by FE analysis and if possible, the generated pressure amplitudes should be verified by subsequent pressure measurements.

4.6. Summary and conclusion

The non-ideal boundary conditions leading to the droplet breakup are studied in this chapter. A novel high temperature fast response miniature pressure probe for use in liquid metals up to 255 °C has been developed. The core consists of a piezoresistive pressure sensor, which is coated for electrical insulation and protection purposes by a silicon elastomer. Reliability and measurement capabilities are assessed by mounting the probe on the nozzle level of the liquid tin dispenser. Static calibration of the probe revealed viable pressure sensitivities up to 255 °C, with variations in the range of 0.5% over a time period of 70 minutes. Dynamic probe calibration yields a first natural frequency occurring around 100 kHz. The probe's resolution is 7 mbar and the overall measurement uncertainty equals 1.3%. Agreement is found between pressure measurements and LDV measurements on the oscillating piston.

A reference pressure measurement, conducted at representative conditions for tin droplet generation, shows a complex pressure response, with peaks distributed over 3 orders of magnitude

and a maximum pressure amplitude of 440 mbar. Peaks are weakly damped with mechanical quality factors in the range of 70. The measured pressure response helps to quantify the non-ideal highly frequency dependent boundary conditions. The temporal change of the pressure response can be monitored in real-time during operation, which helps to quantify the time variance of the excitation mechanism due to thermal transients. The developed probe is a viable diagnostic tool for studying the excitation mechanism of a liquid metal droplet dispenser and for monitoring the performance of the excitation system during long-term operation.

Significant pressure levels are only obtained if the piston is immersed in the liquid. Due to the complex structure of the observed pressure responses, a structural analysis is carried out using LDV. Significant displacements are only observed at the piston tip, which proves that the acoustic pressure is generated by the oscillating piston.

The complex structural response is investigated with a FE analysis, which includes a detailed and validated model of the multilayer piezoelectric stack. The harmonic response of the full assembly of the excitation mechanism, up to the cover flange, is numerically investigated. The FE and LDV results are found to be in good agreement, with a mean deviation of the resonance frequencies of 6.3%. Therefore, the resonance modes can be identified from the numerical model. The key mode at 66.1 kHz, which yields the maximum pressure amplitude, is a 5th order axial mode of the piston with no nodes on the flange or enclosure. This mode is located close the resonance of the piezoelectric stack.

The correlation between the structural displacements around the piston tip and the pressure amplitudes is verified for two different dispensers. The fluid-structure interaction of the piston and the pressure wave propagation in the liquid do not add or shift resonance frequencies. Therefore, the assumption in the design process of a linear relationship between acoustic pressure and structural vibrations is verified. As a consequence, the excitation mechanism can be mechanically tuned to yield a desired resonance peak in the pressure response. Tuning possibilities include the adaptation of the physical dimensions (especially length) of the piston to shift the main system modes. On the other side, the resonance behavior of the piezoelectric stack, which is a function of its material properties, dimensions and clamping inside the assembly, also determines eigenfrequencies and amplitudes of the excitation system. The developed FE model, together with the pressure sensor, supports the design of tailored excitation systems.

Chapter 5

Droplet formation

The correlation between the previously measured nozzle inlet pressure and the resulting droplet train characteristics is investigated in this chapter. A sweep of the excitation frequency is completed with simultaneous measurements of the droplet timing at a fixed distance from the nozzle exit. The corresponding pressure signal is used as an input to a droplet formation model. This model, which includes both the main excitation signal and a noisy perturbation of the droplet stream is used to predict the droplet timing. The key parameters, which influence droplet formation, are identified. The typical noise disturbance level, which must be overcome by the excitation signal, is derived from experiments with the developed droplet dispenser. The physical limits of droplet formation with respect to the EUV requirements are detailed. Validated CFD simulations are used to study the droplet timing jitter for large droplet spacings as a function of the acoustic excitation pressure. Guidelines for optimizing the droplet generation according to the requirements for a LPP source are outlined.

5.1. Introduction

Continuous droplet generation is accomplished by the capillary breakup of a liquid jet, which emanates from the dispenser nozzle. An inviscid jet is unstable with respect to an axisymmetric harmonic perturbation in jet radius, if the wavelength of the perturbation is larger than the circumference of the jet.⁸⁸ The wavelength of the perturbation is determined by the perturbation frequency and the jet velocity.

In the absence of a forced excitation, the jet breaks up in a non-deterministic way. In this case, the origin of the perturbation is noise, which can be transmitted to the flow either inside or outside the nozzle. The dispensing nozzle is a major source for noise contributions to the jet contour. First, high frequency vibrations of the entire nozzle or portions of the nozzle, such as the orifice cross-section, impose perturbations on the jet contour. This principle is for example used in the Berglund-Liu nozzle type¹³⁴ in order to impose the main frequency. Unwanted structural vibrations of the nozzle can be induced by the excitation of nozzle eigenmodes by the primary excitation source. Similar excitations of undesired structural frequencies have been observed in the pressure response of the excitation system. It could be shown that structural eigenmodes and higher order harmonics of the excitation frequency yield additional contributions in the frequency spectrum of the nozzle inlet pressure, as shown in Fig. 68.

Another source for noise is related to the nozzle flow. Indeed the Reynolds number of the tin flow only takes significant values (>100) in the micrometer cross-section of the nozzle orifice. In this section, the flow is sensitive to the nozzle surface roughness. Depending on the mean surface roughness, the induced perturbations can have frequencies in the range of the excitation frequency. The boundary layer can transition from laminar to turbulent flow up to the nozzle exit under the influence of the internal roughness. Experimental studies on the internal nozzle roughness prove the formation of surface ripples on the jet surface.^{170, 171} In case of beneficial growth rates, these ripples become a major cause for jet breakup. The nozzle entrance section can also have an influence on the noise level of the jet by introducing perturbations, which propagate through the nozzle. Wakes with critical frequency content can develop at the nozzle inlet. Some viscous dissipation takes place along the nozzle length. Geometrical irregularities at the separation edge of the nozzle potentially disturb the jet contour. Unsteady wetting behavior between the jet and the nozzle can lead to a high frequency perturbation of the jet mass flow. Perturbations in the nozzle flow can also result from fluid inhomogeneities, which are either related to impurities or non-uniform fluid properties.

An additional noise source is electrical noise in the excitation source of the piezoelectric actuator. The electrical noise either results from signal generation, from the amplifier circuits or from the signal transmission to the piezoelectric actuator.

The generated noise leads to a multi-frequency droplet generation. As a result, droplets of all sizes with irregular spacings are obtained. This regime is called natural breakup. In the present application, an external excitation is imposed to bypass the natural breakup frequencies. The artificial perturbation is induced by a piezoelectrically actuated piston, as described in Sec. 2.2.4.

In this chapter, the correlation between the perturbation, i.e. the measured nozzle inlet pressure and the resulting droplet train characteristics, such as frequency, timing jitter and spacing is studied based on experimental results and numerical models. First, the droplet timing jitter is measured as a function of frequency with the help of the laser-photodiode setup from Sec. 3.2.1.2. A droplet formation model is developed to correlate the droplet timing jitter with the inlet pressure. The

predictions are compared to experimental data. From this comparison, the noise level, which leads to the non-deterministic breakup of the jet, is derived. The model is also useful in determining a more general relationship between droplet timing jitter and the acoustic excitation pressure. Then, the limits of the largest possible droplet spacings are explored using two-dimensional axisymmetric computational fluid dynamics (CFD) simulations. The employed code is validated by comparison of the predicted droplet velocity and size with recorded shadowgraphs of the droplet train. The dependence of the achievable wave numbers (droplet spacings) on the excitation pressure is presented.

5.2. Numerical approach

In order to correlate the measured pressure conditions at nozzle inlet with the droplet train characteristics, a droplet formation model is required. In the present case, the computation of the droplet characteristics must be completed for a large number (greater than 100) of operating frequencies. As the jitter corresponds to a statistical quantity, a sufficiently large number of droplets must be simulated to yield representative results. Therefore, a computationally cheap model, based on linear droplet formation theory is developed. The linear assumption is valid as a first order approach. Indeed, in this initial work, droplet formation is considered in a range where no satellite formation takes place.¹⁷² The main excitation is assumed to be significantly larger than the noise level. For critical ranges with potential satellite formation, droplet formation is modeled using a two-dimensional axisymmetric CFD simulation.

5.2.1. Droplet formation model

The influence of a pressure disturbance on droplet formation is derived from a linear one-dimensional analysis. The underlying linearized continuity and momentum equations, which yield the quasi-stationary equation of the perturbed jet radius are derived in Lee *et al.*¹³³ for an inviscid fluid. The absolute axial coordinate z is transformed to a Lagrangian coordinate η by assuming constant stream velocity v_0 : $\eta = z - v_0 t$. The linearized solution considers only weak curvatures on the jet surface, such that the radius can be written as

$$r(t, \eta) = a(1 - \delta(t, \eta)) \quad (5.1)$$

where a is the initial jet radius at nozzle exit and $\delta(t, \eta)$ is the so-called disturbance function. The linearized equation of motion is written as¹³³

$$\frac{\partial^2 \delta}{\partial t^2} + a^2 \beta^2 \frac{\partial^4 \delta}{\partial \eta^4} + \beta^2 \frac{\partial^2 \delta}{\partial \eta^2} = -\frac{1}{\rho} \frac{\partial^2 f}{\partial \eta^2} \quad (5.2)$$

where $\beta^2 = \frac{\sigma}{2\rho a}$ and f is an external (pressure) excitation term. As a next step, a solution to the initial value problem for a predefined pressure fluctuation is derived. The pressure excitation function first consists of a constant part p_0 (reservoir pressure) and a harmonic part p' , which is generated by the oscillating piston. The second term contains the band-limited white noise of amplitudes p'_i , wave number k_i and phase φ_i . Random noise fluctuations on the capillary stream are required to model the droplet timing jitter. The origins of the noise contributions are described in Sec. 5.1. The noise amplitudes p'_i are random numbers, which are normalized in order to yield a predetermined overall root mean square (RMS) value for the noise. The phase φ_i and the wave number k_i are both random numbers sampled in the intervals $[0, 2\pi]$ and $[0, 1/a]$, respectively. The physically meaningful limits of the wave number are derived later. In fact, the non-dimensional wave number $k^* = 2\pi a/\lambda$ of a perturbation must be contained in the interval $[0,1]$ for the perturbation to grow. The pressure excitation function equals

$$f = p_0 + p' \cos(k\eta) + \sum_i p'_i \cos(k_i\eta - \varphi_i) \quad (5.3)$$

where $k_i = 2\pi/\lambda_i$ is the wave number and λ_i is the wavelength of the perturbation of the stream contour. The general solution, which is similar to the solution derived for a radially disturbed jet in Lee *et al.*¹³³, can be written as

$$\delta(t, \eta) = \frac{k^2}{\rho\gamma^2} (1 - \cosh(\gamma t)) p' \cos(k\eta) + \sum_i \frac{k_i^2}{\rho\gamma_i^2} (1 - \cosh(\gamma_i t)) p'_i \cos(k_i\eta - \varphi_i) \quad (5.4)$$

with the inviscid growth rate γ defined by

$$\gamma_i^2 = \beta^2 k_i^2 (1 - a^2 k_i^2) \quad (5.5)$$

Growth rates have been experimentally measured¹⁷³ and expressions for viscous jets are available.⁸⁹ The inviscid assumption is verified by comparing the inviscid and viscous growth rates. The inviscid and viscous growth rates for tin at potential dispenser operating temperatures are shown in Fig. 69. The growth rate is expressed as a function of the non-dimensional wave number $k^* = 2\pi a/\lambda$. The temperature dependent viscosity and surface tension for tin are taken from Thresh *et al.*¹²⁹ and Melford *et al.*¹³⁰, respectively. The peaks of the growth rates vary within 3% of the peak value. The wave numbers corresponding to the maxima of the growth rate vary only by 1.5% around 0.7. As a consequence, the change of fluid properties in the temperature range from 240°C to 400°C is negligible. Secondly, the inviscid assumption is expected to have a minor effect on droplet formation for tin.

Droplet breakup takes place, when the initial disturbance waves have grown enough to give a jet radius of zero, which is equivalent to $\delta(t, \eta) = l$. If the influence of the noise is neglected, the breakup

time t_b can be written in a closed form. By setting the noise contribution to zero, Eq.(5.4) can be solved for t_b . The following expression is obtained for the breakup time

$$t_b = \frac{1}{\gamma} \operatorname{acosh} \left(1 + \frac{\rho \gamma^2}{k^2 p'} \right) \quad (5.6)$$

and the breakup length l_b is derived by multiplication with the stream velocity v_0

$$l_b = v_0 t_b = \frac{v_0}{\gamma} \operatorname{acosh} \left(1 + \frac{\rho \gamma^2}{k^2 p'} \right). \quad (5.7)$$

The general description of the stream contour by Eq.(5.4) can be used to plot the evolution of the stream contour from time $t=0$ up to the breakup time t_b . The stream contours at the time instances corresponding to 0%, 95% and 100% of the breakup time are shown in Fig. 70. Only a portion of the stream contour of length $\lambda/2$ is considered, which is convected at the stream velocity v_0 up to the breakup point. In this example, the noise level (RMS) equals 1.5% of the main signal. At the exit of the nozzle ($t=0$), the disturbance is much smaller than the jet radius r . During the convection at v_0 , the harmonic disturbance grows up to the breakup point, where the radius of the stream contour equals zero.

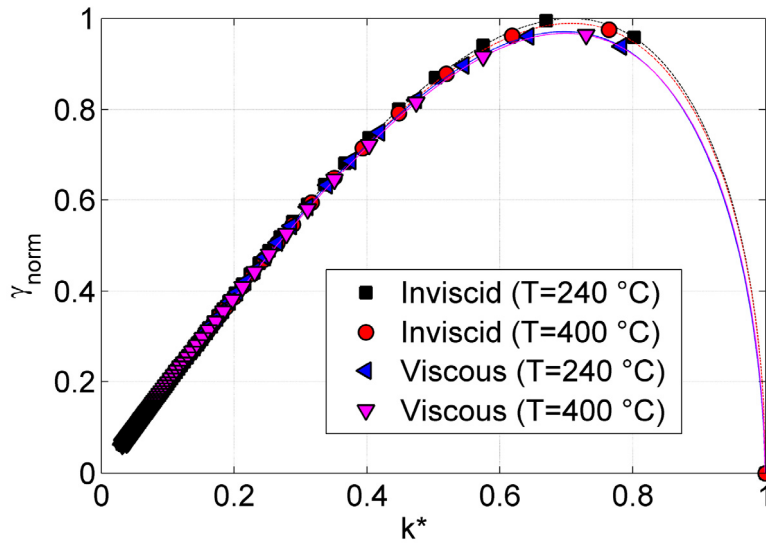


Fig. 69. Viscous and inviscid growth rates of jet disturbance at 240 °C and 400 °C. Temperature and viscosity have a minor influence on the growth rate for tin.

The breakup time can also be determined by considering the infinitesimal fluid element in a Lagrangian frame of reference, which moves at the jet velocity v_0 . The fluid element is chosen, such that it ends up at exactly the breakup point. As a consequence, Eq.(5.4) becomes time dependent only.

$$\delta(t) = \frac{k^2}{\rho\gamma^2}(1 - \cosh(\gamma t)) p' \cos(\omega t - \varphi_0) + \sum_i \frac{k_i^2}{\rho\gamma_i^2}(1 - \cosh(\gamma_i t)) p'_i \cos(\omega_i t - \varphi_i - \varphi_0) \quad (5.8)$$

where $\omega = kv_0$ is the frequency corresponding to the wave number k and φ_0 is an added phase term. The phase term selects the fluid element which will be located at the breakup point. This phase term can only be determined iteratively due to the random noise contributions in the excitation signal. The final solution is found when the resulting breakup time is minimized. Indeed, if the location of the fluid element is chosen before or after the breakup element, the computed breakup time exceeds the physical breakup time. This conclusion is intuitive when considering fluid elements before or after the breakup point in Fig. 70. The initial estimate is determined from the breakup time from Eq.(5.6). The derived initial estimate for the added phase term equals $\varphi_0 = -v_0 k t_b$, where the term $v_0 k$ corresponds to the external excitation frequency. It is assumed that the main perturbation is significantly larger than the noise level in order to ensure convergence of the iterative search of the breakup fluid element. Once the phase term φ_0 has been found, the trajectory of the breakup fluid element can be computed. A series of simulations for different random noise contributions is used to derive the droplet timing jitter.

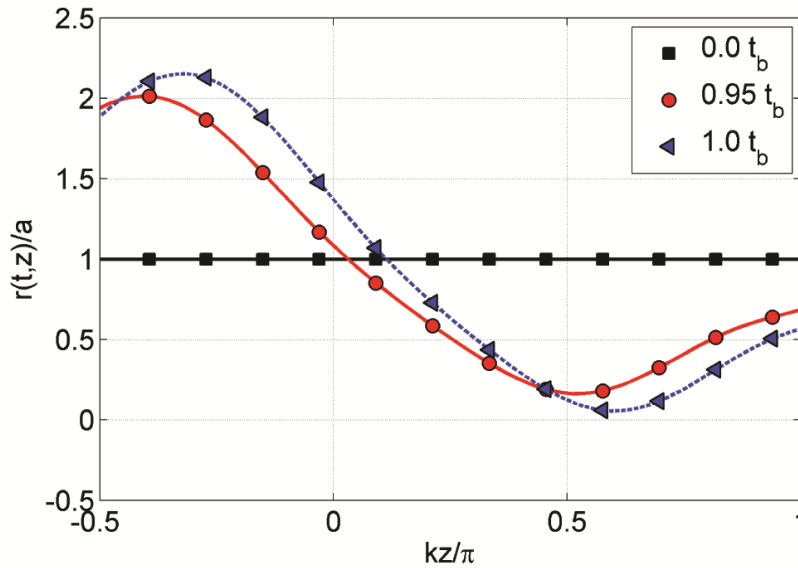


Fig. 70. Temporal evolution of stream contour from $t=0$ to the breakup point $t=t_b$. At the breakup point, the stream radius equals zero. The noise RMS equals 1.5% of the main perturbation amplitude. The axial coordinate z is normalized by $\lambda/2$.

The timing jitter finds its origin in the velocity dispersion, which develops at droplet breakup. The swelling droplet is pulled back towards the jet. The velocity of each droplet can be derived from the rate of change of momentum in a control volume enclosing the breakup location. The relevant forces are the pressure gradient and the surface tension at the liquid-gas interface. The underling

mechanism is detailed in Goedde *et al.*¹⁷⁴ A suited model equation for this work is derived by Orme *et al.*¹⁰² The droplet velocity after breakup can be written as

$$v_{drop} = v_0 - \frac{1}{m} \pi \sigma \int_{t_{bb}}^{t_{bf}} r(t) dt \quad (5.9)$$

where m is the mass of the resulting droplet and $r(t)$ is the change of stream radius during the forward breakup time t_{bf} and backward breakup time t_{bb} of the droplet. The droplet mass equals $m = \rho(t_{bf} - t_{bb})v_0 p a^2$. A typical trajectory of the Lagrangian fluid element, which is convected to the breakup point, is shown in Fig. 71. Both breakup times and the integrated radius $r(t)$ are estimated from this curve. It must be noted that the backward breakup point is derived from the fluid element trajectory, even though the stream radius does not equal zero in this point. This is valid as the noise contributions, which could alter the difference $t_{bb} - t_{bf}$ up to the backward breakup point, are random. The change in radius along the trajectory is conceived to be representative for the change in radius of the forming droplet.

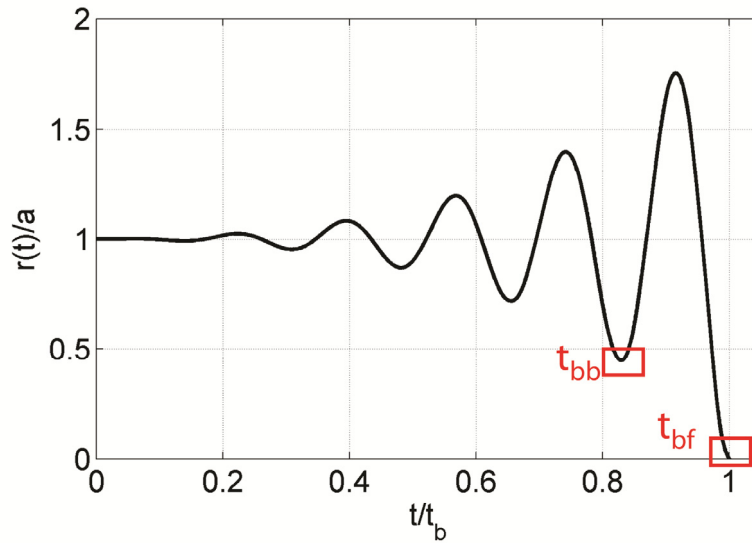


Fig. 71. Trajectory of a Lagrangian fluid element along stream contour. The fluid element is advected to the breakup point t_{bf} . The trajectory is also used to estimate the second breakup point t_{bb} of the droplet.

The solution of the model equations is implemented in MATLAB® / SIMULINK® (Release 2012a). A schematic of the solution procedure is shown in Fig. 72. The main inputs to the simulation are the physical properties of the liquid, the jet velocity and the excitation frequency. The noise RMS is required to be specified explicitly. The excitation pressure can either be specified manually or the transfer function of the excitation system (from the excitation voltage to the pressure) can be included.

In a first iteration loop (blue), the phase φ_{new} is determined by running the SIMULINK[®] model. This model includes the main pressure and the noise contributions. The growth rate model according to Eq.(5.8) is implemented. The simulation runs until the droplet breakup is detected. The numerical solution is advanced with a time step $t_s/100$, where $t_s=a/v_0$ is the smallest time scale of the problem. In order to decrease the sensitivity to the time step, the locations of the stream contour around t_{bb} and t_{bf} are fitted by a fourth order polynomial, which is sampled at a higher resolution of $t_s/10^5$. The derived phase angle is then used in the main simulation step to determine the droplet characteristics, such as the velocity. The model equations are solved repeatedly in the outer loop (red), until the standard deviation of the droplet velocity is converged to less than 1%. Finally, the droplet timing jitter is computed as the standard deviation $\sigma(t)$ of the droplet travel time to a certain observation location (or plasma irradiation site), which is situated at a distance l_{obs} from the breakup point.

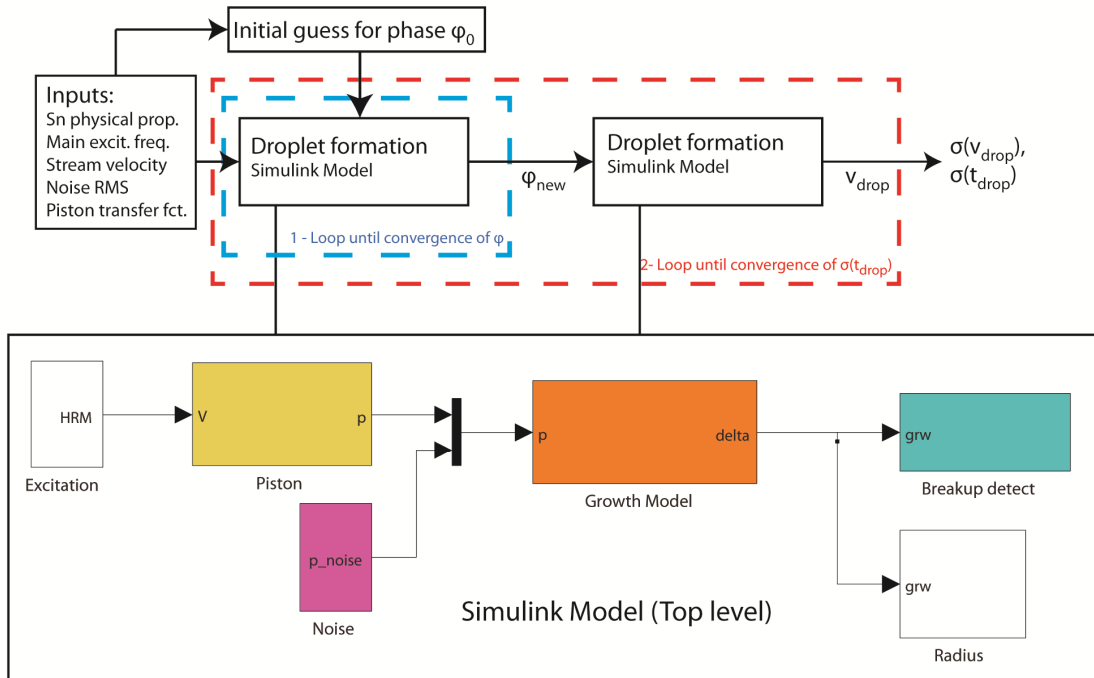


Fig. 72. Overview of the implementation of the droplet formation model.

5.2.2. CFD simulation

In addition to the linear droplet formation model, two dimensional axisymmetric transient multiphase CFD simulations are conducted with the commercial CFD package ANSYS[®] FLUENT. The multiphase modeling is based on the explicit volume of fluid (VOF) approach. The discretization of the phase interface is completed by the geometrical reconstruction method of FLUENT. Faster schemes like CICSAM did not yield accurate results. The non-iterative fractional step scheme is used for time advancement. The PISO algorithm with neighbor correction is used for the pressure-velocity coupling. The flow is considered to be laminar (Sec. 2.2.5). The tin

viscosity and surface tension are taken from Thresh *et al.*¹²⁹ and Melford *et al.*¹³⁰, respectively. Two phases, namely air and tin are considered. The computational domain is shown in Fig. 73.

At time zero, the nozzle is filled with tin, while the rest of the computational domain is filled with air. At the nozzle inlet, a prescribed pressure fluctuation, according to Eq.(5.3) is set. The pressure fluctuation contains the static backpressure term and the pressure fluctuation due to the excitation system. The jet is accelerated out of the nozzle of diameter D_n once the simulation starts. After some distance, the jet starts breaking up into droplets. Droplets form inside the vacuum chamber and move towards the lower end of the domain. The largest simulated domain lengths are in the range of $800D_n$. The domain length is determined by the breakup length and the subsequent droplet relaxation. A monitor point at the lower end of the droplet stream captures the properties of the passing droplets. The width of the domain in the vacuum section is determined by the largest expected droplet sizes.

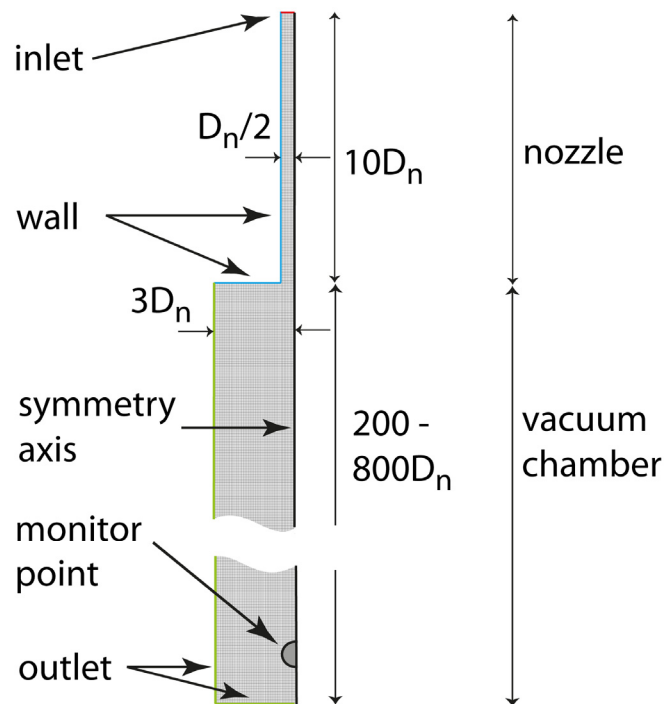


Fig. 73. Computational domain of the two dimensional axisymmetric droplet formation simulation. The domain includes the nozzle section and a fraction of the vacuum chamber.

The wall boundary defines the nozzle contour. In order to include capillary effects at the outlet of the nozzle, a wetting angle for tin and the considered nozzle material is specified. The outlet is defined as a pressure outlet at vacuum level. The simulated droplet formation must be independent of the computational cell size. The grid resolution is chosen in order to generate a perturbation noise level on the stream contour, which is significantly lower than the physical noise level, as determined from the experiments. Details about the mesh resolution and validation of the simulation are found in Sec. 5.4.3.

5.3. Experimental approach

The measurements of droplet timing jitter are performed with the developed droplet dispenser and liquid tin. The dedicated vacuum chamber is equipped with the laser-photodiode droplet tracking system from Sec. 3.2.1.2. The processing of the photodiode signals for the droplet timing jitter derivation is presented in Sec. 5.4.1. The shadowgraphs of a section of the droplet train are also recorded on the same experimental setup. Details about the used imaging system and the image processing are found in Sec. 3.2.1.1.

5.3.1. Non-dimensional numbers

The experimental quantities of Sec. 3.3 are transformed into non-dimensional numbers in order to increase the general validity of the experimental observations.

5.3.1.1. Jet Reynolds number

Shadowgraphy of the droplet train is used to determine the droplet diameter and spacing for a given frequency and pressure setting on the dispenser. The reservoir pressure, which is used in the operating maps in Sec. 3.3.2 is not directly a quantity of interest, as its influence strongly depends on the pressure losses in the flow from the tin reservoir throughout the nozzle.

The jet velocity, or Reynolds number (with respect to the nozzle diameter) $Re = \rho v_0 D_n / \mu$ of the jet are more adequate quantities to non-dimensionalize droplet formation. Although the jet velocity is not directly measured, it can be derived from the equivalence of the jet and the droplet train mass flows. The jet radius can be derived from the nozzle radius. Indeed the jet will contract once it exits the nozzle due to the relaxation of its initial parabolic velocity profile to a uniform profile. The absence of wall shear forces leads to this relaxation. The assumption of a constant laminar jet contraction of 13% for $Re > 200$, as described in Middelmaan *et al.*¹⁷⁵, is valid for the considered range of Reynolds numbers. The jet velocity v_0 can be written as a function of the frequency f , the droplet diameter D_{drop} and the nozzle diameter D_n

$$v_0 = 1.762 \frac{(D_{drop} / 2)^3 f}{(D_n / 2)^2} \quad (5.10)$$

The measurement uncertainty on the droplet diameter is presented in Sec. 3.2.1.1. The accumulated uncertainty on Re , which is determined by the uncertainty on the droplet diameter, liquid viscosity and nozzle diameter, equals $\pm 10\%$.

5.3.1.2. Non-dimensional wave number

The non-dimensional wave number k^* , which has been introduced in Sec. 5.2.1 is commonly used to characterize the perturbation. In many research papers, this non-dimensional wave number is also used to represent the droplet spacing, relative to the nozzle circumference. In that case, the

perturbation wavelength is equal to the droplet spacing. This assumption is valid in the case where the jet velocity is approximately equal to the droplet velocity. As the nozzle size decreases, capillary effects become more important and according to Eq.(5.9), both velocities start to differ significantly. In another approach, the so-called capillary velocity is used to derive the droplet velocity from the jet velocity. The relationship between jet and droplet velocity is written as^{135, 176}

$$v_{drop} = v_0 \left(1 - \left(\frac{v_c}{v_0} \right)^2 \right) \quad (5.11)$$

where v_c is the capillary velocity, which equals $v_c = \sqrt{\sigma/\rho a}$. The capillary velocity only depends on the tin properties and on the jet radius. These quantities are not varied during the presented experiments. For the used nozzle, the droplet velocity typically differs from the jet velocity by 10%. This number is confirmed by Eq.(5.11). The difference between jet velocity and droplet velocity is close to the measurement uncertainty of the jet velocity. As consequence, the non-dimensional wave number gives a good indication of the droplet spacing. If, for a constant non-dimensional wave number $k^* = 2\pi a/\lambda = 2\pi a f/v_0$, smaller droplets should be generated, the corresponding droplet frequency needs to increase. Indeed the jet velocity v_0 needs to increase to compensate for the increased capillary velocity v_c . Additionally, smaller droplets demand smaller jet diameters, hence the frequency must increase to keep the wave number constant.

5.3.1.3. Non-dimensional droplet jitter

The droplet timing jitter finds its origin in the velocity dispersion, which results from momentum transfer between the jet and the droplet, during droplet formation. The droplet jitter is a function of the observation or laser irradiation height, relative to the breakup point. Therefore the measured timing jitter should be non-dimensionalized by the height at which the droplet jitter is measured. The relationship between the non-dimensional droplet velocity dispersion $\sigma(v_{drop})/\bar{v}_{drop}$ and the timing jitter $\sigma(t)$ is derived by a Monte-Carlo simulation. The relationship between the standard deviations of the droplet velocity and timing distributions is not trivial. For this purpose, droplets with different velocities v_{drop} are sampled and advanced from the breakup to the observation point. The timing jitter is derived from the passing of the droplets at the observation point. The mean travel time, which is equal to l_{obs}/\bar{v}_{drop} is used to non-dimensionalize the droplet timing jitter. It is found from the Monte-Carlo simulation that a correction factor of $\sqrt{2}$ is required to have equivalence between the relative velocity dispersion and relative timing jitter, as shown in Fig. 74. The Monte-Carlo simulation is completed for 10^6 droplets for each velocity dispersion ratio $\sigma(v_{drop})/\bar{v}_{drop}$.

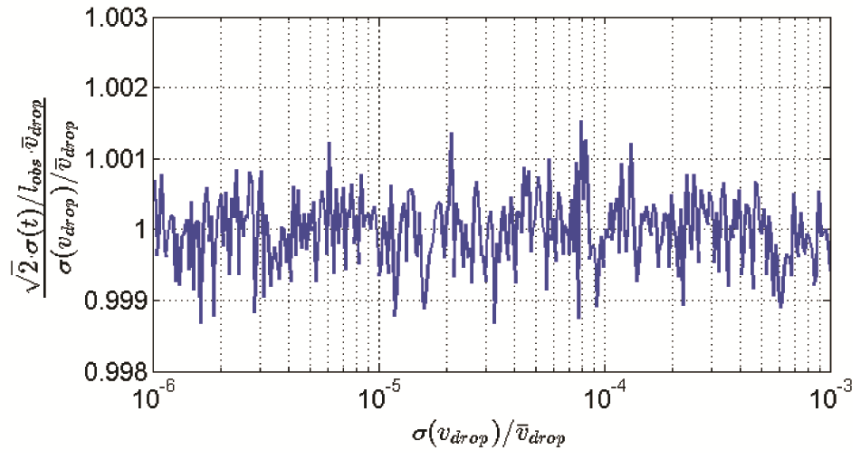


Fig. 74. Derivation of relationship between the droplet velocity dispersion and the timing jitter for non-dimensionalizing timing jitter results.

As a consequence, the measured droplet timing jitter $\sigma(t)$ is non-dimensionalized by the mean droplet velocity and the observation or irradiation height as follows

$$\frac{\sigma(t)\bar{v}_{drop}}{l_{obs}} = \frac{1}{\sqrt{2}} \frac{\sigma(v_{drop})}{\bar{v}_{drop}} \quad (5.12)$$

5.4. Results

5.4.1. Basic observations

The non-dimensional wave number k^* is computed from the dispenser operating maps, which have been described in Sec. 3.3.2. The wave number is plotted in Fig. 75 as a function of the excitation frequency and the Reynolds number for operating points with drop-to-drop jitters below 20% of the respective mean value. The lowest generated non-dimensional wave number is 0.18 (± 0.02) at a frequency of 20 kHz and $Re=800$. The equivalent non-dimensional wave number, which is based on the measured droplet spacing instead of the perturbation wavelength, differs by 6.5%. The measurements are used to generate an interpolated map of the non-dimensional wavelength k^* as a function of excitation frequency and Re .

At constant Reynolds number, a decrease in frequency increases the droplet spacing. On the other hand, droplet spacing increases with increasing Re at a constant frequency. In the experiment, no regular grid of equally spaced operating points with a droplet jitter below 20% could be generated. One important conclusion from the presented results is that, for a fixed reservoir pressure, small changes of frequency have a major impact on droplet jitter. Therefore the complex dependence of the droplet jitter on the excitation frequency and the Reynolds number is further investigated.

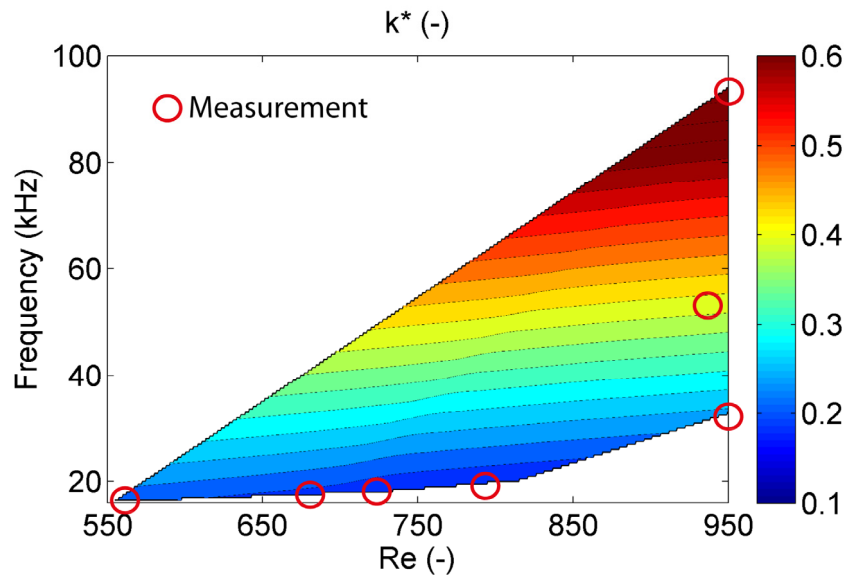


Fig. 75. Map of the non-dimensional wave number k^* as a function of the frequency f and Re for operating points with drop-to-drop jitters below 20%. The lowest generated non-dimensional wave number is 0.18. The measurements are used to generate an interpolated map of non-dimensional wavelength k^* .

Droplet timing jitter is quantified using the laser beam and photodiode setup, which is described in Sec. 3.2.1.2. A typical voltage signal, as recorded from the photodiode for a constant excitation frequency is presented in Fig. 76. The droplets, which cross the laser beam, induce a decrease in the light intensity on the photodiode. The raw photodiode signal needs processing before the timing jitter can be derived.

First, lateral displacements of the droplet stream can lead to unwanted intensity changes on the photodiode and thereby falsify the spectral results. Lateral displacements are frequently observed on the droplet train, as described in Sec. 0. If the jet moves off the laser beam in a given frequency window, the amplitudes of the photodiode signal are underpredicted in the corresponding frequency spectrum. The droplet timing jitter might however remain unchanged in case of lateral motion of the droplet stream.

Secondly, due to the low sampling frequency of the data acquisition system of 200 kHz, the resolution of the droplet traces is coarse. In order to compensate for these effects, the shape of the droplet trace is reconstructed by adding two lines. One line crosses two measurement points on the left of the expected local minimum. The second line crosses two data points on the right. Then, the local minimum of each droplet trace is computed as the intersection of the two lines. The droplet center is then assigned to this computed local minimum. The processed photodiode signal, which contains only information about the droplet center, is shown in Fig. 76a. The signal equals zero, except at the point in time that corresponds to the passage of the droplet center. This signal is then

used to derive the droplet timing jitter by taking the timing difference between two droplet centers. The drop-to-drop time is also included in Fig. 76a. The drop-to-drop time intervals are normalized with respect to their mean value. The corresponding data points are plotted in between the data points, which correspond to the crossing events of the droplets with the laser beam. Finally, the droplet timing jitter is derived as the standard deviation of the distribution of the drop-to-drop time intervals.

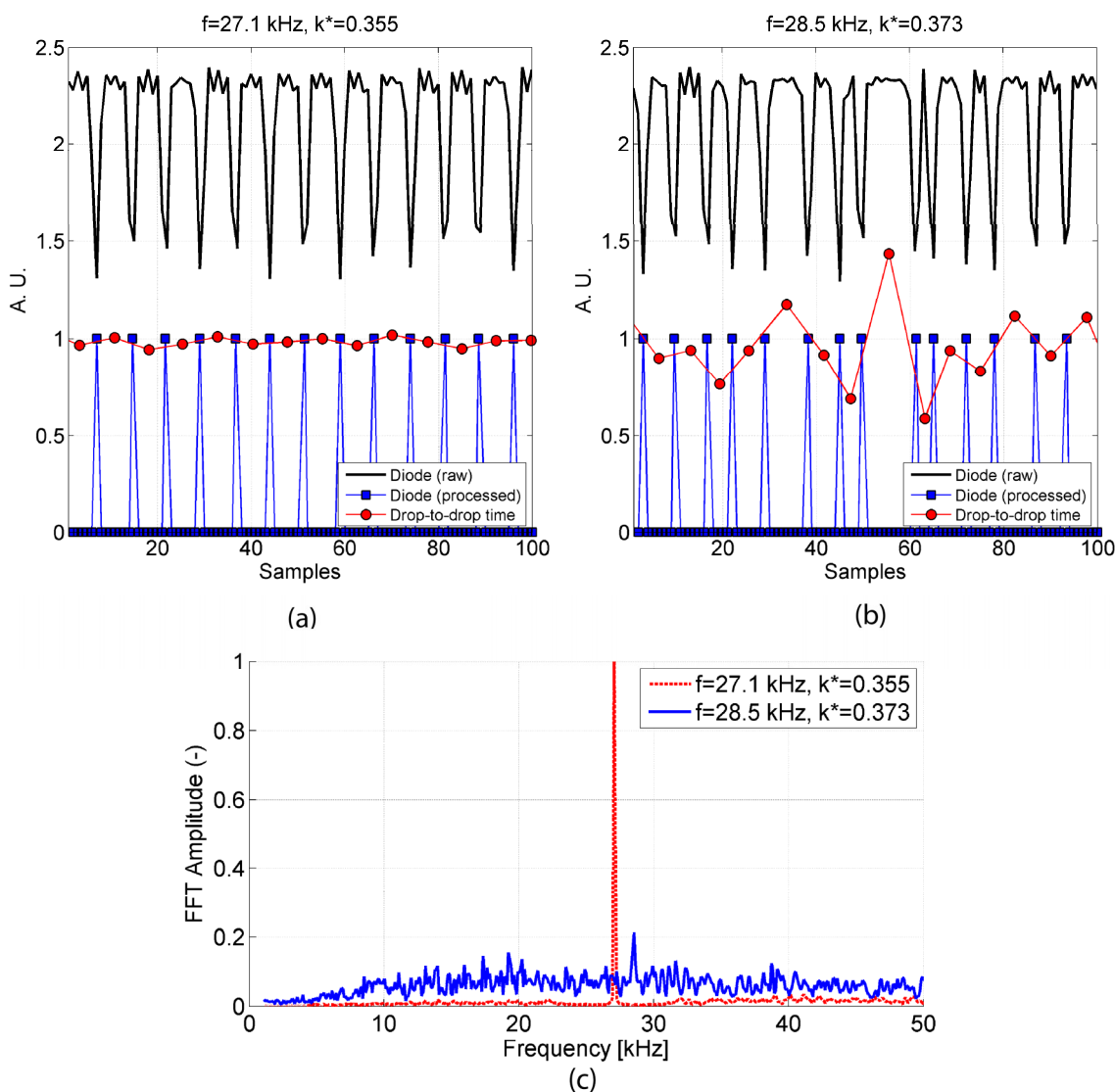


Fig. 76. Photodiode signal analysis. (a) The raw photodiode signal is processed at 27.1 kHz to derive the drop-to-drop time. The timing jitter is 5%. (b) The same signal type at 28.5 kHz reveals a strong timing jitter of 50%. (c) FFT amplitudes of the two signals reveal a dominant frequency and noise suppression for $k^*=0.355$, in comparison to the case with $k^*=0.373$.

The drop-to-drop times for a frequency of 27.1 kHz are shown in Fig. 76a. The variation of the drop-to-drop times is limited to a narrow band of 5%. On the other hand, Fig. 76b shows the recorded photodiode signal and the resulting drop-to-drop time for a frequency of 28.5 kHz. In this

case, the observed drop-to-drop times are contained in a larger band of 50% of the mean value. As a consequence, the timing jitter is one order of magnitude larger. The non-dimensional wave numbers corresponding to 27.1 kHz and 28.5 kHz are $k^*=0.355$ and $k^*=0.373$, respectively. For a variation of the non-dimensional wave number k^* (inversely proportional to the droplet spacing) of 5%, the droplet jitter varies by one order of magnitude.

The photodiode signals are also subjected to a spectral analysis using a Fast Fourier transformation. The response data is presented in Fig. 76c. The photodiode signal, which is recorded at 27.1 kHz reveals an efficient suppression of the noise in the droplet stream. Only one dominant peak is observed at the desired frequency, while the secondary peaks are two orders of magnitude smaller. On the other hand, the large timing jitter signal, which corresponds to an excitation frequency of 28.5 kHz contains only a weak trace of the excitation signal. The noise level steadily increases from 0 kHz to the range from 20 to 30 kHz and decreases slowly from 30 to 50 kHz. The causes for this strong sensitivity of the droplet jitter to the excitation frequency are investigated in the following sections.

5.4.2. Influence of the excitation pressure on droplet timing

In order to investigate the frequency and the non-dimensional wave number k^* dependence of the timing jitter, a frequency sweep of the piezoelectric actuator excitation signal with simultaneous laser-photodiode measurements is completed with the same methodology as for the pressure response measurements. The frequency sweep rate is set to the same value as for the pressure measurements. The timing jitter is calculated for each frequency window, as described in the previous section. No significant sensitivity to the window length is observed if the number of droplets per window exceeds 1000.

The measured droplet timing jitter is derived as a function of the frequency for a frequency range from 10 to 40 kHz, as shown in Fig. 77a. The equivalent non-dimensional wave number k^* is indicated on the top axis. The range of non-dimensional wavelengths extends from 0.131 to 0.524. The droplet timing jitter is normalized by the droplet velocity $v_{droplet}$ and the observation height l_{obs} . At frequencies below 17.5 kHz ($k^*=0.229$), natural breakup dominates droplet generation. The excitation frequency is being well imposed for frequencies around 19.0 kHz ($k^*=0.249$) and in the range from 22.5 kHz ($k^*=0.295$) to 27.5 kHz ($k^*=0.360$) with non-dimensionalized timing jitters in the range of 5×10^{-5} . Low timing jitter is also found around 32.0 kHz ($k^*=0.419$) and 36.0 kHz ($k^*=0.471$). The strong sensitivity of the timing jitter with respect to the excitation frequency is confirmed.

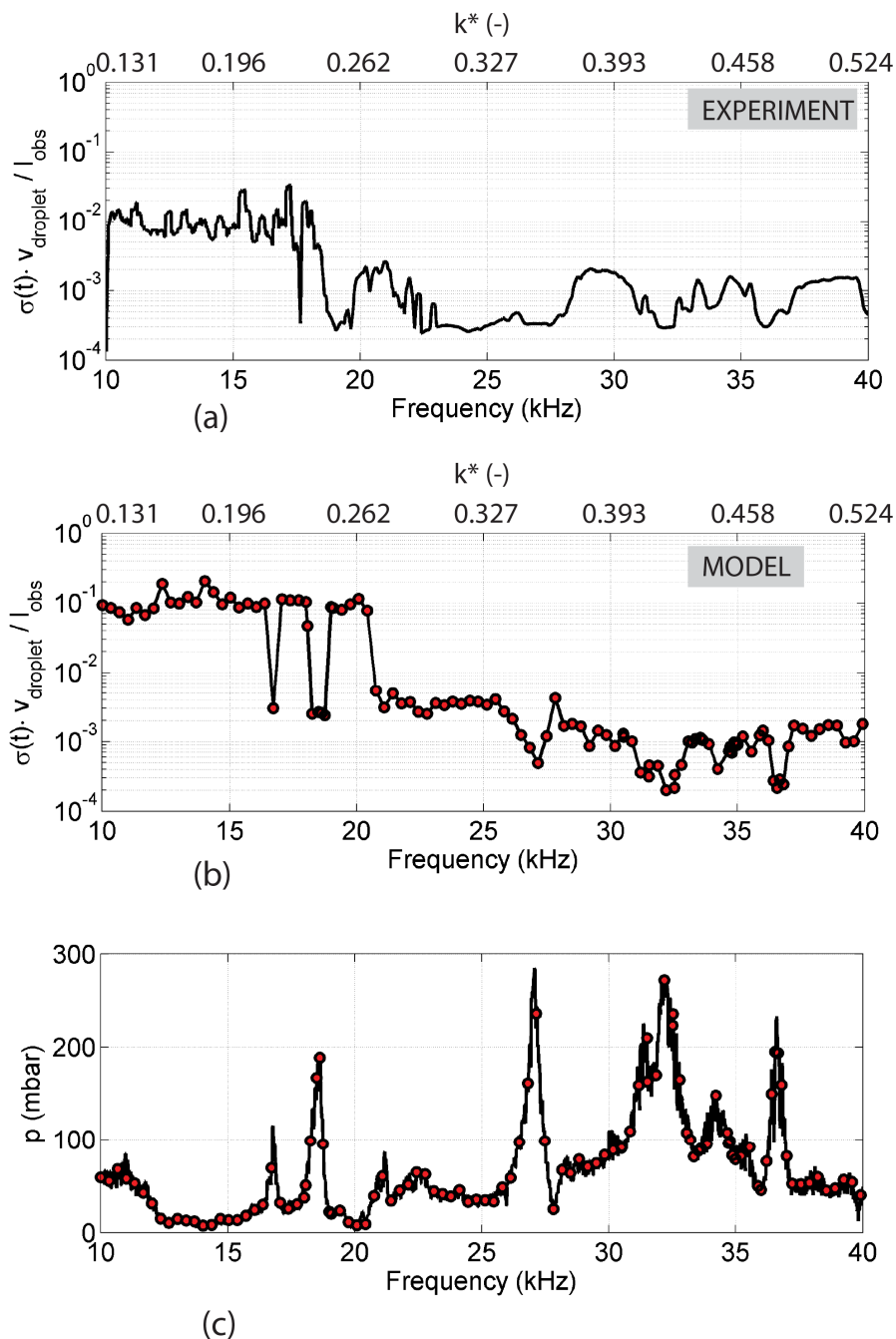


Fig. 77. Comparison of measured and modeled droplet timing jitter, as well as measured nozzle inlet pressure. (a) The excitation frequency is imposed for frequencies around 19.0 kHz ($k^*=0.249$), in the range from 22.5 kHz ($k^*=0.295$) to 27.5 kHz ($k^*=0.360$), around 32.0 kHz ($k^*=0.419$) and 36.0 kHz ($k^*=0.471$). The strong sensitivity of the timing jitter with respect to the excitation frequency is confirmed. (b) The modeled droplet jitter reproduces the trends of the measurements, especially in the frequency range from 30.0 kHz ($k^*=0.393$) to 40.0 kHz ($k^*=0.524$). A mismatch is observed from 20.0 kHz ($k^*=0.262$) to 27.1 kHz ($k^*=0.355$). (c) The specific pressure response presents discrete peaks with pressure amplitudes up to 280 mbar.

In a next step, the measured droplet timing is compared to the measured pressure response at the nozzle inlet. The pressure response, which is mainly determined by the settings of the piezoelectric actuator and the piston type is specific to the studied case and shown in Fig. 77c. Pronounced peaks, with pressure amplitudes up to 280 mbar are located at 16.8, 18.6, 27.1, 32.0 and 36.6 kHz, respectively. The droplet timing jitter, which corresponds to the pressure response at the nozzle inlet, is derived with the help of the linear droplet formation model. The piston pressure response is used as an input to the model. At discrete frequencies (red points in Fig. 77c), the timing jitter is simulated for the corresponding excitation pressure. The jet velocity, which is a major simulation input, is derived from shadowgraphs and Eq.(5.10). Another key simulation input is the noise, which is superimposed on the main excitation pressure. The noise level is adjusted in the simulation to match the computational results to the experimental data.

The modeled droplet timing jitter is presented in Fig. 77b for direct comparison with the experimental jitter of Fig. 77a. Overall, similar trends are evident. In the frequency region from 10 to 20 kHz, low droplet jitters on the order of 10^{-4} are obtained for the pressure peaks at 16.8 kHz ($k^*=0.220$) and 18.6 kHz ($k^*=0.243$). A mismatch between the experimental and modeled timing jitter is observed up to 27.1 kHz ($k^*=0.355$), where the pressures at nozzle inlet are too low to yield the low droplet jitters observed in the experiment. In the frequency range from 30.0 kHz ($k^*=0.393$) to 40.0 kHz ($k^*=0.524$), the modeled timing jitter presents the same trend as the experimental jitter. The noise level RMS, which is set in the simulation to match the experimental results, equals 0.73 mbar, hence 0.3 % of the peak pressure amplitude. A strong sensitivity of the timing jitter to the noise level is observed.

The measured timing jitter reaches low values (5×10^{-5}) in the frequency range from 20.0 kHz ($k^*=0.262$) to 27.1 kHz ($k^*=0.355$), while pressure amplitudes are relatively low. In order to exclude the linear model as the cause for mismatch, the results are reproduced with a CFD simulation at 24.5 kHz. The CFD simulation yields a timing jitter in the same range as the linear model with a deviation of 20 % from the linear model results. Therefore, the low experimental timing jitter cannot be induced by the excitation pressure only. A potential cause for regularly spaced droplet generation around 20 kHz could be found in Fig. 56. Indeed, the LDV measurements revealed increased displacements of the nozzle around 20 kHz, which might indicate an eigenmode of the nozzle around 20 kHz. As a consequence, the low timing jitter could be explained by the positive influence of the vibrating nozzle orifice on the droplet stream, while the influence of the excitation system is limited.

Droplet timing is determined by the growth rate for the non-dimensional wave number of the main perturbation. In addition, the droplet timing is also influenced by the pressure amplitude and the noise level. These effects are further investigated with the help of the linear model. The non-dimensional timing jitter is shown in Fig. 78a for noise levels of 0.14 mbar, 0.82 mbar and 1.3 mbar, respectively. The excitation pressure is kept constant at 100 mbar. As expected, the jitter decreases with decreasing noise level. Interestingly, the region with the jitter increase at low wave

numbers is shifted towards lower wave numbers with decreasing noise level. Therefore, the droplet spacing, which depends on the acceptable droplet jitter, is extended towards larger values by decreasing the noise level.

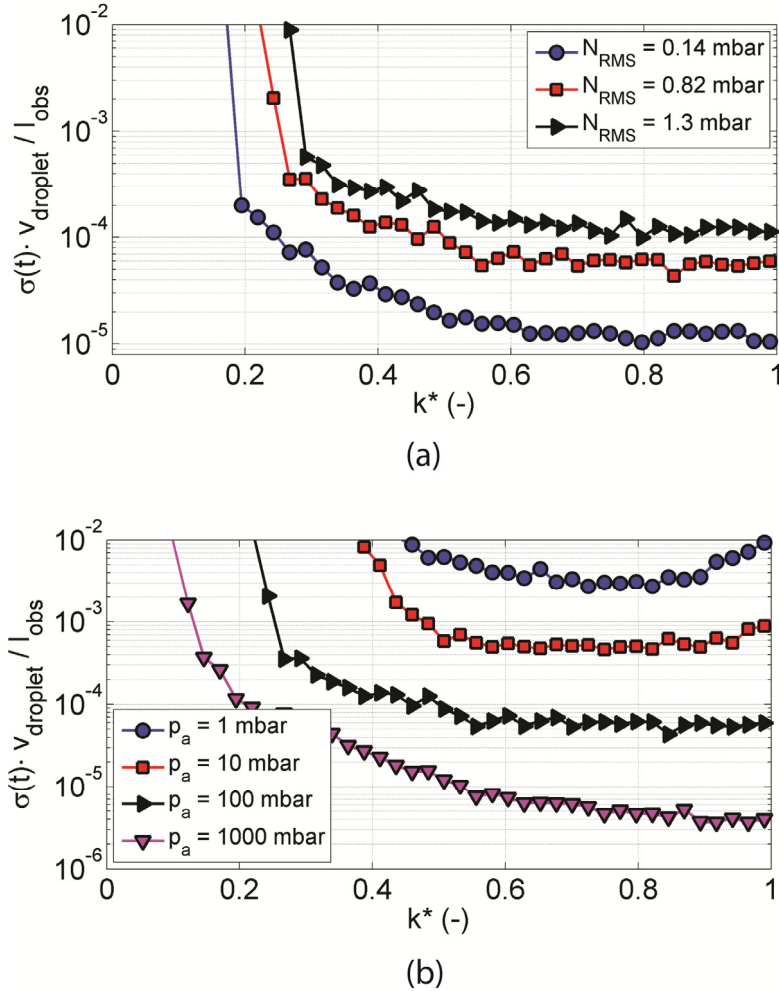


Fig. 78. Influence of pressure amplitude and noise level on droplet timing jitter. (a) At a constant pressure of 100 mbar, the influence of the noise level is quantified. A decrease in noise level lowers the timing jitter for all wave numbers and thereby extends the possible operating range. (b) Noise level is constant with $N_{\text{RMS}} = 0.82$ mbar. An increase in pressure amplitude lowers the overall timing jitter, thereby also extending the operating range.

The influence of the excitation pressure amplitude for a constant noise level of $N_{\text{RMS}} = 0.82$ mbar is shown in Fig. 78b. The investigated pressure levels are 1, 10, 100 and 1000 mbar, respectively. The increase in pressure amplitude yields lower timing jitter. The region of low droplet jitter is extended with increasing pressure amplitude towards lower wave numbers. In conclusion, large droplet spacings with low timing jitter can be achieved by decreasing the noise level on the jet and by maximizing the pressure amplitude at the desired operating point.

5.4.3. Prediction of operating boundaries

The linear model is used in the previous section to predict the general trends of the sensitivity of the timing jitter to the excitation pressure and noise level. For a more accurate prediction of the operating boundaries at low wave numbers, CFD simulations are employed. The simulation setup is described in Sec. 5.2.2. The experimentally determined noise level is integrated in the pressure excitation.

In order to validate the use of the computational tools for droplet modeling, the simulated droplet train is first compared to a typical shadowgraph of a baseline experiment, as shown in Fig. 79. The excitation frequency is 20 kHz and the jet Reynolds number is 690. The droplet diameter and spacing deviations between experiment and CFD are 9% and 3%, respectively.

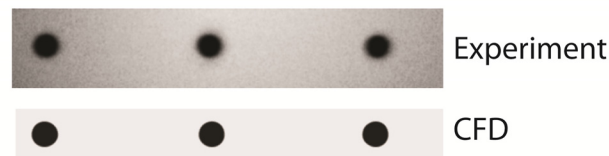


Fig. 79. Comparison of numerically generated droplet train with experimentally recorded droplet at $f=20$ kHz and $Re=690$.

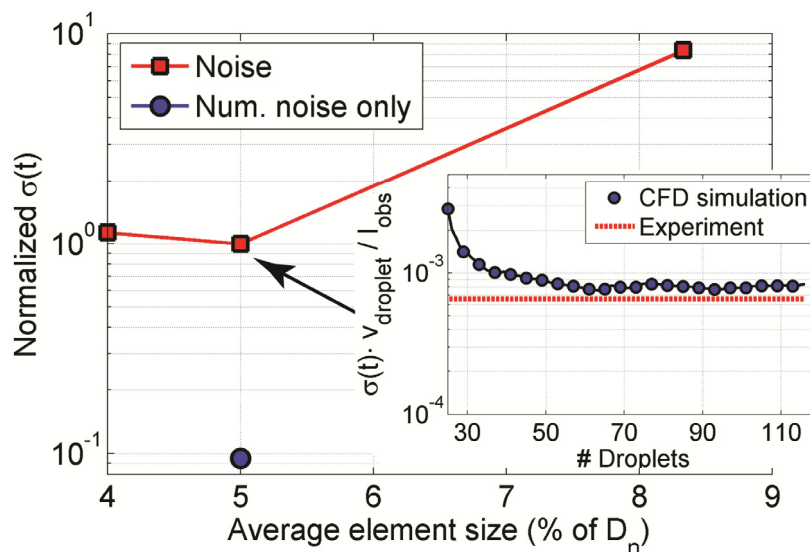


Fig. 80. Timing jitter sensitivity to average mesh element size. For a mesh element size of 5%, the timing jitter is mainly influenced by the specified experimental noise. The noise due to discretization is one order of magnitude smaller. The additional plot shows the convergence of timing jitter with the number of simulated droplets for the medium size mesh. The timing jitter difference between the CFD results and the experimental measurements is 20%.

A major challenge in the CFD simulations is the ability to model the noise level of the experiment. Indeed, the numerical noise due to discretization is required to be significantly smaller than the

measured noise. The timing jitter, which is evaluated for three different meshes, is strongly sensitive to the average element size of the computational mesh, as presented in Fig. 80. For the medium resolution mesh with an average element size of 5% of the nozzle diameter, the timing jitter is mainly influenced by the experimentally determined noise. For the same mesh, the numerical noise is one order of magnitude smaller than the total jitter, which includes the experimental and the numerical noise. Therefore, the medium resolution mesh has been used in the simulations of this section.

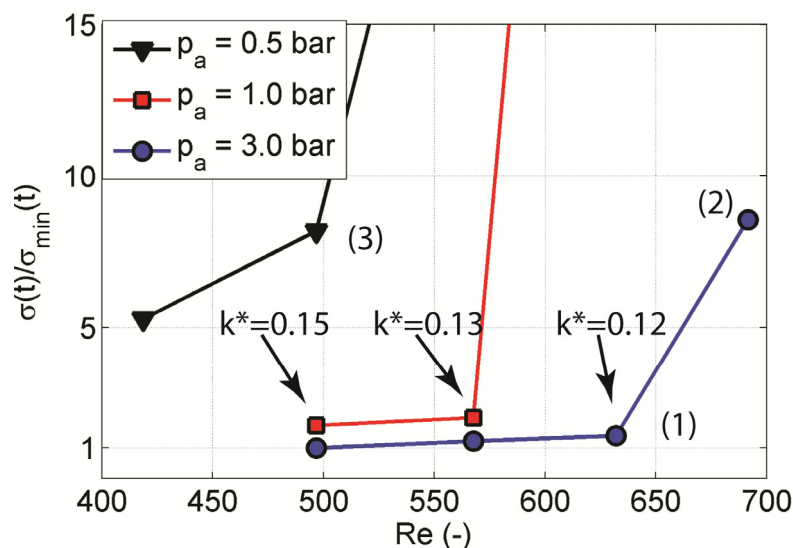


Fig. 81. Non-dimensional timing jitter as a function of Reynolds number. Increasing the acoustic pressure results in lower timing jitter.

For validation purposes, the simulated timing jitter is compared to the results from the experiment. As described in Sec. 5.2.2, the timing jitter is determined at the monitor point at the lower end of the computational domain, where the passing droplets are recorded. The additional plot in Fig. 82 presents the history of the timing jitter as function of droplet number for an excitation frequency of 32 kHz. The pressure amplitude in the CFD simulation is taken from the measured pressure response. The timing jitter is converged to within 10% after 60 droplets. The comparison of the converged timing jitter with the experimental value yields a difference of 20%.

The validated simulation environment is used to study the timing jitter evolution at low wave numbers for high acoustic pressure amplitudes. For this purpose, the operating frequency of 20 kHz is fixed and the reservoir pressure, which sets the Reynolds number of the jet, is varied. The nozzle size is reduced by 50%, when compared to the experiments. The nozzle size reduction should lead to droplet sizes in the range of 30 μm . The computational studies from Sec. 6.3.3.3 predict less debris for such a droplet size. The noise level (RMS) remains unchanged at the experimental value of 0.73 mbar. The timing jitter, which is non-dimensionalized by the minimum jitter for the studied parameter set, is plotted in against the Reynolds number for acoustic pressures, which

range from 0.5 to 3 bar. The lowest simulated non-dimensional droplet jitters are on the order of 10^{-4} . The Reynolds number is averaged over the jet cross-section after relaxation. Similarly to the predictions of the linear model, the timing jitter decreases with increasing acoustic pressure. Furthermore, the point of steep increase of timing jitter is shifted towards lower wave numbers. The lowest simulated wave number $k^*=0.12$ is found at $Re=632$ for an acoustic pressure of 3 bar. The corresponding droplet spacing equals 7 droplet diameters.

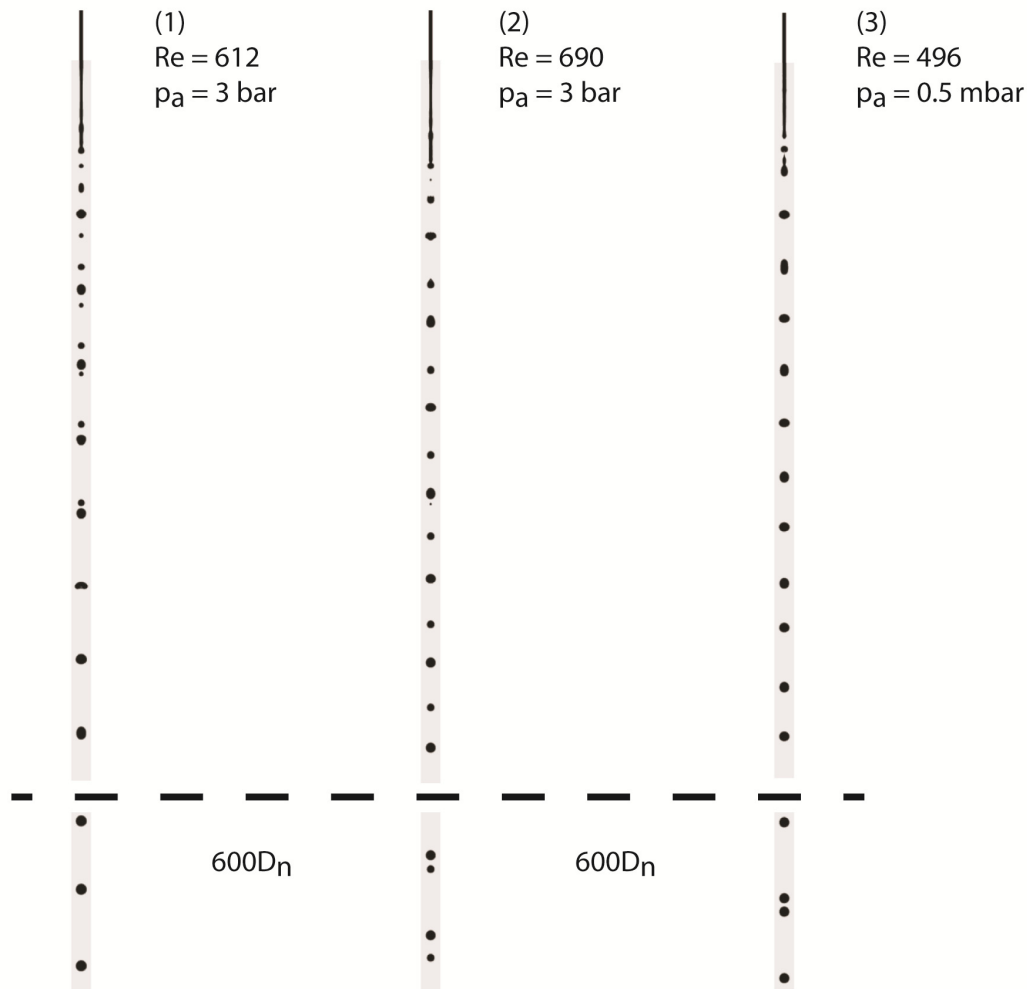


Fig. 82. Droplet breakup and train structure for limit cases of k^* . For point (1), satellite formation with subsequent merging and low timing jitter. Satellite formation is also observed for point (2), with large resulting timing jitter and no merging within computational domain. For point (3), single droplets of different sizes and velocities are generated and the resulting structure has large timing jitter.

Finally, the details of droplet formation, including jet breakup, are shown in Fig. 82 for the three cases, which are marked in Fig. 81. First, point (1), with a low timing jitter and low wave number, is characterized by the formation of one main droplet and two satellite droplets for one excitation wavelength. Firstly, the main droplet coalesces with the satellite droplet in front, before merging

with the droplet at the back. These satellites are so-called forward and backward merging droplets.⁹⁶ The merged droplets form a regularly spaced stream. Merging is due to velocity dispersion, which is described by Eq.(5.9). At point (2), where the perturbation wavelength is further increased, a main droplet and a single satellite are formed. The merging is not captured within the computational domain with a length of $600 D_n$. The droplet stream is less regularly spaced at $600 D_n$ than the stream of point (1). At point (3), the typical case of high timing jitter is presented. Large droplets of different sizes form and their different velocities result in irregular spacing at $600 D_n$. This state is undesirable in LPP-based light sources. The influence of the excitation pressure is limited and the droplet train has a non-deterministic structure. Indeed, the amplitude of the pressure signal cannot compensate for the reduced growth rate at these low wave numbers. The droplet train structure is determined by noise, which contains contributions at larger growth rates than the main signal.

5.5. Summary and conclusion

The correlation between the perturbation (i.e. the measured nozzle inlet pressure) and the resulting droplet train characteristics is studied. Droplet shadowgraphs are used to determine the average droplet diameter and spacing, while a laser beam, which is focused onto the droplet train and aligned with a photodiode, helps to quantify the timing jitter. The lowest experimentally measured wave number equals 0.18. These experiments reveal a strong sensitivity of the droplet timing to the excitation wave number. Therefore, a sweep of the excitation frequency is completed with simultaneous measurements of droplet timing. The corresponding pressure signal is used as an input to a linear droplet formation model to predict the droplet timing. The excitation pressure and a noise contribution term are modeled. Both experimental and numerical results follow similar trends. A noise level (RMS) of 0.3% of the peak pressure amplitude is derived. The influence of the pressure amplitude and noise level on the droplet train structure is numerically investigated. Large excitation pressures and a low noise level lower the timing jitter and extend the operating range towards lower wave numbers, hence larger droplet spacings.

Droplet timing at low wave numbers is investigated as a function of excitation pressure with the help of CFD simulations. The source requirement is to achieve large droplet spacings with a minimum droplet jitter. The mesh element size must be chosen to be small enough for the simulations to yield the experimentally measured noise level. The lowest simulated wave number is 0.12 at an excitation pressure of 3 bar. With decreasing wave number, the growth rate of the main excitation decreases. On the other hand, noise contributions with wave numbers with higher growth rates dominate and lead to a non-deterministic structure of the droplet train. This effect can be delayed by maximizing the acoustic pressure and lowering the noise level.

In conclusion, the requirements for operation in a laser plasma source are best fulfilled when the dispenser excitation system is tuned to generate high acoustic pressures at the desired operation frequency and when the noise level on the jet is limited. The jet velocity is then adjusted by varying

the reservoir pressure in order to find the optimum droplet stream wave number, according to the trade-off between lowest wave number and acceptable timing jitter.

Chapter 6

Numerical modeling of droplet-based laser-produced plasmas

In the first part of this chapter, the numerical tools, which are essential to predict the debris and emission characteristics of the tin droplet-based LPP, are presented. Firstly, the most relevant physical processes in LPPs are outlined. Secondly, the multiscale modeling tools are described. A hydrodynamic code, which is extended with a radiation transport model, is coupled to an atomic physics code for modeling the initial stages of the LPP formation and expansion. As the plasma plume expands and the degree of rarefaction increases, a hybrid hydrodynamic- particle code is applied to predict the debris dynamics up to the EUV collector. The impact of the previously measured droplet characteristics on the LPP is studied in a set of parametric studies.

6.1. Physical processes in laser-produced plasma

In this section, the main physical processes involved in the creation and evolution of the tin based EUV plasma are detailed. High power laser pulse interactions, with intensities above 10 GW/cm^2 , vaporize the tin target. The laser pulse then couples into the plasma and induces the ionization of the plume. The plasma temperature and the mean ionization level are set by tuning the laser

irradiance. The ion populations, together with the most probable atomic energy transitions set the emission characteristics. The radiation emitting ions, the tin vapor and the potential droplet fragments form plasma debris. Debris limits the lifetime of the collector optics by either eroding the reflective multilayers or by depositing onto the collector surface.

6.1.1. Laser coupling into matter and plasma formation

In the case of the nanosecond laser pulses, which are used in EUV or soft X-ray sources, the incident laser pulse increases the surface temperature of the target material. Indeed, free electrons, which result from multiphoton absorption, are accelerated by the electromagnetic field of the laser wave. The kinetic energy of these free electrons is transferred by collisions to the lattice atoms, thereby increasing the temperature of the target. Photon absorption occurs up to the skin depth.¹⁷⁷ At the start of the laser pulse, a significant part of the incident laser energy is reflected. As the thermal diffusivity of the target material is low in comparison to the nanosecond time scales of the laser pulse, only a very limited layer thickness ($\sim 1 \mu\text{m}$) of target material is heated. The resulting vapor atoms leave the liquid-vapor interface, with velocities normal to the target surface. After a few mean free paths, the vapor atoms reach an equilibrium velocity distribution at the exit of a thin region called the Knudsen layer.¹⁷⁸ Outside this layer, the flow regime can be considered as a continuum and the velocity field becomes isotropic. The ablated vapor is transformed into a plasma by additional laser energy absorption.

In EUV plasmas, the main coupling mechanism of laser energy transfer into the plasma is *inverse bremsstrahlung absorption* (IBA). Electrons are released from the ion potential field by photoionization. The resulting ions and electrons oscillate in the electromagnetic field of the laser wave. Ion oscillations can be neglected due to the relatively large mass of ions, while electrons gain kinetic energy. Elastic collisions between electrons and ions result in a conversion of electron kinetic energy into thermal energy of the plasma. Inelastic collisions between these electrons and atoms / ions lead to collisional ionizations. The absorption coefficient of IBA (in units of m^{-1}) has been determined by Johnston *et al.*¹⁷⁹ to be

$$\alpha_{IB} = \frac{13.49}{\lambda_0^2} Z \left(\frac{n_e}{n_c} \right)^2 \frac{\ln \Lambda}{\sqrt{1 - n_e/n_c}} \frac{1}{T_e^{3/2}} \quad (6.1)$$

where λ_0 is the laser wavelength, Z is the mean ionization, n_e is the plasma electron density, n_c is the critical density, T_e (K) is the plasma electron temperature and $\ln \Lambda$ is the Coulomb logarithm. The critical density n_c can be written in S.I. units as follows¹

$$n_c (\text{cm}^{-3}) = \frac{1.12 \cdot 10^{21}}{\lambda_0^2 (\mu\text{m})} \quad (6.2)$$

The Coulomb logarithm $\ln \Lambda$ in S.I units equals

$$\ln \Lambda = \ln \left(1.55 \cdot 10^{13} \frac{T_e^{3/2}}{Z n_e^{1/2}} \right) \quad (6.3)$$

Absorption by inverse bremsstrahlung takes place for electron densities below the critical density, as seen from Eq. (6.1). For electron densities above the critical density, laser light is reflected. The critical density only depends on the laser wavelength, with values of 10^{19} cm^{-3} for the CO_2 laser and 10^{21} cm^{-3} for the Nd:YAG laser. For plasmas produced by nanosecond laser pulses, time scales are long enough for the electron density to drop below the critical density during the expansion of the plasma plume, hence laser energy can be coupled into the plasma. The absorption is more efficient at higher electron densities and ionization levels. If the electron density approaches the critical density, resonant energy transfer between the laser pulse and the plasma takes place.

The efficiency of laser energy coupling into the plasma depends not only on the absorption level, but also on the overlap of the laser beam with the plasma plume and the reflection at the vacuum-plasma interface. Indeed a jump in refractive indices, which is for example observed at the plasma-vacuum interface, leads to a partial reflection of laser light.¹⁸⁰

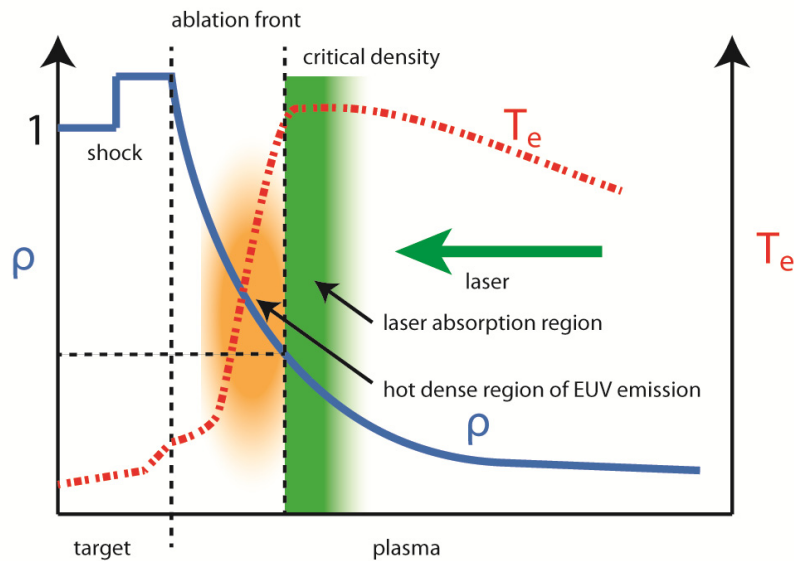


Fig. 83. Overview of the density and temperature profiles at the target surface. The hot dense region of EUV emission is located at the surface of critical density, where laser light is reflected completely.

While the plasma is heated by the incident laser beam, the mean ionization and the electron density increase up to the critical density, as shown in Fig. 83. Above the critical density, laser energy is reflected and the target is shielded from the laser. As a consequence, the target material heating is reduced. The cooling of the plasma core, which is due to expansion and radiation losses, as well as conductive heat transfer, decreases the electron density up to the point of efficient

absorption. This effect helps to stabilize the plasma parameters below the critical density. The vaporization of target material is maintained during plasma shielding of the laser beam. Firstly, radiative heating of the target surface by the plasma takes place. Secondly, a heat flux, which is set by the ion and electron thermal conductivities and the plasma temperature, increases the target surface temperature. This pronounced heat flux is in some cases also responsible for the location of the high temperature region behind the critical surface.²

6.1.2. Radiation emission

The absorption of laser energy near the critical density leads to the formation of a region of high temperature. The plasma temperature is set by the irradiance of the incident laser beam. Plasmas, especially if at high density, can sometimes be modeled as Planckian black-body radiators. However, a LPP of high atomic number is typically not in local thermodynamic equilibrium (LTE).^{35, 124} For typical EUV plasma parameters (tin, Nd:YAG laser), Poirier *et al.*³⁵ determined a lower threshold electron density of $6.8 \times 10^{20} \text{ cm}^{-3}$. As the corresponding critical density is in the order of 10^{21} cm^{-3} , LTE is typically not fulfilled in the major part of the plasma plume.

A laser plasma has a wavelength dependent opacity, as opposed to the fully opaque black-body. Indeed, thermal radiative equilibrium would imply that the number of photons emitted per unit time, volume, solid angle and frequency is equal to the number of absorbed photons. The departure from LTE implies that the local kinetic temperature is not equal to the Planckian temperature of the radiation. In the so-called non-LTE regime, apart from electron collisions, additional processes like radiative deexcitation and photoelectric/ recombination processes become important. If the time scales of the laser plasma ($\sim 1 \text{ ns}$) are larger than the ion-electron relaxation time ($\sim 10 \text{ ps}$), the so-called collisional radiative regime is established.¹

The radiation emitted or absorbed by a LPP is highly complex and consists of the sum of three different contributions, namely (i) the bound-bound (bb) contributions, (ii) the bound-free (bf) contributions and (iii) the free-free (ff) contributions. The bound-bound contributions result from the discrete electronic transitions in atoms. This results in emission and absorption at discrete energies. The bound-free contributions result from photoionization and photorecombination. Energy transitions from electrons, which either leave or return to the bounded states of the atom, can have any energy level. The bound-free emission yields a continuous emission or absorption spectrum. Finally the free-free contributions result from a free electron being either accelerated or slowed down in the potential field of an ion or neutral atom. This process, which is called *Bremsstrahlung*, yields continuum emission and absorption spectra.

Of all three mechanisms, line emission or absorption are the most important processes in laser plasmas of high Z elements. Experimental EUV spectra typically have pronounced line features, as shown in Sec. 6.3.1.2. As the number of potential ion stages increases, the spectra become very complex due to the increasing number of closely spaced line emissions. Spectral lines have a finite

width. One common type of line broadening is Doppler broadening, which is due to the finite thermal velocity of the emitting ions.

The emission from a plasma is determined by radiation transport inside the multi-dimensional heterogeneous plasma plume. The final emission at a given frequency along a line of sight is governed by emission and absorption along the line. Indeed, the plume has a finite optical thickness, which is defined by

$$\tau = \int_0^l \kappa dx \quad (6.3)$$

where $\kappa(\text{cm}^{-1})$ is the macroscopic absorption or opacity coefficient and l is the integration path along the line of sight. A plasma is qualified to be optically thick when $\tau \gg 1$ and optically thin if $\tau \ll 1$. The total opacity is the sum of the absorption and the scattering opacity. The total opacity relates to the average photon mean free path, which corresponds to the travel distance between an absorption or a scattering event. Scattering does not remove photons from the plasma, but redistributes the propagation angles and possibly the frequencies of single photons, while the integrated values are not affected. Typically, low optical thickness is desired, in order not to reabsorb the in-band photons, which are produced in the hot plasma core. Along with the generation efficiency of in-band photons, the efficiency of the radiation transport has a major impact on CE. At the considered electron temperatures, radiation transport is an important energy loss mechanism, which influences the plasma properties, such as electron temperature and density. It therefore plays therefore an active role in the hydrodynamic evolution of the plasma plume.

6.1.3. Debris formation, propagation and damage potential

In a LPP light source, laser energy is not only converted into radiation with different wavelengths, but also into kinetic energy of particles. Indeed, a significant pressure gradient develops between the high temperature and high density plasma and the vacuum environment. The pressure difference leads to a rapid expansion of the plume into vacuum. In the case of a Nd:YAG laser, the induced pressure is in the range of $p = nk_b T \approx 10^9$ Pa for a plasma temperature $T_i = T_e = 30$ eV and a number density $n = 10^{21}$ cm⁻³. Vacuum pressures are typically smaller than 10 Pa. During the expansion, thermal energy is transformed into kinetic energy. As long as the laser beam irradiates the plasma, the expansion is not adiabatic. The electron-ion thermal expansion velocity is approximately equal to the ion acoustic velocity

$$v_{\text{exp}} \approx \sqrt{\frac{Z\gamma k_b T_e}{M_i}} \quad (6.4)$$

where T_e and Z are the ion temperature and mean charge, respectively. M_i is the ion mass and γ the ratio of specific heats, which equals 5/3 in the atomic case. For a tin plasma with a typical electron

temperature $T_e = 30 \text{ eV}$ and an ionization of $Z=10$, the expansion velocity is on the order of 20 km/s. Due to radiation losses and expansion work of the plasma plume, the kinetic energy of ions is however decreasing during expansion, especially during the first nanoseconds after the peak laser intensity.

As the plasma expansion into vacuum continues, the density in the plasma plume decreases. As a consequence, the frequency of particle interactions within the plume decreases. The departure from the collisional equilibrium at high densities is quantified by the Knudsen number $Kn = \lambda/L$, where L is a characteristic length scale, typically the plume size and λ equals the ion mean free path. In case of a full vaporization of a 50 μm tin droplet, the particle number of the plasma plume will not increase the pressure in the vacuum chamber. For a chamber volume of 1 m^3 , the difference in particle number is 6 orders of magnitude. The mean free path in a vacuum system at pressures below 10 Pa is typically smaller than 1 mm. Ionizations and higher temperatures would further increase the mean free path. Therefore, Knudsen numbers easily exceed 0.1 during the expansion up to the collection optics. As a consequence the flow regime transitions from continuum to rarefied during the expansion of the LPP.¹⁸¹

As the ions reach the multilayer surface, sputtering of lattice atoms takes place. The sputtering yield, which gives the average number of atoms ejected from the target per incident ion, depends on numerous parameters of both the incident ion and the target itself. For the impinging ions, the sputtering yield is a function of the ion energy, the angle of incidence and the ion mass. The target parameters include the mass of the target atoms, the surface and lattice binding energies and the displacement energy of the target. The frequency of ion impact determines the sputtering rate of the multilayers and finally the life-time of the collection optics.

The incomplete ionization of the supplied target material under the action of the incident laser beam yields material that is either vaporized or stays in the solid or liquid phase. The vapor expansion is associated with smaller time scales than those of the ion expansion, due to the lower temperature of the vapor. However, the vapor, if not mitigated reaches critical components, such as the collection optics and condenses on the cold surfaces. The vapor also increases the optical thickness around the target irradiation site, thereby reducing EUV emission.

A third kind of debris results from droplet fragmentation. In the case of planar targets⁴³ or large droplets irradiated by smaller laser spots¹⁸², droplet fragments form at the border of the irradiated region. For solid targets, a pool of liquid metal forms at the surface of the target. For the typical case of EUV sources, namely when both the droplet and the laser spot have similar sizes, the ablation pressure wave is expected to yield fragmentation of the droplet. The tin fragment formation has been studied for tin droplets when irradiated by a low power Nd:YAG laser.⁵⁵ The liquid metal pool of the planar target or the droplet target interacts with the recoil pressure wave from the expanding

plasma plume. This interaction leads to the formation of macroscopic (typically micrometer sized) droplet fragments.¹⁸³ Droplet fragments deposit on the collection optics.

6.1.4. Multi-scale considerations

The physical processes, which govern the formation and expansion of a laser plasma, are related to a large range of time and length scales. Ablation takes place on the micrometer length scale, with characteristic length scales of the plasma being a fraction of the micrometer droplet and laser spot sizes. The smallest length scales include, for example, the Knudsen layer or the ablation layer. As the plasma expands up to the collection optics, the relevant length scales go up to several 100 mm. The time scales extend from tens of picoseconds for the electron-ion relaxation times³⁴ to the nanosecond laser pulse duration, before reaching several microseconds for the plasma expansion. The variety of length and time scales results in a major challenge for accurate numerical modeling.

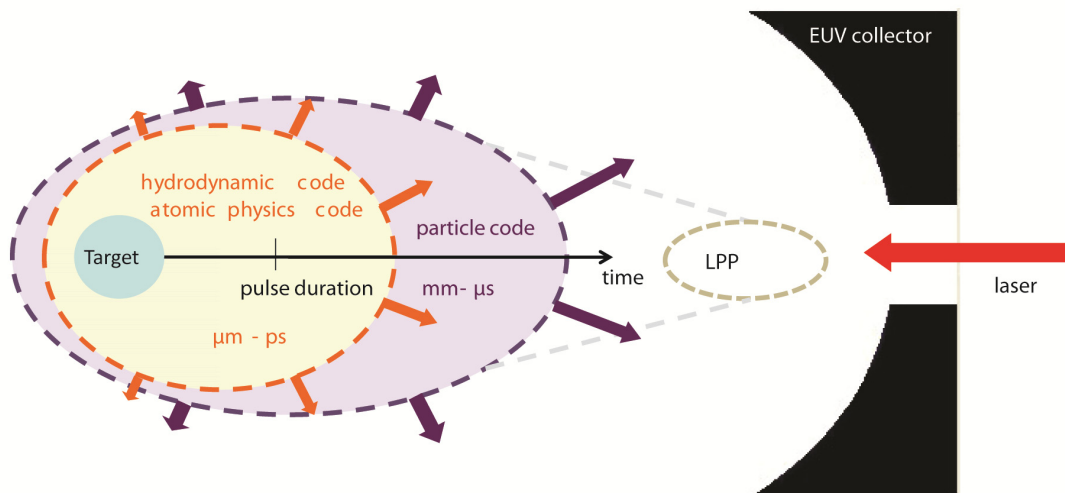


Fig. 84. Overview of the numerical tools for LPP modeling and their range of application. The strong variation of time and length scales during the evolution of the plasma plume defines the need for a hybrid hydrodynamic and particle code approach.

6.2. Numerical modeling

The expansion of the laser-plasma plume is a multi-scale problem. The differences in length and time scales require a particular computational treatment. The early stages of the laser-plasma interaction, which include the laser-target interaction and plasma formation are simulated using a typical plasma modeling approach, which consists of a two-dimensional axisymmetric or planar radiation hydrodynamic (RHD) code. The simulation time of the RHD code is limited to a few multiples of the laser pulse duration. The atomic physics code HULLAC is used to support the radiation predictions of the high temperature (>10 eV) plasma. During the plasma expansion, the density decrease in the plume yields a rarified flow, which can no longer be modeled by a

continuum approach. In this work, the approach is to combine a Particle-In-Cell (PIC) method and Direct Simulation Monte Carlo (DSMC) code into a quasi-neutral PIC-DSMC model so as to model the rarified flow. Boundary conditions are provided by the RHD code, while both codes are running in parallel in a hybrid approach. This allows the simulation to be extended up to the optics' length scale. An overview of the software package with the simulated portions of the plume is presented in Fig. 84. Code details are presented in the subsequent sections.

6.2.1. Radiation hydrodynamic code

Up to the critical degree of rarefaction ($Kn \sim O(0.1)$), the hydrodynamic expansion of the plasma plume is modeled by a radiation hydrodynamic code (RHD). The most relevant physical processes regarding target vaporization, laser energy absorption, plasma ionization, hydrodynamic expansion and radiation transport (with more details in Sec. 6.1) are included in the RHD code. The core of the code consists of the three governing equations of continuity, momentum and energy. The exact forms and solution techniques are presented in the next section. Then, Sec. 6.2.1.2 describes the sophisticated equation of state, which is required to model the multiple phases, including the highly complex plasma phase. The implementation of a detailed radiation transport model, which is essential in order to accurately predict the emitted radiation and ion energies, is described in Sec. 6.2.1.3.

The core of the RHD code has been developed over a few decades at the University of York by the group of Prof. Pert under the name of POLLUX.¹⁸⁴ The included analytical equation of state originates from Thompson *et al.* from Sandia Labs.^{185, 186} Several specific adaptations, which include the full development of a radiation solver, have been completed in the context of this work for modeling EUV laser-produced plasmas.

6.2.1.1. Hydrodynamic model

The differential equations governing the flow of an inviscid and compressible fluid are based on the conservation of mass, momentum and energy. These equations determine the state of the fluid, together with auxiliary equations. The laws of conservation for mass and momentum can be written as

$$\frac{D\rho}{Dt} + \rho \nabla \cdot \underline{v} = 0 \quad (6.5)$$

$$\rho \frac{D\underline{v}}{Dt} + \nabla p = 0 \quad (6.6)$$

where ρ , \underline{v} and p denote the density, velocity vector and pressure, respectively. $\frac{D}{Dt} = \frac{\partial}{\partial t} + \underline{v} \cdot \nabla$ corresponds to the total derivative. The code employs a two-fluid model for ions and electrons. This splitting into ions and electrons does not require the two species to be in thermodynamic

equilibrium. While the mass density ρ is set by the ion mass density, the pressure p is equal to the sum of both ion and electron pressures. The hydrodynamic velocity v is assumed to be equal for both species. The two energy equations for ions and electrons can be written as:

$$\frac{De_e}{Dt} = -p_e \nabla \cdot \underline{v}_e + \nabla k \nabla \frac{e_e}{c_{v,e}} + Q_{las} + Q_{rad} \quad (6.7)$$

$$\frac{De_i}{Dt} = -p_i \nabla \cdot \underline{v}_i + \nabla k \nabla \frac{e_i}{c_{v,i}} \quad (6.8)$$

where e_e and e_i are the energy densities of electrons and ions, respectively. The specific heat is denoted by c_v . Besides the volume work and the thermal diffusion terms, the electron energy equation has two additional source terms. The term Q_{las} corresponds to the absorbed laser power by IBA, while Q_{rad} is the radiation source term, which will be detailed in Sec 6.2.1.3.

The solution of the governing equations is treated in their Eulerian form with a finite-difference scheme. Although the code possess the capability of quasi-lagrangian rezoning,¹⁸⁷ this feature has not been systematically used. Indeed no evolutionary mesh is necessary, as the uniform (and structured) mesh dimensions and resolutions are in general sufficient to handle plasma plumes with the densities and temperatures of the current work.

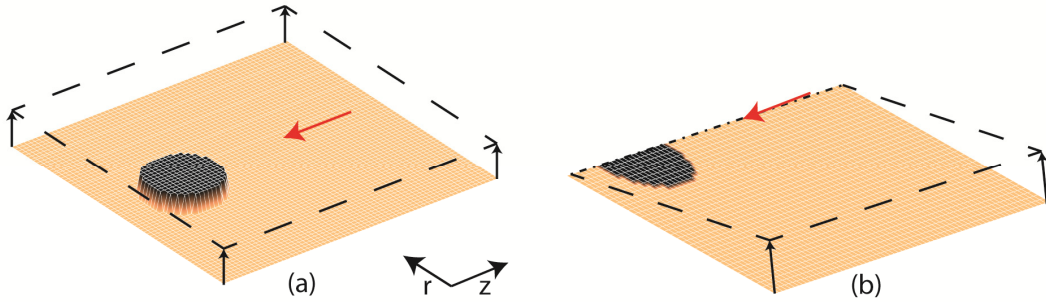


Fig. 85. Domain types simulated in RHD code. (a) The planar domain with unit height contains the full droplet. (b) The axisymmetric domain, with unit angle extension in the third dimensions, includes half of the droplet. The red arrow represents the laser direction. The direction of the laser is termed “axial” (z -coordinate) and the direction perpendicular to the laser termed “lateral” (r -coordinate).

The code works in two-dimensions, with the capability to simulate an axisymmetric (with unit angle) or planar (with unit height) domains, as shown in Fig. 85. The axisymmetric or cylindrical domain possesses three open outflow boundaries and a reflective boundary condition at the symmetry axis. The standard case of laser droplet interaction is studied in this type of domain. The planar domain is used to study the inherent three-dimensional problem of droplet and laser misalignment. The four boundaries of the planar domain are open outflow boundaries.

Numerical schemes for the solution of the coupled equations of hydrodynamics must be conservative and ensure monotonicity and positivity of positive definite variables. Simple central difference advection schemes give strong numerical dispersion, especially in regions of large gradients of the advected quantities. Non-physical ripples and locally negative values for positive definite quantities (mass and energy) may occur.

The solution is computed using the donor cell form of Gentry *et al.*¹⁸⁸ Initial values of density, velocity and specific internal energy are assigned as initial conditions to each mesh cell. The values of the flow quantities advance in time by finite differencing. Two steps are used in the explicit time advancement cycle. Firstly, intermediate values are calculated for the velocity and the specific internal energy. This step is often termed the Lagrangian phase. Secondly, the flow quantities are advected in the transport step. For example, the intermediate velocity values, which are computed during the Lagrangian phase from the acceleration by the pressure gradients across cells, are used to derive the mass flow across cell boundaries during transport step. The flows of momentum and energy are then computed by assuming that the mass flux carries momentum and energy corresponding to the intermediate values of velocity and energy of the donor cell. The approach is illustrated for the axial velocity component u_{ij} in a cell (i,j) for the time advancement from $n \delta t$ to $(n+1) \delta t$.

Step 1: Using the equation of state, the pressure p_{ij}^n is computed in each cell from the specific internal energy e_{ij} and density ρ_{ij} . The tilde denotes intermediate time values.

$$\tilde{u}_{ij}^n = u_{ij}^n - \frac{\delta t}{\rho_{ij}^n S_z} [p_{i+1/2,j}^n - p_{i-1/2,j}^n] \quad (6.9)$$

where S_z is the interface surface area between the cells and $p_{i+1/2,j} = 1/2(p_{ij} + p_{i+1,j})$. The pressure term p_{ij}^n can be extended by an artificial viscosity correction term in order to enhance stability. An example is the pressure correction by *Pert.*¹⁸⁷

Step 2: In the transport step, the mass fluxes across cell boundaries are computed by the donor cell method. For example, the mass flux across the right boundary of the cell (i,j) equals

$$\begin{aligned} \Delta M_{i+1/2,j}^n &= S_z \rho_{i,j}^n \tilde{u}_{i+1/2,j}^n \delta t \\ &= S_z \rho_{i+1,j}^n \tilde{u}_{i+1/2,j}^n \delta t \end{aligned} \quad (6.10)$$

The density in the cell is derived from conservation of mass as follows

$$\rho_{i,j}^{n+1} = \rho_{i,j}^n + \frac{1}{V_j} (\Delta M_{i,j-1/2}^n + \Delta M_{i-1/2,j}^n + \Delta M_{i,j+1/2}^n + \Delta M_{i+1/2,j}^n) \quad (6.11)$$

The final momentum and specific internal energy are derived by assuming that the computed mass flow carries the intermediate time step velocities and internal energies of the donor cell. A general expression for the updated velocities and internal energies is presented in Gentry *et al.*¹⁸⁸

The described donor cell approach is a first order scheme, which is very stable due to a large amount of inherent numerical diffusion. However, this method can be improved to second order accuracy, together with a considerable reduction of numerical diffusion. In addition to the introduction of explicit artificial dissipation terms, the advection algorithm can be directly modified by introducing a flux limiter. This code integrates the flux-corrected transport (FCT) algorithm developed by Boris and Book.¹⁸⁹⁻¹⁹¹ The FCT algorithm enforces positivity in the solution of the continuity equation. It is commonly used for modeling typical processes in LPPs, such as shock and rarefaction waves, contact discontinuities, vaporization, as well as liquid and solid heating. In this code, the SHASTA version of the FCT algorithm is employed.¹⁹⁰

In the FCT approach, the diffusive error is estimated, using, for example, higher order methods. The anti-diffusive flux at the right boundary of a cell (i,j) equals then

$$A_{i+1/2,j} = F_{i+1/2,j}^H - F_{i+1/2,j}^L \quad (6.12)$$

These fluxes are used to derive the transported and diffused solution of the flow quantity $Q_{i,j}^{TD}$ (typically mass in cell). In a next step, the flux limitation is calculated in order to avoid non physical features in the flow field. In general, the limited flux can be written as

$$A_{i+1/2,j}^C = C_{i+1/2,j} A_{i+1/2,j} \quad (6.13)$$

with $0 \leq C_{i+1/2,j} \leq 1$. Finally, the flow quantity of interest $Q_{i,j}^{n+1}$ is corrected by the sum of these limited fluxes. The SHASTA algorithm suggests the following approach for determining the limited fluxes

$$\begin{aligned} A_{i+1/2,j}^C &= S_{i+1/2,j} \max(0, M) \\ S_{i+1/2,j} &= \begin{cases} 1, & A_{i+1/2,j} \geq 0 \\ -1, & A_{i+1/2,j} \leq 0 \end{cases} \\ M &= \min\left(|A_{i+1/2,j}| S_z, S_{i+1/2,j} (Q_{i+2,j}^{TD} - Q_{i+1,j}^{TD}), S_{i+1/2,j} (Q_{i,j}^{TD} - Q_{i-1,j}^{TD})\right) \end{aligned} \quad (6.14)$$

The same treatment is valid at the other three boundaries of the computational cell.

While velocities are advanced to the intermediate time step according to Eq.(6.9), the energy equation requires a more complex treatment. The intermediate solution of the specific energy is determined from the implicit solution of the diffusion equations Eq.(6.7) and Eq.(6.8). These equations are solved by an ICCG sparse matrix solver¹⁹² using a standard five point difference scheme. The volume dilation term appears in the diagonal coefficient only, while the laser and radiation source terms appear on the right hand side. The electron and thermal conductivities are flux limited.¹⁹³

In order to ensure stability and accuracy during the explicit solution of the flow field, the time step is typically limited by the Courant-Lewy-Friedrichs condition, which along the z -direction equals $u_{ij}/dz \delta t < 0.4$. Additional limitations are given by the ratio of absorbed energy or conductive heat flow to the total material energy. The hydrodynamic code uses two types of boundary conditions, namely continuative output and reflective boundaries. Both boundary types require ghost cells. At a continuative output boundary, the flow quantities in the ghost cells are defined in a way that the normal space derivatives disappear. In the case of the reflective boundary, the density and energy in the ghost cells are exactly equal to their neighbor cells in the flow field, while the velocity components must be reversed.

6.2.1.2. Equation of state

As the hydrodynamic code treats both ions and electrons separately, two different equations of state (EOS) are required. In the case of atoms and ions, the analytical EOS of the Chart-D package is used.¹⁸⁶ The results are self-consistent and thermodynamically complete for the considered ranges of temperatures and densities. All thermodynamic functions, such as pressure, entropy, specific energy, heat capacity and speed of sound, are computed from the Helmholtz free energy with the temperature and density as independent variables. Furthermore the solid, liquid and vapor fractions in each cell are computed by the EOS. The Helmholtz free energy is computed as the superposition of three separate phenomena, which include (i) the atomic and electronic interactions at zero temperature, (ii) the thermal motion of atoms and ions and (iii) the thermal motion and ionization of electrons.

The EOS is able to handle solid, liquid, vapor and plasma phases, together with the corresponding transitions. The phase change is typically estimated from the Clausius-Clapeyron equation by assuming that the liquid and the surrounding vapor are in thermodynamic equilibrium. Additional models for the solid and liquid phases are required in order to avoid hydrodynamic explosion. Indeed, the density gradient between the solid-vapor or liquid-vapor phase induces a massive pressure gradient, which leads to the diffusion driven by Eq.(6.9). In the case of solids, the self-diffusion at the vapor interface is suppressed by introducing a yield pressure term. In the case of a liquid, a similar approach is currently used. The self-diffusion is suppressed until a fixed vapor fraction is reached in the computational cell. The optimum solution would consist of a surface tension model. A validation of the EOS for tin is presented in Sec. 6.3.2.1.1.

The electron EOS in use in the hydrodynamic code is the Thomas-Fermi EOS.¹⁹⁴ The version in this code has been extended for low densities by Pert.¹⁹⁵ The Thomas-Fermi EOS is commonly used to accurately determine the electron component of the free energy. Finally, the main thermodynamic parameters (pressure, entropy, specific energy, speed of sound and heat capacity) are derived from the free energy, the atomic number density and electron temperature. The ionization of the plasma plume can be determined from the Thomas-Fermi EOS. The deficiency of

the Thomas-Fermi EOS is the absence of the atomic shell related features, which become more important at lower densities.

The code has been extended to compute the mean ionization in a computational cell from the collisional radiative (CR) model of Colombant *et al.*³⁴ The CR model is typically used for modeling laser plasmas in the studied temperature and density range,¹ especially as it is the most widely applicable. Indeed the model is also valid under the assumption of non-LTE. The computation of the fractional ion density $n(Z)/n_i$ can be derived from the following relationship between two successive ionization stages

$$\frac{n(Z+1)}{n(Z)} = \frac{S(Z)}{\alpha_r(Z) + n_e \alpha_{3b}(Z+1)} \quad (6.15)$$

where $S(Z)$ is the collisional ionization rate from the ion ground state, α_r is the electron-ion radiative recombination rate and α_{3b} is the collisional, three body recombination rate. All ionization and recombination rates can be described analytically.³⁴

The equilibration model between electrons and ions is based on collisions. The corresponding time scales may be large due to the strong mass imbalance. The energy transfer related to equilibration is modeled by the Spitzer expression modified for degeneracy.¹⁹⁶ The two EOS provide the two component values of specific energy and heat capacity to estimate the equilibration time, according to Brysk *et al.*¹⁹⁷ The thermal conductivity for electrons is calculated according to Lee *et al.*¹⁹⁸ The non-degenerate thermal conductivity of Spitzer is used for the ion thermal conductivity.¹⁹⁶

6.2.1.3. Radiation transport

Laser light is transported inside the plasma by the straight line path approach.¹⁹⁹ A predefined number of laser light rays enters the computational domain and is either absorbed in the plasma by IBA or in the solid / liquid / vapor phase by using modified experimental values for the skin depth. Additionally, the refractive index is evaluated as the real part of the complex wave vector and is used in the straight line path model.

The radiation generated by the plasma significantly influences its hydrodynamic response. Furthermore, the purpose of the present LPP simulations is to predict EUV radiation. Therefore, the governing equations presented in Sec. 6.2.1.1 must be extended by a fourth equation, which describes the spatial and temporal evolution of the radiation energy density.

In regions of high optical thickness, photons interact more frequently and therefore “diffuse” through matter before being absorbed. High electron temperature and density increase the frequency of the photon scattering events. Under these conditions, the equation of radiation transfer can be simplified and reduced to the so-called diffusion approximation. The principal assumption is that the photon mean free path is much shorter than the typical length scale of the considered problem. This assumption will be verified later, when typical opacities are computed. In

this work, radiation transport is modeled using the flux-limited diffusion approximation for the radiation energy density E .²⁰⁰

$$\frac{DE}{Dt} = -\nabla \cdot (D\nabla E) + 4\pi\kappa B - c\kappa E \quad (6.16)$$

where D is the radiation diffusion coefficient, κ is the opacity, B is the emissivity function and c is the speed of light. The coupling to the material energy density equations is accomplished by the electron temperature and density dependence of the opacity and diffusion coefficients, as well as the emissivity function.

The radiation transport equation is simplified in the simulations of this work to a quasi-steady equation, which is evaluated at each hydrodynamic time step. It is assumed that the radiation field reaches equilibrium within the hydrodynamic time step. Typical diffusion coefficients in the plasma are in the range of $10^8 \text{ cm}^2/\text{s}$ (from Sec. 6.3.2.1.5). The corresponding diffusion length scale, which equals $l = \sqrt{4Dt}$, is smaller than the plasma size for typical hydrodynamic time steps (10 ps).

The system of the coupled electron and radiation energy density equations can be written as

$$\begin{aligned} \frac{De_e}{Dt} &= -p_e \underline{\nabla} \cdot \underline{v}_e + \nabla k \nabla \frac{e_e}{c_{v,e}} + Q_{las} - 4\pi\kappa B + c\kappa E \\ \underline{\nabla} \cdot (D\underline{\nabla} E) &= 4\pi\kappa B - c\kappa E \end{aligned} \quad (6.17)$$

The solution of the radiation diffusion equation is tightly coupled to the material energy density equation of the electrons. The system of both energy equations is solved at the intermediate time step.

The solution procedure is described below:

Step 1. At the beginning of the Lagrangian phase, the specific energy equation is solved for ions and electrons, without the radiation source term. An initial guess of the electron temperature \tilde{T}_{ij}^n is obtained.

Step 2. The diffusion and opacity coefficients are evaluated at the average temperature $\bar{T}_{ij}^n = 1/2(\tilde{T}_{ij}^n + T_{ij}^n)$ of the intermediate time step.

Step 3. The radiation diffusion equation Eq.(6.17) is solved with the emissivity function evaluated at \bar{T}_{ij}^n .

Step 4. The electron energy equation is solved again with the computed right hand side term $4\pi\kappa B - c\kappa E$ from step 3.

Step 5. The equation of state is used to derive the temperature corresponding to the electron energy density determined in step 4.

Step 6. Convergence of the electron temperature \tilde{T}_{ij}^n is assessed. In case the temperature in question has not yet converged sufficiently, the iteration restarts at step 2.

Step 7. The converged temperature \tilde{T}_{ij}^n is used to obtain the final solution of the radiation energy field.

6.2.1.3.1. Flux limitation

For the discussion of the flux limitation, it is useful to look at the radiation flux, which is the physical quantity inside the divergence in Eq. (6.16).

$$\underline{F} = -D\underline{\nabla}E \quad (6.18)$$

In regions of low optical thickness, the diffusion takes place at large velocities, which approach the speed of light. This situation corresponds to a departure from LTE. In the case of LTE, the diffusion coefficient can be written as $D = c/3\kappa$. A flux limiter is needed in order to apply the diffusion approximation everywhere in the computational domain. The magnitude of the flux must be smaller than the energy density, which is a positive definite quantity. Flux limiting is a crude assumption, as the full radiation transport equations are angle dependent. The diffusion approximation linearizes the angular dependency and removes the time derivative of the radiation flux.²⁰⁰

Multiple flux limiters have been developed over the years and are application dependent. The flux limiters typically agree with theoretical predictions in the two extreme cases of optically thick and thin media. In the present work, the Levermore-Pomraning flux limiter is used.²⁰¹ The corresponding diffusion coefficient equals

$$D = \frac{c}{3\kappa} \frac{6 + 3 \left(\frac{|\nabla E|}{\kappa E} \right) + \left(\frac{|\nabla E|}{\kappa E} \right)^2}{2 + \left(\frac{|\nabla E|}{\kappa E} \right)} \quad (6.19)$$

where the radiation energy density gradient is evaluated using a central difference scheme.²⁰² The diffusion coefficient is not only a function of the electron temperature and density, but also of the radiation energy field.

6.2.1.3.2. Diffusion equation solution

The diffusion equation $\nabla \cdot (D \nabla E) + c \kappa E = 4 \pi \kappa B$ is discretized using a central difference scheme on a two-dimensional cartesian grid with a total number of $n_x n_y$ cells of width dx and dy as follows:

$$\begin{aligned} & \frac{1}{(dx)^2} \left(D_{i+1,j} (E_{i+1,j}^n - E_{i,j}^n) - D_{i,j} (E_{i,j}^n - E_{i-1,j}^n) \right) \\ & + \frac{1}{(dy)^2} \left(D_{i,j+1} (E_{i,j}^n - E_{i,j+1}^n) - D_{i,j} (E_{i,j}^n - E_{i,j-1}^n) \right) + c \kappa_{ij} E_{i,j}^n = 4 \pi \kappa_{ij} B_{ij} \end{aligned} \quad (6.20)$$

The diffusion of the radiation energy field can be represented by a simple linear system

$$A \underline{E}^n = \underline{B} \quad (6.21)$$

Eq.(6.20) is used to determine the coefficients of the Poisson matrix A , which has 5 bands and the dimension $n_x n_y$. The cells (i,j) are re-indexed accordingly. The diagonal coefficient of $E_{i,j}^n$ equals

$$c \kappa_{ij} + \frac{1}{(dx)^2} (D_{i+1,j} + D_{i,j}) + \frac{1}{(dy)^2} (D_{i,j+1} + D_{i,j}) \quad (6.22)$$

And the non-diagonal coefficients are

$$\begin{aligned} & -\frac{1}{(dx)^2} D_{i+1,j} \text{ for } E_{i+1,j}^n, -\frac{1}{(dx)^2} D_{i,j} \text{ for } E_{i-1,j}^n, \\ & -\frac{1}{(dy)^2} D_{i,j+1} \text{ for } E_{i,j+1}^n, -\frac{1}{(dy)^2} D_{i,j} \text{ for } E_{i,j-1}^n \end{aligned} \quad (6.23)$$

On the boundary cells, special conditions have to be implemented for a physical behavior of the radiation diffusion. In this work, different boundary conditions have been investigated before selecting a normal parabolic outflow condition. The radiation energy density in the ghost cell is expressed as function of the radiation energy densities of its neighboring cells. In the case of the left domain boundary, the radiation energy density in the ghost cell equals

$$E_{0,j} = 3E_{1,j} - 3E_{2,j} + E_{3,j} \quad (6.24)$$

The boundary conditions are also integrated in the Poisson matrix A . The linear system is finally solved using a sparse matrix solver. Today, a multitude of highly optimized solvers are available. In this work, the Pardiso solver²⁰³ from the Intel MKL library has been used. This solver comes in a parallelized version for shared and distributed memory systems.

6.2.1.3.3. Multigroup transport

In multigroup transport, the frequency spectrum is split up into an arbitrary number of groups. For each group or frequency window, the radiation transport equation is solved, with mean quantities

for the opacities and emissivity functions.²⁰⁴ As the number of frequency groups goes to infinity, the mean opacities and emissivity functions effectively represent their actual physical values. The number of groups is typically determined by computational resources.

In the present work, two groups are used in a similar approach. In the solution procedure of the radiation energy density and the electron energy density, the full-band (from zero to infinity wavelength) problem is solved. When determining the electron energy density at the intermediate time step, the full frequency spectrum is relevant. The second group includes the EUV window (2% bandwidth centered at 13.5 nm) only. Once the electron temperature has been determined at the intermediate time step by considering the full-band group, the radiation energy density field equation is solved for the EUV window only. In this case, the diffusion equation is solved in exactly the same approach as for the full-band problem, except that the opacity and emissivity functions correspond to their mean values in the EUV window.

6.2.1.3.4. Opacity and emissivity function

The radiation energy computation is very sensitive to the physical values of opacity and emissivity functions. The opacity coefficients must be determined for the two considered radiation groups, namely full-band and in-band.

Even though radiation transport is mainly linked to the plasma, the other three phases are present in the computational domain, and therefore their opacity must be included in the radiation transport model. The wavelength specific opacities of the liquid, solid and vapor phase are calculated using the same approach as for the laser absorption. First, the frequency spectrum is split into a discrete number of grid points (>20) and for every frequency, the specific skin depth, which is half the absorption length, is determined in every grid cell. Then the computed absorption coefficients are weighted by the Planck function, which is evaluated at the electron temperature in the computational cell. Indeed LTE is valid in computational cells, which are not in the plasma phase. Mathematically, the weighting of the absorption coefficients yields the mean absorption coefficient $\bar{\alpha}_{abs}$ in the following way

$$\bar{\alpha}_{abs} = \frac{\int_{\nu_1}^{\nu_2} B(\nu, T_e) \alpha_{abs}(\nu) d\nu}{\int_{\nu_1}^{\nu_2} B(\nu, T_e) d\nu} \quad (6.25)$$

where the Planck function is written as

$$B(\nu, T_e) = \frac{2h\nu^3}{c^2} \frac{1}{\exp\left(\frac{h\nu}{kT_e}\right) - 1} \quad (6.26)$$

In the plasma phase, the opacity depends on the level populations of the different ions, the ionization balance and the electron density. Typically the opacity versus photon energy spectrum is highly complex. Different approaches exist to deal with this complexity. The most expensive, but also very accurate solution is to experimentally acquire opacity data.²⁰⁵ In another approach, sophisticated equations of state are used to generate tabulated opacity data for the material in question. A very popular database is the Sesame library from LANL.²⁰⁶ As an alternative, atomic physics codes, which model the detailed atomic shell structures, can be used to predict at least a portion of the opacity spectrum. This approach is used in this work to determine the in-band EUV opacity as a function of electron temperature and density. The detailed procedure is presented in Sec. 6.3.1. For the full-band mean opacity value, two similar approaches have been implemented. The opacity is derived as a Planck or Rosseland mean opacity, following the philosophy of a diffusion based grey transport problem.²⁰⁰ While the Rosseland mean opacity guarantees accurate radiation transport in the high optical thickness case, the Planck opacity is used for the optically thin limit. A simple non-trivial representation of the opacity κ is a power law of the form

$$\kappa = aT_e^s \rho^r \quad (6.27)$$

The constants a, s and r have been determined for tin by Tsakiris et al.²⁰⁷ to be $a=72.19$, $s=-.0571$ and $r=0.160$ for the Rosseland mean opacity and $a=328.55$, $s=-1.588$ and $r=0.228$ for the Planck mean opacity. The ranges of validity of the tables are $30 \text{ eV} \leq T_e \leq 1 \text{ keV}$ and $0.1 \text{ g/cm}^3 \leq \rho \leq 10.0 \text{ g/cm}^3$. Although some portion of the plasma plume is out of range, the working ranges are still relatively close and the data is used without modifications. Alternatively, the expression of the Rosseland mean opacity from the Chart-D library has been implemented in the RHD code, but is not used in this work. In the present work, the Planck mean opacity is used, as it yielded better validation results in the case of the Nd:YAG and tin plasma.

The emissivity function B in the source terms of the energy equations takes different forms, according to the full-band or in-band radiation transport model. In the full-band radiation transport, the emissivity function is typically represented by the Planck function from Eq.(6.26), integrated over all wavelengths. However, in case the plasma in a computational cell has an electron temperature and density, which are within or close to the EUV emission conditions, the emissivity is taken from tabulated atomic physics code computations (Sec. 6.3.1.3). For the in-band conditions, the emissivity function is typically equal to the Planck function, integrated in the EUV window only. Again, for conditions close to or at EUV emission, the in-band emissivities are taken from the atomic physics code.

6.2.1.4. Overview

A simplified logical flow diagram of the RHD code is presented in Fig. 86. All user input is specified in a textual input file, which is read at the beginning of the runtime. After initializing the equation of state for the material specified in the input files, the domain is initialized by setting the

user specified temperature and density distributions on the grid. The code can accommodate arbitrary target shapes inside the computational domain. At the end of the initialization, the EOS is evaluated for a first time in order to determine the pressure and specific material energy densities for both ion and electrons. A multitude of other relevant physical parameters, such as the heat capacity, speed of sound, optical properties like absorption and refraction are determined.

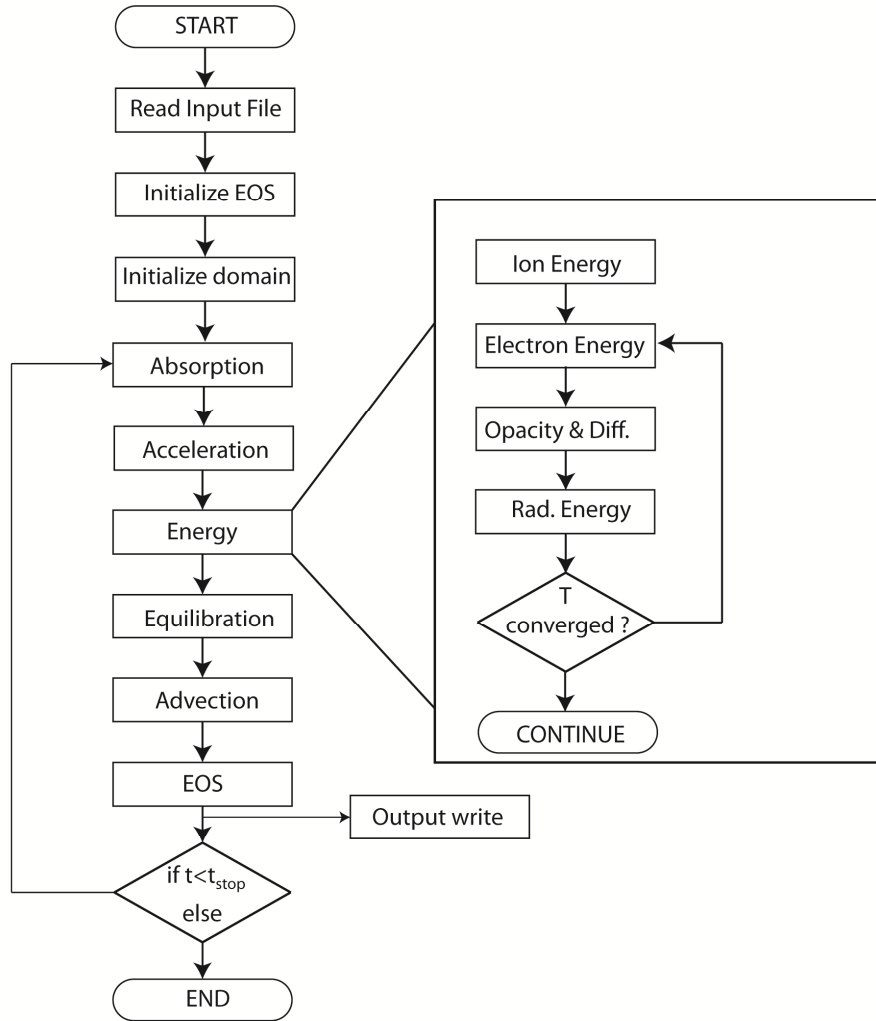


Fig. 86. Simplified logical flow diagram of the RHD code.

The main loop starts with the laser absorption routine. The straight line path absorption is used to follow the laser beam and evaluate the absorbed laser energy in every cell. In the next step, both velocity components and the energies are advanced to the intermediate time step. The advancement of the electron energy equation is related to the iterative solution of the radiation transport equation. Indeed, the electron energy and radiation density equations are solved in a coupled way up to the convergence of the electron temperature in each cell to a level of 1% (RMS). Both ion and electron energy densities are equilibrated at the end of the intermediate time step according to the electron-ion collision rate. Then, the advection step advances the relevant flow

quantities to the final time step. The EOS routine computes electron/ ion temperatures and pressures, which are necessary to start over again with the intermediate time advancement. At the end of the main loop, the time step is adjusted according to the conditions mentioned in Sec. 6.2.1.1.

Output files are written at predefined times at the end of the main loop. The generated files are read by MATLAB for further processing or data visualization.

6.2.2. Atomic physics code

One of the research objectives of this thesis is the prediction of the conversion efficiency of a tin-based laser-produced plasma. Simple LTE models based on Planckian blackbody assumptions are not valid to model the complex opacity field of the considered plasma plumes. LTE methods yield conversion efficiencies that are far below experimental values. Indeed, the spectral efficiency, when based on the Planck blackbody assumption, equals 1.5%.²⁰⁸ For this reason, more detailed studies of the radiative properties of the target material are required.

In the case of tin, configuration interaction (CI) plays an important role.^{35, 209-211} Indeed CI results in a strong redistribution of the transition probabilities between the different configurations. As a consequence, single-configuration approximations, such as the average atom or the monoconfiguration Hartree-Fock or Dirac-Fock approaches, are insufficient. So-called detailed term accounting (DTA) methods are required. In these methods, a detailed calculation of several millions of lines is completed. These DTA methods rely on the diagonalization of the Hamiltonian in a multiconfiguration basis. The mathematical technique is typically Racah algebra. The eigenvectors and energies, which result from the diagonalization of the Hamiltonian, are used to compute cross-sections for all relevant radiative transitions.

In this work, the HULLAC¹²² code is used for atomic physics calculations. The Dirac equation is solved in the parametric central potential approximation. The relativistic energies and the one-electron wave functions are derived. The efficiency of the code relies on the fact that the parametric potential is optimized by minimizing the total energy of groups of relativistic configurations. As a consequence, a solution is obtained for each configuration. A drawback of the code is that it requires some prior knowledge of the relevant transitions to be included. The included atomic processes are collisional excitation and ionization, radiative recombination, photoionization and autoionization.

The latest version of Hullac²¹² includes the Mixed Unresolved Transition Array (MUTA)²¹³ model. The complete fine-structures transition array is computed, including configuration interaction. Then the set of transitions is refined by removing transitions, which contribute to the overall intensity by only a small fraction. The remaining transitions are lumped together in an asymmetrical Gaussian distribution of intensity. This approximation drastically reduces the overall computational time and made the detailed computations in this work possible.

Once the atomic structures (energy levels), cross-sections and transition rates have been determined by HULLAC, the final module, namely the collisional rate model (CRM) solver, can be used. The previously determined rates are used to predict the population kinetics in the plasma. The population density N_i of an ion stage i is derived from the balance between the population ($R_{j \rightarrow i}$) and depopulation ($R_{i \rightarrow j}$) rates, respectively, as follows

$$\frac{dN_i}{dt} = -N_i \sum_{j \neq i} R_{i \rightarrow j} + \sum_{j \neq i} N_j R_{j \rightarrow i} \quad (6.28)$$

For a given electron temperature and density, the main results of the CRM solver are the ion populations and the emission and absorption spectra. In this way, maps of the in-band and full-band emissivity and opacity are generated as a function of electron temperature and density. The tabulated values are then integrated in the RHD code and applied during the solution of the radiation transport.

The details of the used CI groups for the tin case, as well as a validation of the predicted emission and absorption characteristics, are presented in the next chapter in Sec. 6.3.1.2.

6.2.3. Particle code

One research objective of the present work consists of predicting the ion debris load on the collector optics for the tin droplet target. The evolution of ion debris, from laser ablation to the interaction with the collector optics is studied. In order to overcome the inability of the RHD code to model the plasma expansion at low densities, a particle code has been developed in the framework of this project. In the rarified flow regime, the motion of particles is determined by collisions and self-induced or external electrostatic or magnetic fields. Collision modeling is completed using the Direct Simulation Monte Carlo (DSMC) method of Bird.¹⁸¹ The electrostatic and magnetic effects are reproduced by the (collisionless) Particle-In-Cell (PIC) approach.²¹⁴ Eventually the particle and RHD code are combined in a hybrid approach. An unsteady interface, which is determined by the local degree of rarefaction, is used to transfer information from the continuum simulation to the particle code.

In the subsequent sections, a summary of the particle code and the coupling to the RHD code is presented. The DSMC code has been made available by Prof. G. Bird. More details about the particle code can be found in the reports of the student projects supervised by the author on this topic. The PIC code and the interface to the RHD code have been largely developed in the Master's Thesis of Giovannini.²¹⁵ Different refinements have been completed in the Bachelor Thesis of Rebholz²¹⁶ and the code parallelization has been started in the Master's Thesis of Hochreutener.²¹⁷

6.2.3.1. Direct Simulation Monte Carlo Method

The governing equations of Sec. 6.2.1.1 for inviscid flow assume that ions and electrons have velocity distributions equal to the local Maxwell velocity. Indeed the collision frequencies inside each of the two flows are high enough to equilibrate the velocities according to a Maxwellian distribution. The collision frequencies are proportional to the density of the considered flow. With increasing Knudsen numbers ($Kn = \lambda/L$), the velocity distribution function departs from the Maxwellian distribution. The only closed equation available is the Boltzmann equation. This equation describes atomic / molecular velocities, instead of macroscopic flow quantities. No useful solutions of the Boltzmann equation are available for finite Knudsen numbers. Solutions exist only for the infinite Knudsen limit of the collisionless regime. Approaches, which can handle flows with large Knudsen numbers are the Lattice Boltzmann (LB) method or the Direct Simulation Monte Carlo (DSMC) method. For a given number of particles N , all processes in the DSMC approach either scale with N or $N \log(N)$ and not with N^2 , which is the case in the N -body problem.

DSMC is applied in flow simulations with large Knudsen numbers, which result either from large mean free paths or small characteristic dimensions. Typical applications include the resolution of shock waves, where the characteristic length is limited to a few mean free paths. Other applications are found in the areas of rarefied gas dynamics, which includes vacuum systems and reentry problems.

The modeling of gas or plasma flows relies on the computation of the motion and collisions of millions of representative particles, which are called macro-particles. The velocity and positions of each particle are stored in a computational array and modified with time as the particles are concurrently followed through representative collisions in the computational domain. One requirement prescribes that the mean spacing between particles is large in comparison with the molecular diameter. The basic assumption behind DSMC is that the particle motion and collisions can be decoupled over time intervals, which are smaller than the mean collision time. All calculations are unsteady, although steady flows can be simulated. The physical time can be identified with the simulation time parameter. The computational effort scales with the number of simulated particles, which typically increases with decreasing Knudsen number.

The DSMC algorithm contains three major stages. The first stage includes the collisionless motion of the particles. In this step, the position of the particle is updated according to the post-collision velocities. In case of external forces, the particle trajectories are updated accordingly. In the second stage, the collision sampling takes place. First, indexing of particles according to their collision cell is completed. Collisions only happen within a cell at a certain collision probability. At the end of this stage, the particle velocities are updated. A third stage models the interaction of particles with boundaries.

The DSMC method typically uses two grids, one for collision sampling and one for deriving the macroscopic flow properties. Initially, the collision cells were chosen to be small enough to have a high macroscopic flow resolution and modeling accuracy with typically at least 10 particles for statistically meaningful results. In the sophisticated DSMC approach,^{218, 219} adaptive collision cells are used, which limit the number of particles per cell to 8.

The collision probability between two particles is proportional to their relative speed and the total collision cross-section. The so-called no-time-counter (NTC) method is used in the sophisticated DSMC approach. If V_c is the volume of a collision cell and F_n is the number of particles represented by one computational particle (macro-particle factor), the number of potential collision pairs at each time step Δt equals

$$\frac{1}{2} N(N-1) F_n (\sigma_T c_r)_{\max} \Delta t / V_c \quad (6.29)$$

where N is the number of particles per cell, σ_T is the total collision cross-section and c_r is the relative speed of the collision partners. The product of the total cross-section and the relative speed is constantly updated by the largest value found in each cell. After the number of collisions has been fixed, the collision pairs are selected. The first partner is selected randomly, while the so-called nearest neighbor method²¹⁹ (limited to the collision cell) is used for the second one. The probability of a collisional event i is given by

$$\frac{(\sigma_T c_r)_i}{(\sigma_T c_r)_{\max}} \quad (6.30)$$

An acceptance-rejection scheme is used to decide whether a collision takes place. In this way, the number of candidate collisions is determined.

A minimum number of possible collisions is implemented in the current version of the particle code. The accuracy of the particle model strongly depends on the collision cross-sections. Indeed the cross-sections are a measure of the collision probability and do not necessarily correspond to the physical cross-section of the particle. In the case of tin, no experimental data has been available.

The electron flow is not directly modeled in the DSMC approach. Indeed electron collisions with ions are very probable and would therefore decrease the computational time step significantly. The simplified integration of electrons in the model is described below. Inelastic collisions are modeled by the Larsen-Borgnakke model,¹⁸¹ which redistributes the sum of the pre-collision energies among the collision partners. In the case of ionization, this energy is subtracted from the collisional energy, which determines the post-collision velocities. In the case of the studied tin plasma, ionization is possible up to Sn^{12+} . Additionally, charge-exchange collisions are included. In this case, one or more electrons are exchanged between an atom and an ion. The relation for the charge-exchange cross-sections of any non-transition-element is provided in Sakabe *et al.*²²⁰ In elastic

collisions, which include atom-atom and ion-atom collisions, the post-collision velocities are determined from the conservation of linear momentum and the assumption of isotropic scattering. The applied model has been developed by Banks²²¹ and Dalgarno²²². All types of collisions are possible for tin and background gas atoms. Coulomb collisions²²³ between charged particles are not included. This type of collision is computationally very expensive, as the corresponding cross-sections are very large. The angular deflection and momentum exchange in Coulomb collisions is small, but the cumulative effect, especially at high densities, should be considered in more detailed studies.

The simulations include a background gas, which is representative for the vacuum environment. At the open boundaries, the corresponding Maxwellian thermal flux is added.²²⁴

6.2.3.2. Particle-In-Cell Approach

The Particle-In-Cell (PIC) approach is commonly used in laser plasma interactions. Particles are tracked in a Lagrangian frame of reference, while the self-induced or external fields are computed in the Eulerian frame of reference. In this work, only the self-induced electrostatic field is considered. The PIC algorithm comprises four steps.²¹⁴

Initially, the position, velocity and charge of each particle are known. In a first step, the velocity change of a particle is computed from the forces acting on the particle. Then, the new particle position is determined. The particle positions and charges are used to derive the spatial charge density, which is used to compute the electric field in the stationary frame. The electric field induces electrostatic forces on each particle, which are then used in the next time step to update the particle position again. Time advancement is completed by using a 2nd order leap frog method.²¹⁴

The PIC model is limited to the heavy ions, while electrons are modeled as a fluid. For the case where electrons are modeled as particles, the time step of the PIC computation decreases by two orders of magnitude. Indeed, due to the large disparity in mass between ions and electrons, electrons diffuse at velocities that are more than two orders of magnitude larger than that of ions.

The charge density and electric field are interpolated to the PIC grid by using a first order weighting method, which differs for the planar and axisymmetric grids. The size of the grid cells depends on the approach used to derive the electric field from the charge density. The electric field is computed by assuming local quasi-neutrality. The electrons are not tracked individually and are assumed to have a Maxwellian distribution. This work focuses on the motion of the heavy debris particles.

By assuming quasi-neutrality, the electric potential can be derived in each cell by a simple algebraic relationship.²²⁴ The PIC cell size must be chosen in order to accommodate a quasi-neutral portion of the plasma. The measure of the size of the globally neutral region is the Debye length. As a consequence, in the case of the quasi-neutral model, the cell size must be larger than the Debye

length. The upper limit is typically given by a reasonable resolution of the gradient in the electric potential. Formerly a Poisson solver has been implemented to overcome the assumption of quasi-neutrality. The computational time penalty consists of an increase of runtime by a factor of 20 when compared to the quasi-neutral approach. The grid size must not exceed the Debye length in order to use the Poisson equation. Both methods have been compared with experimental results for a xenon Hall Thruster plume with ion stages up to Xe^{2+} . The accuracy of the quasi-neutral solution is sufficient in this case. The Hall Thruster simulation has been used to validate the code.

6.2.3.3. Combined PIC-DSMC Code

The DSMC code is integrated into the in-house developed PIC code. The collision modeling routines of the DSMC code are added to the particle motion routines of the PIC code. A simplified logical flow diagram of the two codes is presented in Fig. 87. The combination of the code accounts for the low range Coulomb force effects on the particles, as well as for the main types of possible collisions.

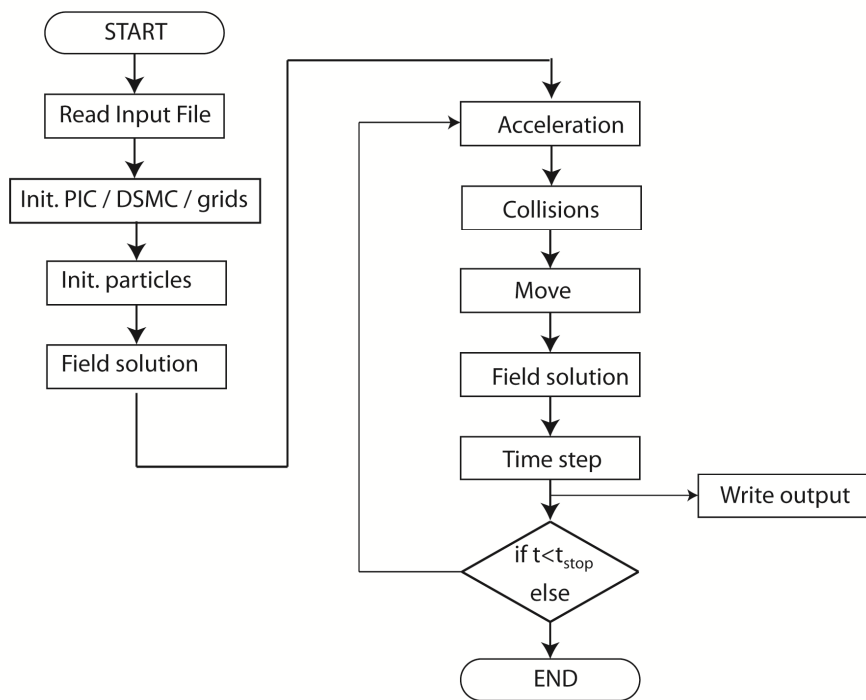


Fig. 87. Simplified logical flow diagram of the PIC-DSMC code

The code initialization includes the setup of the 3 grids (DSMC sampling, collisions, PIC fields) and the particle initializations (position and velocity). Before starting the main loop, the induced electric fields are computed. The first step of the main loop includes the computation of the individual accelerations due to the field forces. In the 2nd step, the DSMC code comes into play for modeling collisions. After the particle position and velocity update by the collision routines, the position is updated according to the PIC acceleration. The 2nd and 3rd steps are interchangeable. At

the end of the main loop, the particle densities are weighted onto the PIC grid and the electric field is derived. Finally the time step of the combined code is determined by the PIC part. The maximum particle travel distance should not exceed 10% of the PIC cell size in the next iteration step.

6.2.3.4. Hybrid RHD-PIC-DSMC Code

A hybrid code, which includes the RHD and PIC-DSMC code is used to simulate the ion formation and propagation from the droplet target to the collector. At the beginning of the simulation, only the RHD code is executed, up to a (user defined) point. At this point in time, a spatial interface is initialized, which is used to pass the flow field information from the RHD to the particle code. The unsteady interface is determined by the local Knudsen number ($Kn=0.1$) in the plasma plume. The characteristic length in the computation of the Knudsen number corresponds to the size of the plasma plume. The interface separates the computational domain into the continuum and rarefied regions, as shown in Fig. 88. The interface contains a layer of buffer cells. Typically 4 buffer cells are chosen. Their role is to transfer the effect of the charge density on the continuum side of interface to the rarefied side of the interface.

After the initialization of the interface, the RHD and particle code run in parallel for the regions inside (RHD code) and outside (particle code) of the interface. After a fixed number of time steps of the RHD code, the interface is recomputed and data is transferred from the RHD to the particle code. As the interface position is moving outwards, the inner region, which is modeled by the RHD code, expands. As the two codes run in parallel, the overlapping region is computed by each code separately. However, at each data transfer point, the data at the interface is passed from the RHD code to the particle code. As a consequence, the final flow field of the inner region is computed by the RHD code. At the end of the simulation time of the RHD code, the particle code continues with the plasma expansion. The final time of the RHD code is chosen such that the number of generated ions at the interface is small when compared to the total number of ions in the particle code.

At every interface cell, the hydrodynamic velocities and temperatures are used to derive the drift and thermal velocities, respectively. The thermal velocity is assumed to follow a Maxwellian distribution. Ion fractions are derived according to the CR model described in Sec. 6.2.1.2.

A key feature of the PIC-DSMC code is the domain extension algorithm. The domain is initialized with the dimensions of the hydrodynamic code. As the plasma expansion is modeled up to collector length scales (>100 mm), a domain extension is required. As soon as one of the plasma particles leaves the computational domain, the domain is extended by an expansion factor, which is fixed in the input file. The three grids, namely DSMC collision, DSMC sampling and PIC grids, are extended and the particle positions are interpolated to the new grids. New background gas particles are initialized at every domain extension. The collector position, shape and dimensions are specified

in the input file. The physical properties of particles, which cross the virtual collector surface in the particle code, are recorded and used for evaluating the collector damage.

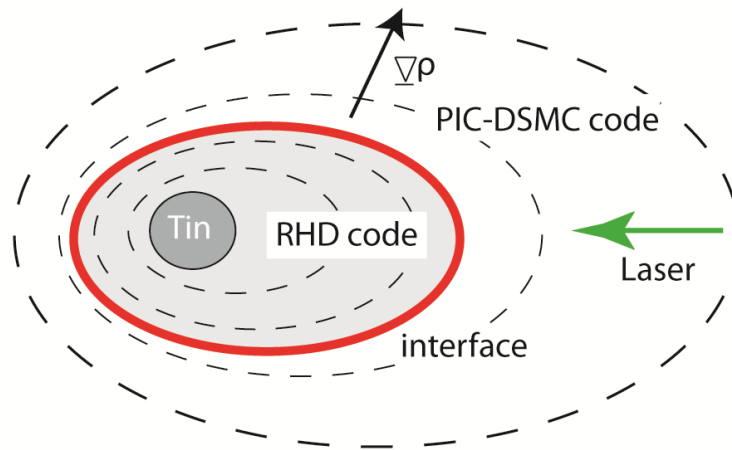


Fig. 88. Particle generation interface. The interface transfers RHD data to the particle code and is located at the transition from continuum to rarefaction at $Kn=0.1$.

6.3. Numerical results

The computational modeling results of a tin droplet-based LPP are outlined in the present chapter. First, the detailed atomic model is used to derive the opacities and emissivities, which are required for accurate modeling of EUV emission. Then, a baseline case, which uses experimental boundary conditions, such as the droplet size and the laser settings, is presented with a focus on emission and debris. A set of parametric studies on the main laser and droplet parameters yields information about the influence these parameters on the source performance. The studies include variations of the laser power, the pulse duration and the spot size, as well as of the droplet size, the relative spot size, the lateral stability and the droplet spacing. Together with the previous droplet train measurements, general conclusions about droplet generation in LPP EUV sources are derived.

6.3.1. EUV opacity and emissivity

The numerical prediction of the plasma emission requires a detailed radiation transport model. The model, which is described in the previous chapter in Sec. 6.2.1.3, requires opacity and emissivity coefficients from an atomic physics computation. Due to the departure from LTE in EUV LPP plasmas, a detailed computation using the atomic physics code HULLAC is conducted. A full collisional radiative model, which is based on the modeling of atomic processes by HULLAC, is employed to determine the opacity and emission spectra as a function of electron temperature and density. In the first subsection, the modeled transitions and groups of transitions are presented. Then, the obtained atomic model is first compared to an experimentally measured emission spectrum. Secondly, experimental opacity data are used for the validation of the atomic model. In the last section, the emissivities and opacities are derived as a function of electron temperature and density.

6.3.1.1. Atomic model setup

In the case of tin plasmas, the most relevant emission in the EUV window, is obtained from the $4p^6 4d^N \rightarrow 4p^5 4d^{N+1} + 4p^6 4d^{N-1} 4f$ ($1 \leq N \leq 6$) transitions in ion stages around Sn^{10+} .³⁵ Configuration interaction (CI) induces a shift and narrowing of the spectral contributions of the 4d-4f and 4p-4d transitions towards lower wavelengths.²¹¹ Tin ions have a large number of excited configurations. In the computational model not all the configurations can be included. Furthermore, CI cannot be computed for all of the modeled configurations, due to the limitations in computational resources. Groups of configurations have the same core configuration and one excited atom in different outer orbitals. In the development of an accurate atomic model, a sufficient number of groups of configurations must be included. This is a non-trivial task and many research papers have been published on this topic for the case of the tin EUV LPP.^{35, 209, 225, 226} The approach in this work follows the methodology of Sasaki *et al.*²¹⁰ Table 8-I summarizes the different groups of configurations for Sn^{7+} to Sn^{13+} .

Table 8-I. Main configuration groups from Sn^{7+} to Sn^{13+} , which are included in atomic model. The term **nl** represents the possible orbitals with higher quantum numbers.

Sn^{7+}	Sn^{8+}	Sn^{9+}	Sn^{10+}	Sn^{11+}	Sn^{12+}	Sn^{13+}
$4p^6 4d^6 \text{nl}$	$4p^6 4d^5 \text{nl}$	$4p^6 4d^4 \text{nl}$	$4s^2 4p^6 4d^3 \text{nl}$	$4s^2 4p^6 4d^2 \text{nl}$	$4s^2 4p^6 4d \text{nl}$	$4s^2 4p^6 \text{nl}$
$4p^6 4d^5 5s \text{nl}$	$4p^6 4d^4 5s \text{nl}$	$4p^6 4d^3 5s \text{nl}$	$4s^2 4p^6 4d^2 5s \text{nl}$	$4s^2 4p^6 4d 5s \text{nl}$	$4s^2 4p^5 4d^2 \text{nl}$	$4s^2 4p^5 4d \text{nl}$
$4p^6 4d^5 5p \text{nl}$	$4p^6 4d^4 5p \text{nl}$	$4p^6 4d^3 5p \text{nl}$	$4s^2 4p^5 4d^4 \text{nl}$	$4s^2 4p^5 4d^3 \text{nl}$	$4s^2 4p^5 5s \text{nl}$	$4s 4p^6 4d \text{nl}$
$4p^6 4d^5 4f \text{nl}$	$4p^6 4d^4 4f \text{nl}$	$4p^6 4d^3 4f \text{nl}$	$4s^2 4p^6 4d^2 4f \text{nl}$	$4s^2 4p^6 4d 4f \text{nl}$	$4s^2 4p^6 4f \text{nl}$	$4s^2 4p^4 4d^2 \text{nl}$
$4p^5 4d^7 \text{nl}$	$4p^5 4d^6 \text{nl}$	$4p^5 4d^5 \text{nl}$	$4s^2 4p^6 4d^2 5p \text{nl}$	$4s^2 4p^6 4d 5p \text{nl}$	$4s^2 4p^6 5p \text{nl}$	$4s^2 4p^5 4f \text{nl}$

More than 70% of the emission is determined by modeling these five configurations groups for each ion.²¹⁰ The range of the orbitals occupied by the single electron is ideally modeled up to the principal and orbital quantum numbers of $n \leq 8$ and $l \leq 3$, respectively. For orbitals with higher quantum numbers, no change of results is expected.²¹⁰ In the case of the low ion stages, the resulting computational effort is too large and therefore the principal quantum number n is limited to 6.

In the second part of the model, the level populations are derived from Eq.(6.28) by using the population and depopulation rates, which have been determined by HULLAC in the previous step. The opacity and emission spectra are calculated by considering bound-bound, bound-free and free-free transitions. The in-band radiation is determined by integrating the contributions in the EUV window of the emission spectrum. The value is influenced by the finite width of the bound-bound lines. Line broadening due to Doppler and Stark broadening is estimated to be in the range of 0.1 eV. Therefore, the spectral resolution in the computed emission spectrum is set to 0.1 eV. The energy corrections from Sasaki *et al.*²¹⁰ are used and validated below.

6.3.1.2. Comparison with experimental results

6.3.1.2.1. Emission spectrum validation

In a first validation case, the simulated emission spectrum is compared to experimental emission spectra. For this comparison, the plasma is modeled as a slab with a mean optical thickness τ . The emission spectrum computed by the CRM solver yields the spectral emissivity function $B(T_e, n_e, \nu)$ in units of $\text{W}/\text{cm}^{-3}\text{eV}$. The source function $S(T_e, n_e, \nu) = B(T_e, n_e, \nu) \cdot \kappa(T_e, n_e, \nu)$ is corrected by the mean optical depth in order to yield the emission intensity $I(T_e, n_e, \nu)$ in $\text{W}/\text{cm}^{-2}\text{eV}$. For a slab of length l , the correction can be written as

$$I(T_e, n_e, \nu) = S(T_e, n_e, \nu) \left(1 - e^{-\tau(T_e, n_e, \nu)}\right) \quad (6.31)$$

The optical depth is computed from the frequency dependent opacity as $\tau(T_e, n_e, \nu) = \kappa(T_e, n_e, \nu) \cdot l$. In order to avoid the assumption of a mean optical thickness, the spectrum could be modeled using the previously described multi-group diffusion. However, the number of required groups is very large (>1000) in order to reproduce the key features of the experimental spectrum. In the experimental comparison, the electron temperature and density, as well as the plasma length scale l , are unknown. While the temperature and density can be estimated for a known irradiance, the length l is iteratively adjusted to optimize the match between computational and experimental results

The computed spectrum is first compared to the experimental spectrum obtained by Tao *et al.*²²⁷ The spectrum with a resolution smaller than 0.1 nm is obtained from the irradiation of a planar solid tin target by a CO₂ laser beam with an intensity of 20 GW/cm². The simplified plasma plume is modeled in the CRM solver at a temperature of 38 eV and an electron density of 10¹⁹ cm⁻³. The slab length equals 100 μ m, although it must be noted that for the CO₂ laser, the results are less sensitive to the slab length. Indeed the CO₂ laser produces a lower density plasma plume than the Nd:YAG laser. The match between the experimental and computed spectrum is good, especially in the EUV window. The overall width of the EUV peak is well reproduced. The energy shift²¹⁰ leads to matching peaks. The larger wavelength satellite line contributions are underestimated by the atomic model due to the limited number of modeled transitions. The number of transitions is optimized for the EUV window, where the mean opacity and emissivity are extracted for the radiation transport model.

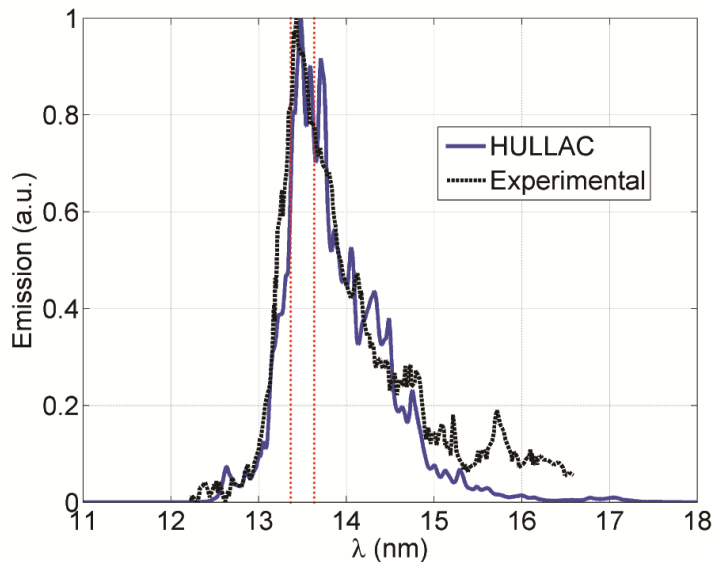


Fig. 89. Comparison of computational tin EUV emission spectrum with experimental values. The red dotted lines represent the boundaries of the EUV window. Both spectra match well, especially around the EUV window, which is the region of interest.

6.3.1.2.2. Comparison to transmission measurements

The goal of this second validation step is to separately validate the opacity. Indeed in the validation of the emission spectra, both opacity and emissivity have been used (Eq.(6.31)). Very few measurements of the opacity of tin in the EUV range of temperatures and densities exist. One such experiment has been performed by Fujioka *et al.*²⁰⁵ A tin sample is radiatively heated in a dog-bone cavity up to the Planckian temperature $T_r=50$ eV. Then the sample is backlit by EUV radiation from another tin EUV plasma. The transmitted EUV radiation spectrum is measured by a grazing incidence spectrograph. Computationally, the attenuation of the EUV radiation emitted by a blackbody with the experimental radiation temperature T_r is studied. Furthermore, the experimental area density of the tin sample is used.

The comparison of the measured transmission with the computational prediction is shown in Fig. 90. The experimental curve corresponds to a smoothed response of the spectrograph. The computational model uses an electron density of $5 \times 10^{20} \text{ cm}^{-3}$ and temperature of 30 eV. The trends of the transmission curve are well reproduced by the atomic physics code. The width of the transmission dip is comparable. Good agreement is observed between the experimental and computational minima of the transition curve. A major source of disparities is the modeling assumption of a homogeneous tin sample.

In conclusion, the validation of the developed atomic model and the CRM solver shows good agreement with experimental results for emission spectra and opacity measurements. Therefore, the EUV in-band emissivity and opacity can be derived with the help of the atomic physics code.

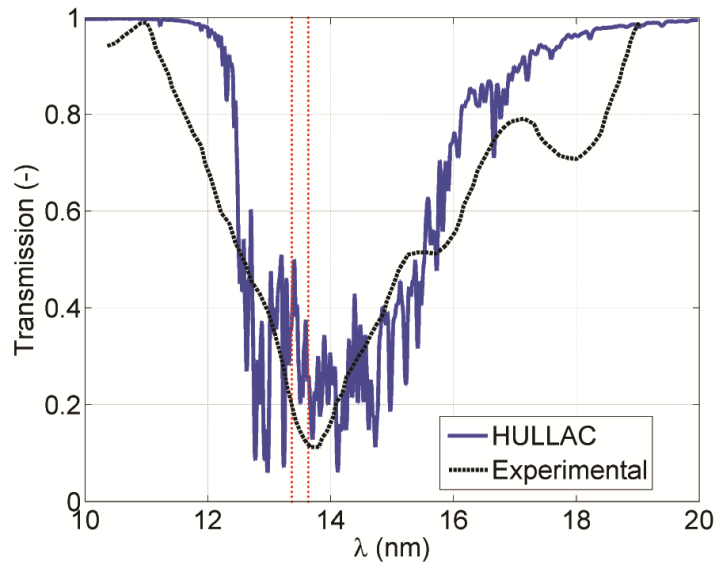


Fig. 90. Comparison of transmission curves in the EUV region for experimental and computational results. The red dotted lines represent the boundaries of the EUV window and the experimental curve is smoothed. The data is taken from Fujioka *et al.*²⁰⁵

6.3.1.3. Emissivity and opacity computation

The CRM solver uses the rates of all relevant atomic processes to compute the emissivity function $B(T_e, n_e, \nu)$ and the opacity $\kappa(T_e, n_e, \nu)$. An example of the wavelength dependent emissivity function at an electron density $n_e=10^{21} \text{ cm}^{-3}$ and an electron temperature $T_e=33 \text{ eV}$ is shown in Fig. 91. At these plasma conditions, a large fraction of the total emission lies in the EUV window. The ratio of the in-band energy density and the full-band energy density is called the spectral efficiency. Due to the finite number of modeled configurations, the full-band energy density computation is of limited accuracy. Especially the smaller satellite line contributions are not fully taken into account. The spectral efficiency equals 13.0%. If the blackbody approximation is used for estimating the full-band energy density, the spectral efficiency equals only 0.9%. The blackbody approximation underpredicts the spectral efficiency. Indeed typical experimental CEs at these plasma conditions are larger than the spectral efficiency based on the blackbody assumption. Furthermore the conversion efficiency of the EUV LPP must be smaller than the spectral efficiency. The difference between the conversion efficiency and the spectral efficiency is mainly due to the optical thickness of the plasma and other loss mechanisms, such as inefficient absorption and expansion losses in the conversion process from laser energy to EUV. More details are presented in the next sections.

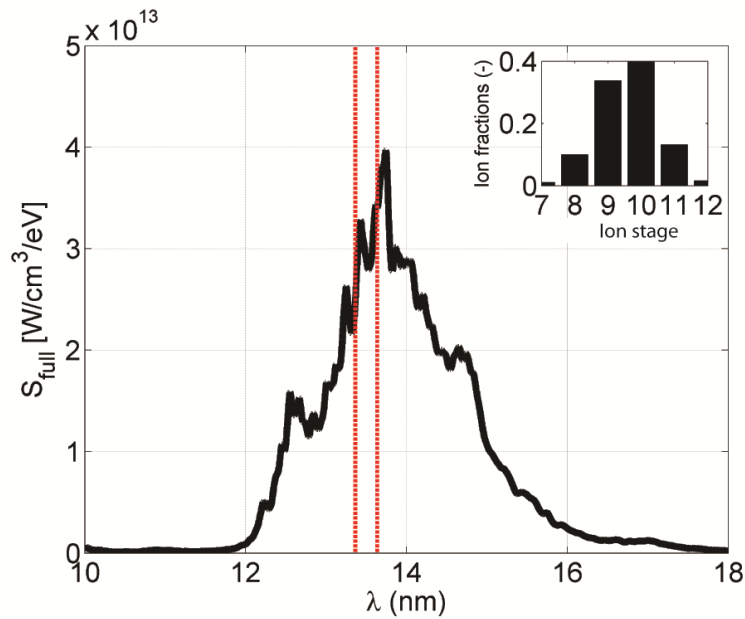


Fig. 91. Wavelength spectrum of emissivity function at $n_e=10^{21} \text{ cm}^{-3}$ and $T_e=33 \text{ eV}$. The plasma emission has significant contributions in the EUV window at these conditions. The EUV window is represented by the red dotted lines. The ion fractions for the given plasma conditions are indicated.

The ion fractions, as predicted by the CR model are shown in the upper right corner of Fig. 91. At $n_e=10^{21} \text{ cm}^{-3}$ and $T_e=33 \text{ eV}$, ions from Sn^{7+} up to Sn^{12+} are present. The most dominant ion stages are Sn^{9+} and Sn^{10+} , which have significant contributions in the EUV window through 4d-4f, 4d-4p and 4d-6p transitions.³⁵ The opacity spectrum has the same features as the emission spectrum. The peak opacity for the specified plasma parameters equals $2 \times 10^4 \text{ cm}^{-1}$.

The CRM solver computes the emissivity and opacity coefficients by considering bound-bound, bound-free and free-free transitions. Although, the final values of the radiation transport coefficients include all types of transitions, the CRM results indicate which transition type is the most important. The total emissivity function, together with the bound-bound, bound-free and free-free contributions is shown in Fig. 92.

The emissivity function is determined by bound-bound transitions. As a consequence, the spectra must be expected to mainly contain broadened line emissions. The continuum contributions from bound-free and free-free transitions are negligible, especially around the EUV window. For the largest simulated electron density of 10^{23} cm^{-3} , the continuum contributions slightly increase. Overall, the continuum contributions remain insignificant. The dominance of the bound-bound contributions justifies the use of a detailed atomic physics calculation for determining the radiation transport coefficients.

The complete emission spectrum can not only be decomposed into the three basic types of emission, but also into the spectra from each contributing ion stage. In general, this is useful in determining the origin of certain spectroscopic features in the full spectrum. The ion stage, which is responsible for a given feature, can be generated or avoided by tuning the plasma temperature and density accordingly.

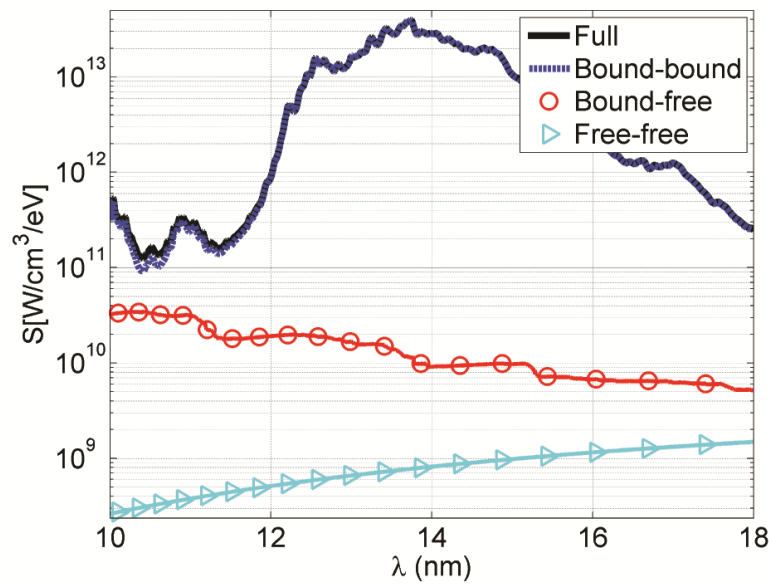


Fig. 92. Wavelength spectrum of total, bound-bound, bound-free and free-free emissivity at $n_e=10^{21} \text{ cm}^{-3}$ and $T_e=33 \text{ eV}$. The bound-bound contributions are dominating, especially around the EUV window.

The decomposition of the emission spectrum for an electron density $n_e=10^{21} \text{ cm}^{-3}$ and electron temperature $T_e=33 \text{ eV}$ is shown in Fig. 93. Sn^{9+} and Sn^{10+} , which are the most frequent ion stages for the studied plasma conditions, have significant contributions in the EUV window. Although all

other simulated ions also contribute to the EUV window, they have broader distributions without a pronounced peak in the EUV window. Overall, the dominant wavelength decreases as the charge state increases. For the studied plasma temperature and density, the presence of the 4d-4f and 4d-4p resonance lines from Sn^{9+} and Sn^{10+} lead to the large spectral efficiency of 13.0%.

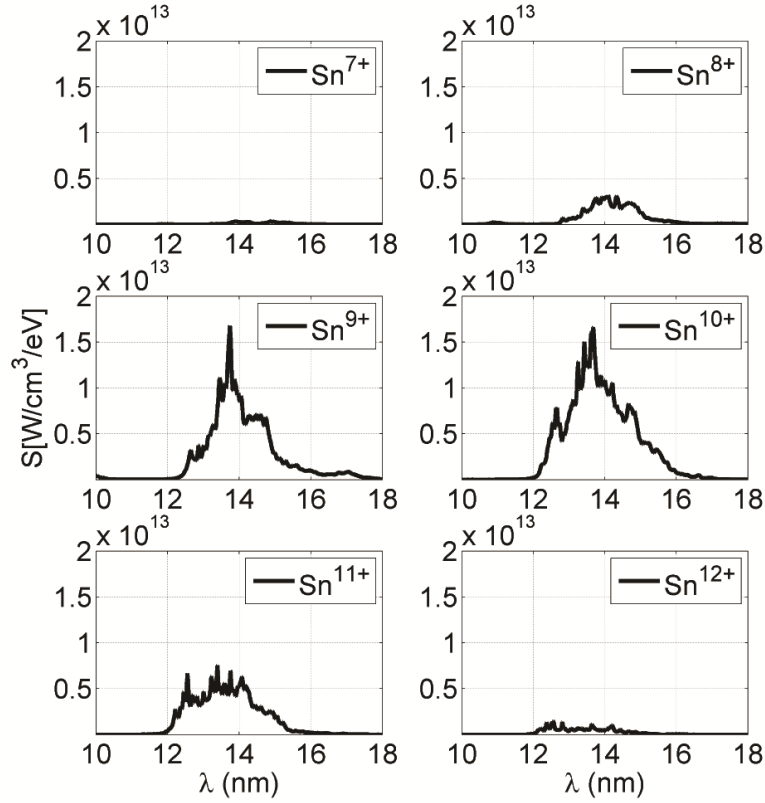


Fig. 93. Individual ion spectra at $n_e=10^{21} \text{ cm}^{-3}$ and $T_e=33 \text{ eV}$. The largest contributions to the full spectrum come from Sn^{9+} and Sn^{10+} .

Similar to the temperature dependence, the density dependence of the spectral emissivity is derived from the CRM results, as shown in Fig. 95. The electron temperature is kept constant at 38 eV. The emissivity variation with density is much more pronounced than with temperature. As a consequence, the spectra are plotted on a logarithmic scale. The difference in emissivity between the low density spectrum at $n_e=10^{17} \text{ cm}^{-3}$ and the high density spectrum at $n_e=10^{23} \text{ cm}^{-3}$ is in the range of 10 orders of magnitude. The emissivity increase with density is mainly due to the increased number of emitting ions. For all densities, the emissivity is highest in the wavelength region from 12 to 16 nm with a main peak around 13.5 nm.

Finally, the computed spectra are used to derive the emissivity and opacity as a function of electron temperature and density. The in-band emissivity is computed by integrating the spectral emissivity in the EUV window. The emissivity is presented in Fig. 96 for an electron temperature range from 25 to 60 eV and an electron density range from 10^{17} cm^{-3} to 10^{23} cm^{-3} . The results confirm the tendency observed for the density dependence of the emissivity at a constant temperature of 38 eV,

as shown in Fig. 95. In the studied temperature range, the EUV emissivity increases with density over several orders of magnitude. The temperature dependence is more complex with EUV emissivity peaks around 50 eV and a fall-off at lower or higher temperatures.

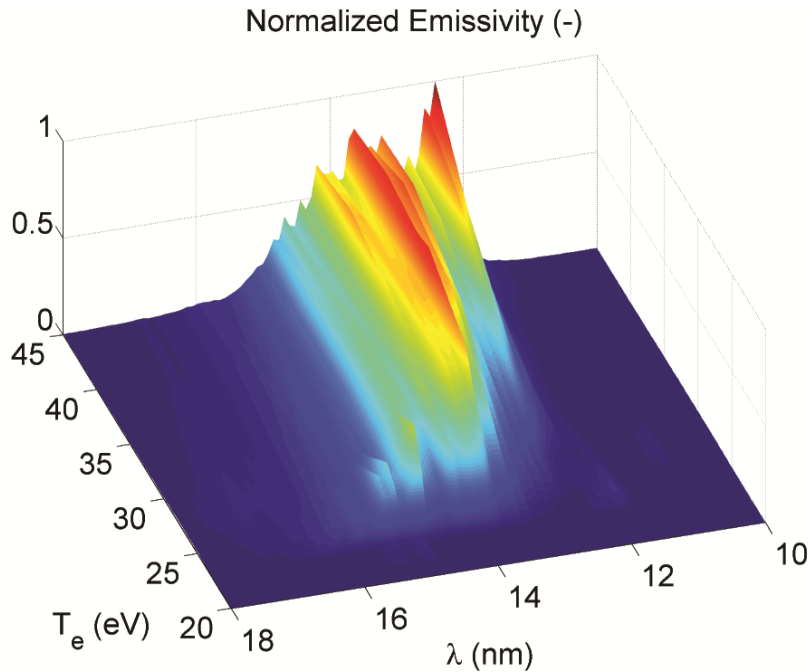


Fig. 94. Spectral emissivity as a function of wavelength and temperature in the EUV region at a fixed density $n_e=10^{19} \text{ cm}^{-3}$. The largest EUV emissivity is found around 40 eV.

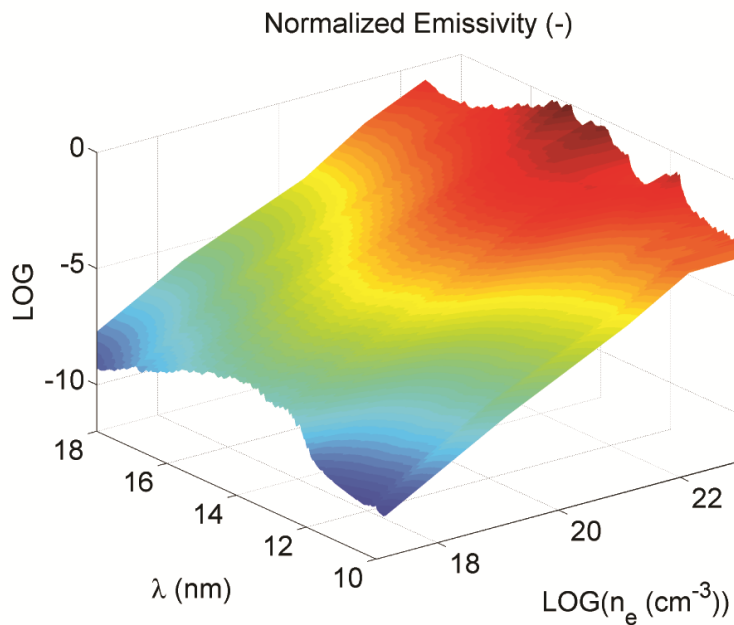


Fig. 95. Spectral emissivity as a function of wavelength and density in the EUV region at a fixed electron temperature of 38 eV.

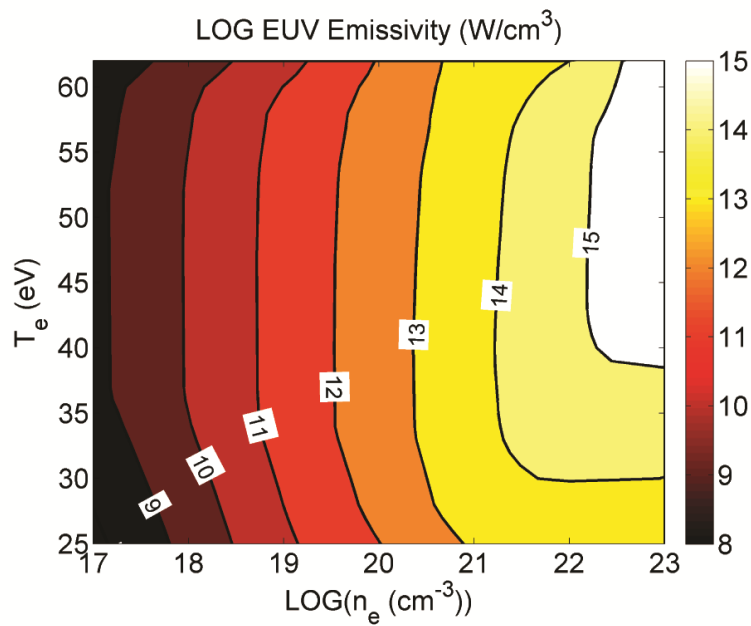


Fig. 96. EUV emissivity in the range of electron temperatures $T_e=25\text{-}60 \text{ eV}$ and electron densities $n_e=10^{17}\text{-}10^{23} \text{ cm}^{-3}$. The largest EUV emissivities are found at large electron densities and electron temperatures around 50 eV.

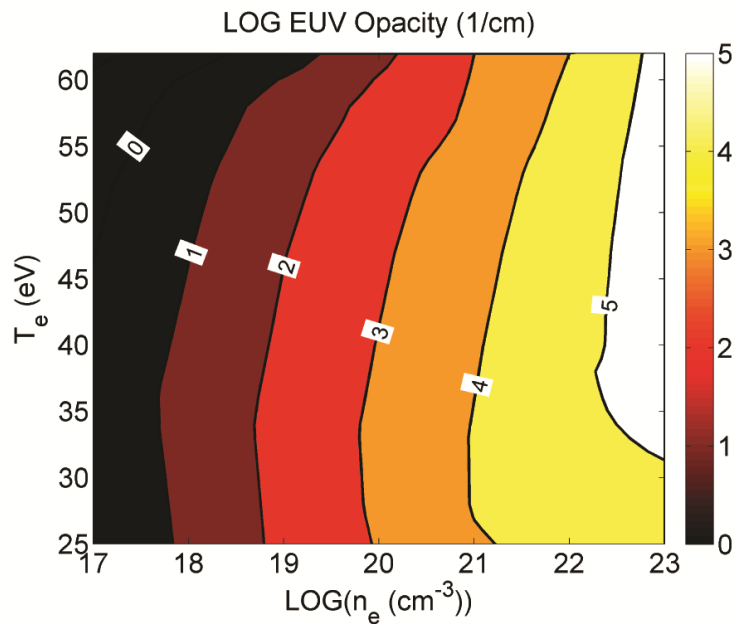


Fig. 97. EUV opacity in the range of electron temperatures $T_e=25\text{-}60 \text{ eV}$ and electron densities $n_e=10^{17}\text{-}10^{23} \text{ cm}^{-3}$. Similar to the EUV emissivity, the largest EUV opacity is found for the largest density and a temperature around 38 eV.

The opacity is derived by averaging the spectral opacity in the EUV window. The temperature and density dependence of the opacity is shown in Fig. 97. In general, the opacity follows a similar

trend to that of the emissivity. The increase of opacity with electron density is straightforward. For a given density, the peak EUV opacity is obtained for temperatures around 35 eV.

The results of the temperature and density dependence of the emissivity and the opacity are used to extract tabulated values for the emissivity and opacity, respectively. The resulting tables are integrated in the RHD code, which interpolates the emissivity and opacity according to the electron temperature and density of a computational cell.

6.3.1.4. Discussion

Along with the determination of the emissivity and opacity for the radiation transport model in the RHD code, the results in this section can be used to further understand and optimize LPP EUV sources. The spectral efficiency, which is defined as the ratio of in-band over full-band radiation, is a key result from the atomic physics code. The spectral efficiency is shown in Fig. 98 for electron temperatures $T_e=25-60$ eV and electron densities $n_e=10^{17}-10^{23}$ cm⁻³.

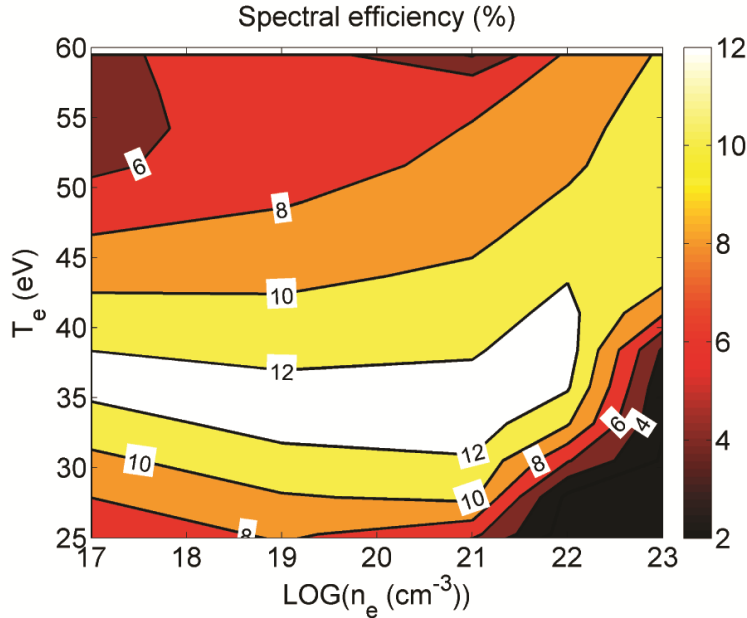


Fig. 98. Spectral efficiency for the range of electron temperatures $T_e=25-60$ eV and electron densities $n_e=10^{17}-10^{23}$ cm⁻³. The largest spectral efficiencies are found in band around 35 eV for densities smaller than $n_e=10^{22}$ cm⁻³.

The spectral efficiency is found to be larger than 12% in a band around 35 eV for electron densities up to 10^{22} cm⁻³. The maximum spectral efficiency of 16% is found at an electron density $n_e=10^{19}$ cm⁻³ and an electron temperature $T_e=33$ eV. The spectral efficiency decreases with higher densities. Indeed, Fig. 94 shows that for the spectral emissivity, secondary peaks appear in the spectrum with increasing density. The spectral efficiency should be matched to an acceptable optical thickness ($\tau \leq 1$). For a typical plasma size of 100 μ m, the opacity at an electron density of 10^{19} cm⁻³ and temperature of 33 eV is on the order of 10^2 cm⁻¹. Under these conditions, the optical

thickness equals unity and therefore a large CE can be expected. Such conditions are obtained for CO₂ LPPs, as the corresponding critical density is $n_c=10^{19} \text{ cm}^{-3}$. In contrast, Nd:YAG LPPs are expected to yield lower CE due to the larger critical density when compared to CO₂ LPPs. However, the better focusing capability of the Nd:YAG when compared to the CO₂ laser and the resulting smaller plasma size partially counterbalance these effects. Still, the difference in CE persists and is confirmed by experiments.²²⁸

6.3.2. Baseline tin droplet results

After determining the radiation transport coefficients with the help of the the atomic physics code HULLAC, the RHD and particle codes can be used to study the formation and expansion of the tin LPP. The modeling tools are applied to a baseline simulation, which consists of a tin droplet irradiated by a Nd:YAG laser at representative conditions for the LPP studies at ETH Zurich. The first section is related to the small-scale modeling. This includes the laser absorption, the plasma formation, the EUV radiation emission and the first steps of the plasma expansion. The second section describes the plasma expansion up to the collector optics, as well as the induced damage on the collector.

6.3.2.1. Small-scale radiation hydrodynamic studies

6.3.2.1.1. Validation of RHD code

In the first subsection, the equation of state is compared with experimental data. In the following three sections, the full RHD code is validated according to a standardized benchmarking procedure for EUV LPP source models. The procedure has been defined by SEMATECH in order to increase the confidence in modeling in the EUVL community.²²⁹ The performance of the numerical tools is assessed by using a standardized set of experimental data.

Equation of state

The system of basic hydrodynamic equations is closed by the EOS for heavy particles and electrons. In this section, the validation of the heavy particle tin EOS, namely the analytical EOS from the Chart-D¹⁸⁶ package is presented. The tin EOS requires a significant number of input parameters, such as a reference bulk modulus, the Grüneisen coefficient,²³⁰ the Debye temperature²³⁰ and the lattice separation energy.

The ρ - T phase diagram for tin, as computed by the analytical EOS is presented in Fig. 99. The phase-diagram includes the transition boundaries between the solid, liquid and vapor phases. The transition between liquid and solid includes the so-called melt transition. A close-up view of the melt transition region is shown in Fig. 100c. The solidus and liquidus lines separate the liquid-solid region from the solid or liquid regions, respectively. A first comparison to experimental results is related to the critical point. In the work of Ternovoi *et al.*,²³¹ the critical temperature and pressure have been determined to be $T_{crit}=7850 \text{ K}$ and $p_{crit}=0.25 \text{ GPa}$, respectively. The analytical EOS

predicts $T_{crit}=7781\text{ K}$ and $p_{crit}=0.48\text{ GPa}$, which results in a deviation of 0.9% for the critical temperature and 125% for the critical pressure. The large deviation between experimental and numerical critical pressure can be partially explained by an experimental uncertainty. Although the uncertainty is not explicitly specified in Ternovoi *et al.*,²³¹ the critical point region in the experimental p - T diagram (Fig. 3 in Ternovoi *et al.*²³¹) includes the value predicted by the analytical EOS.

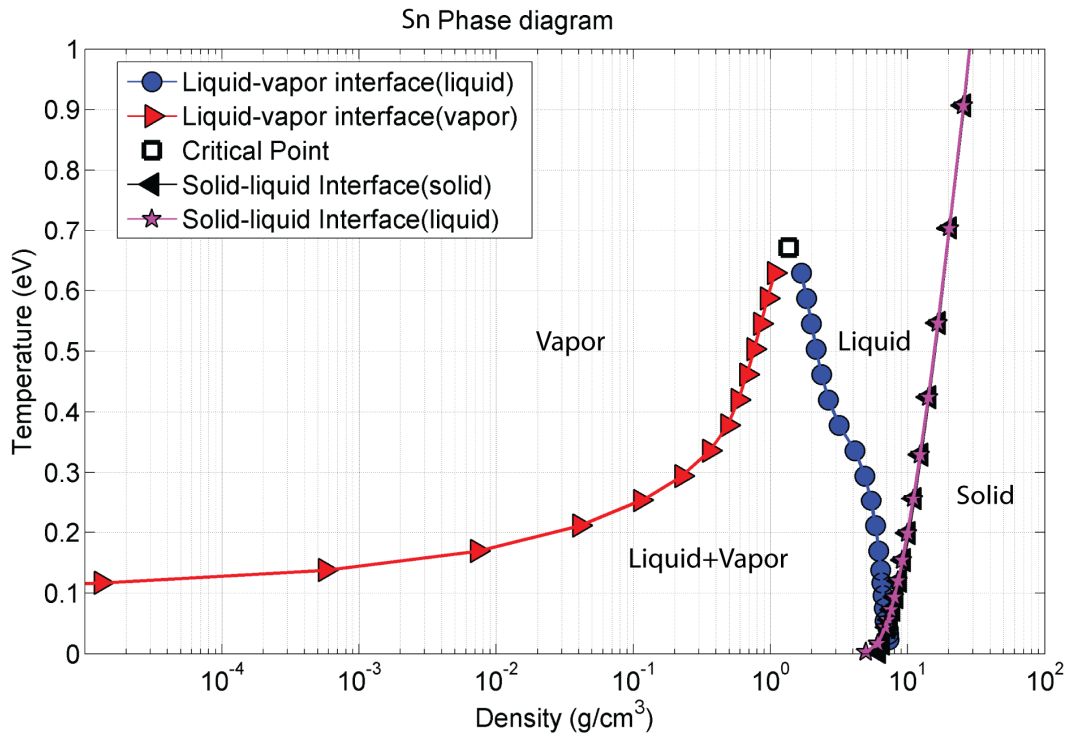


Fig. 99. Tin phase diagram for a wide range of densities. The transition boundaries between liquid, solid and vapor phases and the critical point are included in the EOS computation.

The most relevant validation case of the EOS is related to the shock Hugoniot curve.²³⁰ Indeed the correct prediction of thermodynamic states after the passage of shock wave is essential in the hydrodynamic modeling. The shock Hugoniot curve for tin has been measured by Khishchenko *et al.*²³² The experimental and numerical curves are shown in Fig. 100a. The agreement between the Hugoniot curves is good, with a mean pressure deviation at a fixed temperature in the range of 20%. In the work of Khishchenko *et al.*,²³² the p - T melting curve is modeled with excellent agreement with experimental results. A comparison between the experimental and numerical melting curve yields excellent agreement, as shown in Fig. 100b.

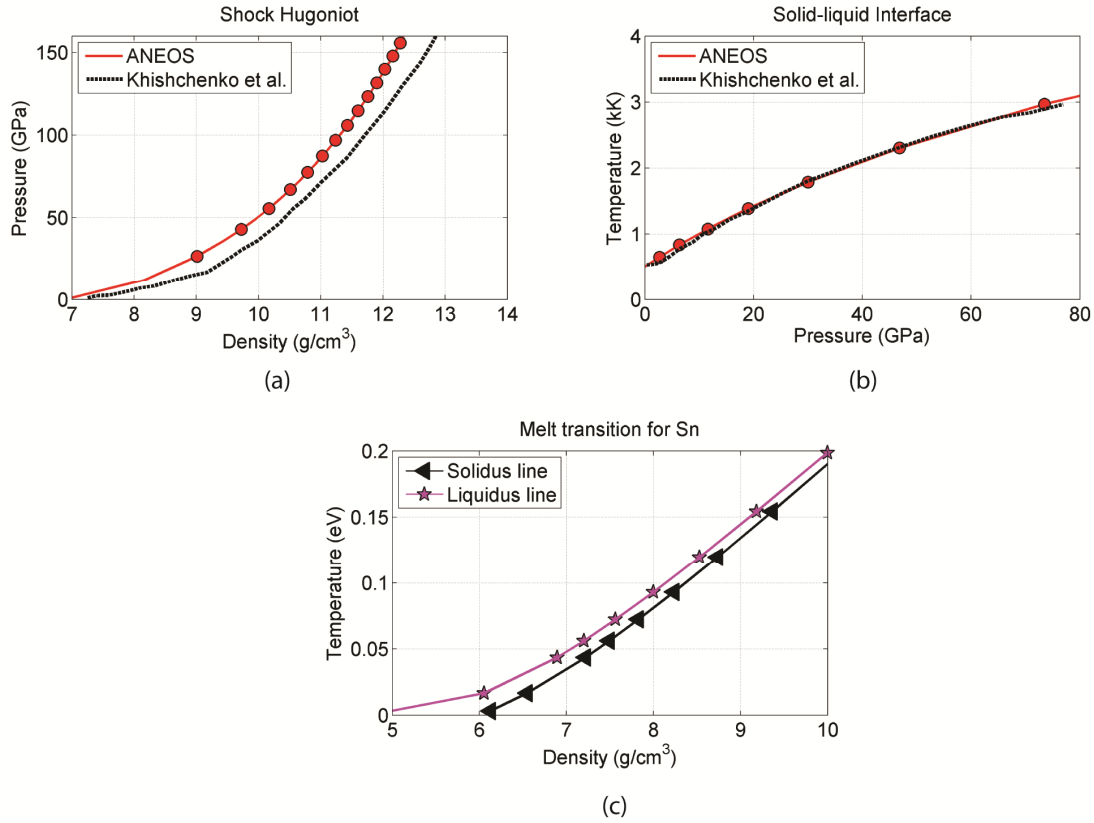


Fig. 100. (a) Comparison of experimental and numerical shock Hugoniot curves for tin. (b) Comparison of melt curve from Kishchenko *et al.*²³² and numerical equation of state in p - T diagram. (c) Close-up view of melt transition region from T - ρ diagram.

The final validation case is related to the liquid and solid density at the melting point. Experimental values yield $\rho_{liq}=6.96 \text{ g/cm}^3$ and $\rho_{sol}=7.29 \text{ g/cm}^3$. The numerical values of $\rho_{liq}=6.89 \text{ g/cm}^3$ and $\rho_{sol}=7.22 \text{ g/cm}^3$ can be derived from solidus and liquidus lines in Fig. 100c for a melting temperature $T=0.044 \text{ eV}$. The derivation equals 1.01% for the liquid density and 0.96% for the solid density at the melting point, which results in an excellent agreement. In summary, the detailed equation of state for tin, which is integrated in the RHD code, gives good agreement with experimental data.

Electron density

In a first benchmarking case of the full RHD code, the numerically predicted electron density distribution is compared to experimental results. Firstly, the comparison of the contours of electron density in the z - r plane is useful in validating the shape of the expanding plume. Secondly, the comparison of the magnitudes of electron density verifies the degree of ionization, which is mainly coupled to the temperature distribution and the applied ionization model. The first validation case is based on experimental results from Aota *et al.*²³³ The profiles of electron density are recorded as interferograms by a gated CCD. In the experiment, a planar tin target is irradiated by a Nd:YAG laser of 8 ns pulse duration. The target is irradiated at 60 GW/cm^2 (flat-top profile).

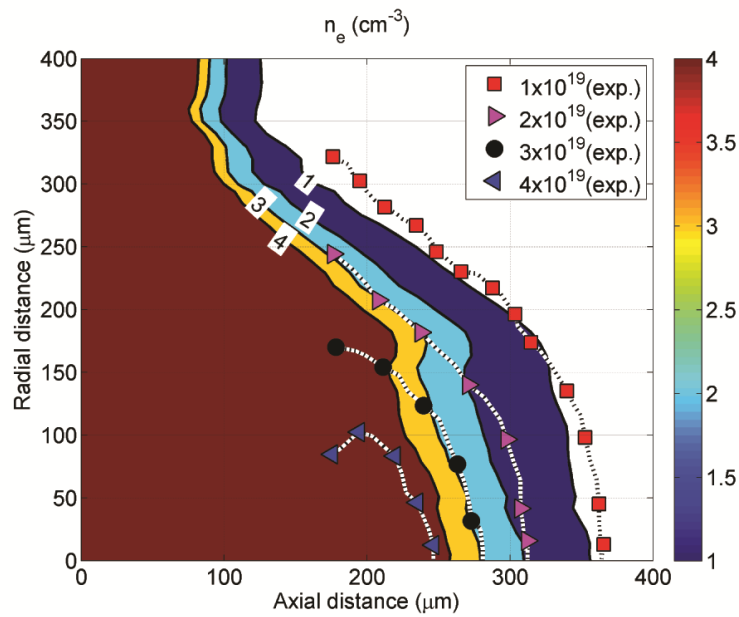


Fig. 101. Numerical (contours) and experimental²³³ (lines) electron density profiles at peak laser intensity. A flat tin target is irradiated at 60 GW/cm² by a Nd:YAG laser pulse of 8 ns duration. Overall the agreement between simulated and experimental profiles is good.

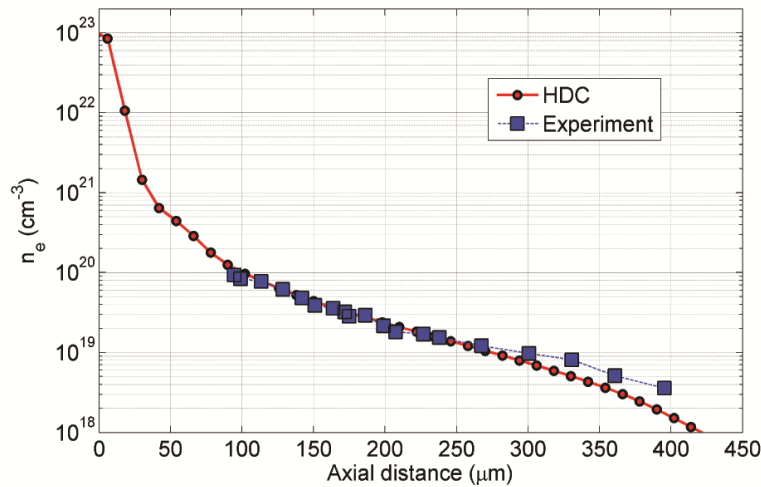


Fig. 102. Numerical (RHD) and experimental²³⁴ electron density profile along the laser axis at peak laser intensity. A flat tin target is irradiated at 100 GW/cm² by a Nd:YAG laser pulse of 10 ns duration. The agreement between the simulated and experimental profile is excellent.

In Fig. 101, the numerical and experimental electron density profiles are compared at peak laser intensity. The x-axis corresponds to the laser axis. The numerical profiles are represented by contours and the experimental profiles by lines. Overall, the agreement between simulated and measured electron density profiles is good. Along the laser axis, the magnitudes of electron density agree very well, while the radial decay of electron density is underpredicted by the RHD code. Two major reasons can be identified. First, the simulations are limited to two dimensions (planar in this

case), while the real expansion is three-dimensional. Secondly, the real pulse profile is unknown. The profile is simply specified as a flat-top profile.

In a second benchmark, the numerically predicted electron density profiles are compared to measured profiles from Tao *et al.*²³⁴, which are not part of the SEMATECH benchmarking procedure. The Nd:YAG laser intensity equals 100 GW/cm^2 for a pulse duration of 10 ns. The focal spot size equals $220 \text{ }\mu\text{m}$. The comparison of the electron density profiles along the laser axis is shown in Fig. 102. The interferometry measurements are limited to the range of distances from 100 to $400 \text{ }\mu\text{m}$ from the target surface. The excellent agreement between simulated and experimental results confirms the modeling accuracy of the RHD code.

Conversion efficiency

A major benchmarking case is the study of the dependence of CE on the laser irradiance and pulse duration for the planar tin target. This comparison between experimental and simulated CEs takes all physical process into account, which are relevant up to the end of EUV emission. The key processes, which determine the CE, are the amount of ablated mass, the laser absorption in the plasma, the plasma expansion and the radiation generation and transport. The experimental results are part of the SEMATECH benchmark.²³⁵ The results are similar to the study of Ando *et al.*⁴¹ Two different Nd:YAG lasers with pulse durations (FWHM) of 2.2 ns and 8 ns, respectively, are used to irradiate a planar tin target. In the case of 2.2 ns pulse duration, the laser spot size equals $270 \text{ }\mu\text{m}$ for irradiances larger than 200 GW/cm^2 and $660 \text{ }\mu\text{m}$ for irradiances smaller than 200 GW/cm^2 . In the case of 8 ns pulse duration, the laser spot size equals $270 \text{ }\mu\text{m}$ for irradiances larger than 200 GW/cm^2 and $660 \text{ }\mu\text{m}$ for irradiances smaller than 200 GW/cm^2 .

In Fig. 103, the comparison between experimental and simulated CEs is presented for a pulse duration of 2.2 ns. The peak CE is predicted in the experimental case for an irradiance of 50 GW/cm^2 , while the simulations predict the peak value of 2% at 100 GW/cm^2 . In both cases the fall off for higher irradiances is comparable. The decrease in CE for irradiances smaller than the peak value is more pronounced in the computational results. Similarly, the RHD code predicts a higher irradiance for the peak CE using the 8 ns pulse, as shown in Fig. 103b. In this case, the predicted peak CE is 10% larger than the experimental value. Again, the fall-off at lower irradiances is more pronounced in the simulated results. Overall the same trends are reproduced, with the largest discrepancy at irradiances lower than the irradiance of optimum CE.

The causes for the disagreement can be found on the experimental and computational sides. On the experimental side, a major uncertainty on CE results from the extrapolation into 2π of the discrete point measurements. Indeed, the measurement angle plays a vital role in determining the emitted EUV power. Additional uncertainties are related to the laser pulse characteristics and the calibration of the EUV powermeter. Additional measurements for the CE of the planar target can be found in the work of Hayden *et al.*,²³⁶ Koay *et al.*,²³⁷ Tao *et al.*⁴² and Harilal *et al.*⁴⁹ In the work of Tao *et*

al.,⁴² a 7 ns Nd:YAG laser pulse, which is focused to a 200 μm spot size irradiates a pure tin target. The optimum CE of 2% is obtained in the range from 100-200 GW/cm^2 .

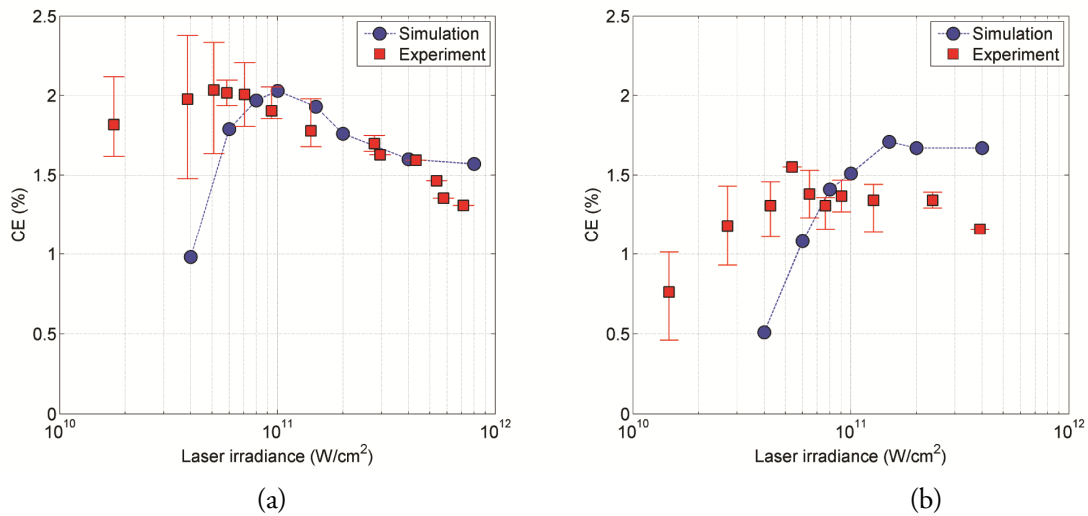


Fig. 103. Simulated (RHD) and measured²³⁵ dependence of CE on the incident Nd:YAG laser intensity and the pulse duration for the planar tin target. (a) The pulse duration equals 2.2 ns. (b) The pulse duration equals 8 ns.

It is observed that the simulations reproduce the trends of the experiments more accurately if the computational results are shifted towards lower irradiances. Under the assumption that the experiment is more accurate than the RHD code, the computational results seem to underestimate the plasma temperature, which is obtained at a given irradiance. Indeed, for a pulse duration of 2.2 ns and an irradiance of 40 GW/cm^2 , the computed mean electron temperature is in the range of 22 eV. Therefore, no significant EUV emission can be expected at this irradiance.

Potential reasons for the underestimation of the electron temperature are an underestimated laser absorption or, most probably, overpredicted radiation losses. A possible cause for the overprediction of the radiation losses could be the full-band emissivity computation. Indeed, the full-band emissivity is estimated by the black body assumption for electron temperatures and densities, which are not included in the tabulated results from the atomic modeling. At the lower temperature boundary of the tables of emissivity and opacity, the emissivities predicted by the black-body assumption are significantly larger than the ones predicted by the atomic physics code.

Angular EUV emission

A possible benchmark for the radiation transport model relies on the anisotropy of the radiation emission. The experimental results are taken from Morris *et al.*²³⁸ A Nd:YAG laser with a pulse duration of 7 ns and a pulse energy of 400 mJ irradiates a planar tin target. The study addresses the angular distribution of EUV emission.

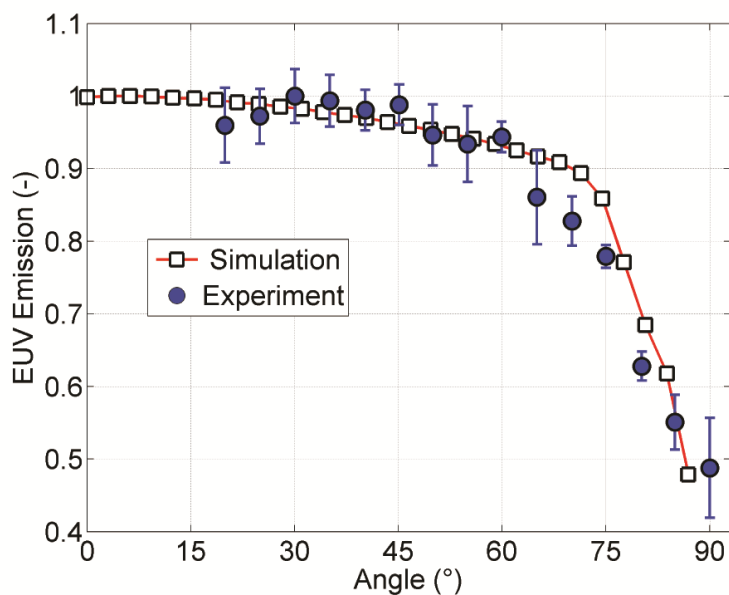


Fig. 104. Simulated (RHD) and experimental angular distributions of in-band emission.

In Fig. 104, the simulated and measured angular distribution of EUV emission is presented. The angle of 0° corresponds to the line of sight along the laser axis, while 90° corresponds to the direction along the target surface. The agreement between computational and experimental results is very good. As a consequence, the radiation transport model, which is based on flux-limited diffusion accurately predicts the anisotropy of the EUV emission for a planar tin target.

In summary, the agreement between experimental and numerical results has been assessed by a set of studies, which include the emission and absorption spectra, the main equation of state characteristics, the plasma electron density, the CE and the anisotropy of EUV emission. The general agreement between numerical and experimental results justifies the use of the RHD code for further studies.

6.3.2.1.2. Baseline simulation setup

The baseline simulation is conducted at operating conditions, which are representative for the irradiation of tin droplets in the EUV sources at ETH Zurich. The main inputs to the simulations are the droplet size, the collector geometry and the laser settings.

A large range of droplet sizes have been generated in the facilities at ETH Zurich. In this study, the droplet size is fixed to $50\ \mu\text{m}$. The target material is pure tin. The displacement of the droplet during the laser irradiation is neglected. Indeed, for a droplet velocity of $10\ \text{m/s}$ and a total laser pulse duration of $70\ \text{ns}$, the displacement along the axis of propagation is $0.7\ \mu\text{m}$, which corresponds to 1.4% of the droplet diameter. Furthermore, the tin droplet is assumed to be circular. In the baseline case, perfect targeting, namely a perfect alignment of the laser spot and the tin droplet, is assumed. The vacuum pressure is fixed to $10^{-4}\ \text{mbar}$.

The Nd:YAG laser is operated at 1064 nm. The laser repetition rate can be adjusted up to 20 kHz. The simulated irradiance is 200 GW/cm². The adjustable spot size is fixed to 80 μm. The characteristics of the real pulse profile in time and space are shown in Fig. 105. The temporal profile is following a Gaussian, except for the tail of the pulse. The simulated laser pulse duration (FWHM) is 21 ns. From the laser spot image, recorded with a SPIRICON beam profiler, the mean spatial profile is derived. The error bars are due to non-uniformities in the real pulse profile. The fitted Gaussian has 25% lower energy than the real pulse. The real pulse shape is implemented in the RHD code.

On the computational side, the domain size and number of grid cells are the most important input parameters. The domain size must be chosen such that the plume is included in the domain. In case the plume crosses the boundaries of the domain, the laser absorption and radiation transport become non physical. The result is an overprediction of CE. For accurate modeling, a “layer” of vacuum should always be included between the plume and the domain boundaries.

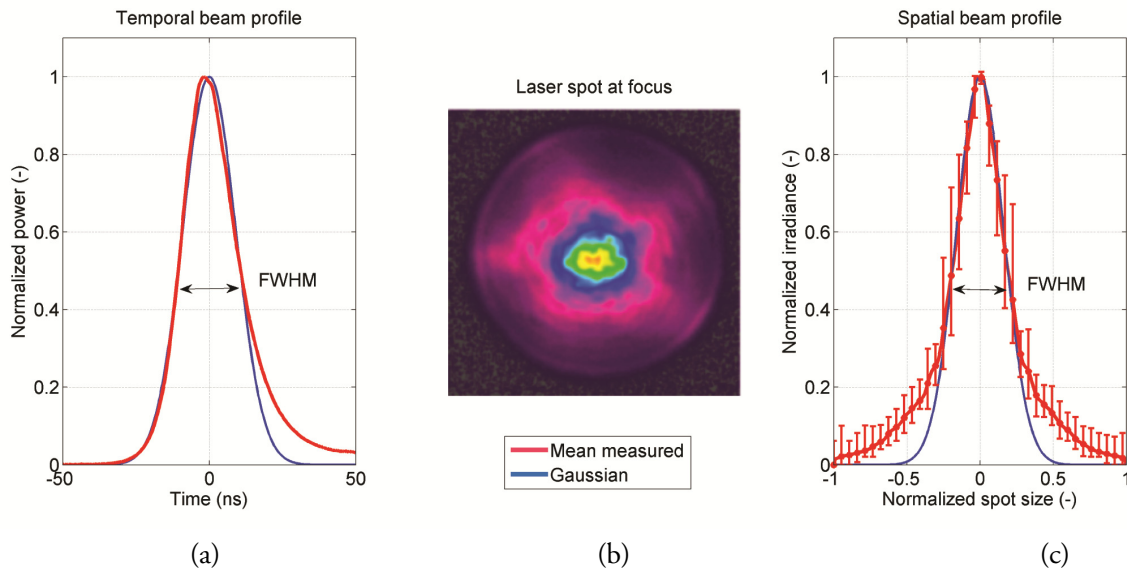


Fig. 105. (a) Beam profile in time and Gaussian fit. (b) Spiricon image of focused laser spot. (c) Measured spatial beam profile and Gaussian fit.

The number of grid cells is determined by the cells’ length scales in comparison to the laser spot and droplet size. The grid sensitivity has been studied for the validation case of the planar target, which is irradiated by a 2.2 ns pulse. The normalized CE is presented as a function of the numbers of cells included in the laser spot diameter (FWHM) in Fig. 106. A minimum resolution of the laser spot diameter of 50 cells is derived to achieve an accuracy of ~1% when compared to the larger resolution cases. In order to achieve this accuracy for an 80 μm laser spot, the cell size should be 1.6 μm. The normalized computational times are also indicated for each grid resolution in Fig. 106.

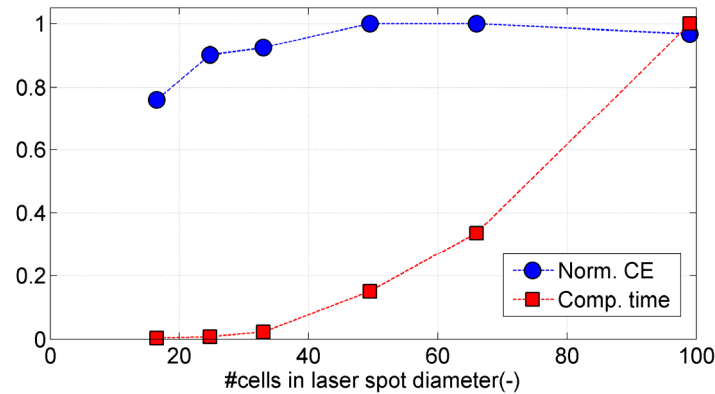


Fig. 106. Grid sensitivity for the planar tin target validation case. The CE is used as a monitor for the grid sensitivity. The CE converges if the laser spot (FWHM) is resolved by 50 computational cells. The required computational time for each grid size is also indicated.

6.3.2.1.3. Plasma formation

The initial target ablation strongly influences the plasma formation. The laser ablation, which is mainly determined by the equation of state and the absorption model, is a major step in generating accurate predictions of the LPP dynamics. A pronounced sensitivity of the key plasma characteristics, such as temperature and density to the amount of ablated mass, has been observed.

In order to illustrate the physics of the initial target ablation, snapshots of the mass density, electron temperature and density are taken at 0.8% and 3.2% pulse duration, as shown in Fig. 107. The laser enters the computational domain from the right and irradiates the right hemisphere of the droplet. Figure 105a presents the mass density distributions during the target ablation. For a pulse duration of 21 ns (FWHM), an initial high density layer of less than then 10 μm forms after 0.5 ns. The initial ablation layer is uniform along the surface of the right hemisphere, which implies that the net ablated mass per unit area is relatively constant.

After 2 ns, the ablation layer has transformed into an anisotropic plasma plume. The largest velocities occur along the laser axis and along the direction perpendicular to the laser axis. A kink is found in the expansion plume around 45° . The plume also weakly expands in the free space around the left hemisphere of the droplet. At 2 ns, a small vapor layer is observed on the backside of the droplet. This layer is a modeling artifact. Indeed, both the surface temperature of the droplet and the vapor pressure of tin are too low to generate such a layer. The layer formation is related to the applied evaporation model and the flux transport.

The explanation for the origins of the expansion anisotropy can be found in the distributions of electron temperature, as shown in Fig. 107b. The peak electron temperature increases from 5 eV to 8 eV between 0.5 ns and 2 ns. The laser absorption in the section of the plume, which is oriented towards the laser, is responsible for an increased kinetic energy in this portion of the plume. As a

result, the plume experiences the largest acceleration along the laser axis. In the region of the kink around 45° , the velocity vectors present a deflection from the radial direction towards to the laser axis. As stated above, the ablated mass per unit surface area is relatively constant. Therefore the more pronounced acceleration along the laser axis entrains the flow from the peripheral region. In the direction perpendicular to the laser axis, the plume expansion is no longer influenced by the expansion along the laser axis. As a consequence, the expansion velocity increases in this direction.

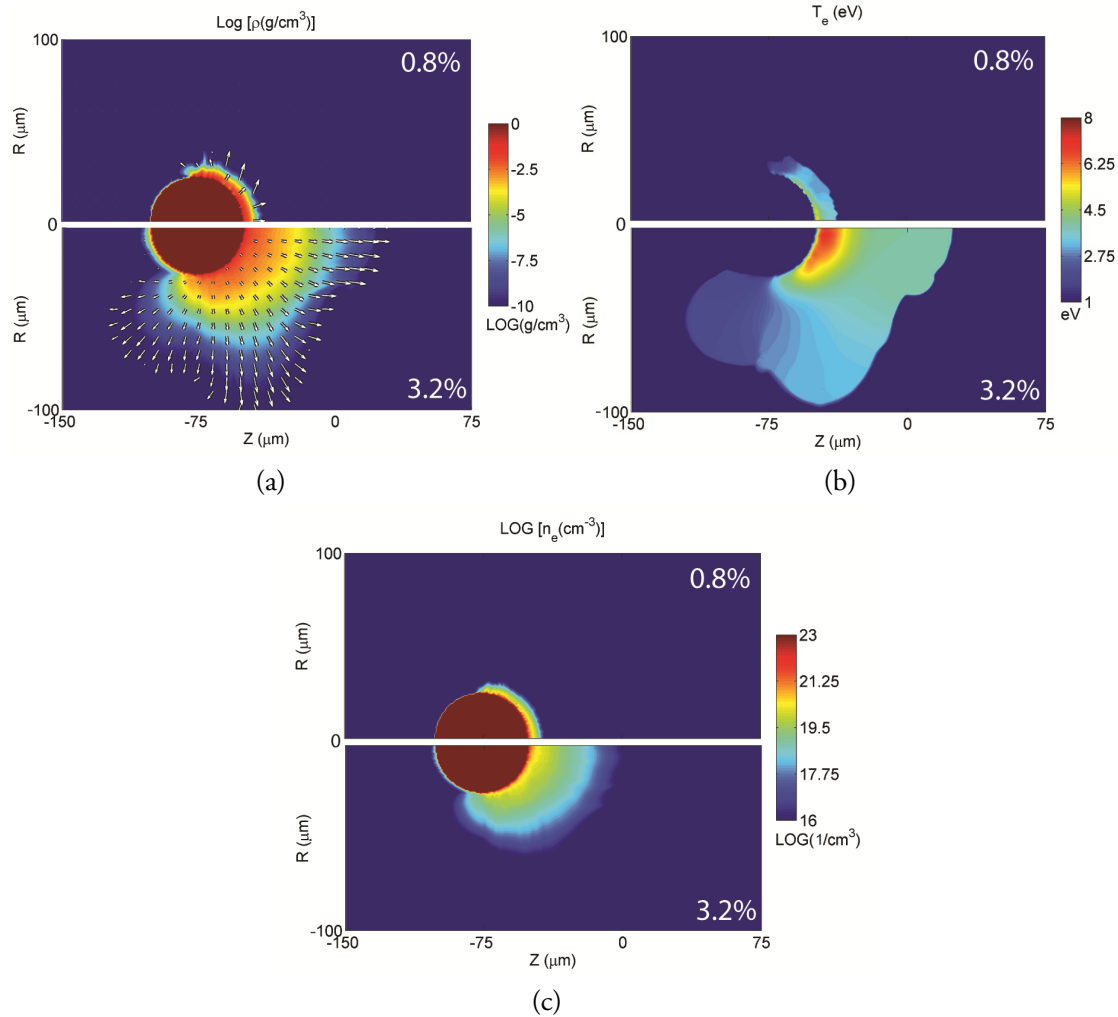


Fig. 107. Initial stages of target ablation and plasma formation after 0.8% (upper) and 3.2% (lower) pulse duration. The Nd:YAG laser is incident from the right. (a) Mass density (contours) and velocity (vectors), (b) electron temperature and (c) electron density. The laser is incident from the right.

The increase in peak electron temperature is limited by the growing plume, which absorbs laser energy along the laser axis. This absorbed laser energy is redistributed by thermal diffusion inside the plume. The time scale of the thermal diffusivity of the plasma is significantly smaller than the one of the liquid tin. Indeed, the temperature of the droplet remains largely unaffected by the ablation.

The temperature distribution is determined by thermal diffusion and laser absorption, both of which strongly depend on electron density. Radiation transport can be neglected at low electron temperatures. The electron density decreases radially between the target surface and the vacuum environment, as shown in Fig. 107c. As described in Sec. 6.1.1, the region of resonance absorption is located just in front of the surface of critical density of $n_e=10^{21} \text{ cm}^{-3}$ (for a Nd:YAG laser). According to Fig. 107c, the surface of critical density sits close to the target surface for both time instances of 0.5% and 3.2% of the total pulse duration. This explains the position of the high temperature region, which also develops close to the target surface. The position of the high temperature region plays a crucial role in target heating, as well as in the radiation transport.

6.3.2.1.4. Hydrodynamics at peak laser intensity

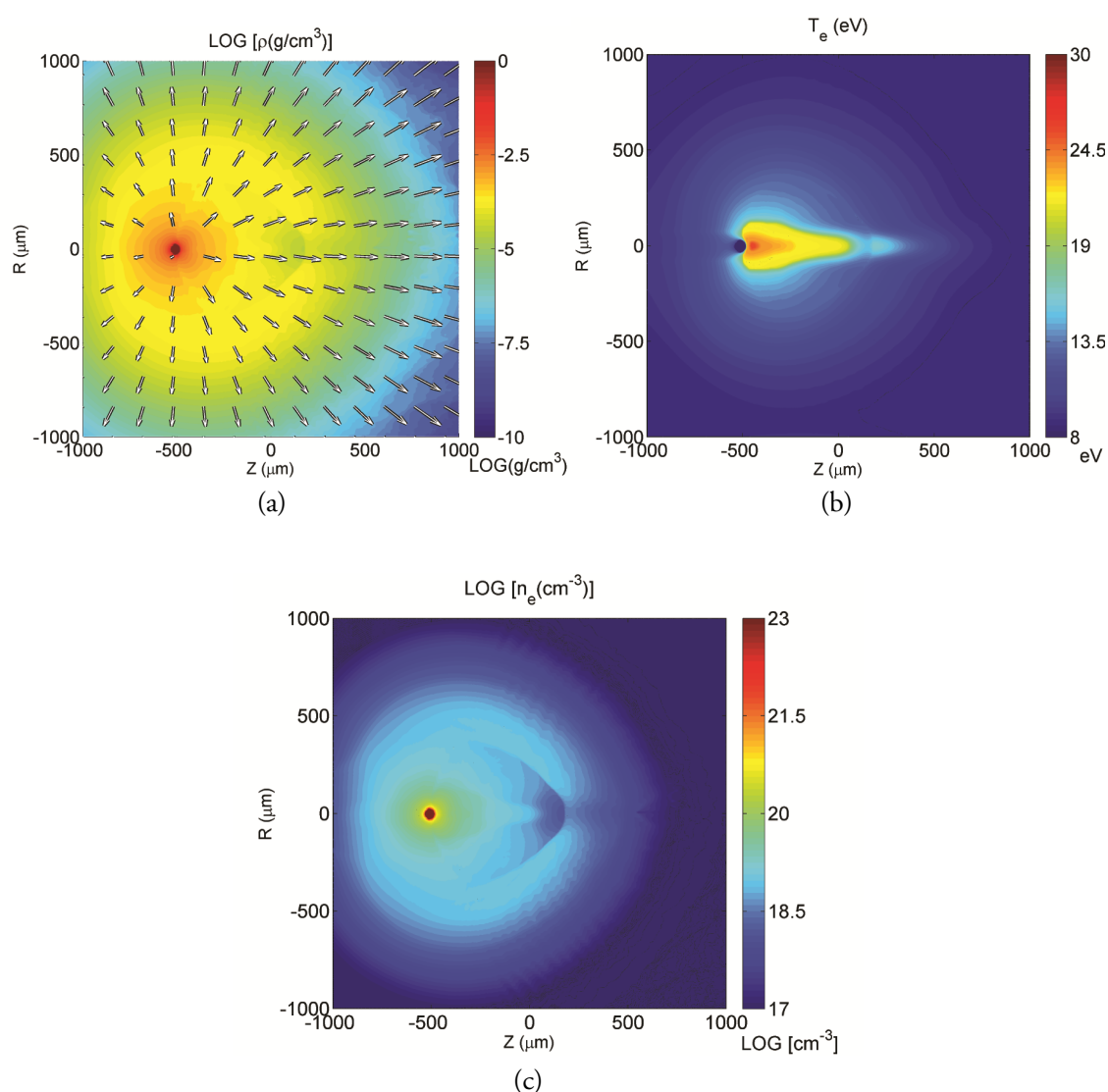


Fig. 108. Spatial distribution of (a) mass density and velocity field, (b) electron temperature and (c) electron density at peak laser intensity. The laser is incident from the right.

The plasma characteristics around the peak laser intensity, which is equivalent to 50% pulse duration are of particular interest, as the peak electron temperature and EUV emission are typically obtained around 50% pulse duration. The main physical quantities, namely the mass density, the electron temperature and density are shown in Fig. 108.

The plasma expansion is not isotropic, as illustrated by the spatial mass density distribution and the velocity field in Fig. 108a. Indeed, the radial density gradient varies as a function of angle. Along the laser axis, the density decreases by 7 orders of magnitude over a distance of 1.5 mm. The largest velocities are found along the laser axis, due to the direct heating by laser energy of this fraction of the plume. For the same reason, the lowest velocities are found on the backside of the irradiated droplet. Overall the velocities on the front-side are approximately two times larger than on the back-side at peak laser intensity. A major discontinuity in the mass density distribution is formed in front of the droplet around $z=200 \mu\text{m}$. The formation of this discontinuity is detailed below.

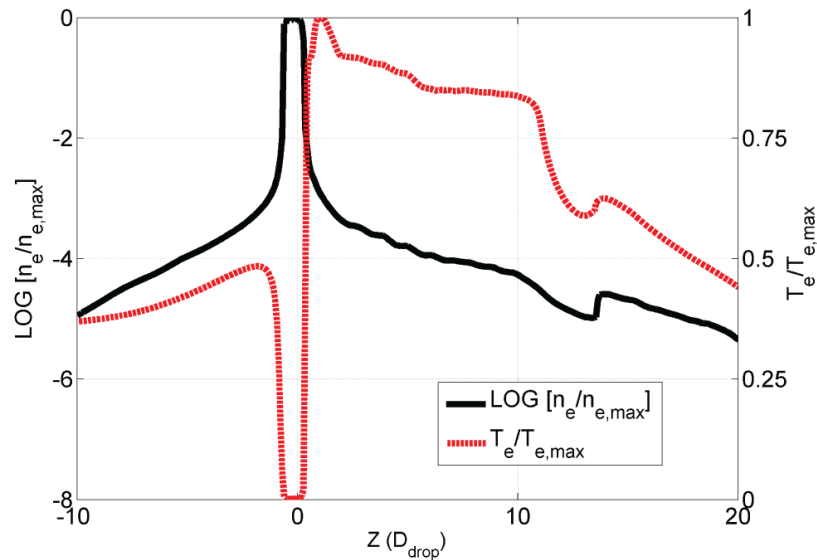


Fig. 109. Spatial dependence of electron density and temperature along laser axis. The highest temperature is observed in front of the layer of critical density.

The high temperature region is located in front of the droplet and stretched along the laser axis, with peak temperatures close to the droplet surface, as shown in Fig. 108b. Peak temperatures of 28 eV are obtained at peak laser intensity for the present laser settings. The discontinuity, which is observed in the mass density distribution is also present in the electron temperature distribution at $z=200 \mu\text{m}$. On the side of laser irradiation, a small region of high temperature separates from the main region. The electron density is set by the electron temperature and the ion (mass) density. The distribution of electron density mainly follows the distribution of mass density, as shown in Fig. 108c. The high temperature region with its increased mean ionization is barely visible. While the mean ionization varies by 1 order of magnitude, the ion density varies by 10 orders of magnitude.

The surface of critical density of $n_e=10^{21} \text{ cm}^{-3}$ (for a Nd:YAG laser) is closely located to the target surface.

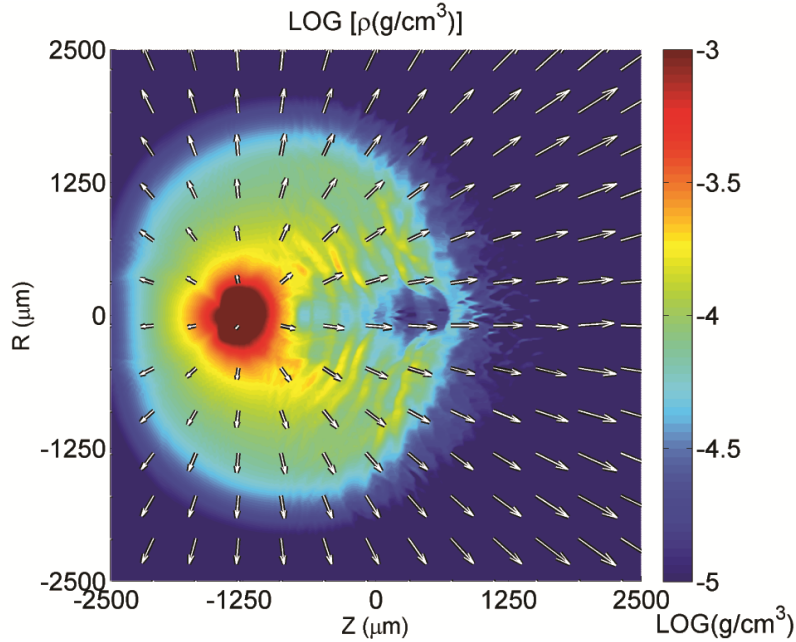


Fig. 110. Mass density distribution at the end the laser pulse with the formation of the lower density region in front of the target and along the laser axis.

The distributions of electron temperature and density can be plotted along the laser axis in order to generate a plot similar to Fig. 83. The axial distance is non-dimensionalized by the droplet diameter and all values are taken at peak laser intensity. The electron density decays almost symmetrically on both sides of the droplet, as shown in . The electron density on the irradiated side of the droplet is slightly higher due to an increased electron temperature and mean ionization. The maximum electron density is reached at the target surface, due to the large ion density. The lowest electron temperature is found in the droplet, while the peak is reached in front of the layer of critical density of $n_e=10^{21} \text{ cm}^{-3}=10^{-2}n_{e,max}$. The stand-off distance of the high temperature region from the target equals approximately 1 droplet diameter. The electron temperature decays to about 80% within 10 droplet diameters from the peak temperature. The previously described discontinuity is also observed in Fig. 109 at a distance of 13 droplet diameters from the target.

The discontinuity appears around 30% pulse duration, when a fraction of the high temperature core starts to separate. This front part of the high temperature core expands to a level where it becomes almost transparent to laser light. Indeed the mass supply from the target is restricted to the regions closer to the target. The initially high thermal energy is continuously transformed into kinetic energy. A shock wave forms as the flow has a larger kinetic energy (and thermal energy) as the surrounding plume. Eventually this mechanism leads to a separation of the plume, as illustrated in the mass density distribution at the end of the laser in Fig. 110. The expansion of the hot plasma core into the high density and vacuum regions after peak laser intensity is observed in experiments from Tao *et al.* for a planar tin target.²³⁹

The electron temperature and density determine the distributions of the individual ion populations. The spatial distributions of the tin ions, which contribute to EUV, are summarized in Fig. 111. The results are obtained from the collisional radiative model, which is described in Sec. 6.2.1.2. The EUV emitting ions are all found in the region of high electron temperature from . At peak laser intensity, the most dominant ion species is Sn^{8+} with a fraction around 50% in the high temperature region. The core region of EUV emission mainly contains Sn^{8+} and Sn^{9+} . At peak electron temperature, ions up to Sn^{10+} are found at significantly lower fractions than Sn^{8+} . In the next section, the EUV emission from these ions and especially the related radiation transport is further investigated.

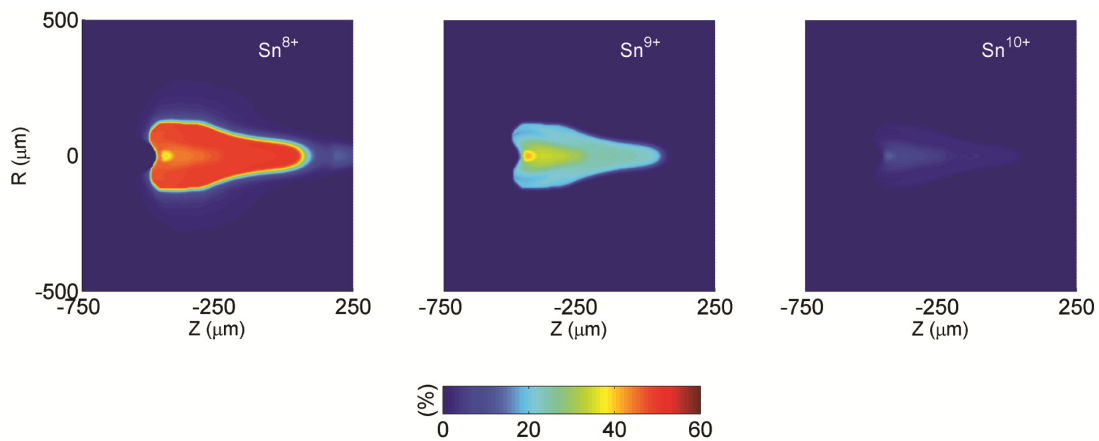


Fig. 111. Ion fractions in the high temperature region on the irradiated side of the droplet. The most dominant ion fraction is Sn^{8+} , while ions up to Sn^{10+} are found.

6.3.2.1.5. Radiation characteristics at peak laser intensity

This section presents the radiative characteristics of the LPP at peak laser intensity, as determined by the RHD code. First the spatial distribution of absorbed laser energy is detailed. Then, the main results of the radiation transport, which include the spatial distribution of EUV energy density, are presented. A key result is the full-band and EUV angular flux distribution on the collector. This section concludes with the temporal evolution of the full-band and EUV emission with respect to the absorbed laser energy.

The distribution of laser energy correlates with the distribution of electron temperature, as shown in Fig. 112. The distribution has the lateral extension of the laser profile, which has a FWHM of $80 \mu\text{m}$. The electron temperature has a larger extent, due to thermal and radiative diffusion. As expected, most of the laser energy is absorbed near the critical surface. The contours of absorbed laser energy also confirm that the discontinuity, which is observed in the mass density and electron temperature distributions at $z=200 \mu\text{m}$, is transparent to the laser wavelength.

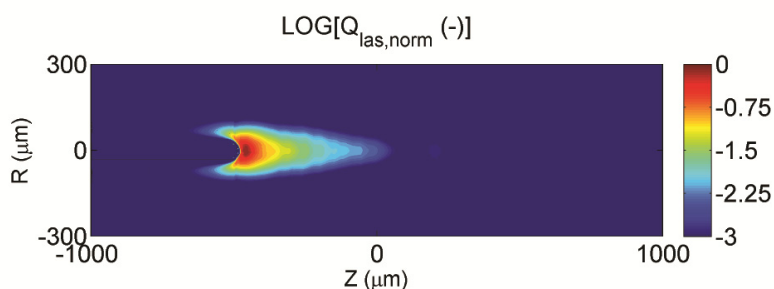


Fig. 112. Spatial distribution of absorbed laser energy for an 80 μm (FWHM) Nd:YAG laser and 50 μm tin droplet at peak laser intensity. The largest absorption is observed near the surface of critical density.

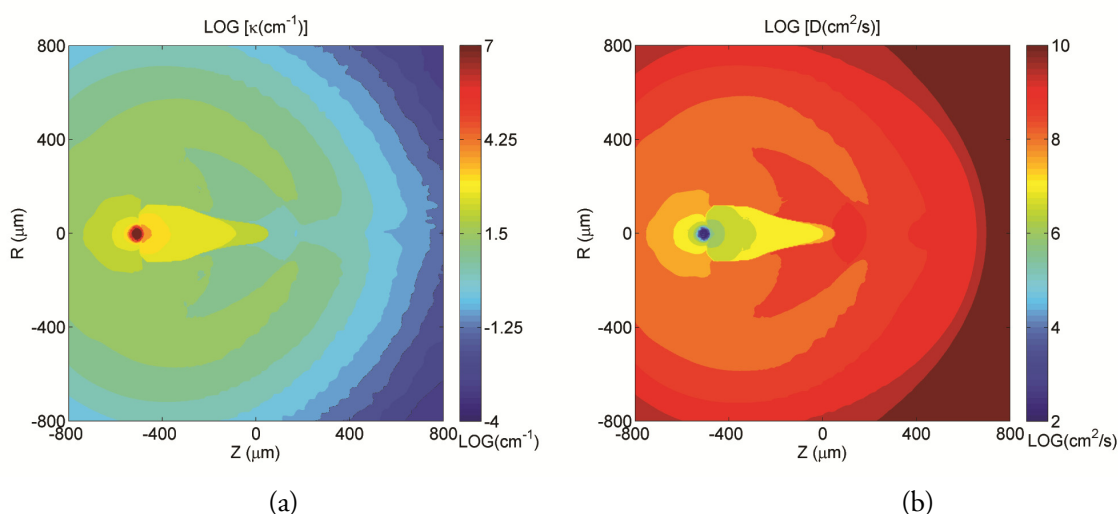


Fig. 113. (a) In-band opacity and (b) diffusion coefficient at peak laser intensity. The strong variations in optical thickness imply an angular variation of the EUV flux.

In order to determine the radiation characteristics of the LPP, the flux-limited diffusion model is applied. The diffusion is determined from the opacity of the plasma. The spatial distribution of the EUV opacity, which is equal to the inverse of the photon mean free path, is shown in Fig. 113a. As the opacity depends on electron temperature and density (Sec. 6.3.1.3), it essentially follows these distributions. The largest in-band opacity is found for the droplet and the high-temperature plasma core. The EUV opacity is lower along the laser axis than in the perpendicular direction. Furthermore, the optical thickness, which corresponds to the opacity integrated along a line of sight, increases with increasing angle from the laser axis. As a consequence, the EUV flux can be expected to be maximized along the laser axis, while the lower temperature coronal region absorbs the EUV flux and reemits at a lower spectral efficiency. The EUV diffusion coefficient follows the distribution of the in-band opacity. In the coronal region, the diffusion coefficient is reduced by approximately one order of magnitude when compared to the diffusion coefficients in the plasma core and the region along the laser axis. The variation in opacity and diffusion coefficient is reflected in the distribution of the angular emission fluxes.

The radiation solver also predicts the EUV radiation energy density, which gives an idea of the source etendue, as shown in Fig. 114. The EUV energy density, which is determined by the in-band emissivity and opacity, correlates with the ion distributions of Sn^{8+} , Sn^{9+} and Sn^{10+} , which are presented in the previous section. The spatial distribution of EUV energy yields a source size on the order of $100\ \mu\text{m}$, which is confirmed by pinhole camera measurements at ETH Zurich.⁵⁸

The angular dependence of the full-band and in-band fluxes is shown in Fig. 115. The fluxes are normalized for better comparison. The zero angle corresponds the laser axis, while 90° corresponds to the direction perpendicular to the laser axis. The full-band flux decays from its maximum value at the laser axis to 10% of its initial value at 30° . The full-band flux at 90° equals 66% of the flux at the laser axis. In general, a lower decay than in the planar case is expected, as the expansion is more isotropic. The decay of the EUV flux is however more pronounced. At 30° , the EUV flux is reduced to 76% of its value at the laser axis. At 90° from the laser axis, the EUV flux has been reduced to 39% of its peak value. This distribution, with a more pronounced peak around the laser axis, can be expected from the EUV opacity distribution, which reveals a strong variation of optical thickness with angle.

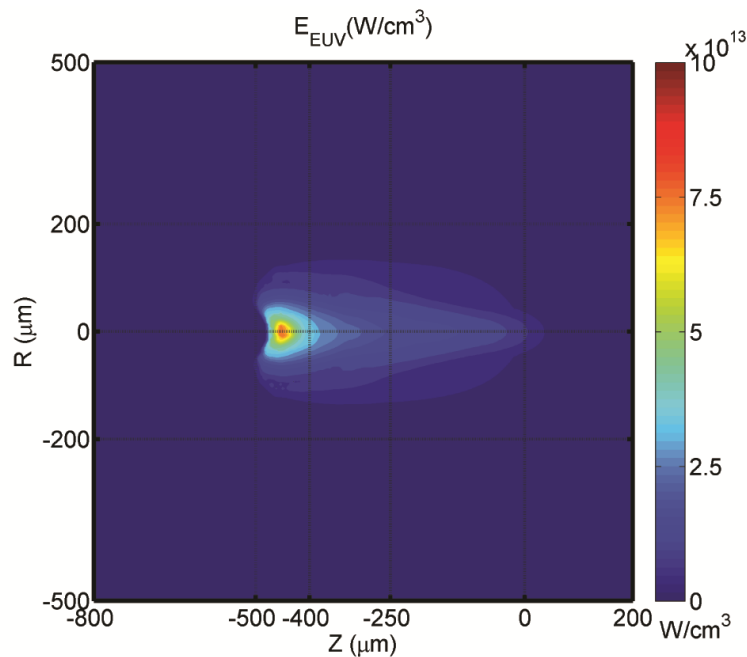


Fig. 114. Spatial distribution of EUV radiation energy density at peak laser intensity for a $50\ \mu\text{m}$ tin droplet irradiated by a Nd:YAG laser.

The decay of the full-band emission with increasing angles should be smaller than for the EUV emission. Indeed for the full-band emission, the spectral efficiency in the reemission process is 100%, while EUV emission is only partially reemitted. In all cases, a fraction of the reabsorbed radiation energy is also transformed into thermal energy.

The computed time dependences of the EUV and full-band emission are presented in Fig. 116. Both, the EUV and full-band fluxes are integrated in 2π sr. The applied laser energy and the absorbed fraction of laser energy are also included in the plot. All quantities are integrated in time up to the considered time instance.

For the given laser-target configuration, laser energy is almost completely absorbed, except in the initial phase. Indeed, during plasma formation, a fraction of the laser energy is reflected at the target surface and later at the surface of critical density. After 25% pulse duration, the laser coupling into the plasma is very efficient. The absorbed laser energy is only partially transformed into radiation. In the studied case, more than 40% of the absorbed energy is transformed into expansion work or remains as thermal energy in the plasma at the end of the laser pulse. A minor fraction of the full-band emission is located in the EUV window.

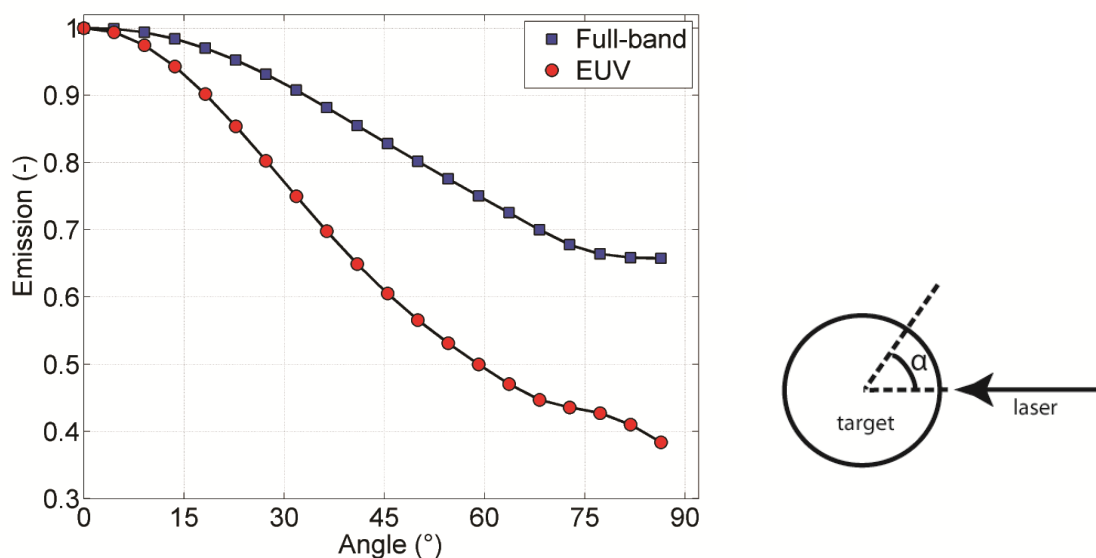


Fig. 115. Angular dependence of (a) the full-band and (b) EUV fluxes. The zero angle corresponds the laser axis, while 90° corresponds to the direction perpendicular to the laser axis.

EUV emission is maximized at peak laser intensity, with 85% of the radiation generated in a band of $\pm 15\%$ (10 ns) of the total pulse duration, centered at the peak laser intensity. Although the integrated full-band emission has not converged at the end of the laser pulse, the major part of the full-band emission also takes place around peak laser intensity. The generated full-band radiation equals 68% in the band of $\pm 15\%$ (10 ns) of the total pulse duration, centered at the peak laser intensity.

In the next section, the large scale evolution of the plasma debris is studied using the PIC-DSMC particle code. The hydrodynamic results, which are obtained from the RHD code provide the initial conditions for these large scale studies.

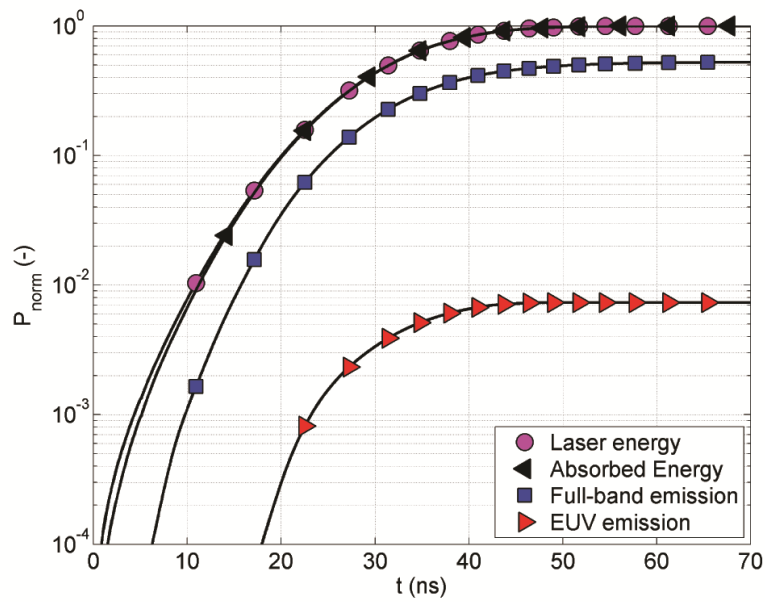


Fig. 116. Time dependence of the EUV and full-band emission, relative to the supplied laser energy. The radiation fluxes are integrated in 2π sr, according to their detailed spatial distribution. All quantities are integrated in time up to the considered time instance. The absorbed laser energy is also indicated.

6.3.2.2. Large-scale debris prediction

The expansion of the LPP comprises different length scales, ranging from the ablation layer (10^{-6} m) up to the mirror location (1 m). These length scales, which range over 6 orders of magnitude, correspond to an 18 order of magnitude decrease in density. After continuum breakdown, the particle code is employed to detail the spatial and temporal characteristics of the ion debris up to the optics' length scales. The boundary and initial conditions for the particle code are specified at an unsteady interface on which sampled particles with Maxwellian distributions are determined from the RHD code, as described in Sec. 6.2.3. The hybrid hydrodynamic-particle code is applied to the previously described laser-target configuration, that is a $50\ \mu\text{m}$ Sn droplet and a Nd:YAG laser with an irradiance of $200\ \text{GW}/\text{cm}^2$.

6.3.2.2.1. Baseline simulation setup

The most relevant simulation input parameters, such as the laser and target characteristics are defined for the RHD. The main setup parameters for the particle code are the collector dimensions, the PIC grid and the macro-particle factor. The number of PIC grid cells, as well as the macro-particle factor, is chosen according to the studies of Rebholz.²¹⁶

The modeled collector has an elliptic shape. A first focus includes the irradiation site and the second focus corresponds to the intermediate focus. The dimensions correspond to the first generation collector, which has been developed at ETH Zurich with a diameter of approximately 300 mm.⁵⁷ In

the following baseline study, the collection angle ranges from 8° to 75° .

6.3.2.2.2. Tin ion dynamics up to the EUV collector

The evolution of tin ions up to the EUV collector is studied. The contours of the spatial distributions of the number density of the charged particles are presented in Fig. 117. The snapshots are taken at $8.3 \mu\text{s}$ at which time the expansion has reached the sub-meter scale. The laser is incident from the right. Ionized particles up to Sn^{6+} reach the optics, while more highly charged particles (up to Sn^{10+}) are found during EUV emission. Particles with large ionization stages partially recombine after laser irradiation, before reaching optics. Additionally, it should also be noted that the number densities of the higher ion stages are below the resolution threshold of the particle code. Fast ions are generated, while the overall density of the plume is relatively high. This resolution threshold is determined by the macro-particle factor.

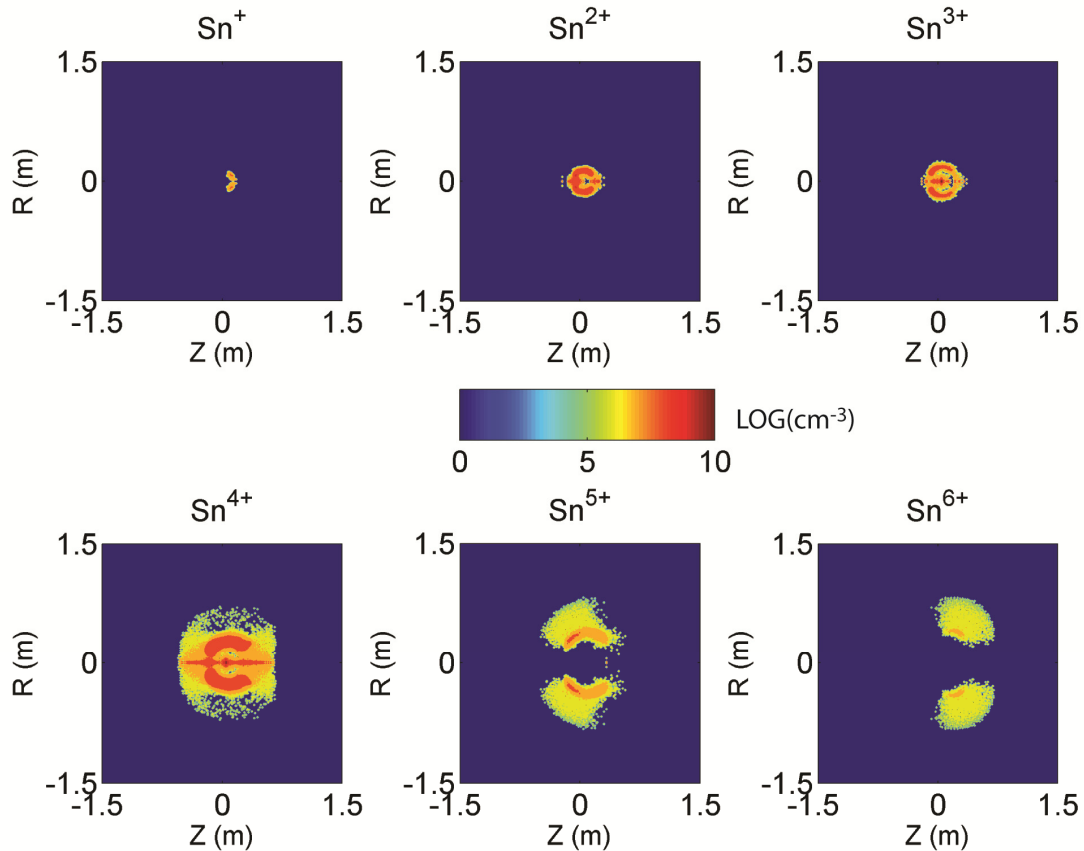


Fig. 117. Spatial density distribution of tin ions at large scales. The snapshots are taken at $8.3 \mu\text{s}$.

In general, the expansion velocity increases with the degree of ionization, as reflected by the ion-acoustic velocity from Sec. 6.1.3. In the PIC model approach, the acceleration of a particle by the self-induced electric field is proportional to its charge. Furthermore the number density drops as the charge state increases. This is due to recombination after peak laser intensity and to the limited

amount of highly ionized particles in the plasma plume during the laser-plasma interaction. The expansion of Sn^{2+} , Sn^{3+} , Sn^{4+} ions is radially relatively uniform, with comparable number densities in all directions, except along the laser axis. The only ion that expands along the laser axis is Sn^+ . For the studied laser-target configuration, Sn^{5+} and Sn^{6+} are the most energetic ions, which are resolved. The distributions of both ion types are strongly non-uniform. For Sn^{5+} an elevated number density is found in the back part of the plume (90° - 150°). For Sn^{6+} , the number density reaches a maximum around 60° from the laser axis. The most energetic ions do not expand at a significant number density in the forward region along the laser axis ($\pm 30^\circ$).

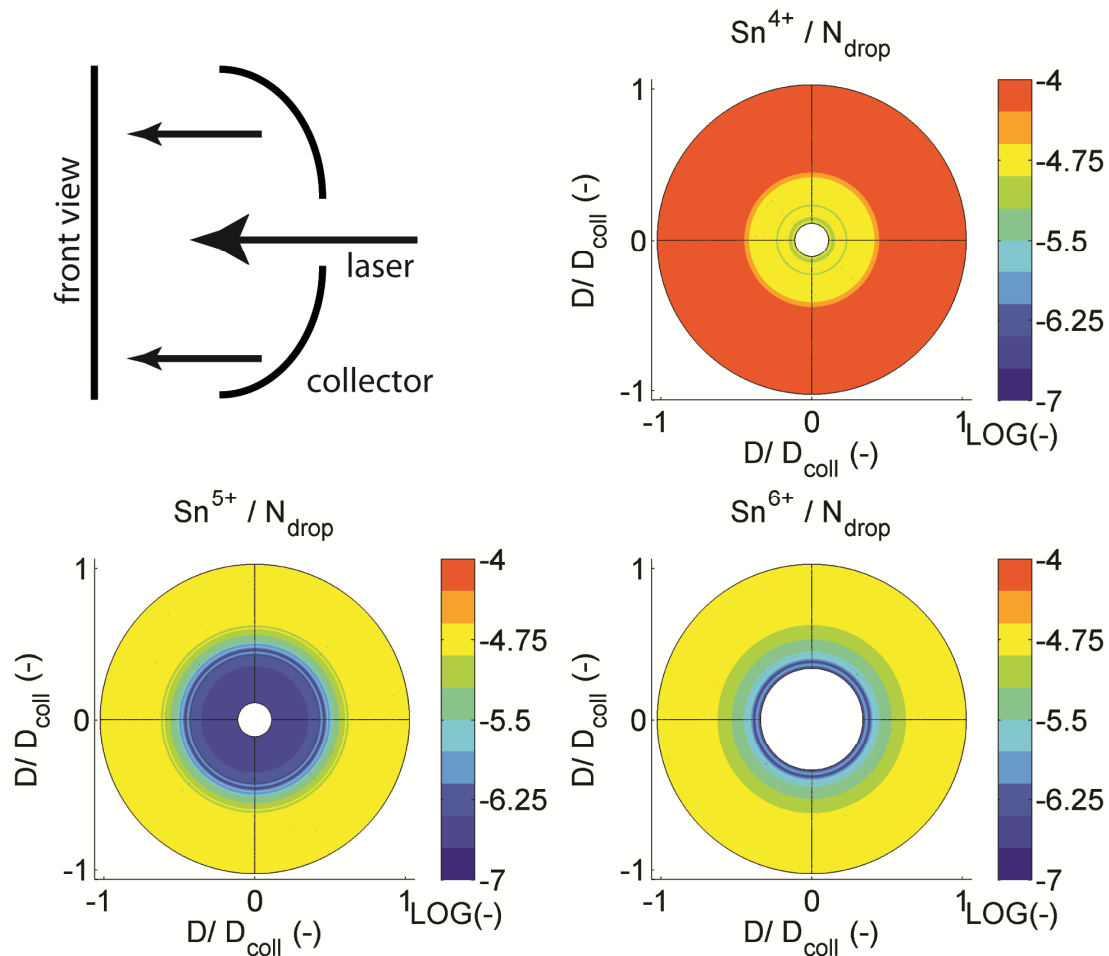


Fig. 118. Spatial distribution of tin ions Sn^{4+} , Sn^{5+} and Sn^{6+} on the EUV collector.

The temporal and spatial number density distributions are next used to evaluate the temporally integrated particle distributions at the EUV collector, as shown in Fig. 118. The angular particle distributions show low differences for plasma sizes in the sub-meter scale. This trend is confirmed by the radial kinetic energy plots of . Therefore the obtained angular particle abundances are valid for typical EUV collector sizes of a several 100 mm. A frontal mirror view of the spatial distribution of the ratio of ions to the initial number of particles in the target is shown in Fig. 118. The largest abundances of Sn^{4+} , Sn^{5+} and Sn^{6+} are found close to the outer border of the collector (50°). The

lowest abundances are found on the inside of the collector between 0° and 30° . The most energetic ion, namely Sn^{6+} has no contribution in this inner region.

The simulation typically underestimates the abundance of weakly ionized and neutral tin atoms. Indeed, the hydrodynamic simulation is terminated before these slow particles are transferred to the particle simulation. This especially occurs for neutrals, which are formed during the ongoing droplet evaporation and are therefore not captured. The diffusion velocity of neutrals is several orders of magnitude smaller than the expansion velocity of the highly energetic ions. The focus of the hybrid code is on fast ion erosion prediction, while the neutral diffusion can be predicted by extrapolation from the RHD code.

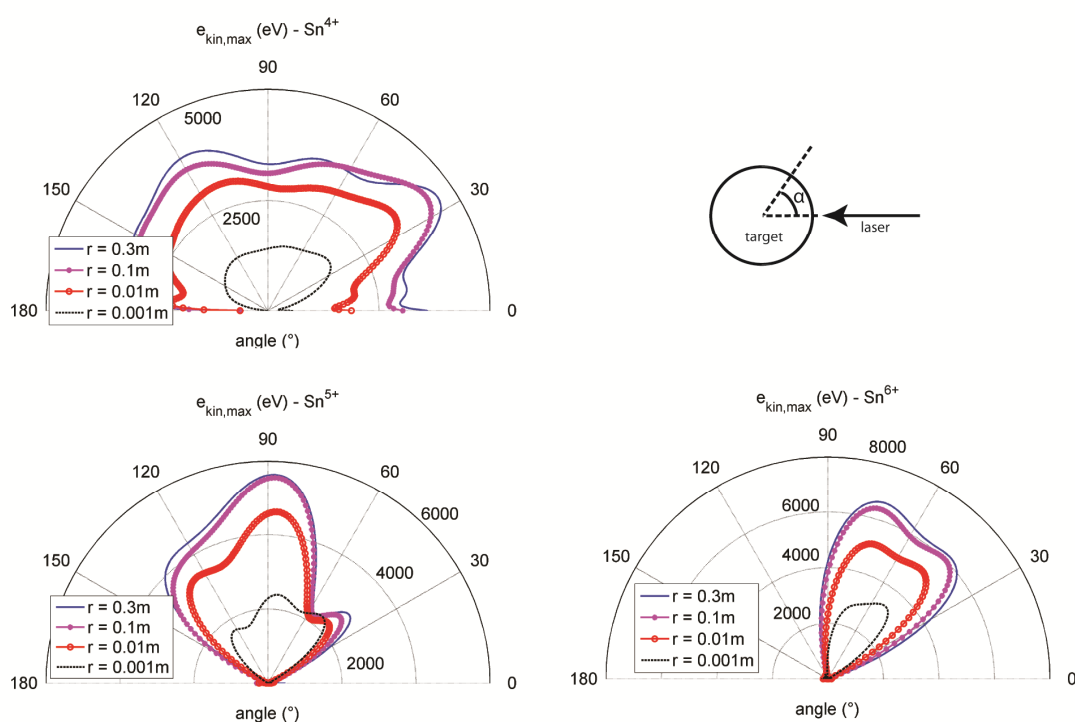


Fig. 119. Angular distribution of kinetic energies of Sn^{4+} , Sn^{5+} and Sn^{6+} at different radii ($r=0.001,0.01,0.1,0.3\text{m}$)

For the prediction of collector erosion, the two key physical parameters are the ion kinetic energies and the ion density distributions. The angular distribution of the maximum kinetic energies for Sn^{4+} , Sn^{5+} and Sn^{6+} as function of radius are shown in Fig. 119. Overall, the kinetic energies are significantly dependent on the expansion radius with minor changes for radii larger than 0.1 m. The peak of the angular distribution of Sn^{4+} is approximately located at 40° with ion energies up to 4 keV for a radius in the centimeter scale. At 1 mm the kinetic energies of Sn^{5+} are approximately 3 keV. The kinetic energies of Sn^{5+} reach 5.5 keV at 90° from the laser axis. Kinetic energies larger than 6 keV are obtained for Sn^{6+} at radii above 0.1 mm for angles between 45° and 75° .

A key physical parameter, which affects the collector erosion time is the ion kinetic energy. The spatially and temporally integrated kinetic energy distributions of ions onto the elliptical collector are shown in Fig. 120. Kinetic energy is found to increase with increasing ionization stage. The kinetic energy distributions of Sn^{2+} , Sn^{3+} , Sn^{4+} , Sn^{5+} and Sn^{6+} are peaking at 260 eV, 330 eV, 500 eV, 1300 eV and 1700 eV respectively. Good agreement is found with an experimentally measured kinetic energy distribution for a tin slab target.²⁴⁰ The EUV energy per pulse is equivalent to the value used in the computational study.

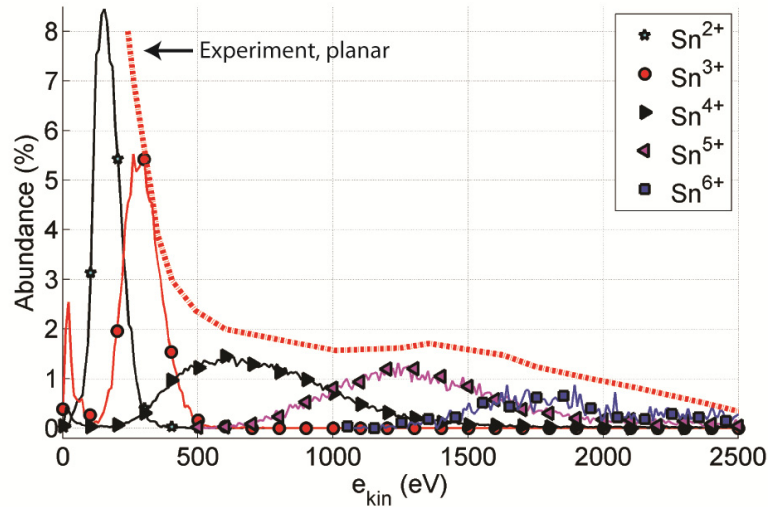


Fig. 120. Computed abundance of ion kinetic energies on EUV collector for droplet target. Experimental results²⁴⁰ (red dotted line) for equivalent EUV energy for planar target.

6.3.2.2.3. Collector erosion

The erosion of the EUV collector by fast ions is determined by the ion sputtering rate. The sputtering yield, which gives the average number of atoms ejected from the target per incident ion, depends on numerous parameters for both the incident ion and the target itself. For the impinging ions, the sputtering yield is dependent on the ion energy, the angle of incidence and their mass. The target parameters include the mass of the constituent atoms, the surface and lattice binding energies and the displacement energy of the target. The sputtering yields for tin on Mo and Si as a function of incidence angle and ion energy are presented in Fig. 121. These results have been obtained using *The Range of Ions in Matter* (TRIM) software package.²¹ This Monte Carlo simulation calculates the interactions of energetic ions, in the range of 10 eV to 2 GeV/amu, with amorphous targets. Calculations are carried out for Sn ion energies from 0.5 to 10 keV and for angles of incidence from 0 to 89 degrees with respect to target normal. The target parameters (included in the TRIM software packare) are listed in Table 6-I.

Table 6-I: Target parameters used in the TRIM sputtering calculations.

	Mo	Si
Density (g/cm ³)	10.21	2.32
Displacement Energy (eV)	25	15
Lattice Binding Energy (eV)	3	2
Surface Binding Energy (eV)	6.83	4.7

At 0° with respect to target normal, the sputtering yield for Sn onto Mo equals 0.42 and 1.44 for ion energies of 1keV and 4keV, respectively. The induced damage is 3.4 times larger. On the other hand, at 4 keV, the sputtering yield for Sn onto Mo equals 1.44 at 0° incidence and 5.05 at 50° incidence. As similar results are found for the sputtering of Sn onto Si, it can be concluded that the erosion of the multilayer collector strongly depends on both the ion energy and incidence angle.

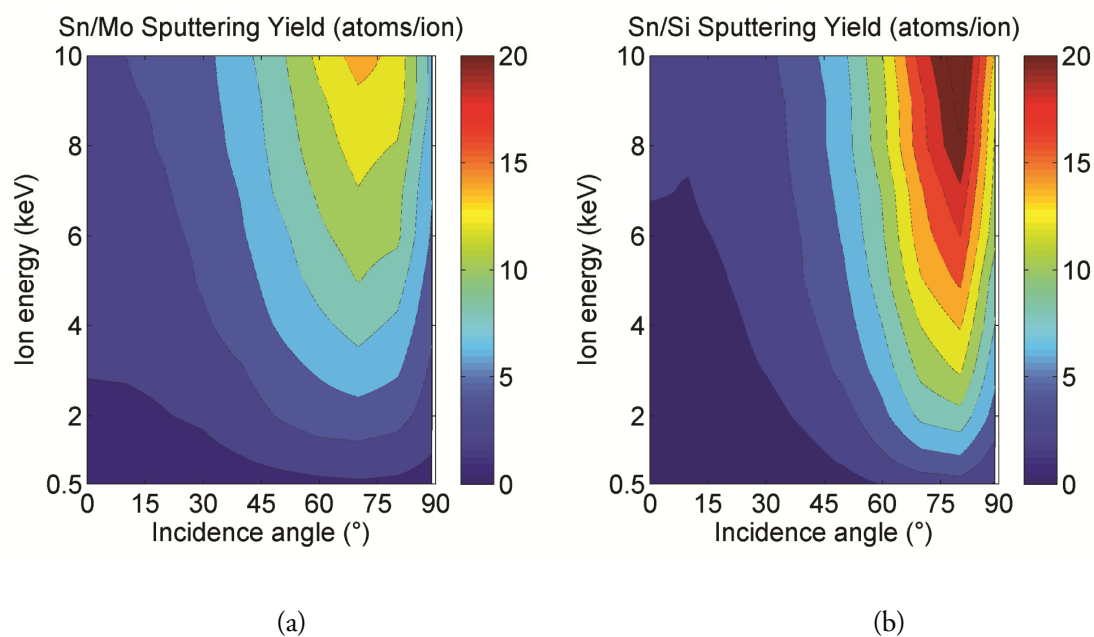


Fig. 121. Sputtering yields for (a) Sn onto Mo and (b) Sn onto Si

The ion impact angles on the EUV collector can be extracted from the particle code. The impact angle is defined as the angle between the collector surface normal and the velocity vector of the impinging ion. Angles that are directed towards the laser axis have a negative sign, while angles turned towards the outer border of the collector have a positive sign. A front view of the elliptical collector with the mean impact angle distribution is presented in Fig. 122. Only negative impact angles are found. In the central region, ions impinge with 0° incidence on the collector, while on the outer border, impact angles up to -40° can be found.

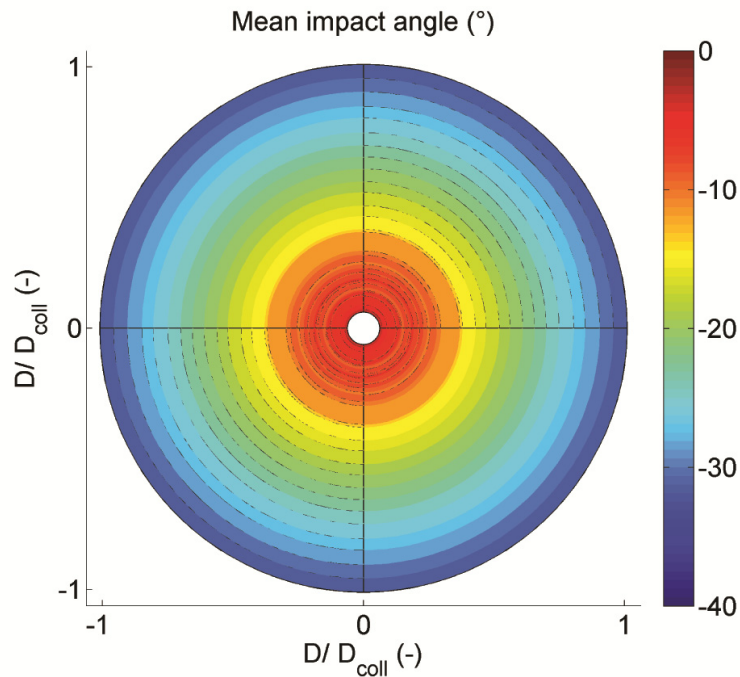


Fig. 122. Spatial distribution of mean impact angles on EUV collector.

The kinetic energy distributions predict ion energies up to 6 keV. These energetic ions cause erosion of the multi-layer coating. The time corresponding to a tolerable reflectivity loss from 70% to 60% is evaluated under the assumption that the multi-layer mirror consists of bilayers of Si (4.14 nm) and Mo (2.09 nm). The influence of the B_4C interlayer (0.25 nm) is neglected. A reflectivity loss from 70% to 60% implies an erosion of 20 bilayers.²⁴¹ This assumes that no sacrificial layers or debris mitigation is present. The number of pulses required to erode 20 bilayers can be calculated using the ion and kinetic energy distributions from the particle simulation. Assuming a source repetition rate of 6 kHz, the local sputtering time for a reflectivity drop from 70% to 60% is shown in Fig. 123. The shortest erosion time is obtained on the outer border for angles larger than 50° . In this region ion abundances and ion kinetic energies reach maximum values. Furthermore the impact angles are maximized on the outer border. The erosion times are in the range of a few hours for this laser-target configuration.

The computed reflectivity degradation can be used, together with the EUV flux distribution, to study the temporal degradation of the reflected EUV flux. The corresponding results are presented in Fig. 124. As the collector is more rapidly degrading on the outer border from angles of 45° outwards, that is also where EUV fluxes reduce most rapidly. The distribution of EUV fluxes can be integrated over the surface of the collector to determine the overall reflectivity degradation with time. The 10% reflectivity degradation, which corresponds to the tolerable loss, is achieved after 3 hours.

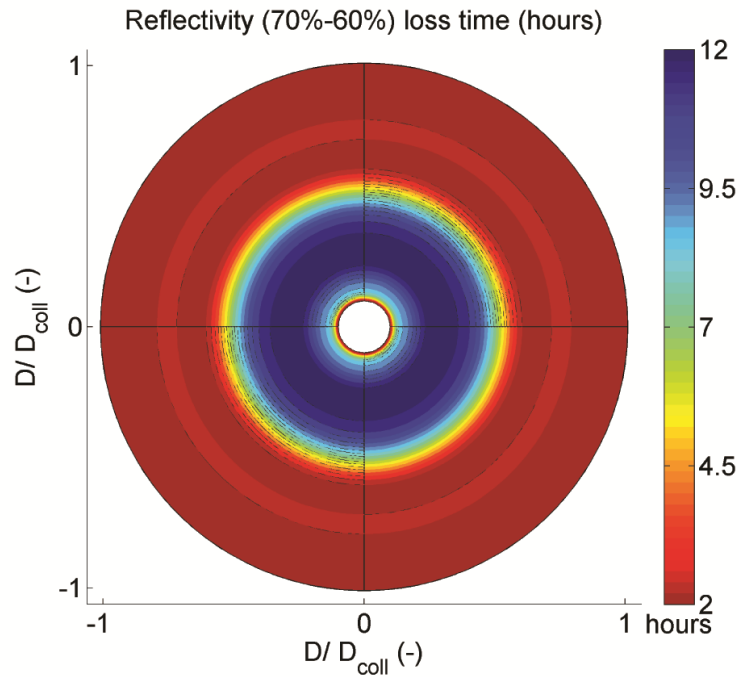


Fig. 123. Erosion time for 70% to 60% reflectivity drop, without debris mitigation

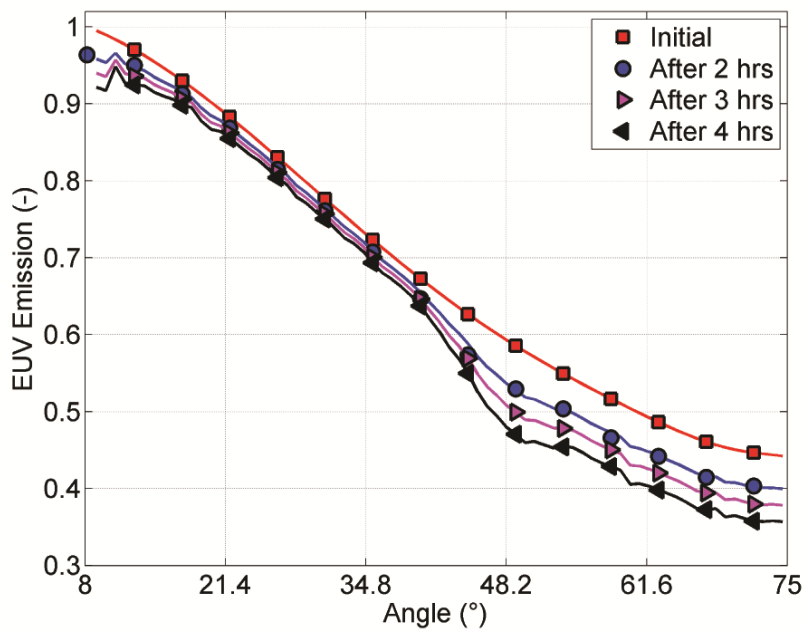


Fig. 124. Temporal degradation of reflected EUV fluxes on collector

The EUVL source collector requirement is for 1 year of continuous operation.²³ One approach to extend the life-time of the collection optics is to substantially (factor 2×10^3) reduce the ion flux. Another, less efficient approach would be to slow down the ions to sub-keV energies in order to lower the sputtering rate. However, this results in tin deposition on the collector.

6.3.2.3. Deposition on the EUV collector

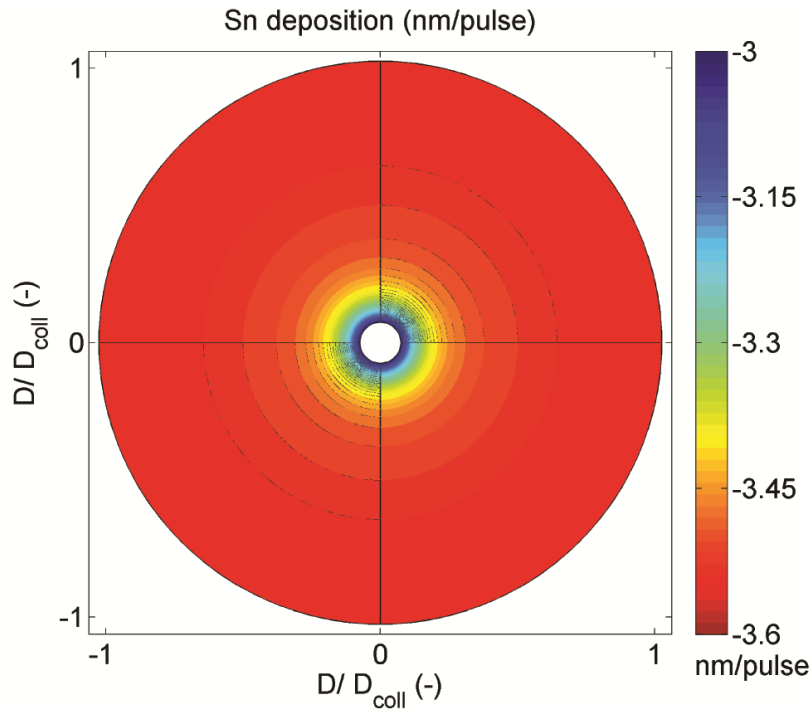


Fig. 125. Deposition thickness of tin vapor on EUV collector per pulse.

The second mechanism, which limits collector life-time, is the deposition of tin neutrals and ions with energies below the sputtering threshold onto the collector surface. These low energy atoms are difficult to capture with the particle code, as their abundance is much larger than that of the ions. The speed is also too slow for the vapor to reach the collector within the simulation time of the particle code. Therefore the RHD code is run for a large time scale, typically 5 times greater than the total laser pulse duration. The density of the neutral plume is above the rarefaction threshold for the simulated time scales. The obtained density distributions are extrapolated to the collector, assuming a radial expansion over a prolonged period. The radial expansion assumes no momentum exchange with additional flows in the vacuum chamber. The particle distributions are then extrapolated onto the collector surface. In order to estimate the deposition layer thickness, tin is assumed to crystallize on the collector surface. The interaction with the sputtering ions is neglected. The computed tin deposition layer thickness for one pulse is presented in Fig. 125. Although the expansion of the tin vapor is assumed to be radial, the angular density distributions are non-uniform. The deposition of tin neutrals increases towards the outer border of the collector. The values vary in the range of 10^{-3} and 2.5×10^{-4} nm per pulse. Experimental values for planar tin targets are in the range of 10^{-2} nm per pulse for the same EUV energy.²⁴⁰ The layer thickness reaches the critical threshold of 1 nm^{56, 242} after a few thousand pulses. As a consequence, a debris mitigation and / or collector cleaning system is required to increase the collector life-time. Potential solutions are under development, as described in Sec. 1.2.4.5.3. The tin deposition is also efficiently reduced by limiting the droplet size, as reported in the next section.

6.3.3. Studies

In this section, the computational tools are employed to conduct studies of different laser-droplet configurations. The baseline simulation, which is presented in the previous section serves as a starting point for the parametric studies on laser-droplet configurations. On the laser side, the influence of the laser pulse duration, the irradiance and the spot size is studied. On the droplet side, investigations on the influence of the droplet diameter and the droplet spacing are conducted. The impact of a potential misalignment between the droplet and the laser pulse is studied. A combination with experimental results for the lateral stability yields the energy stability of the corresponding source.

6.3.3.1. Impact of laser irradiance and pulse duration on the LPP

One of the most influential parameters, which determines the characteristics of an LPP is the laser irradiance. The two other key laser parameters are the pulse duration and spot size. In the following study, the dependence of the EUV conversion efficiency on the incident laser irradiance is studied for different pulse lengths. The impact of the spot size is studied separately in the next section. For a given laser, the pulse energy and pulse duration are typically coupled to the repetition rate. For this case, EUV output is to be maximized, this complex (non-linear) coupling must be considered. This study is based on the baseline configuration, except for the laser pulse duration and irradiance, which are varied. A 50 μm tin droplet is irradiated by a Nd:YAG laser with a spot size of 80 μm .

The computationally predicted CEs are shown in Fig. 126 as a function of laser irradiance for pulse durations (FWHM) of 2.2 ns, 8 ns and 21 ns, respectively. For the shortest pulse, namely 2.2 ns, the optimum CE of 1.94% is obtained at 100 GW/cm^2 . For smaller irradiances, the decay from the optimum CE is more pronounced than for larger irradiances. Similarly to the results obtained for the planar target, the CE decreases for larger pulse durations. For a pulse duration of 8 ns, the optimum CE of 1.53% is obtained at 800 GW/cm^2 , although similar values for the CE are obtained already at 150 GW/cm^2 . For a pulse duration of 21 ns, the optimum CE of 1.29% is obtained at 800 GW/cm^2 . Overall, the CE decreases with increasing pulse duration. For irradiances above 800 GW/cm^2 , the pulse duration has less effect on CE and similar values are obtained. The same trend has been observed for planar targets.⁴¹

The decrease of CE with low irradiances is due to a reduced plasma temperature. As the plasma temperature decreases, the fraction of EUV emitting ions decreases. The respective temperature profiles of the plasma and the droplet along the laser axis are shown in Fig. 127 at a pulse duration of 50% of the total pulse length. At 40 GW/cm^2 , the electron temperature at peak laser intensity equals 23 eV. For large irradiances, the plasma temperature increases. As a consequence, the amount of ablated mass and the size of the plasma plume is increased. At an irradiance of 800 GW/cm^2 , the plume is significantly larger than the plumes, which correspond to the lower irradiances of 40 GW/cm^2 and 80 GW/cm^2 , respectively. The plume size can be inferred from Fig. 127. Two mechanisms are responsible for the drop in CE. Firstly, the larger plume causes more reabsorption

of EUV photons. Secondly, for large electron temperatures the EUV emissivity decreases, as shown in Fig. 96.

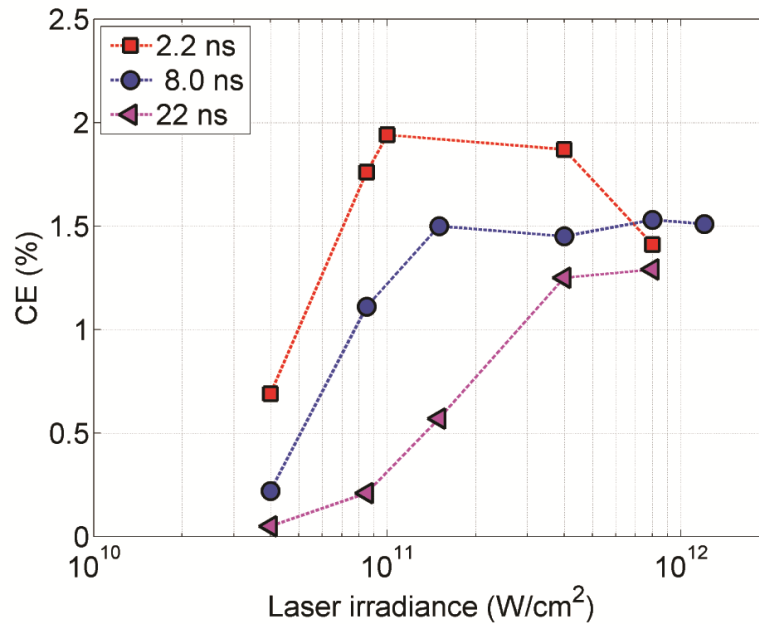


Fig. 126. Conversion efficiency of tin droplet LPP for pulse durations (FWHM) of 2.2, 8 and 22 ns.

Another observation from the study of pulse duration and irradiance is that the CEs decrease at a fixed irradiance with increasing pulse duration. The spatial distributions of mass density and electron temperature for three different pulse lengths are presented in Fig. 128. The irradiance is kept constant at 200 GW/cm². The snapshots are taken at peak laser intensity. The mass density distribution clearly shows an increase of the plume size and ablated mass with pulse duration. Interestingly, the expansion shockwave, which is described in Sec. 6.3.2.1.4, is more pronounced for longer pulse durations. On the other hand, the electron temperature decreases with increasing pulse duration. The drop in temperature is in the order of 10% between the 2.2 ns and the 21 ns pulse. One reason for this decrease in electron temperature is the larger absorption length for a larger plume. Indeed the hot, EUV emitting core region is of similar size for the 2.2 ns and 8 ns pulses. The plasma plume is however significantly larger for the 8 ns pulse. As a consequence, part of the incident laser energy is absorbed and diffuses as thermal energy within the plume, instead of being transmitted to the EUV emitting core. The losses due to the multidimensional expansion also increase with plume size. Additionally, a larger plume increases the optical thickness of the LPP, hence the probability of reabsorption of EUV photons increases.

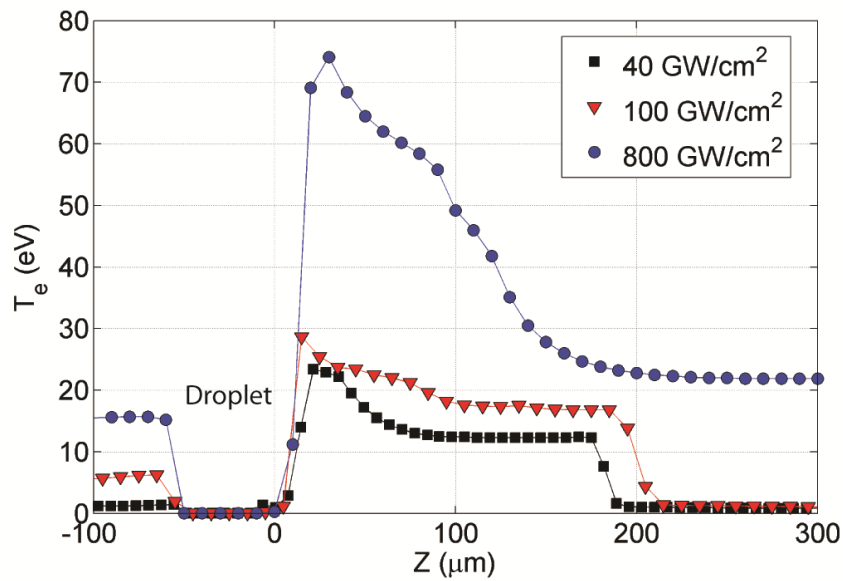


Fig. 127. Electron temperature profile along the laser axis for irradiances of 40 GW/cm^2 , 100 GW/cm^2 and 800 GW/cm^2 , respectively.

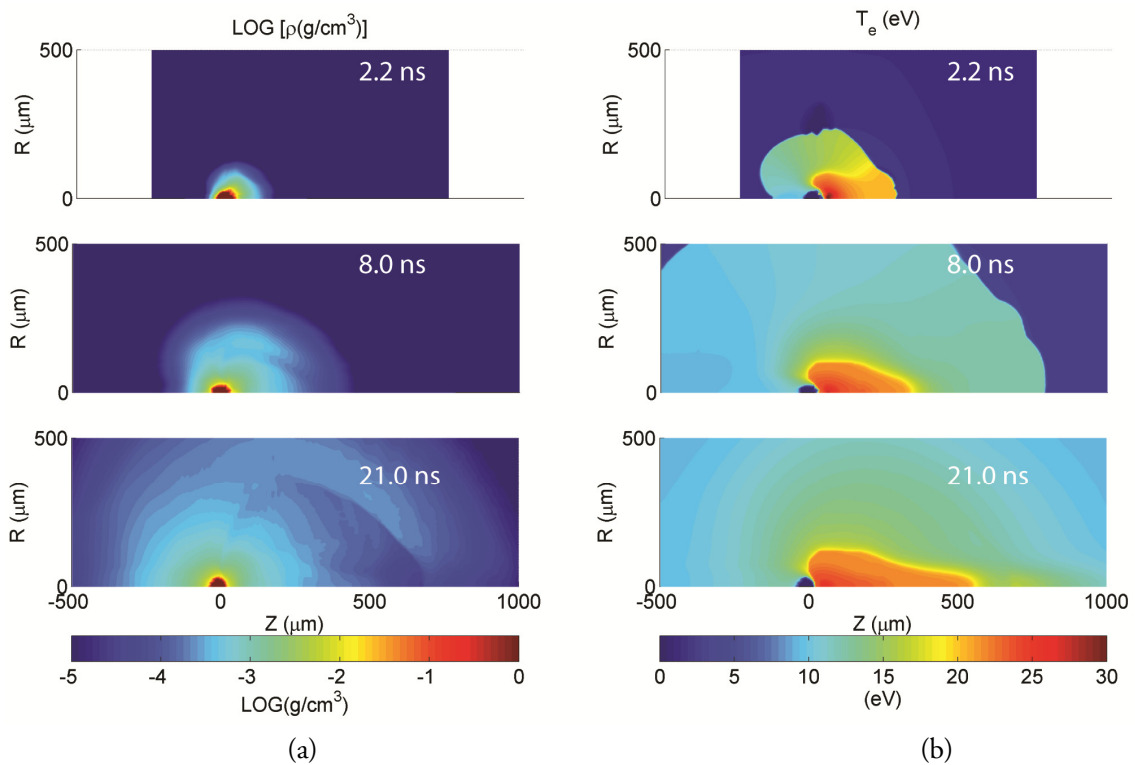


Fig. 128. Spatial distributions at peak laser intensity of (a) mass density and (b) electron temperature for pulse durations of 2.2 ns, 8 ns and 21 ns, respectively. The plume sizes increase with pulse duration, which lowers the electron temperature and increases reabsorption of EUV photons. The CE decreases with increasing pulse duration.

The described general increase of reabsorption and decrease of electron temperature for larger plume sizes also explain the increase of the optimum irradiance with pulse duration. Indeed, as the plume dimensions increase with pulse duration, increased irradiances are required to reach EUV emission temperatures within the plume. The larger plume induces a larger source size, which then compensates for the increased optical thickness.

Long laser pulses are computationally more expensive than shorter pulses. Indeed, the larger plume sizes requires a larger computational domain. In order to ensure a sufficient grid resolution on the droplet, the number of computational cells has to increase. Therefore the computational runtime increases with increasing laser pulse duration.

6.3.3.2. Impact of laser spot size on LPP

In this study, the influence of the spot size on the characteristics of the LPP is presented. The 50 μm tin droplet is irradiated by a Nd:YAG laser with 8 ns pulse duration and a spot size of 50 μm and 80 μm , respectively. The irradiance is kept constant at 200 GW/cm^2 . Experimental studies on the influence of laser spot sizes have been conducted for planar tin targets.⁴²

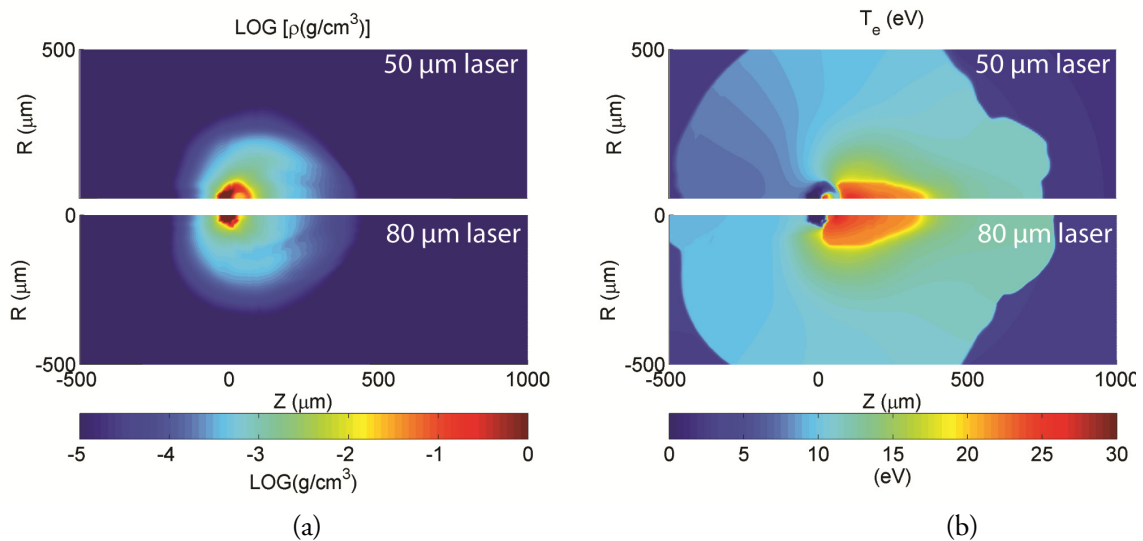


Fig. 129. Spatial distributions of (a) mass density and (b) electron temperature for spot sizes of 50 μm and 80 μm respectively. The laser irradiance is 200 GW/cm^2 and the pulse duration is 8 ns.

When comparing the spot sizes of 50 μm and 80 μm , a difference in CE of 8.6% is observed. The largest CE is obtained for an 80 μm spot size. In order to understand this difference in CE, the spatial distributions of mass density and electron temperature are shown in Fig. 129. The plasma plume generated by the 80 μm spot size is slightly ($\sim 15\%$) larger than the plume obtained for the 50 μm spot. The temperature distribution reveals a larger EUV emitting region for the larger spot size. The radial extension of the plasma core is more pronounced for the larger spot size. In the case of the 80 μm spot, more energy is wasted during the initial ablation than for the 50 μm spot. After the creation of the plasma plume, the larger spot helps to increase the size of the EUV emitting

region. As a consequence, more EUV photons are created in the case of the 80 μm spot when compared to the 50 μm spot. The larger plume partially attenuates this increased EUV generation in the case of the 80 μm spot.

In the case of the 50 μm spot size, a second high temperature region develops on the droplet surface. This high temperature region develops in a cavity, which forms at the droplet surface. The cavity is induced by the smaller spot size of similar length scale than the droplet diameter and the Gaussian energy distribution. The density in this cavity is too high for the laser to be transmitted. As a consequence, the typical high temperature region is located further away from the droplet than in the baseline case. Heat transfer by radiation and thermal conduction leads to the formation of the high temperature region at the droplet surface. EUV emission from this second high temperature region is very limited, due to the large optical thickness around this region.

6.3.3.3. Impact of droplet size on LPP

The generation of micrometer sized droplets is a challenging task, especially for small droplet sizes. The smallest droplet sizes, which have been achieved in this work, are on the order of 40 μm . A parametric study of the droplet size is of major interest. The reduction in droplet size is driven by the reduction of debris. The droplet size study also helps to quantify the influence of variations in the droplet diameter, which have been observed in Sec. 3.3.3.1.

First, the impact of the droplet size on CE is studied. For this purpose, the laser irradiance is kept constant at 200 GW/cm^2 . The laser pulse duration equals 8 ns. The spot size is adjusted according to the ratio given by the baseline configuration, where the laser spot (FWHM) equals 80 μm and the droplet diameter equals 50 μm . The investigated droplet sizes are 50 μm , 30 μm , 20 μm and 10 μm , respectively. Spatial distributions of mass density and electron density are presented in Fig. 130. The snapshots are taken at 50% pulse duration.

Interestingly, the mass density distributions reveal similar plume sizes for three different droplet sizes. The lateral extensions of the three plumes in Fig. 130 are of similar dimensions. On the other hand, the dimensions of the EUV emitting plasma core decrease significantly with droplet size, as shown in Fig. 130b. Therefore a decrease of CE with decreasing droplet sizes can be expected. The CEs equal 1.65%, 1.58% and 1.28% for droplet sizes of 50 μm , 30 μm and 20 μm , respectively. A major reason for the decreased source size is the reduced mass of the plasma for smaller droplets. Indeed, in the case of the smaller droplet, the expansion shock wave, which is a measure for the ablated mass is very pronounced, as shown in Fig. 130a. The expansion shockwave is more closely located to the droplet for smaller droplet sizes. As a consequence, the axial length scale of the high density EUV emitting region is limited, when compared to larger droplet sizes.

A major criterion, which determines the droplet size, is the amount of EUV generated per pulse. For small droplet sizes, the small amount of generated EUV energy might imply laser repetition rates that are no longer feasible. The EUV pulse energy is plotted in Fig. 131 for the laser pulse

duration of 8 ns. The EUV pulse energy at the IF is derived from the single pulse EUV emission by assuming a collector of 5 sr collection angle with a reflectivity of 60%. The drop in EUV energy between the 50 μm and the 10 μm droplet is equal to a factor of 30. An EUV source, which operates at a repetition rate of 100 kHz, yields 65 W at IF for a 50 μm droplet, while the 10 μm droplet yields only 2.5 W. Smaller droplet sizes also require an increased droplet frequency for reliable generation, as derived in Sec. 5.3.1.3.

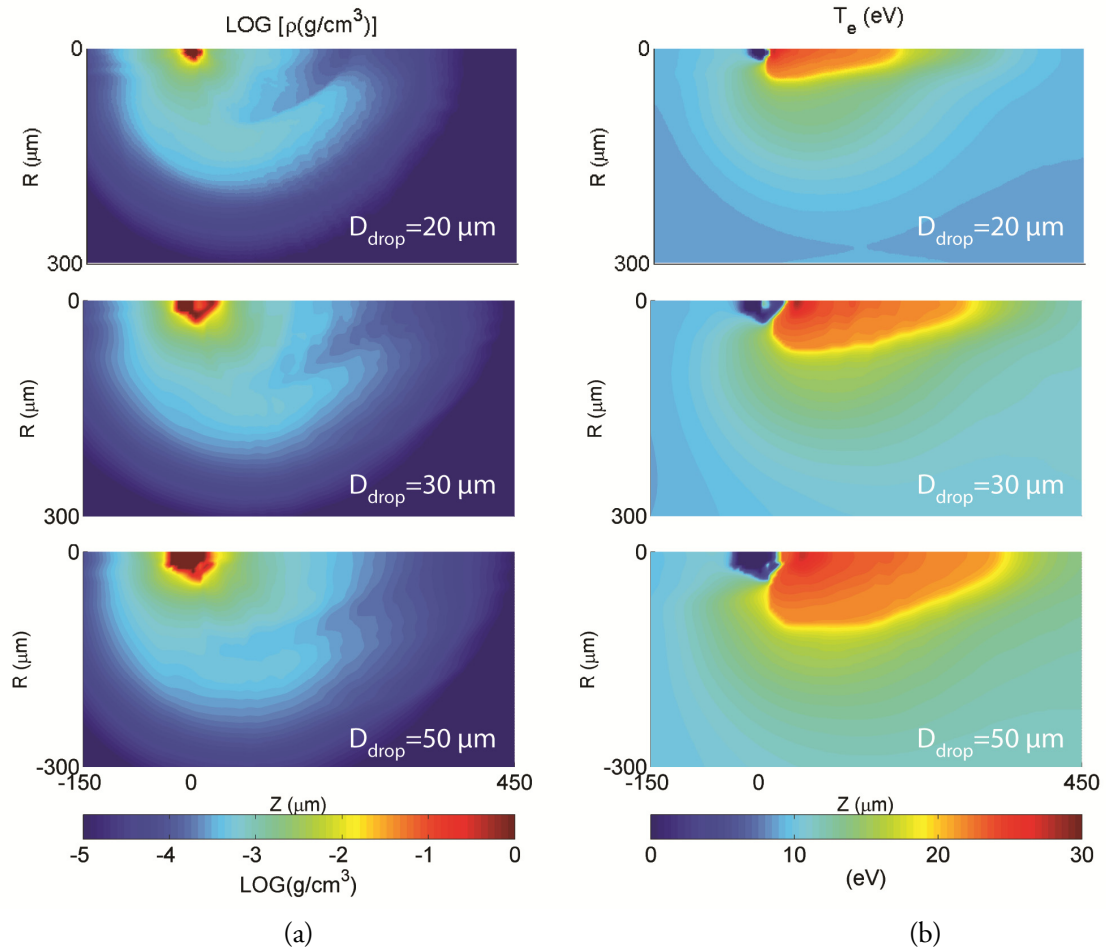


Fig. 130. Spatial distributions of (a) mass density and (b) electron temperature for droplet sizes of 20 μm , 30 μm and 50 μm , respectively.

Energetic ions, which cause sputtering of the multilayer surfaces are required for EUV emission. The fraction of highly energetic ions scales with the amount of EUV energy. The other typical byproducts of the LPP are the tin vapor, droplet fragments, residual target material and low ion stages, which all result in deposition on the EUV collector. Reducing the droplet size should help to reduce the overall amount of low energy debris. The distributions of ions, tin vapor and residual target material are evaluated for droplet diameters of 50 μm , 30, 20 μm and 10 μm , respectively. The individual mass fractions at the end of the laser pulse are presented in Fig. 132. The mass fractions are normalized by the residual droplet mass of the 50 μm droplet. The ratio between the number of ions of the 50 μm droplet and the 10 μm droplet is 16. The vapor fraction is the lowest

fraction for all droplet diameters. The residual droplet mass exceeds 50% of the initial droplet mass in the case of the 50 μm droplet. In the case of the 30 μm droplet, the residual droplet material and the ablated mass are in the same range. The 20 μm droplet is more efficiently ionized, as the residual mass is lower than the ionized mass. Full vaporization of the tin droplet is achieved for diameters on the order of 10 μm . In the case of a 10 μm droplet, the ion cloud forms 80% of the total mass in the computational domain at the end of the laser pulse. The largest ion fraction is Sn^{3+} . Due to the full vaporization of the droplet, no material is available for fragmentation. The tin vapor is reduced by more than one order of magnitude for the 20 μm droplet and by two orders of magnitude for the 10 μm droplet when compared to the 50 μm droplet. The tin deposition on the collector scales accordingly. It must be noted that, as the computational domain is planar, the reduction in debris is underestimated.

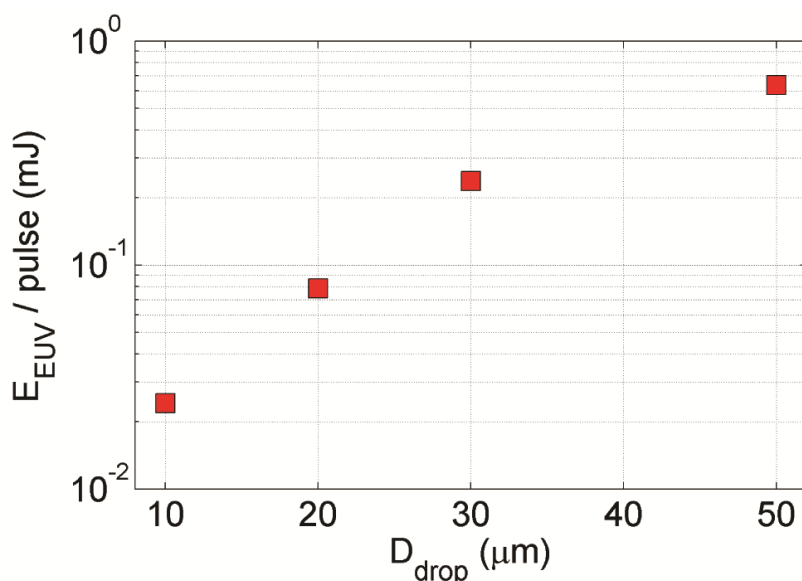


Fig. 131. EUV pulse energies for droplet sizes of 50 μm , 30 μm , 20 μm and 10 μm , respectively. The laser pulse irradiance is 200 GW/cm^2 for a pulse duration of 8 ns.

The choice of the droplet sizes results from a trade-off between debris and EUV pulse energy. The droplet size is chosen as a function of the overall application and the properties of subsystems, such as the drive laser and the debris mitigation system. For smaller sources, with less stringent power requirements and less sophisticated debris mitigation systems, a smaller droplet size is desirable, while for HVM applications, the overall power output is the key optimization parameter.

A droplet diameter variation on the order of 15% (3σ), which has been observed in Sec. 3.3.3.1, leads to remarkable fluctuations in EUV emission and generated debris. For a mean droplet diameter of 50 μm , this variation in diameter leads to a variation in EUV of 23% (3σ) per pulse. The variations in terms of residual target material and tin vapor are 25% (3σ) and 32% (3σ), respectively.

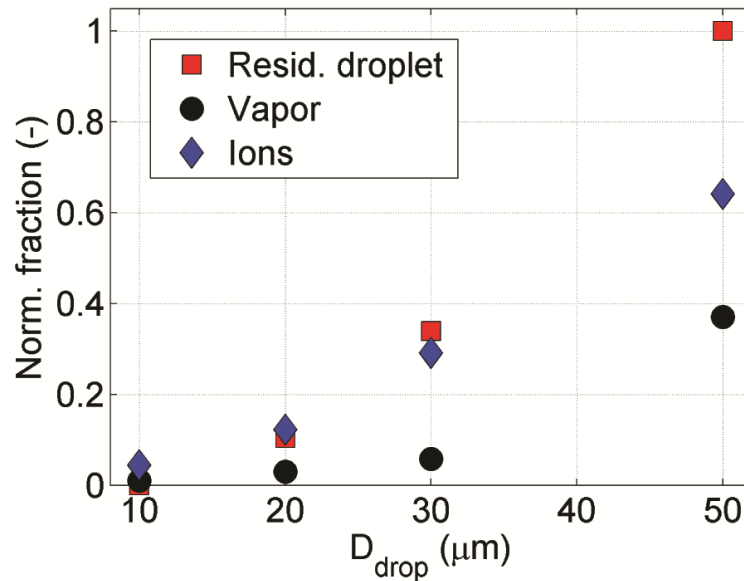


Fig. 132. Normalized mass fractions of residual droplet, vapor and ions at the end of the laser pulse for droplet diameters of 50 μm, 30 μm, 20 μm and 10 μm, respectively.

6.3.3.4. Influence of the LPP on the subsequent droplet

In this work, target material is provided in the form of a high frequency (kHz) droplet train to the laser irradiation site. The key parameters of this droplet train are the droplet frequency and velocity, which both define the droplet spacing. The two major criteria, which determine the droplet spacing in an EUV source, are the irradiation of more than one droplet and the interaction of the LPP with the subsequent droplet. The supersonic plasma flow is expected to transfer momentum to the droplet. The interaction scales with droplet spacing. In this study the laser settings are kept constant. The Nd:YAG laser irradiates the 50 μm tin droplet at 400 GW/cm² with a pulse duration of 8 ns and a spot size of 80 μm (FWHM). The varied parameter is the droplet spacing.

The expanding plasma forms a shockwave in front of the subsequent droplet, as shown in Fig. 133a. A similar experimental observation has been made for an SnO₂ jet.²⁴³ The droplet spacing equals 5 droplet diameters. Overall, the pressure is highest at the surface of the irradiated droplet. The average ablation pressure on the front side of the droplet equals 9 GPa, which is in the expected range.¹⁸² The spatial pressure distribution from Fig. 133a is taken at peak laser intensity. The pressure field around the subsequent droplet is increased, not only because of the expanding plasma flow, but also due to a weak evaporation of this droplet. Indeed heat is transferred from the plasma plume to the droplet by conduction and radiation. In order to evaluate the pressure influence on the droplet, the pressure is recorded along the droplet contour, as shown in Fig. 133b. The angle of 0° corresponds to the location on the droplet trajectory on the side, which is oriented towards the plasma. A pressure increase is noticeable after 30% pulse duration. At 50% pulse duration, the pressure reaches 1.25 GPa. The peak pressure decreases by 50% up to the end of the

pulse. The peak pressures are located around an angle of $+45^\circ$. Indeed, the velocity vectors are pointing towards the center of the plume, which is located in front of the irradiated droplet.

The pressure distributions at the droplet surface can be integrated to derive the net force acting on the droplet. The temporal dependence of the force amplitude, relative to the laser pulse, is plotted in Fig. 134. The force, which is induced by the non-uniform pressure field, increases from the beginning to 75% of the pulse duration. The droplet force then decays up to 1.5 times the pulse duration, before a second peak of similar amplitude is reached. While the first peak is due to the high velocity, and low density ions, the second peak is induced by a high density cloud of fast neutrals. Around peak laser intensity, net pressures up to 1 GPa are reached for a droplet spacing of 5 droplet diameters.

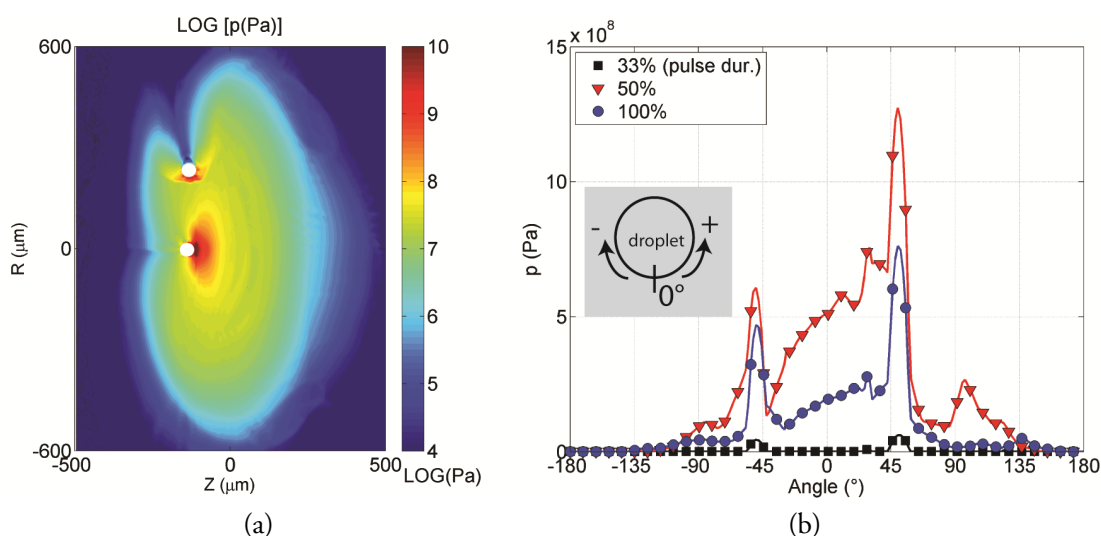


Fig. 133. (a) Spatial pressure distribution of the irradiated droplet and its subsequent droplet for a droplet spacing of 5 diameters. A shock wave forms in front of the subsequent droplet. (b) Angular distribution of pressure along the surface of the subsequent droplet at different time instances.

The consequences of the pressure pulse and the flow around the droplet are the subject of ongoing investigations at ETH Zürich. Two mechanisms could lead to fragmentation of the subsequent droplet. Firstly, the pressure pulse, which has been previously described is comparable to the ablation pressure pulse of the irradiated droplet. No systematic quantitative studies are available for tin droplets under the presented conditions. The current RHD code is not expected to correctly model the shockwave-droplet interaction, as no surface tension model is used. In the study of Yuspeh *et al.*,¹⁸² a 340 μm tin droplet has been subjected to a pressure wave of 15 ns with a peak pressure of 6 GPa. The droplet deformed and micrometer fragments are generated. The deformation and mist formation time scales are in the range of microseconds. The interaction of tin targets with shock waves has been studied by De Rességuir *et al.*²⁴⁴ for a similar pressure pulse. In the liquid phase, the pressure pulse induces cavitation, which results in the ejection of fragments.

Secondly, the high velocity flow around the droplet could lead to the breakup of the subsequent droplet. The ratio of the kinetic energy of the flow and droplet surface is expressed by the gas Weber number. In the previously studied case of a droplet spacing of 5 diameters, fragmentation is expected. The Weber number is estimated from the flow density and free stream velocity around the droplet. The resulting Weber number is $O(3)$ and the Ohnesorg number (derived in Sec. 2.1.3) is $O(-3)$. According to Hsiang *et al.*,²⁴⁵ the droplet should split into fragments. The different breakup modes are presented in Theofanous *et al.*²⁴⁶ The main parameters, which determine the fragmentation, are the Weber number and the shock wave intensity.

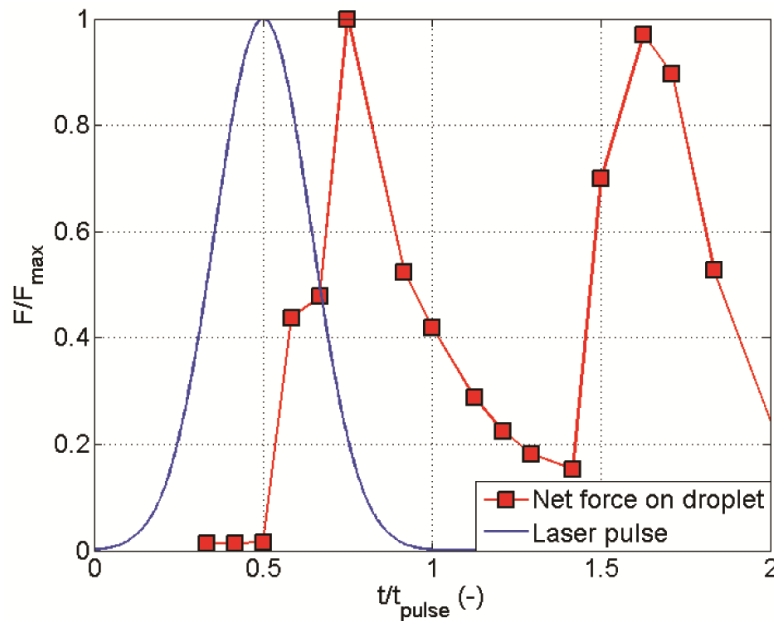


Fig. 134. Time dependence of net droplet drag force, relative to laser pulse. The droplet spacing equals 5 droplet diameters.

The study on droplet spacing has been conducted for droplet spacings of 5, 7.5 and 10 droplet diameters. In the case of a spacing of 7.5 droplet diameters, the integrated force is reduced by a factor of 4, while in the case of 10 droplet diameters, the net force is reduced by a factor 6. The Weber number decreases by one order of magnitude for a spacing of 7.5 droplet diameters and by another order of magnitude for a spacing of 10 droplet diameters. At 10 droplet diameters, the Weber number is $O(1)$ and the droplet is at the limit between splitting and oscillatory deformations.²⁴⁵ Two major points could however lead to an overprediction of the droplet breakup.

Firstly, it must be noted that the studies on droplet breakup are typically conducted at steady conditions. In the current case the time scales of the high velocity flow and the life-time of the shockwave are on the order of tens of nanoseconds. These time scales are comparable to the travel time of the acoustic wave for one droplet diameter, which is in the range of 20 ns. Secondly, the

two-dimensional planar simulation underpredicts the multidimensional expansion. Therefore the expected Weber number should be lower.

6.3.3.5. Misalignment between laser and droplet

The experimental droplet studies reveal an inherent jitter in the droplet timing. In order to evaluate the impact of this droplet jitter onto EUV emission, a computational study is conducted. The influence on EUV emission of a misalignment between the laser pulse and the droplet is investigated by computational means. An equivalent experimental study would be very challenging to complete. The results relate the temporal stability of the droplets to the temporal stability of EUV emission. The studies are conducted for the baseline simulation settings, except for the pulse duration, which is fixed to 2.2 ns. Two different irradiances are investigated, namely 100 GW/cm² and 400 GW/cm². The misalignment between laser spot and droplet is quantified by an arbitrarily defined overlap parameter:

$$overlap = 1 - \frac{d}{R_{drop} + R_{laser}} \quad (6.32)$$

where R_{drop} is the droplet radius, R_{laser} is the laser spot radius and d is the distance between the laser center and droplet center. The parameter R_{laser} is set to 2.25 times the FWHM of the spot diameter, which equals 80 μm . The misalignment of the droplet relative to the laser spot is illustrated in Fig. 135a for an overlap of 5%. The droplet radius is 25 μm . The distance d between the center of the laser spot and the droplet equals $4R_{drop}$. The ablation region, hence the section of the laser spot where the energy density is sufficient to cause ablation, is also marked. The ablation energy has been determined computationally to be 1 J/cm². A value of 2 J/cm² is proposed by Masnavi *et al.*²⁴⁷ The spatial temperature distribution, which is equivalent to the schematic in Fig. 135a is presented in Fig. 135b. The laser irradiation equals 100 GW/cm². The temperature increases along the front surface of the droplet with increasing laser irradiance. It can be seen that the lower part of the droplet is not ablated, while a hot temperature region develops on top of the droplet. The obtained electron temperature is insufficient for EUV generation.

In the case of an extreme misalignment, such as the one presented in Fig. 135, only a small fraction of the laser spot interacts with the tin droplet. As the fluence of the laser pulse is however several orders of magnitude larger than the ablation threshold, a small fraction of the laser spot is sufficient to ablate material. The initial vapor velocity is normal to the ablation surface, as described in Sec. 6.1.1. As a consequence a plume of reduced size forms on the upper side of the droplet and expands into the more energetic part of the laser spot. If the misalignment is not too large, the plume is heated up to EUV emission. The resulting plume is usually of lower optical thickness than in the zero misalignment case. Although EUV can escape more efficiently, the laser absorption and source size are reduced.

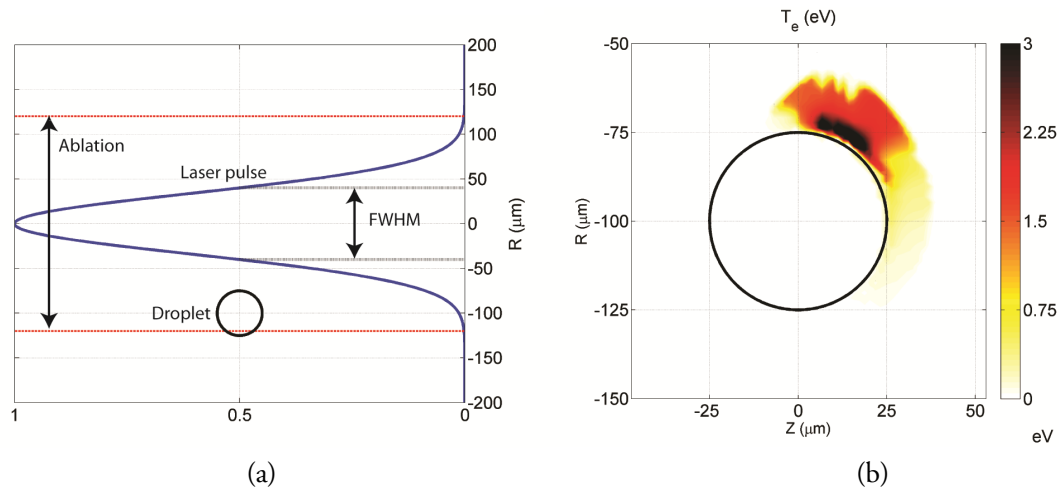


Fig. 135. (a) Misalignment of $4R_{drop}$ between the $50 \mu\text{m}$ tin droplet and the $80 \mu\text{m}$ (FWHM) Gaussian laser pulse. The overlap equals 5%. The red lines mark the ablation threshold energy. (b) Spatial temperature distribution at 30% pulse duration for an overlap of 5% and an irradiance of $100 \text{ GW}/\text{cm}^2$.

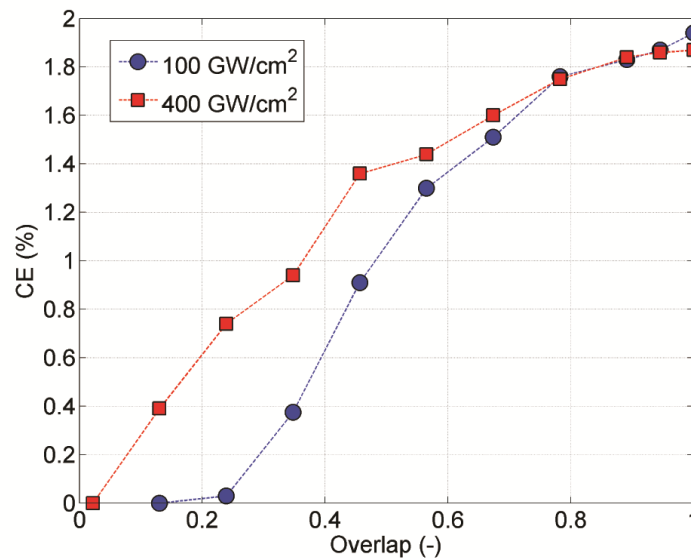


Fig. 136. Dependence of CE on the misalignment between droplet and laser spot for irradiances of $100 \text{ GW}/\text{cm}^2$ and $400 \text{ GW}/\text{cm}^2$, respectively.

The dependence of the CE on the overlap between droplet and laser spot is summarized in Fig. 136 for laser irradiances of $100 \text{ GW}/\text{cm}^2$ and $400 \text{ GW}/\text{cm}^2$, respectively. The drop in CE is most pronounced for small overlaps. On the other hand, for large overlaps, the CE is less sensitive to misalignments. The drop in CE from 100% to 80% overlap equals 8.7% and 5.6% for an irradiance of $100 \text{ GW}/\text{cm}^2$ and $400 \text{ GW}/\text{cm}^2$, respectively. An overlap of 80% corresponds to a misalignment of $0.92R_{drop}$. The larger irradiance reduces the drop in CE. Indeed, for the same

misalignment more material is ablated at 400 GW/cm^2 than at 100 GW/cm^2 . Therefore a larger plume develops, which has an increased intersection with the more energetic part of the laser spot.

6.3.3.6. Impact on dose stability

The computed dependence of the CE on the misalignment between laser spot and droplet can be used to study the impact of the lateral droplet instability on EUV energy stability. The EUV energy for a specific laser-droplet interaction is derived from the CE, the supplied laser energy and the spatial misalignment between droplet and laser spot. Fluctuations of EUV energy at the source level lead to unwanted dose (light per wafer exposure) fluctuations at the wafer level, as described in Sec. 1.2.5. The dose energy equals 896 mJ per exposure step. The dose stability can be simulated with the help of the dependence of the CE on lateral displacements and the measured lateral displacement distribution.

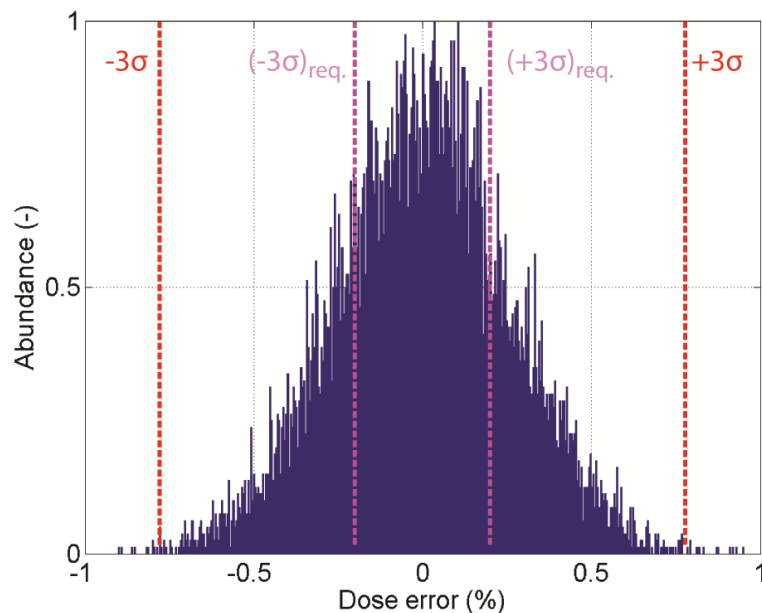


Fig. 137. Dose error distribution for a Nd:YAG pulse of 8 ns with an irradiance of 100 GW/cm^2 and the experimentally measured distribution of lateral displacements.

The lateral misalignment of the droplet with respect to the laser spot is sampled from the experimentally measured distribution of lateral instability from Fig. 32. The three standard deviations of the lateral displacement are equal to one droplet diameter. The number of irradiated droplets per dose is derived from the required dose energy and the emitted EUV energy per pulse. In the case of an irradiance of 100 GW/cm^2 , the required number of droplets per dose equals 1140 in order to reach the dose energy. The dose stability, which is computed for 10'000 doses, is shown in Fig. 137. Three standard deviations of the dose distribution are equal to 0.8%, which exceeds to required dose stability of 0.2% (3σ).

The simulation of the dose stability can be used to find the threshold standard deviation on the lateral droplet displacements in order to meet the EUV source requirements. For this purpose, the distribution of lateral displacements is assumed to follow a normal distribution. Similar to the experimental case study, the dose stability (3σ) can be derived for different standard deviations of the lateral droplet displacement. The dose stability is computed for irradiances of 100 GW/cm^2 and 400 GW/cm^2 , respectively. The number of droplet per dose equals 1140 and 301 for 100 GW/cm^2 and 400 GW/cm^2 , respectively. When the droplet number per dose is kept constant, the so-called open loop dose stability is derived. The obtained dose stability, computed as a function of the standard deviation of the lateral displacement, is shown in Fig. 138, together with the EUV requirement for dose stability and the experimentally measured lateral displacement.

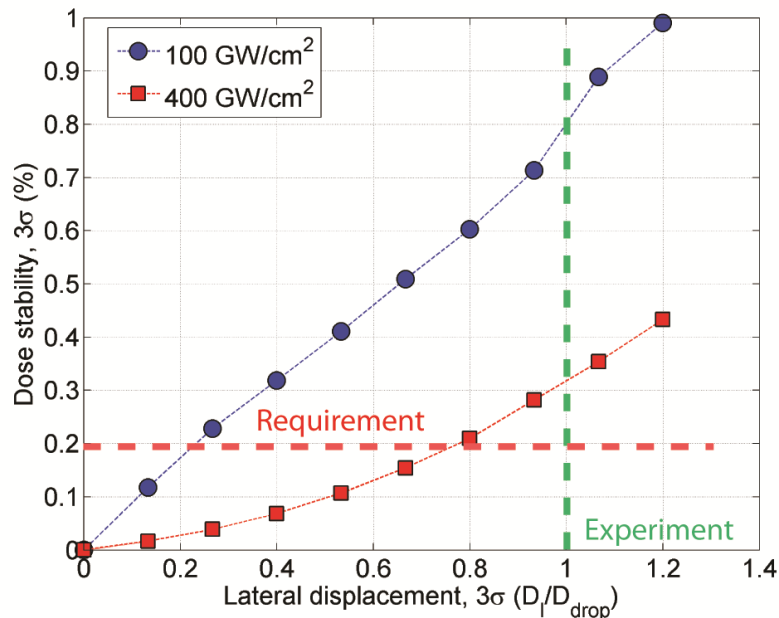


Fig. 138. Dependence of dose stability on standard deviation of lateral displacement distribution. The lateral stability threshold (3σ) are 0.79 and 0.23 droplet diameters for irradiances of 400 GW/cm^2 and 100 GW/cm^2 , respectively.

As expected, dose stability increases with decreasing lateral displacements. At an irradiance of 100 GW/cm^2 , the three standard deviations of the lateral displacements need to be lower than 0.23 droplet diameters in order to meet the source requirements. In the case of an irradiance of 400 GW/cm^2 , the required threshold equals 0.79 droplet diameters. The increase in the droplet stability threshold can be expected from the trend in the misalignment curves from Fig. 136. At 400 GW/cm^2 , EUV generation is less sensitive to misalignments than at 100 GW/cm^2 . On the other hand, the larger irradiance implies a smaller number of irradiated droplets per dose. This increases the standard deviation on the generated EUV energy. The net effect is however positive in the

present case. In recent data obtained with the developed dispenser,²⁴⁸ the measured lateral stability has been equal to 24% of the droplet diameter (3σ).

In general, the high repetition rates of LPP sources make dose control much easier than for DPP sources. The dose stability can be controlled with a feedback loop. One approach consists of adjusting the irradiance of the last droplet irradiation of a dose in order to meet the stability requirement.⁵⁹ This work provides the relationship between EUV energy and laser irradiance in Fig. 126, which could enable a similar feedback loop approach.

It must be noted that the timing jitter can also lead to misalignment between the droplet and the laser pulse. In the absence of triggering, three standard deviations of the measured droplet timing in Fig. 36, are equal to 5% of the mean droplet timing interval. This leads to a misalignment along the droplet trajectory of 0.5 droplet diameters, which does not compromise the dose stability at an irradiance of 400 GW/cm². In combination with the lateral displacement or at lower laser irradiances, the required dose stability might not be achieved.

6.4. Summary and conclusion

Accurate predictions of LPP emissions require atomic physics computations to be coupled to the hydrodynamic code. The atomic model could be validated by comparison with emission and absorption spectra. The peak spectral efficiency of 16%, which corresponds to the ratio of in-band to full-band energy, is predicted for an electron density of 10^{19} cm⁻³ and an electron temperature of $T_e=33$ eV.

Firstly, the multi-scale tools are applied to a baseline case, which is based on representative laser and droplet settings for the experiments conducted at ETH Zurich. The plasma formation and the initial stages of the plasma expansion, together with the in-band and full-band emissions, are modeled with the help of the RHD code. The code is validated in terms of electron density distributions and CE for planar targets. The expanding plume develops a significant anisotropy in terms of electron temperature and density, which is mainly due to laser energy absorption.

The developed radiation solver is used to determine the full-band and EUV fluxes, which are crucial for collector design. The angular full-band flux distribution defines the heat load on the collector, which is essential for the thermal design of the collector. On the other hand, the EUV flux distribution determines the collection angle, which is a major cost factor for the whole EUV source. The radiation transport from the high temperature plasma core to the vacuum environment is strongly influenced by the non-uniformities in the plasma plume. The optical thickness increases with increasing angle from the laser axis. From the laser axis (0°) to the direction perpendicular to the laser axis (90°), the full-band and EUV fluxes decrease by 34% and 61%, respectively. The

radiation transport model also yields the spatial distribution of EUV. A source size of 100 μm determined.

The initial conditions for the particle code, which is employed to predict the debris distributions on the collector, are not uniform. Due to the limited resolution of the particle code, only highly energetic ions are resolved. The velocity and particle density distributions at the EUV collector are not uniform. The particle and kinetic energy distributions are used to predict the collector life-time. The sputtering yields for Mo and Si are derived as a function of the ion impact angle and energy. On the outer border of the collector, a reflectivity loss of 10% is obtained after 2 hours of exposure from a 6 kHz source. The time dependence of the reflected EUV flux is used to predict an overall reflectivity loss of 10%, hence a collector life-time of 3 hours. The tin deposition for the baseline case is on the order 10^{-3} nm per pulse. As a conclusion, different debris mitigation subsystems, including fast ion mitigation and collector cleaning are required to meet the source requirements.

The study of laser pulse duration shows a decrease of maximum CE with increasing pulse durations. For longer pulses, the optimum irradiance shifts towards larger values. The CE is larger for a spot size exceeding the droplet diameter by a factor 1.6 than for a spot size equal to the droplet diameter.

Different droplet diameters in the range 50-10 μm have been investigated. The drop in EUV energy between the 50 μm and the 20 μm droplet is one order of magnitude. On the other hand, the drop in the flux of high energy ions and low energy ions / atoms is also one order of magnitude. As a consequence, the choice of droplet diameter results from a trade-off between the amount of acceptable debris and the required EUV energy per pulse. RHD simulations of the irradiated and the subsequent droplet reveal nanosecond pressure fluctuations at the droplet surface, with amplitudes up to 1 GPa for a droplet spacing of 5 diameters. The pressure amplitudes decrease by a factor of 6 for a droplet spacing of 10 diameters. The detailed influence of the pressure fluctuations on the tin droplets is the subject of ongoing work at ETH Zurich. Furthermore, the formation of a high velocity flow (>1 km/s) around the droplet is observed. Up to a spacing of 10 droplet diameter, the flow velocities and densities are large enough to induce droplet breakup.

The misalignment between the irradiated droplet and the laser pulse has been investigated for an 8 ns laser pulse. The drop in CE from 100% to 80% overlap equals 8.7% and 5.6% for an irradiance of 100 GW/cm^2 and 400 GW/cm^2 , respectively. The overlap of 80% corresponds to a shift of 0.92 times the droplet radius between the laser axis and the droplet center. The dose stability, which corresponds to the experimental lateral instability, equals 0.8%. The EUV source requirements are fulfilled for a lateral instability (3σ) below 0.23 % of the droplet diameter at an irradiance of 100 GW/cm^2 . Higher irradiances increase this threshold.

Chapter 7

Conclusions, summary and future work

7.1. Conclusions

Droplet generation in a soft X-ray source is investigated with the help of an in-house developed droplet dispenser. The patent pending droplet dispenser, which is integrated in a fully functional tin droplet-based higher power EUV LPP light source at ETH Zurich, generates a coherent and monodisperse stream of tin droplets at tens of kilohertz. An experimental methodology, which is based on measurements with the help of a fast CCD and LED flash, as well as laser-photodiode light barrier, yields a temporal and spatial characterization of individual droplets within the soft X-ray source. Additionally, systematic studies on laser irradiated tin droplets are conducted with a novel multidimensional multiscale software package.

- The instability modes of the droplet stream are classified into droplet timing jitter, as well as high and low frequency lateral displacements. The other key droplet parameters in a LPP light source are the droplet spacing and size.
- The required EUV dose stability of 0.2% is obtained for a lateral instability (3σ) below 23 % of the droplet diameter (for a droplet diameter of 50 μm , a laser spot of 80 μm and an

irradiance of 100 GW/cm²). Larger laser irradiances increase this threshold. The same findings are valid for laser-droplet misalignments due to the timing jitter.

- The high frequency (> 0.5 Hz) part of the lateral droplet instability has three standard deviations of one droplet diameter at an excitation frequency of 20 kHz and a droplet spacing of 7.5 droplet diameters. The corresponding dose stabilities equal 0.8% and 0.3% for laser irradiances of 100 GW/cm² and 400 GW/cm², respectively.
- The low frequency part (< 0.5 Hz) of the lateral displacement varies by ten droplet diameters (3 σ) and can therefore be compensated by active position control.
- Contamination control is crucial for stable operation of the droplet generator. A correlation between fluid inhomogeneities and the droplet train stability is observed. In addition, the droplet diameter is found to vary up to 15% (3 σ) during operation. The underlying mass flow fluctuation is also related to fluid inhomogeneities.
- The interaction of the plasma with the subsequent droplet is predicted to lead to droplet fragmentation for the typical droplet spacings obtained from Rayleigh breakup. The largest experimental droplet spacings of 7.5 droplet diameters are at the limit of fragmentation.
- The droplet size is determined by a trade-off between required source power and acceptable debris. Vaporization of the complete droplet occurs for a droplet diameter of 10 μm . However, the EUV energy per pulse for the 10 μm droplet is 30 times smaller than for the 50 μm droplet. The developed droplet dispenser generates droplets with diameters from 38 to 65 μm .
- The lowest experimentally measured droplet timing jitter is on the order of 5% (3 σ) (at a frequency of 16 kHz). Such timing jitters require individual droplet triggering.
- The droplet timing jitter is found to be strongly sensitive to the excitation frequency.
- A novel fast response high temperature pressure probe for use in liquid metals is successfully employed for measuring the pressure response at the nozzle inlet. The probe is also useful for online monitoring of the nozzle pressure.
- The boundary conditions of droplet breakup are found to be highly frequency dependent. The pressure response at the nozzle inlet has a complex, non-linear structure with pressures distributed over three orders of magnitude.

- The good match between the measured structural and pressure responses confirms that a linear relationship between the pressure and the velocity of the piston tip can be assumed in the design of the excitation system.
- The resonance peaks of the pressure response can be assigned to the axial modes of the piston, which are found to be most pronounced when efficiently coupled to the axial mode of the piezoelectric actuator. The main tuning possibilities for the piston resonance include the physical dimensions of the piston and the resonance behavior of the piezoelectric stack.
- The timing jitter could be successfully predicted with the help of the droplet formation model from the measured nozzle pressure. The timing jitter depends on the excitation wavelength (or frequency and jet velocity), the pressure amplitude and the perturbation noise level.
- Large excitation pressures and low noise firstly lower the timing jitter and secondly extend the operating range of the dispenser towards lower wave numbers, hence larger droplet spacings.
- A radiation hydrodynamic code is used for the first time together with a sophisticated atomic model of tin and a particle code for modeling the emission and debris characteristics of a droplet-based LPP source. Good agreement with experimental results is obtained.
- A strong anisotropy of the temperature and density distribution in the plasma plume is observed, which significantly determines the emission and debris characteristics of the LPP. The ion number density and kinetic energy distributions on the EUV collector are not uniform, hence tailored debris mitigation techniques are required.
- Due to the reduced optical thickness along the laser axis, the EUV and full-band emissions are highest in this region. At representative source conditions, the angular distribution of EUV emission, which is useful for collector design decays from the laser axis (0°) to 90° by more than 60%.
- The full-band emission of the plasma is on the order of 60% of the incident laser energy. With the help of the computed angular flux distribution, the collector heat load, which sets the boundary conditions for thermal design can be estimated.
- The requirements for a debris mitigation system are quantified by numerical means for a tin droplet-based EUV LPP source.

- The collector life-time is estimated to be in the range of 3 hours (at 6 kHz operation). Ions need to be decelerated to sub-keV energies or the ion flux needs to be reduced by more than 3 orders of magnitude to meet the 10'000 hours operation requirement.
- Without debris mitigation, the layer of deposited tin reaches the threshold of 1 nm after only a few thousand pulses.

7.2. Summary and concluding remarks

The main objective of this work is to study droplet generation in the harsh environment of a high power EUV source. For this purpose a droplet dispenser is designed and manufactured. Different experimental methods and numerical models are employed to determine the causes for the main issues related to droplet generation in an EUV source. Guidelines for an optimized droplet dispenser design are derived. In the second part of the work, sophisticated modeling tools are employed to predict the emission and debris characteristics of the tin droplet-based LPP. The droplet characteristics from the experimental work are taken as boundary conditions for the plasma simulations. The influence of the main droplet and laser parameters on the LPP is investigated in a set of parametric studies. Additionally, the plasma simulations help to refine the initially vague droplet requirements.

7.2.1.1. Droplet dispenser

Rayleigh breakup of the tin jet is identified as being a potential mechanism to generate a monodisperse stream of droplets at several tens of kilohertz in vacuum. The modular design of the dispenser is based on easily replaceable cartridges, which consist of the material reservoir and the nozzle. The tin cartridges are inserted into a cold and protective casing, which is mounted on a motion stage in the vacuum chamber. The excitation mechanism relies on the generation of pressure waves at the tip of a piezoelectrically actuated piston, which is immersed in the liquid tin. These pressure waves result in a growing perturbation of the jet contour, which leads to the jet breakup into droplets at the desired excitation frequency. Active cooling of the piezoelectric actuator, which has a limited operating temperature, ensures stable operation. Furthermore the cooling is designed in order not affect the tin reservoir and nozzle temperatures. For this reason, the dispenser can be operated well above the melting point of tin (> 300 °C). The reliability of droplet generation is found to strongly depend on nozzle design and contamination control. Contamination management is crucial to avoid nozzle clogging and achieve the required droplet stream stability. A multitude of different nozzle designs has been studied in the context of this work. The development of the droplet generator is a very multidisciplinary challenge. The dispenser enables further research on tin droplet-based LPPs.

7.2.1.2. Droplet generation

The experimental methods, which are used to quantify the quality of the droplet stream, rely on direct imaging of the droplet train with the help of a fast CCD, a macroscopic lens and an ultra-bright LED flash. Exposure times in the sub-microsecond range are achieved. Droplets are tracked in time with a laser-photodiode light barrier. Firstly, the droplet train is imaged for a variation of the main dispenser operating parameters, which are the reservoir backpressure and the excitation frequency. The largest measured droplet spacing is in the range of 7.5 droplet spacings, which exceeds the theoretical optimum by 70%. It is found that the smallest droplet diameters are found for small frequencies and large pressure, while the droplet spacing is maximized for the inverse settings. For a given nozzle size, this results in a trade-off between droplet size and droplet spacing.

The temporal dependence of the droplet diameter, the lateral stability and the droplet timing jitter is studied by post-processing image series of the droplet stream, which have been recorded at an excitation frequency of 20 kHz and a backpressure of 20 bar. A variation of the droplet diameter of 15% is measured, which, at a constant droplet frequency translates into a variation of the nozzle mass flow. Potential causes are thermal transients and fluid impurities in the nozzle. For deriving the lateral stability of the droplet train, the time signal of the droplet train position is split into a high and low frequency part at a frequency of 0.5 Hz. Although, the low frequency fluctuations are in the range of ten droplet diameters, they can be compensated by active position control of the dispenser. The high frequency variations of the lateral position yield three standard deviations of one droplet diameter. These instabilities are again, at least partially related to flow disturbances in the nozzle due to fluid impurities. A droplet timing jitter of 5.1% is determined at an excitation frequency of 20 kHz. The acceptable jitter depends on the characteristics of the drive laser. Overall a strong dependence of the droplet jitter on the excitation frequency is observed.

In the context of this work, a novel high temperature fast response miniature pressure probe for use in liquid metals up to 255 °C has been developed. The uncooled probe is based on a piezoresistive sensor. The static calibration in the dispenser and the dynamic calibration in a shock tube prove that the probe is highly suited for operation in liquid tin. The baseline measurements in liquid tin at the nozzle inlet reveal a complex pressure response with amplitudes up to 440 mbar. The developed probe is a useful tool for studying the excitation mechanism of a liquid metal droplet dispenser and for monitoring the performance of the excitation system during long-term operation.

The developed probe is used to investigate the non-ideal boundary conditions, which lead to droplet breakup. Due to the complex structure of the observed pressure responses, a structural analysis is carried out using LDV. Significant displacements are only observed at the piston tip, which proves that the acoustic pressure is generated by the oscillating piston. The comparison of the structural response with finite-element simulations is useful in determining the origins of the observed resonance peaks. The resonances are mainly due to axial eigenmodes of the piston, which are amplified in the frequency region, where the axial eigenfrequency of the piezoelectric actuator is

located. A good match between the structural response and the pressure response is observed for two different oscillating piston designs. The fluid-structure interaction of the piston and the acoustic medium do not add or shift resonance frequencies. The excitation mechanism can be mechanically tuned to yield a desired resonance peak in the pressure response. Tuning possibilities include the adaptation of the physical dimensions (especially length) of the piston, as well as the resonance behavior of the piezoelectric stack. The resonant frequency of the piezoelectric stack is a function of its material properties, dimensions and clamping inside the assembly. The developed FE model and the pressure sensor are useful tools in designing a tuned excitation system.

Next, the correlation between the nozzle inlet pressure and the resulting droplet train characteristics, namely droplet timing jitter and droplet spacing is detailed. The source requirement is to achieve a maximum droplet spacing with a minimum droplet jitter. A sweep of the excitation frequency is completed with simultaneous measurements of droplet timing. The pressure response is recorded under the same conditions. In order to understand the correlation between the two signals, the measured pressure response is used as an input to a droplet formation model. The droplet formation model predicts a frequency dependent timing jitter, which is comparable to the experimental measurements. The correlation between pressure and jitter is determined by the growth rate of the main perturbation, the noise level and the acoustic pressure. A noise level (RMS) of 0.3% of the peak pressure amplitude is derived by comparing the numerical and experimental results. Large excitation pressures and a low noise level lower the overall timing jitter and extend the operating range towards lower wave numbers, hence larger droplet spacings. It is observed, that as the perturbation wave number decreases, the growth rate of the main excitation decreases. On the other hand, noise contributions with wave numbers with higher growth rates dominate and lead to a non-deterministic structure of the droplet train. This effect can be delayed by increasing the acoustic pressure and lowering the noise level.

A CFD model is employed to study the droplet timing for large droplet spacings. CFD is required, as the linear droplet formation is unable to predict satellite formation. The lowest simulated wave number equals 0.12 at an excitation pressure of 3 bar for a non-dimensional droplet jitter on the order of 10^{-4} . Eventually, the following design guidelines can be derived for optimizing the developed droplet dispenser with application in an EUV source at a predetermined (multiple of the laser repetition rate) frequency:

- i. The dispenser excitation system is tuned to generate high acoustic pressures at the desired operation frequency. Tuning is mainly achieved by adapting the piston geometry and the resonant frequency of the piezoelectric stack.
- ii. The noise level on the jet needs to be minimized. Prominent noise sources are multi-frequency nozzle vibrations, fluctuations in the nozzle flow such as ripples due to the surface roughness or fluid inhomogeneities and electrical noise on the piezoelectric actuator.

- iii. The jet velocity is then adjusted by varying the reservoir pressure in order to find the optimum droplet stream wave number, according to the trade-off between lowest wave number and acceptable timing jitter.

7.2.1.3. Tin droplet-based LPP modeling

A set of computational tools has been developed in order to be able to model the full range of physical processes, which are included in the generation and the expansion of the LPP. The main efforts are invested into the development of a radiation solver, which is based on the flux-limited multigroup diffusion approximation. The code uses emissivity source terms and transport coefficients, namely opacity coefficients, which are computed with the help of a coupled atomic physics code. The emissivities and opacities are derived as a function of electron density and temperature. As an intermediate result, a maximum spectral efficiency of 14% is determined for electron densities around 10^{19} cm^{-3} , while at higher electron densities, the contributions from satellite lines lower the spectral efficiency. The radiation solver, together with a two-dimensional hydrodynamic code, yields a reliable prediction of the in-band and full-band emission from the LPP. The detailed atomic model is validated by comparison with experimental emission and absorption spectra. On the other hand, the RHD code is validated by comparison with results from the official SEMATECH benchmark case for EUV source modeling tools. Additional benchmarks for the electron density and the angular EUV distribution for planar targets are completed. The hydrodynamic code is coupled to a particle code, which is based on the Particle-In-Cell and Direct Simulation Monte Carlo methods. This hybrid code is employed to simulate debris dynamics up to the EUV collector. Eventually, the results are used to predict the collector life-time.

First, a baseline case of a $50 \mu\text{m}$ tin droplet irradiated by a Nd:YAG laser of 21 ns pulse duration (FWHM) is studied. Overall, the distributions of electron temperature and density are found to be strongly non-uniform. The largest velocities are found along the laser axis. As a result, the lowest densities are found in this region at the end of the laser pulse. As a consequence, the in-band and full-band angular emissions have peaks along the laser axis, with a decrease towards 90° of 34% and 61%, respectively. The energy balance at the end of the laser pulse reveals a full-band radiation energy of 60% of the supplied laser energy. This quantification of the radiated energy, when combined with the angular distribution of the full-band emission is useful for the thermal design of the collector. The radiation transport model also yields the spatial distribution of EUV. The source size of $100 \mu\text{m}$ is comparable to the measured source size. Small source sizes are essential for high brightness oriented source designs.

The large scale studies, which are based on the results from the particle code, reveal strongly non-uniform particle and ion kinetic energy distributions on the EUV collector. Ions up to Sn^{6+} are modeled by the particle code. More energetic ions have too low abundances to be resolved. Their long-term effect could however be significant. For the global distribution of kinetic energies, good agreement is observed with experimental results from a planar target. The collector life-time is

estimated with the help of computed values for the sputtering yields for Mo and Si. The computation takes the impact angle into account, which is found to be largest on the outer boarder. The local reflectivity loss of 10% can be derived from the particle, energy and impact angle distributions on the collector. Locally, a 10% reflectivity drop is observed after 2 hours of operation, while the overall reflectivity loss of 10% is achieved after 3 hours only (for 6 kHz operating frequency). As a conclusion, debris mitigation of fast ions is essential. Reduction in the ion flux by more than three orders of magnitude is required or alternatively a deceleration of ions to sub-keV energies. The second mechanism, which limits life-time is tin deposition. The tin deposition rate is on the order of 0.001 nm per shot, which results in a collector life-time of a few thousand shots only. Again, debris mitigation techniques and collector cleaning methods are needed to achieve a collector life of 10'000 hours.

A set of parametric studies of the main laser and droplet parameters is completed. Firstly, the dependence of the CE, hence EUV energy on the laser irradiance is studied. It is found that long laser pulses lower the CE and shift the optimum irradiance towards higher values. The same trend is observed in experiments for planar tin targets. Secondly, the influence of the laser spot size on the CE is investigated for the 50 μm droplet. The CE is 10% lower for the spot size, which matches the droplet size, than for the spot, which exceeds the droplet diameter by 60%.

A study for droplet sizes in the range from 10 to 50 μm is conducted. The laser spot to droplet diameter ratio is kept constant. It is observed that the EUV energy per pulse decreases with decreasing droplet size. The EUV emission per pulse for the 50 μm droplet is 30 times smaller for the 10 μm . For the same source power, a smaller droplet requires higher repetition rates. From the droplet formation studies, it could be seen that smaller droplets also require higher excitation frequencies for reliable generation. On the other hand, the debris characteristics drastically change with a decrease in droplet diameter. Especially, the remaining droplet fraction, which typically decomposes into fragments, equals 50% of the initial droplet for the 50 μm droplet, while the 10 μm droplet is completely vaporized. As a consequence, the choice of the droplet size results from a trade-off between the acceptable level and types of debris, and the required EUV emission. The trade-off depends on the major components of the system, which are the laser and the debris mitigation system. In the case of a high repetition rate laser, where a small focusing capability is available, the specifications for the debris mitigation system can be less stringent. In the case of a very efficient debris mitigation system, especially for tin neutrals and fragments, is available, the laser can be operated at a lower repetition rate and irradiate large droplets. In conclusion, a general specification for the droplet size is not possible, although sizes in the range of 20-30 μm can be suggested. The droplet spacing has been numerically investigated. The formation of a shockwave in front of the target is observed. For a spacing of five droplet diameters, fragmentation can be expected. The hydrodynamic code is however supposed to overpredict the pressure, as the plasma expansion is modeled in two dimensions and the considered problem is three dimensional.

Experimental studies are required to further quantify the effect of the plasma on the subsequent droplet.

The dependence of the EUV energy per pulse on the misalignment between the laser spot and the droplet is investigated by numerical means. It is found that, even for relatively large misalignments, the laser fluence on the outer boarder of the Gaussian pulse is sufficient to ablate material. This vapor expands into the center of the spot and reaches the plasma temperatures required for EUV emission. An increased laser irradiance yields a weaker drop of CE with misalignment. The computed relationship between EUV energy and the misalignment between the droplet and the laser spot, can be combined with the experimentally measured lateral droplet displacements to predict the dose stability, under the assumption of zero timing jitter. A negligible timing jitter can be achieved by individual droplet triggering. The dose stability, which is obtained from the experimental results, equals 0.8% at an irradiance of 100 GW/cm². This exceeds the source requirements. The requirements are met if three standard deviations of the droplet displacement are smaller than 0.23 droplet diameters. For an irradiation of 400 GW/cm², this threshold increases to 0.8 droplet diameters. This sets the requirements for lateral stability.

At this point the conclusions should be brought to a closure by referring to the objectives of this work: An in-house developed, patent pending droplet dispenser design is proposed, manufactured and tested. The dispenser is operational in the main EUV source of the Laboratory for Energy Conversion, ETH Zurich. Innovative experimental methods have been applied to identify the main issues related to droplet generation in an EUV source. These issues are reliable operation and droplet stream stability in time and space. The stability and reliability need to be achieved for large droplet spacings, which limit the influence of the supersonic expansion of the plasma on the subsequent droplet. The observed timing jitter requires individual droplet triggering. The acceptable jitter then depends on the drive laser design. The lateral stability needs to ensure the required dose stability. Furthermore, precise control of droplet sizes is required, with a droplet size determined by the trade-off between acceptable debris and the required EUV energy. Tuning guidelines are proposed for achieving resonant frequencies in the droplet generation. This helps to increase the stream's stability and the droplet spacing. Validated numerical tools have been employed to derive the radiation and debris characteristics of the tin droplet-based plasma, which are essential for the source design and more specifically for the debris mitigation and collector design.

7.3. Future work

This work addresses issues related to droplet generation in an EUV source, as well as the computational modeling of the tin droplet-based LPP. A meaningful continuation of the present work should therefore be related to these two topics.

7.3.1. Droplet generation

The droplet dispenser has been developed for short-term operation with operating times in the range of 1-2 hours. Droplet dispensers in EUV sources are required to operate 24 hours, 7 days a week during several weeks. For this purpose, the current design should be scaled for long-term operation in an EUV source. New long-term issues, especially related to tin chemistry and the exposure to plasma debris can be expected. In the same context, the nozzle size should be further reduced. Ideally the nozzle size should be extended to sizes of a few microns in order to yield droplets with sizes below 30 μm . Based on such nozzle sizes, the yearly tin consumption should be in the range of a few liters and a drastic reduction of low energy debris should be obtained.

The developed imaging method should be extended to two dimensions, either by projecting two dimensions onto one CCD or by using two separate cameras. The last approach is probably the more feasible solution. Another issue, which is related to droplet train imaging is the reduction of the uncertainty on the droplet diameter, which is essential in determining the jet velocity, hence perturbation wave number. The uncertainty is mainly reduced by increasing the optical and digital resolutions of the imaging system. Furthermore, the threshold level detection of the droplet contour should be automated.

Lateral stability is crucial for meeting the source stability requirements. A methodology, which relies on new diagnostic tools and numerical models should be developed to gain more insight into the potential causes for this droplet instability. In this context, the developed droplet CFD model could be used to study the influence of fluid contaminations on the lateral stability of the droplet stream. Noisy perturbations of the jet, which are potentially related to the drive electronics of the piezoelectric actuator or to the nozzle design have to be further minimized in future dispenser designs. The noise level can be quantified by studying the jet's breakup length in the absence of an external excitation.

In order to improve the design rules for the excitation system, the structural measurements by LDV should be completed at the operating temperature ($>280^\circ\text{C}$). In general, high temperature effects, such as the change of properties of the piezoelectric stack should be investigated at the operating temperature.

The relevance of the droplet spacing on source stability is not trivial from a computational point of view and should be investigated experimentally by imaging the droplet train in the vicinity of the plasma.

7.3.2. Droplet-based LPP modeling in an EUV source

An almost infinite number of physical models can be added to the developed plasma codes. The engineering judgment determines which models are necessary to achieve accurate modeling of a

given problem. A few code extensions are required for an improved modeling of the debris and emission characteristics of the droplet-based LPP.

The interaction of the laser pulse with the tin droplet is inherently a three dimensional problem, when misalignment or any other imperfections, such as the real beam profile are considered. Accurate modeling of the interaction of the plasma with the subsequent droplet also demands a three dimensional code. The parallelization capabilities of modern supercomputers should allow for extending the RHD and the particle code into three dimensions.

The atomic model is limited to the minimum number of transitions, which are relevant to predict the emissivity and opacity in the EUV window. Outside the EUV window, additional transitions gain in importance, as observed in experimental spectra. Due to computational limitations, these transitions have not been modeled yet. More transitions could be included by running long-term simulations (> 1 week) or by parallelizing the main solver for the atomic model.

The most important extension of the RHD code is required in the context of the liquid tin droplet model. The effect of surface tension needs to be included in order to accurately simulate the influence of the ablation pressure on the droplet. Potential fragmentation could be predicted. Liquid surface tension also plays an essential role in the interaction of the plasma with the subsequent droplet.

The laser model in the RHD code should be extended to include the laser beam divergence. Indeed, during the laser heating, the plasma plume can expand to length scales at which the beam divergence needs to be considered.

A major challenge in current RHD simulations is the computational effort required when simulating long laser pulses. Indeed the corresponding plasma plume requires large domain sizes (> 1 million cells), which render a sufficient resolution of the droplet challenging. One option is the use of an adaptive mesh in order to reduce the computational effort for long pulse simulations. Another option is the parallelization of the main loops of the hydrodynamic code, similarly to the radiation solver, which is already parallelized for shared and distributed memory systems.

The resolution of the particle code is determined by the number of simulated particles, which also determines the computational running time. The resolution limit should be increased in order to resolve highly energetic particles and to make simulations at low vacuum levels (up to 1 Pa) possible. Running the code on parallel architectures is a potential option to increase its resolution. An assessment on the relevance of additional collision types, such as recombination and Coulomb collisions is required.

Appendix

References

1. I. C. E. Turcu and J. B. Dance, *X-rays from laser plasmas*. (Wiley, 1999).
2. D. T. Attwood, *Soft x-rays and extreme ultraviolet radiation*. (Cambridge University Press, 2000).
3. M. H. Key and R. J. Hutcheon, *Spectroscopy of laser-produced plasmas*. (Academic Press, 1980).
4. D. A. Jaroszynski, R. Bingham and R. A. Cairns, *Laser-plasma interactions*. (CRC Press, 2009).
5. H. M. Hertz, G. A. Johansson, H. Stollberg, J. de Groot, O. Hemberg, A. Holmberg, S. Rehbein, P. Jansson, F. Eriksson and J. Birch, *J. Phys IV* **104**, 115-119 (2003).
6. L. Rymell and H. M. Hertz, *Opt. Commun.* **103** (1-2), 105-110 (1993).
7. R. J. Tompkins, I. P. Mercer, M. Fettweis, C. J. Barnett, D. R. Klug, L. G. Porter, I. Clark, S. Jackson, P. Matousek, A. W. Parker and M. Towrie, *Rev. Sci. Instrum.* **69** (9), 3113-3117 (1998).
8. D. T. Goodhead, *Synchrotron Radiation in the Biosciences*. (Oxford University Press, 1994).
9. U. Schwenn and R. Sigel, *J. Phys. E Sci. Instrum.* **7** (9), 715-718 (1974).
10. J. Brunetea, E. Fabre, C. Salet and P. Vasseur, *Phys. Lett. A* **24** (12), 687 (1967).
11. A. F. Haught and D. H. Polk, *Phys. Fluids* **13** (11), 2825-2841 (1970).
12. E. W. Sucov, J. L. Pack, A. V. Phelps and A. G. Engelhardt, *Phys. Fluids* **10** (9), 2035-2048 (1967).
13. S. I. Association, *www.sia-online.org*.
14. P. Gargini, *Proceedings of the Sematech EUVL Symposium*, Miami (2011).
15. ITRS, *www.itrs.net*.
16. G. Hughes, L. C. Litt, A. Wuest and S. Palaiyanur, *Proc. SPIE* **7028**, 70281P (2008).
17. T. Wallow, D. Civay, S. Wang, H. F. Hoefnagels, C. Verspaget, G. Tanriseven, A. Fumar-Pici, S. Hansen, J. Schefske, M. Singh, R. Maas, Y. v. Dommelen and J. Mallman, *Proc. SPIE* **8322**, 83221J (2012).
18. T. W. Barbee, S. Mrowka and M. C. Hettrick, *Appl. Optics* **24** (6), 883-886 (1985).
19. S. Bajt, J. Alameda, T. Barbee, W. M. Clift, J. A. Folta, B. Kaufmann and E. Spiller, *Proc. SPIE* **4506**, 65-75 (2001).
20. K. Hiruma, S. Miyagaki, H. Yamanashi, Y. Tanaka and I. Nishiyama, *Thin Solid Films* **516** (8), 2050-2057 (2008).
21. P. Kuerz, *Proceedings of the Sematech EUVL Symposium*, Kobe (2010).
22. K. Murakami, *Proceedings of the Sematech EUVL Symposium*, Lake Tahoe (2008).
23. V. Bakshi, *EUV lithography*. (SPIE Wiley, 2009).
24. R. Peeters, *Proceedings of the Sematech EUVL Symposium*, Miami (2011).
25. B. BC Cha, *Proceedings of the Sematech EUVL Symposium*, Kobe (2010).
26. G. Zhang, *Proceedings of the Sematech EUVL Symposium*, Kobe (2010).

27. D. Hellweg, M. Weiss, S. Perlitz, J. H. Peters, W. Harnisch and M. Goldstein, Proc. SPIE **8322**, 83220L (2012).
28. J. R. Hoffman, A. N. Bykanov, O. V. Khodykin, A. I. Ershov, N. R. Bowering, I. V. Fomenkov, W. N. Partlo and D. W. Myers, Proc. SPIE **5751**, 892-901 (2005).
29. S. Churilov, Y. N. Joshi and J. Reader, Opt. Lett. **28** (16), 1478-1480 (2003).
30. H. Shields, S. W. Fornaca, M. B. Petach, M. Michaelian, R. D. McGregor, R. H. Moyer and R. J. S. Pierre, Proc. SPIE **4688**, 94-101 (2002).
31. P. Mandelbaum, M. Finkenthal, J. L. Schwob and M. Klapisch, Phys. Rev. A **35** (12), 5051-5059 (1987).
32. A. Cummings, G. O'Sullivan, P. Dunne, E. Sokell, N. Murphy and J. White, J. Phys. D. **38** (19), 3756-3756 (2005).
33. S. S. Harilal, T. Sizyuk, V. Sizyuk and A. Hassanein, Appl. Phys. Lett. **96** (11), 111503 (2010).
34. D. Colombant and G. F. Tonon, J. Appl. Phys. **44** (8), 3524-3537 (1973).
35. M. Poirier, T. Blenski, F. D. de Dortan and F. Gilleron, J. Quant. Spectrosc. **99** (1-3), 482-492 (2006).
36. S. F. Horne, F. M. Niell, M. J. Partlow, M. M. Besen, D. K. Smith, P. A. Blackborow and D. Gustafson, Proc. SPIE **7271**, 72713A (2009).
37. M. Yoshioka, Y. Teramoto, J. Jonkers, M. C. Schurmann, R. Apetz, V. Kilian and M. Corthout, Proc. SPIE **7969**, 79691G (2011).
38. G. Schriever, O. Semprez, J. Jonkers, M. Yoshioka and R. Apetz, J. Micro-Nanolith. Mem. Moems **11** (2), 021104 (2012).
39. H. Yabuta, S. Mori, T. Inoue, Y. Teramoto, H. Sato and K. Hotta, Proc. SPIE **7969**, 79692U (2011).
40. G. Bianucci, A. Bragheri, G. L. Cassol, R. Ghislanzoni, R. Mazzoleni and F. E. Zocchi, Proc. SPIE **7969**, 79690B (2011).
41. T. Ando, S. Fujioka, H. Nishimura, N. Ueda, Y. Yasuda, K. Nagai, T. Norimatsu, M. Murakami, K. Nishihara, N. Miyanaga, Y. Izawa, K. Mima and A. Sunahara, Appl. Phys. Lett. **89** (15), 151501 (2006).
42. Y. Tao, S. S. Harilal, M. S. Tillack, K. L. Sequoia, B. O'Shay and F. Najmabadi, Opt. Lett. **31** (16), 2492-2494 (2006).
43. H. A. Bender, D. Oconnell and W. T. Silfvast, Appl. Optics **34** (28), 6513-6521 (1995).
44. K. Nagai, Q. C. Gu, Y. Yasuda, M. Nagata, T. Norimatsu, H. Nishimura, S. Fujioka, S. Uchida, Y. Shimada, M. Yamaura, K. Hashimoto, H. Fujita, M. Nakatsuka, K. Nishihara, N. Miyanaga, K. Mima and Y. Izawa, J. Phys. IV **133**, 875-880 (2006).
45. Y. Tao, F. Sohbzadeh, H. Nishimura, R. Matsui, T. Hibino, T. Okuno, S. Fujioka, K. Nagai, T. Norimatsu, K. Nishihara, N. Miyanaga, Y. Izawa, A. Sunahara and T. Kawamura, Appl. Phys. Lett. **85** (11), 1919-1921 (2004).
46. H. Tanaka, K. Akinaga, A. Takahashi and T. Okada, Appl. Phys. A **79** (4-6), 1493-1495 (2004).
47. S. George, C. S. Koay, K. Takenoshita, R. Bernath, M. Al-Rabban, C. Keyser, V. Bakshi, H. Scott and M. Richardson, Proc. SPIE **5751**, 779-788 (2005).
48. M. Richardson, C. S. Koay, K. Takenoshita, C. Keyser and M. Al-Rabban, J. Vac. Sci. Technol. B **22** (2), 785-790 (2004).
49. S. S. Harilal, B. O'Shay, M. S. Tillack, Y. Tao, R. Paguio, A. Nikroo and C. A. Back, J. Phys. D **39** (3), 484-487 (2006).
50. T. Aota and T. Tomie, Phys. Rev. Lett. **94** (1), 015004 (2005).

51. P. A. C. Jansson, B. A. M. Hansson, O. Hemberg, M. Otendal, A. Holmberg, J. de Groot and H. M. Hertz, *Appl. Phys. Lett.* **84** (13), 2256-2258 (2004).
52. R. Rakowski, J. Mikolajczyk, A. Bartnik, H. Fiedorowicz, F. D. de Dortan, R. Jarocki, J. Kostecki, M. Szczurek and P. Wachulak, *Appl. Phys. B-Lasers* **102** (3), 559-567 (2011).
53. M. Kaku, S. Touge, M. Katto and S. Kubodera, *Proc. SPIE* **7271**, 727132 (2009).
54. I. V. Fomenkov, B. L. Fontaine, D. Brown, I. Ahmad, P. Baumgart, N. R. Bowering, D. C. Brandt, A. N. Bykanov, S. D. Dea, A. I. Ershov, N. R. Farrar, D. J. Golich, M. J. Lercel, D. W. Myers, C. Rajyaguru, S. N. Srivastava, Y. Tao and G. O. Vaschenko, *J. Micro-Nanolith. Mem. Moems* **11** (2), 021110 (2012).
55. J. Fujimoto, T. Abe, S. Tanaka, T. Ohta, T. Hori, T. Yanagida, H. Nakarai and H. Mizoguchi, *Journal of Micro/Nanolithography, MEMS and MOEMS* **11** (2), 021111 (2012).
56. A. Endo, H. Hoshino, T. Suganuma, K. Nowak, T. Yanagida, T. Yabu, T. Asayama, Y. Ueno, M. Moriya, M. Nakano, H. Someya, T. Nishisaka, T. Abe, G. Soumagne, H. Komori, H. Mizoguchi, A. Sumitani and K. Toyoda, *Proc. SPIE* **6921**, T9210-T9210 (2008).
57. A. Z. Giovannini, F. Dieterich, I. Henderson, N. Chokani and R. S. Abhari, *Proc. SPIE* **7636**, 763613 (2010).
58. A. Z. Giovannini, O. Morris, I. Henderson, S. Ellwi and R. S. Abhari, *Proc. SPIE* **7969**, 79692X (2011).
59. V. Bakshi, *EUV sources for lithography*. (SPIE Press, 2006).
60. T. Feigl, M. Perske, H. Pauer, T. Fiedler, S. Yulin, M. Trost, S. Schroder, A. Duparre, N. Kaiser, A. Tunnermann, N. R. Bowering, A. I. Ershov, K. Hoffmann, B. L. Fontaine and K. D. Cummings, *Proc. SPIE* **8322**, 832217 (2012).
61. G. Bianucci, G. L. Cassol, J. Kools, M. Prea, G. Salmaso, G. Valsecchi, F. E. Zocchi, D. Bolshukhin, M. Schurmann, G. Schriever, A. Mader and P. Zink, *Proc. SPIE* **7271**, 72710C (2009).
62. N. R. Bowering, United States Patent No. 7309871 (2007).
63. N. Benoit, S. Yulin, T. Feigl and N. Kaiser, *Phys. B-Condensed Matter* **357** (1-2), 222-226 (2005).
64. K. Takenoshita, C. S. Koay and I. C. E. Turcu, *Proc. SPIE* **5037**, 792-800 (2003).
65. R. Abhari, A. Giovannini, B. Rollinger and D. Bleiner, Patent No. WO2010112171-A1.
66. S. S. Harilal, B. O'Shay, Y. Z. Tao and M. S. Tillack, *J. Appl. Phys.* **99** (8), 083303 (2006).
67. S. Bollanti, F. Bonfigli, E. Burattini, P. Di Lazzaro, F. Flora, A. Grilli, T. Letardi, N. Lisi, A. Marinai, L. Mezi, D. Murra and C. Zheng, *Appl. Phys. B-Lasers* **76** (3), 277-284 (2003).
68. S. S. Harilal, B. O'Shay, Y. Tao and M. S. Tillack, *Appl. Phys. B-Lasers* **86** (3), 547-553 (2007).
69. D. N. Ruzic, *Proceedings of the Sematech EUVL Symposium*, Lake Tahoe (2008).
70. D. R. Bates, A. E. Kingston and W. P. Mcwhirter, *Proc. R. Soc. London* **270** (1341), 155 (1962).
71. D. R. Bates, A. E. Kingston and R. W. P. Mcwhirter, *Proc. R. Soc. London* **267** (1330), 297 (1962).
72. H. Mizoguchi, T. Abe, Y. Watanabe, T. Ishihara, T. Ohta, T. Hori, T. Yanagida, H. Nagano, T. Yabu, S. Nagai, G. Soumagne, A. Kurosu, K. M. Nowak, T. Suganuma, M. Moriya, K. Kakizaki, A. Sumitani, H. Kameda, H. Nakarai and J. Fujimoto, *Proc. SPIE* **7969**, 796908 (2011).

73. T. Ariga, H. Hoshino and A. Endo, *High Energy /Average Power Lasers and Intense Beam Applications* **6454**, 45403-45403 (2007).
74. K. Okazaki, D. Nakamura, T. Akiyama, K. Toya, A. Takahashi and T. Okada, Proc. SPIE **7201**, 74881T (2009).
75. B. Rollinger, O. Morris, N. Chokani and R. S. Abhari, Proc. SPIE **7636**, 76363F (2010).
76. L. Rymell, M. Berglund and H. M. Hertz, Appl. Phys. Lett. **66** (20), 2625-2627 (1995).
77. M. Poulter, N. Hay, B. Fulford, P. Campton, M. Mason and D. Burns, Proc. SPIE **7193**, 719309 (2009).
78. T. Ariga, H. Hoshino, T. Miura and A. Endo, Proc. SPIE **6151**, M1513-M1513 (2006).
79. K. Suzuki, A. Miyake and N. Harned, *Proceedings of the Sematech EUVL Symposium*, Prague (2009).
80. H. Mizoguchi, T. Abe, Y. Watanabe, T. Ishihara, T. Ohta, T. Hori, A. Kurosu, H. Komori, K. Kakizaki, A. Sumitani, O. Wakabayashi, H. Nakarai, J. Fujimoto and A. Endo, Proc. SPIE **7636**, 763608 (2010).
81. S. Wurm, *Proceedings of the Sematech EUVL Symposium*, Miami (2011).
82. A. Frohn and N. Roth, *Dynamics of droplets*. (Springer, 2000).
83. A. U. Chen and A. B. Osman, United States Patent No. 6513894 (2002).
84. D. B. Bogy and F. E. Talke, IBM J. Res. Dev. **28** (3), 314-321 (1984).
85. S. P. Lin and R. D. Reitz, Annu. Rev. Fluid. Mech. **30**, 85-105 (1998).
86. M. Otendal, O. Hemberg, T. T. Tuohimaa and H. M. Hertz, Exp. Fluids. **39** (5), 799-804 (2005).
87. M. J. McCarthy and N. A. Molloy, Chemical Engineering Journal **7**, 1 (1974).
88. J. W. S. Rayleigh, Proc. London Math. Soc. **10** (4), 4-13 (1878).
89. C. Weber, Z. Angew. Math. Mech. **11**, 136 (1931).
90. D. A. Caulk and P. M. Naghdi, J. Appl. Mech. **46** (2), 291-297 (1979).
91. J. B. Keller, S. I. Rubinow and Y. O. Tu, Phys. Fluids **16** (12), 2052-2055 (1973).
92. S. J. Leib and M. E. Goldstein, J. Fluid Mech. **168**, 479-500 (1986).
93. S. J. Leib and M. E. Goldstein, Phys. Fluids **29** (4), 952-954 (1986).
94. P. Lafrance, Phys. Fluids **18** (4), 428-432 (1975).
95. A. H. Nayfeh, Phys. Fluids **13** (4), 841-847 (1970).
96. W. T. Pimbley and H. C. Lee, IBM J. Res. Dev. **21** (1), 21-30 (1977).
97. A. E. Green, Int. J. Eng. Sci. **14** (1), 49-63 (1976).
98. N. N. Mansour and T. S. Lundgren, Phys. Fluids **2** (7), 1141-1144 (1990).
99. D. W. Bousfield, R. Keunings, G. Marrucci and M. M. Denn, J. Non-Newtonian Fluid Mech. **21** (1), 79-97 (1986).
100. L. Crane, S. Birch and P. D. S. McCormack, Brit. J. Appl. Phys. **15** (6), 743 (1964).
101. R. W. Faidley and R. L. Panton, Exp. Therm. Fluid. Sci. **3** (4), 383-387 (1990).
102. M. Orme and E. P. Muntz, Phys. Fluids **2** (7), 1124-1140 (1990).
103. N. Ashgriz and F. Mashayek, J. Fluid. Mech. **291**, 163-190 (1995).
104. H. Wijshoff, Phys. Rep. **491** (4-5), 77-177 (2010).
105. A. Schober, R. Gunther, A. Schwienhorst, M. Doring and B. F. Lindemann, Biotechniques **15** (2), 324-329 (1993).
106. B. de Heij, M. Daub, O. Gutmann, R. Niekrawietz, H. Sandmaier and R. Zengerle, Anal. Bioanal. Chem. **378** (1), 119-122 (2004).
107. N. Lass, A. Tropmann, A. Ernst, R. Zengerle, and P. Koltay, Microfluidics and Nanofluidics **12**, 75 (2012).
108. J. M. Waldvogel and D. Poulikakos, Int. J. Heat Mass Transfer **40** (2), 295-309 (1997).
109. S. Haferl and D. Poulikakos, J. Appl. Phys. **92** (3), 1675-1689 (2002).

110. D. J. Hayes, D. B. Wallace and W. R. Cox, 1999 International Conference on High Density Packaging and MCMS **3830**, 242-247 (1999).
111. M. Orme, J. Courter, Q. Liu, J. Zhu and R. Smith, Mater. Res. Soc. Symp. P **624**, 17-22 (2000).
112. D. Poulidakos and J. M. Waldvogel, Advances in Heat Transfer **28**, 1-74 (1996).
113. P. A. C. Jansson, B. A. M. Hansson, O. Hemberg, M. Otendal, A. Holmberg, J. d. Groot and H. M. Hertz, Appl. Phys. Lett. **84** (13), 2256-2258 (2004).
114. B. A. M. Hansson, *Proceedings of the Sematech EUVL Symposium*, San Diego (2005).
115. G. Zimmerman, D. Kershaw, D. Bailey and J. Harte, J. Opt. Soc. Am. **68** (4), 549-549 (1978).
116. T. R. Young, A. M. Landsberg and J. P. Boris, High Performance Computing Symposium 1993, 143-148 (1993).
117. R. E. Olson, L. J. Suter, J. L. Kline, D. A. Callahan, M. D. Rosen, K. Widmann, E. A. Williams, D. E. Hinkel, N. B. Meezan, G. A. Rochau, A. L. Warrick, S. H. Langer, C. Thomas, S. N. Dixit, E. L. Dewald, M. B. Schneider, J. D. Moody, P. Michel, R. J. Wallace, O. L. Landen, J. Edwards, B. J. MacGowan and S. H. Glenzer, *Proceedings of the Sixth International Conference on Inertial Fusion Sciences and Applications Vol. 244*, San Francisco, 2010.
118. J. P. Christiansen, D. E. Ashby and K. V. Roberts, Comput. Phys. Commun. **7** (5), 271-287 (1974).
119. S. V. Zakharov, *Proceedings of the Sematech EUVL Symposium*, Santa Clara (2011).
120. A. Hassanein, V. Sizyuk, V. Tolkach, V. Morozov and B. Rice, Proc. SPIE **5037**, 714-727 (2003).
121. S. V. Zakharov, *Proceedings of the Sematech EUVL Symposium*, Miyazaki, Japan (2004).
122. A. Bar-Shalom, M. Klapisch and J. Oreg, J. Quant. Spectrosc. **71** (2-6), 169-188 (2001).
123. R. D. Cowan, J. Opt. Soc. Am. **58** (6), 808 (1968).
124. J. White, A. Cummings, P. Dunne, P. Hayden and G. O'Sullivan, J. Appl. Phys. **101** (4) (2007).
125. C. B. Alcock, V. P. Itkin and M. K. Horrigan, Canadian Metallurgical Quarterly **23** (3), 309-313 (1984).
126. H. Haj-Hariri and D. Poulidakos, J. Appl. Mech. **67** (3), 626-628 (2000).
127. A. H. Lefebvre, *Atomization and sprays*. (Hemisphere Publishing Corporation, 1989).
128. S. Badertscher, Master's Thesis ETH Zurich, 2011.
129. H. R. Thresh and A. F. Crawley, Metall. Trans. **1** (6), 1531 (1970).
130. D. A. Melford and T. P. Hoar, J. I. Met. **85** (5), 197-205 (1957).
131. J. Bachmann, Master's Thesis ETH Zurich, 2011.
132. G. Brenn and U. Lackermeier, Phys. Fluids **9** (12), 3658-3669 (1997).
133. H. C. Lee, IBM J. Res. Dev. **18** (4), 364-369 (1974).
134. R. N. Berglund and B. Y. H. Liu, Environ. Sci. Technol. **7** (2), 147-153 (1973).
135. A. Takeuchi, T. Yamada and K. Sakai, Jpn. J. Appl. Phys. **49** (7) (2010).
136. C. J. Frederickson, D. J. Hayes, D. B. Wallace, D. Ussery, C. J. Arcoria, M. Motamedi, E. Jennett, and D. Diven, Proc. SPIE **2396**, 248 (1995).
137. M. Orme, J. Courter, Q. B. Liu, C. Z. Huang and R. Smith, Phys. Fluids **12** (9), 2224-2235 (2000).
138. D. W. Gore, United States Patent No. 5598200 (1997).
139. J. C. Yang, W. Chien, M. King and W. L. Grosshandler, Exp. Fluids **23** (5), 445-447 (1997).
140. K. H. Lam, C. L. Sun, K. W. Kwok and H. L. W. Chan, Rev. Sci. Instrum. **80** (7) (2009).

141. *Catalog on Piezoelectric Ceramic Products*. (PI Ceramics, 2011).
142. O. V. Abramov, *High-intensity ultrasonics*. (Gordon and Breach Science Publishers, 1998).
143. M. Bruneau, *Fundamentals of acoustics*. (ISTE Ltd, 2006).
144. J. D. J. S. Samuel, R. Steger, G. Birkle, R. Zengerle, P. Koltay and J. Ruhe, *Anal. Chem.* **77** (19), 6469-6474 (2005).
145. J. de Groot, G. A. Johansson and H. M. Hertz, *Rev. Sci. Instrum.* **74** (8), 3881-3882 (2003).
146. R. B. Rao, K. L. Krafcik, A. M. Morales and J. A. Lewis, *Adv. Mater.* **17** (3), 289 (2005).
147. B. Lemmermeyer, *Ein hochtemperaturbeständiger Einzeltropfenerzeuger für flüssige Metalle*. (VDI Verlag, 2006).
148. A. Aboudheir, P. Tontiwachwuthikul, A. Chakma and R. Idem, *Ind. Eng. Chem. Res.* **43** (10), 2568-2574 (2004).
149. M. Orme and E. P. Muntz, *Rev. Sci. Instrum.* **58** (2), 279-284 (1987).
150. P. Kupferschmied, P. Koppel, W. Gizzi, C. Roduner and G. Gyarmathy, *Meas. Sci. Technol.* **11** (7), 1036-1054 (2000).
151. M. Mansour, N. Chokani, A. I. Kalfas and R. S. Abhari, *Meas. Sci. Technol.* **19** (11), 115401 (2008).
152. C. Lenherr, A. I. Kalfas and R. S. Abhari, *J. Eng. Gas Turb. Power* **133** (1), 11603 (2011).
153. A. D. Kurtz, B. Kochman, A. A. Ned and ASME, *Proceedings of the ASME Turbo Expo 2008*, Berlin, 2008, p.295.
154. M. Mersinligil, J. F. Brouckaert and J. Desset, *Proceedings of the ASME Turbo Expo 2010*, Glasgow, 2010, p.385.
155. C. Lenherr, *High temperature fast response aerodynamic probe*. (ETH, 2010).
156. H. Lamb, *P. R. Soc. Lond.* **98** (690), 205-216 (1920).
157. Y. Kozlovsky, *J. Sound Vib.* **326** (1-2), 332-339 (2009).
158. M. F. Culpin, *P. Phys. Soc. Lond. B* **70** (11), 1069-1078 (1957).
159. D. J. Ewins, *Modal testing*. (Research Studies Press, 2000).
160. A. Abdullah, M. Shahini and A. Pak, *J. Electroceram.* **22** (4), 369-382 (2009).
161. *Ansys 13.0 Mechanical User's Reference*. (Ansys, Inc., 2010).
162. PI Ceramics, *Personal Communication* (2012).
163. *IEEE T. Ultrason. Ferr.* **43** (5), A1-A54 (1996).
164. G. Chevallier, S. Ghorbel and A. Benjeddou, *Smart Mater. Struct.* **17** (6) (2008).
165. S. Sherrit, S. P. L. Y. Bar-Cohen, B. P. Dolgin and R. Tasker, *Proceedings of the IEEE Ultrasonics Symposium*, San Juan, 2000, p.1037-1040.
166. K. Ruschmeyer, *Piezokeramik*. (Expert Verlag, 1995).
167. S. Sherrit, C. M. Jones, J. B. Aldrich, C. Blodget, X. Q. Bao, M. Badescu and Y. Bar-Cohen, *Proc. SPIE* **6929**, 692909 (2008).
168. Q. M. Wang, T. Zhang, Q. M. Chen and X. H. Du, *Sensor Act.* **109** (1-2), 149-155 (2003).
169. F. J. Arnold and S. S. Muhlen, *Ultrasonics* **39** (1), 7-11 (2001).
170. R. Brown and J. L. York, *Aiche J.* **8** (2), 149-153 (1962).
171. M. Ida, H. Nakamura, H. Nakamura, H. Nakamura, K. Ezato and H. Takeuchi, *Fusion Eng. Des.* **63-64** (0), 333-342 (2002).
172. P. Lafrance, *Phys. Fluids* **18** (4), 428-432 (1975).
173. M. Rohani, F. Jabbari and D. Dunn-Rankin, *Phys. Fluids* **22** (10), 107103 (2010).
174. E. F. Goedde and M. C. Yuen, *J. Fluid Mech.* **40**, 495 (1970).
175. S. Middleman and J. Gavis, *Phys. Fluids* **4** (3), 355-359 (1961).
176. J. L. Dressler, *Phys. Fluids* **10** (9), 2212-2227 (1998).

177. B. Braren, *Laser ablation in materials processing: fundamentals and applications*. (Materials Research Society, 1993).
178. S. I. Anisimov and V. A. Khokhlov, *Instabilities in laser-matter interaction*. (CRC Press, 1995).
179. T. W. Johnston and J. M. Dawson, *Phys. Fluids* **16** (5), 722-722 (1973).
180. K. Garloff, M. van den Donker, J. van der Mullen, F. van Goor, R. Brummans and J. Jonkers, *Phys. Rev. E* **66** (3), 036403 (2002).
181. G. A. Bird, *Molecular gas dynamics and the direct simulation of gas flows*. (Clarendon, 1994).
182. S. Yuspeh, Y. Ueno, M. S. Tillack, R. Burdt, Y. Tao and F. Najmabadi, *J. Appl. Phys.* **109** (7), 076102 (2011).
183. T. Trucano, D. Grady, R. Olson and A. Farnsworth, *OSA Proceedings on Soft X-Ray Projection Lithography* **18**, 146-150 (1993).
184. G. J. Pert, *J. Plasma Phys.* **41**, 263-280 (1989).
185. S. L. Thompson, *B. Am. Phys. Soc.* **14** (8), 847 (1969).
186. S. L. Thompson and H. S. Lauson, *Sandia Labs Reports SC-RR-71 0714* (1972).
187. G. J. Pert, *J. Comput. Phys.* **49** (1), 1-43 (1983).
188. R. A. Gentry, R. E. Martin and B. J. Daly, *J. Comput. Phys.* **1** (1), 87-118 (1966).
189. D. L. Book, J. P. Boris and K. Hain, *J. Comput. Phys.* **18** (3), 248-283 (1975).
190. J. P. Boris and D. L. Book, *J. Comput. Phys.* **11** (1), 38-69 (1973).
191. J. P. Boris and D. L. Book, *J. Comput. Phys.* **20** (4), 397-431 (1976).
192. D. S. Kershaw, *J. Comput. Phys.* **26** (1), 43-65 (1978).
193. R. A. Cairns, *Laser-plasma interactions*. (SUSSP Publications, 1980).
194. R. P. Feynman, N. Metropolis and E. Teller, *Phys. Rev.* **75** (10), 1561-1573 (1949).
195. G. J. Pert, *J. Phys. B* **32** (2), 249-266 (1999).
196. L. Spitzer, *Physics of fully ionized gases*. (Interscience Publishers, 1962).
197. H. Brysk, *Plasma. Phys. Contr.* **16** (10), 927-932 (1974).
198. Y. T. Lee and R. M. More, *Phys. Fluids* **27** (5), 1273-1286 (1984).
199. G. J. Pert, *J. Phys. B* **12** (16), 2755 (1979).
200. D. Mihalas and B. W. Mihalas, *Foundations of radiation hydrodynamics*. (Oxford University Press, 1984).
201. C. D. Levermore and G. C. Pomraning, *Astrophys. J.* **248** (1), 321-334 (1981).
202. G. L. Olson, *J. Comput. Phys.* **226** (1), 1181-1195 (2007).
203. O. Schenk and K. Gartner, *Electron T. Numer. Ana.* **23**, 158-179 (2006).
204. R. B. Williams, MIT, 2005.
205. S. Fujioka, H. Nishimura, K. Nishihara, A. Sasaki, A. Sunahara, T. Okuno, N. Ueda, T. Ando, Y. Z. Tao, Y. Shimada, K. Hashimoto, M. Yamaura, K. Shigemori, M. Nakai, K. Nagai, T. Norimatsu, T. Nishikawa, N. Miyanaga, Y. Izawa and K. Mima, *Phys. Rev. Lett.* **95** (23), 235004 (2005).
206. N. H. Magee, J. Abdallah, R. E. H. Clark, J. S. Cohen, L. A. Collins, G. Csanak, C. J. Fontes, A. Gauger, J. J. Keady, D. P. Kilcrease and A. L. Merts, *Astr. Soc. P* **78**, 51-55 (1995).
207. G. D. Tsakiris and K. Eidmann, *J. Quant. Spectrosc.* **38** (5), 353-368 (1987).
208. M. Murakami, S. Fujioka, H. Nishimura, T. Ando, N. Ueda, Y. Shimada and M. Yamaura, *Phys. Plasmas* **13** (3), 21 (2006).
209. R. D'Arcy, O. Morris, H. Ohashi, S. Suda, H. Tanuma, S. Fujioka, H. Nishimura, K. Nishihara, C. Suzuki, T. Kato, F. Koike and G. O'Sullivan, *Phys. Scripta T* **144**, 014026 (2011).

210. A. Sasaki, A. Sunahara, H. Furukawa, K. Nishihara, S. Fujioka, T. Nishikawa, F. Koike, H. Ohasni and H. Tanuma, *J. Appl. Phys.* **107**, 113303 (2010).
211. W. Svendsen and G. O'Sullivan, *Phys. Rev. A* **50** (5), 3710-3718 (1994).
212. M. Klapisch, M. Busquet and A. Bar-Shalom, *Atomic Processes in Plasmas* **926**, 206-215 (2007).
213. S. Mazevet and J. Abdallah, *J. Phys. B* **39** (16), 3419-3429 (2006).
214. C. K. Birdsall and A. B. Langdon, *Plasma physics via computer simulation*. (Taylor & Francis, 2005).
215. A. Giovannini, Master's Thesis ETH Zurich, 2008.
216. P. Rebholz, Bachelor's Thesis ETH Zurich, 2009.
217. J. Hochreutener, Master's Thesis ETH Zurich, 2011.
218. G. A. Bird, M. A. Gallis, J. R. Torczynski and D. J. Rader, *Phys. Fluids* **21** (1) (2009).
219. G. A. Bird, presented at the DSMC07 meeting, Santa Fe, 2007 .
220. S. Sakabe and Y. Izawa, *Phys. Rev. A* **45** (3), 2086-2089 (1992).
221. P. Banks, *Planet. Space. Sci.* **14** (11), 1085 (1966).
222. A. Dalgarno, M. R. C. Mcdowell and A. Williams, *Philos. Tr. R. Soc.* **250** (982), 411-425 (1958).
223. K. Nanbu, *IEEE T Plasma Sci* **28** (3), 971-990 (2000).
224. D. Oh, MIT, 1997.
225. S. S. Churilov and A. N. Ryabtsev, *Phys. Scripta* **73** (6), 614-619 (2006).
226. A. Sasaki, A. Sunahara, H. Furukawa, K. Nishihara, T. Nishikawa, F. Koike and H. Tanuma, *H. Ener. Dens. Phys.* **5** (3), 147-151 (2009).
227. Y. Tao, M. S. Tillack, K. L. Sequoia, R. A. Burdt, S. Yuspeh and F. Najmabadi, *Appl. Phys. Lett.* **92** (25), 251501 (2008).
228. A. Endo, H. Hoshino, T. Suganuma, M. Moriya, T. Ariga, Y. Ueno, M. Nakano, T. Asayama, T. Abe, H. Komori, G. Soumagne, H. Mizoguchi, A. Sumitani and K. Toyoda, *Proc. SPIE* **6517**, O5170-O5170 (2007).
229. V. Bakshi, *Proceedings of the Sematech EUVL Symposium*, Vancouver (2006).
230. Y. B. Zeldovich, Y. P. Raizer and W. D. Hayes, *Physics of shock waves and high-temperature hydrodynamic phenomena*. (Dover, 2002).
231. V. Y. Ternovoi, A. S. Filimonov, V. E. Fortov, I. V. Lomonosov, D. N. Nikolaev and A. A. Pyalling, *Shock Compression of Condensed Matter* **429**, 87-90 (1998).
232. K. V. Khishchenko, *Joint 21st AIRAPT and 45th EHPRG International Conference on High Pressure Science and Technology Vol. 121*, Catania, 2008.
233. T. Aota, *Proceedings of the Sematech EUVL Symposium*, Barcelona (2006).
234. Y. Tao, H. Nishimura, S. Fujioka, A. Sunahara, M. Nakai, T. Okuno, N. Ueda, K. Nishihara, N. Miyanaga and Y. Izawa, *Appl. Phys. Lett.* **86** (20), 201501 (2005).
235. K. Nishihara, *Proceedings of the Sematech EUVL Symposium*, Vancouver (2006).
236. P. Hayden, A. Cummings, N. Murphy, G. O'Sullivan, P. Sheridan, J. White and P. Dunne, *J. Appl. Phys.* **99** (9), 093302-093304 (2006).
237. C. S. Koay, S. George, K. Takenoshita, R. Bernath, E. Fujiwara, M. Richardson and V. Bakshi, *Proc. SPIE* **5751**, 279-292 (2005).
238. O. Morris, P. Hayden, F. O'Reilly, N. Murphy, P. Dunne and V. Bakshi, *Appl. Phys. Lett.* **91** (8), 081506 (2007).
239. Y. Tao, M. S. Tillack, K. L. Sequoia, R. A. Burdt and F. Najmabadi, *Ultrafast X-Ray Sources and Detectors* **6703**, A7030-A7030 (2007).

-
240. Y. Ueno, H. Hoshino, T. Ariga, T. Miura, M. Nakano, H. Komori, G. Soumagne, A. Endo, H. Mizoguchi, A. Sumitani and K. Toyoda, Proc. SPIE **6517**, B5173-B5173 (2007).
 241. K. Takenoshita, C. S. Koay, S. George, S. Teerawattansook, M. Richardson and V. Bakshi, J Vac. Sci. Technol. B **23** (6), 2879-2884 (2005).
 242. N. R. Bowering, I. V. Fomenkov, D. C. Brandt, A. N. Bykanov, A. I. Ershov, W. N. Partlo, D. W. Myers, N. R. Farrar, G. O. Vaschenko, O. V. Khodykin, J. R. Hoffman, C. P. Chrobak, S. N. Srivastava, I. Ahmad, C. Rajyaguru, D. Golich, D. A. Vidusek, S. De Dea and R. R. Hou, J. Micro-Nanolith. Mems Moems **8** (4) (2009).
 243. T. Tomie, S. Sarjono, H. Yashiro, H. Moriwaki and I. Matsushima, Proc. SPIE **6151**, 61511P (2006).
 244. T. de Resseguier, L. Signor, A. Dragon, M. Boustie, G. Roy and F. Llorca, J. Appl. Phys. **101** (1), 013506-013507 (2007).
 245. L. P. Hsiang and G. M. Faeth, Int. J. Multiphase Flow **21** (4), 545-560 (1995).
 246. T. G. Theofanous, G. J. Li and T. N. Dinh, J. Fluids Eng. **126** (4), 516-527 (2004).
 247. M. Masnavi, M. Nakajima, K. Horioka, H. P. Araghy and A. Endo, J. Appl. Phys. **109** (12), 123306 (2011).
 248. B. Rollinger, L. S. Bozinova and R. S. Abhari, *Proceedings of the Sematech EUVL Symposium*, Miami (2011).

Nomenclature

Abbreviations

CE	Conversion Efficiency
CFD	Computational Fluid Dynamics
CI	Configuration Interaction
CRM	Collisional Radiative Model
DSMC	Direct Simulation Monte Carlo
EOS	Equation Of State
EUV	Extreme Ultraviolet
EUVL	Extreme Ultraviolet Lithography
FE	Finite-Element
FFT	Fast Fourier Transform
FWHM	Full-Width at Half Maximum
HVM	High Volume Manufacturing
IBA	Inverse Bremsstrahlung Absorption
IF	Intermediate Focus
LDV	Laser Doppler Vibrometry
LPP	Laser-produced plasma
LTE	Local Thermodynamic Equilibrium
ML	Multi-Layer
NA	Numerical Aperture
OOB	Out-Of-Band
PIC	Particle-In-Cell
PZT	Lead Zirconate Titanate
RHD	Radiation Hydrodynamic

Symbols

a	Jet radius
c	Speed of sound
c_v, c_p	Specific heats
d_{drop}	Droplet spacing
e_e	Electron energy density
e_i	Ion energy density
F	Frequency
H	Planck constant
I	Emission intensity
J	Imaginary unit
k^*	Non-dimensional wave number

l_{obs}	Observation distance
M	Mass
n	Number density
n_c	Critical density
n_e	Electron density
p	Pressure
p_a	Acoustic pressure
t	Time
t_b	Breakup time
t_{drop}	Droplet timing interval
u, v	Velocity
v_c	Capillary velocity
v_{drop}	Droplet velocity
v_0	Jet velocity
B	Emissivity function
D_{drop}	Droplet diameter
D_l	Lateral droplet displacement
D_n	Nozzle diameter
E	Radiation energy density
Kn	Knudsen number
L	Length
Mx	Mode x
Oh	Ohnesorg number
Q_{las}	Laser power
Q_{rad}	Radiated power
Re	Reynolds number
T	Temperature
T_e	Electron temperature
U	Voltage
We	Weber number
Y	Admittance
Z	Mean ionization

Greek Symbols

γ	Growth rate
δ	Disturbance function
ε	Dielectric permittivity
ζ	Damping coefficient
η	Lagrangian coordinate
κ	Opacity coefficient
λ	Wavelength

μ	Dynamic viscosity
ν	Photon frequency
ρ	Density
σ	Surface tension
τ	Optical thickness
φ	Phase
ω	Frequency in radians

Superscripts

<i>0</i>	Initial, reference, constant value
<i>bb</i>	Backward breakup time
<i>bf</i>	Forward breakup time
<i>crit</i>	Critical point value
<i>liq</i>	Liquid phase
<i>max</i>	Maximum value
<i>mean</i>	Mean value
<i>membr</i>	Probe membrane
<i>min</i>	Minimum value
<i>norm</i>	Normalized value
<i>opt</i>	Optimum value
<i>p</i>	Pressure signal
<i>sol</i>	Solid phase

Subscripts

,	Unsteady component
-	Mean value

List of Publications

Conference Proceedings

B. Rollinger, D. Bleiner, N. Chokani and R. S. Abhari, Proc. SPIE **6921**, 92110 (2008).

D. Bleiner, B. Rollinger and R. S. Abhari, Proc. SPIE **6921**, X9210 (2008).

B. Rollinger, A. Giovannini, D. Bleiner, N. Chokani and R. S. Abhari, Proc. SPIE **7271**, 72712W (2009).

B. Rollinger, A. Giovannini, D. Bleiner, N. Chokani and R. S. Abhari, *Proceedings of the Sematech EUVL Symposium*, Prague, 2009.

B. Rollinger, O. Morris, N. Chokani and R. S. Abhari, Proc. SPIE **7636**, 76363F (2010).

B. Rollinger, A. Giovannini, O. Morris, I. Henderson and R. S. Abhari, *Proceedings of the Sematech EUVL Symposium*, Kobe, 2010.

B. Rollinger, O. Morris and R. S. Abhari, Proc. SPIE **7969**, 79692W (2011).

B. Rollinger, L. S. Bozinova and R. S. Abhari, *Proceedings of the Sematech EUVL Symposium*, Miami, 2011.

B. Rollinger, L. Bozinova, N. Gambino and R. S. Abhari, Proc SPIE **8322**, 83222P (2012).

Journal Publications

B. Rollinger, M. Mansour and R. S. Abhari, Rev. Sci. Instrum. **83** (6), 065002 (2012).

R. S. Abhari, B. Rollinger, A. Z. Giovannini, O. Morris, I. Henderson and S. S. Ellwi, J. Micro-Nanolith. Mem. Moems **11** (2), 021114 (2012).

Patents

R. S. Abhari, A. Z. Giovannini, B. Rollinger, D. Bleiner, United States Patent No. 2012/0025109 (2012).

B. Rollinger, R. S. Abhari, A. Z. Giovannini, I. Henderson, WO No. 2012/136343 (2012).

Curriculum Vitae

Bob Rollinger

Born on March 26, 1981 in Luxembourg, citizen of Luxembourg.

Education

1987-1993 Primarschule Mamer, Luxembourg.
1993-2000 Athénée de Luxembourg, Luxembourg.
2000 Diplôme de fin d'études secondaires de la section B mathématiques.

Studies

2001-2006 Study of mechanical engineering at the Swiss Federal Institute of Technology (ETH Zurich), Switzerland.
2006 Master's thesis at the Laboratory for Energy Conversion (LEC), ETH Zurich.
2006 MSc ETH in Mechanical Engineering, ETH Zurich.
2007-2012 Doctoral student at LEC, ETH Zurich.
2012 PhD graduation

Professional Experience

2001 Internship at Delphi Automotive, Luxembourg.
2004 Internship at Alstom Power, Switzerland.
2007-2012 Research assistant and student coordinator at LEC, ETH Zurich.